Investigating the role of curvature on the formation and thermal transformations of soot

Jacob W. Martin

Supervisor: **Prof. Markus Kraft**

Department of Chemical Engineering and Biotechnology

University of Cambridge

This dissertation is submitted for the degree of

Doctor of Philosophy

Churchill College   July 2020

"I ... express a wish that you may, in your generation, be fit to compare to a candle;
that you may, like it, shine as lights to those about you; that, in all your actions,
you may justify the beauty of the taper by making your deeds honourable and
effectual in the discharge of your duty to your fellow-men."
– Michael Faraday, *The Chemical History of a Candle (1861), 183*

"No one after lighting a lamp hides it under a jar, or puts it under a bed, but puts it
on a lampstand, so that those who enter may see the light."
– New Revised Standard Edition *Luke 11:33*

Declaration

I hereby declare that except where specific reference is made to the work of others, the contents of this dissertation are original and have not been submitted in whole or in part for consideration for any other degree or qualification in this, or any other university. This dissertation is my own work and contains nothing which is the outcome of work done in collaboration with others, except as specified in the text and Acknowledgements. This dissertation contains fewer than 65,000 words including appendices, bibliography, footnotes, tables and equations and has fewer than 150 figures. Some of the work in this dissertation has been published:

1. **Martin, J. W.**, Slavchov, R. I., Yapp, E. K., Akroyd, J., Mosbach, S., and Kraft, M. (2017). The polarization of polycyclic aromatic hydrocarbons curved by pentagon incorporation: the role of the flexoelectric dipole. The Journal of Physical Chemistry C, 121(48):27154–27163.

2. **Martin, J. W.**, Bowal, K. L., Menon, A., Slavchov, R. I., Akroyd, J., Mosbach, S., and Kraft, M. (2019). Polar curved polycyclic aromatic hydrocarbons in soot formation. Proceedings of the Combustion Institute, 37(1):1117–1123.

3. **Martin, J. W.**, Botero, M., Slavchov, R. I., Bowal, K., Akroyd, J., Mosbach, S., and Kraft, M. (2018). Flexoelectricity and the Formation of Carbon Nanoparticles in Flames. The Journal of Physical Chemistry C, 122(38):22210–22215.

4. Bowal, K., **Martin, J. W.**, Misquitta, A. J., and Kraft, M. (2019). Ion-induced soot nucleation using a new potential for curved aromatics. Combustion Science and Technology, 191(5):1–19.

5. **Martin, J. W.**, Menon, A., Lao, C. T., Akroyd, J., and Kraft, M. (2019). Dynamic polarity of curved aromatic soot precursors. Combustion and Flame, 206:150–157.

6. **Martin, J. W.**, de Tomas, C., Suarez-Martinez, I., Kraft, M., and Marks, N. A. (2019b). Topology of disordered 3D graphene networks. Physical Review Letters, 123(11):116105

7. **Martin, J. W.**, Hou, D., Menon, A., Akroyd, J., You, X., and Kraft, M. (2019). Reactivity of polycyclic aromatic hydrocarbon radicals: implications for soot formation. The Journal of Physical Chemistry C, 123(43):26673.

The work presented in this dissertation has also contributed, to a lesser degree, to the following publications:

8. Grančič, P., **Martin, J. W.**, Chen, D., Mosbach, S., and Kraft, M. (2016). Can nascent soot particles burn from the inside? Carbon, 109:608–615

9. Botero, M. L., Sheng, Y., Akroyd, J., **Martin, J. W.**, Dreyer, J. A., Yang, W., and Kraft, M. (2018). Internal structure of soot particles in a diffusion flame. Carbon, 141:635–642.

10. Bowal, K., **Martin, J. W.**, and Kraft, M. (2019). Partitioning of polycyclic aromatic hydrocarbons in heterogeneous clusters. Carbon, 143:247–256.

11. Bowal, K., Grancic, P., **Martin, J. W.**, and Kraft, M. (2019). Sphere encapsulated Monte Carlo: Obtaining minimum energy configurations of large aromatic systems. The Journal of Physical Chemistry A, 123(33):7303–7313.

12. Menon, A., Dreyer, J. A., **Martin, J. W.**, Akroyd, J., Robertson, J., and Kraft, M. (2019). Optical band gap of cross-linked, curved, and radical polyaromatic hydrocarbons. Physical Chemistry Chemical Physics, 21(29):16240–16251.

13. Pascazio, L., **Martin, J. W.**, Botero, M. L., Sirignano, M., D'Anna, A., and Kraft, M. (2019). Mechanical properties of soot particles: The impact of crosslinked polycyclic aromatic hydrocarbons. Combustion Science and Technology, pages 1–21.

14. Salamanca, M., Botero, M. L., **Martin, J. W.**, Dreyer, J. A., Akroyd, J., and Kraft, M. (submitted). Influence of cyclic fuels on the soot formation process in co-flow diffusion flames

15. Pascazio, L., **Martin, J. W.**, Bowal K., and Kraft, M. (submitted). Exploring the internal nanostructure of soot with nanoindentation: A reactive molecular dynamics study

Jacob W. Martin

July 2020

Acknowledgements

Abstract

In this work, the role of curved polycyclic aromatic hydrocarbons (cPAH) on the initial formation mechanism and thermal transformations of soot was explored. Experimental and computational techniques were used to probe the integration, presence and impact of internal pentagonal rings on the nucleation mechanism of these particulates. A significant charge polarisation was found to occur when an internal pentagonal ring pyramidalises the aromatic network. Phase contrast transmission electron microscopy allowed for the extent of conjugation and degree of curvature to be determined in early soot nanoparticulates with 15 aromatic rings and two pentagons being the median species. The dipole moment of such a species was calculated to be 5.32 debye. The polarity was found to be persistent at flame temperatures with inversion and fluctuations being minimal. Homogeneous nucleation was considered with homodimerisation energies with one or two internal pentagonal rings within cPAH found to be comparable in energy to flat PAH (fPAH) homodimers of similar weight, with more pentagons reducing the binding energy. Ion-induced nucleation was considered with binding energies calculated between chemi-ions and cPAH suggesting small stable clusters at flame temperatures. However, physical and ion-induced nucleation of cPAH were found to be insufficient alone to explain the formation of soot. The impact of curvature on the reactivity of PAH were then studied. Strong crosslinks between σ-radicals and cPAH were found to form at their rim due to decreased aromaticity. Partially saturated rim-based pentagonal rings were also found to form localised π-radicals that allow stacked and bonded complexes to form, suggesting a covalently stabilised soot nucleation. Finally, the curved geometry of highly annealed soot, otherwise known as non-graphitising carbon, was explored using annealed molecular dynamics simulations and a discrete mesh analysis method. Analysis of the angular defect of the meshes revealed an excess of negative curvature. The coexistence of curved and layered ribbon-like structures was found to be possible due to the presence of a small number of non-sp^2 defects such as screw dislocations and free edges, which will impact the synthesis of novel carbon materials and the oxidation of thermally annealed soot. The incorporation of curvature and pentagonal rings is therefore considered critical for understanding the properties, formation and destruction of combustion generated carbonaceous particles and other carbon materials.

Contents

List of Figures

List of Tables

Chapter 1

Introduction

> *"... I asked him whether there was a great fire anywhere? For the streets were so full of dense brown smoke that scarcely anything was to be seen. "O dear no, miss," he said. "This is a London particular".".*
>
> – Charles Dickens, *Bleak House (1852), 13-4*

1.1 Introduction by candlelight

When staring into the yellow light of a candle flame you are, in fact, observing glowing microscopic soot particles formed from the incomplete combustion of the candle wax. Michael Faraday made the simple candle flame the focus of his famous Christmas lectures in the mid-1800s [118]. Firstly, by placing a clay pipe into the base of the flame he showed that the white wax vapour, the fuel for the candle, could be extracted and subsequently lit (see Figure 1.1a for a modern reproduction). Then, raising the tube into the yellow part of the flame, he extracted black smoke or carbon particulate that could not sustain a flame (Figure 1.1b).

(a) White smoke due to wax vapour.

(b) Black smoke due to soot.

(c) Shadow cast by soot in the flame.
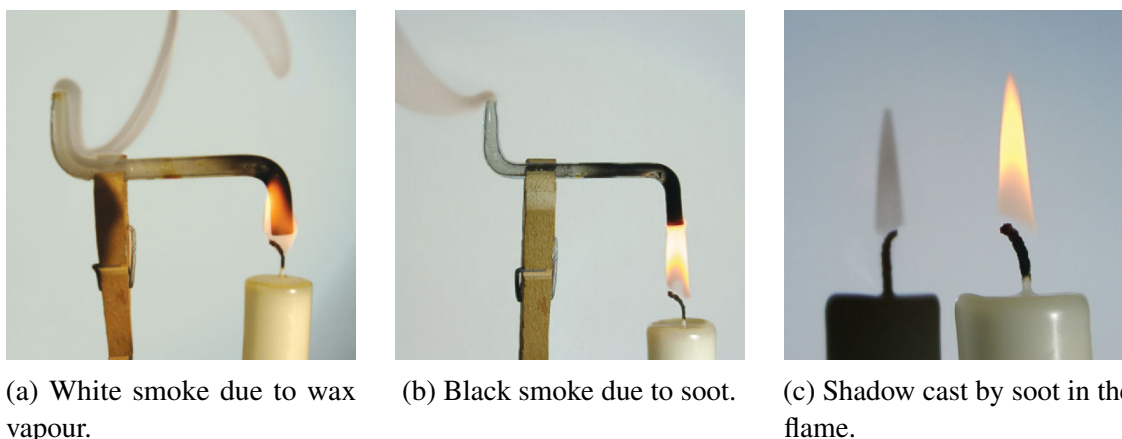
Figure 1.1 Experiments performed by Faraday in his 1848 Christmas lectures [351]. Used with permission from Wiley ©.

Faraday then shone a light on the flame to cast a shadow, showing that while the soot emits light it also absorbs it (Figure 1.1c). This soot was then able to be collected by placing a piece of metal into the yellow flame to leave a black soot deposit.

We are now able to directly examine these microscopic soot particulates from Faraday's early experiments using electron beams. Figure 1.2 shows the microscopic structures that are found in a flame. Figure 1.2a shows the secondary electrons emitted from scanning electrons over the small soot particulates on the micron scale. These structures are a hundredth of the width of a hair (so approximately 1 micron across). Figure 1.2b shows the shadow cast in the transmitted electron beam from a single soot particle. By tilting the soot particle in the TEM, a 3D reconstruction can be drawn (Figure 1.2c).

A self-similar or fractal-like structure is observed, where small carbon spheres (primary particles) of 0.01–0.05 microns (10–50 nanometres) in diameter are attached in a random arrangement, making up what is called an aggregate.
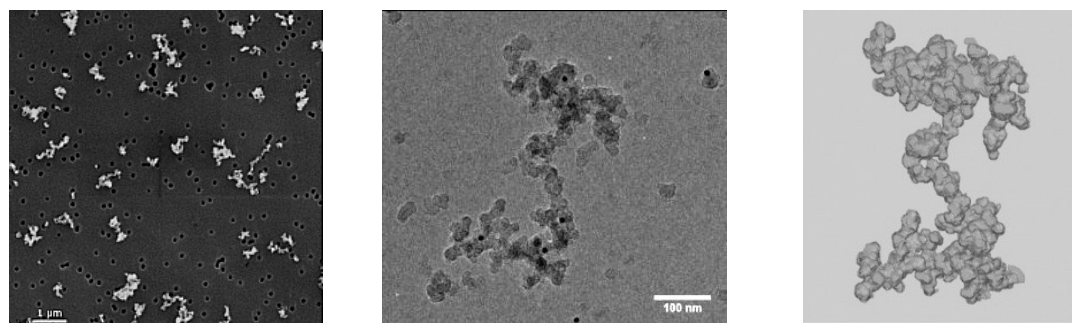
(a) Scanning electron micrograph [367].

(b) Transmission electron micrograph [310].

(c) 3D reconstruction of 1.2b [310].

Figure 1.2 Imaging of soot aggregates. Used with permissions from John Wiley and Sons © and Elsevier CC BY 4.0.

Imaging the internal structure of these primary particles can be achieved by collecting the transmitted electrons scattered from molecules within. Disc-shaped molecules aligned with the electron beam scatter electrons most effectively and appear as dark fringes in this imaging technique (phase contrast or high resolution transmission electron microscopy). Figure 1.3a shows such an image and highlights the concentric arrangement of aromatic molecules within the particle.
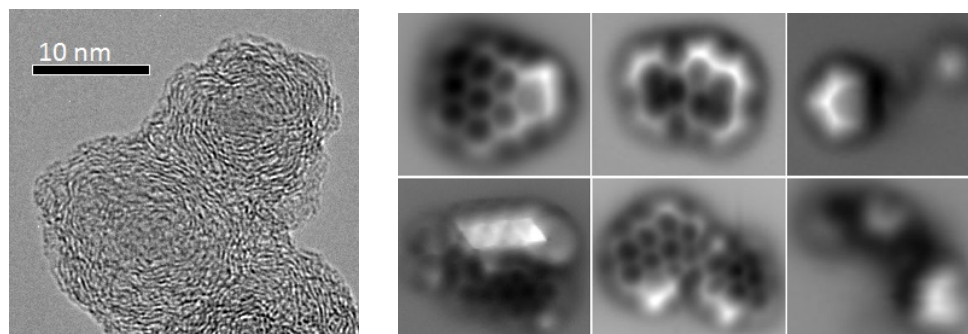
(a) HRTEM image of the internal structure of soot primary particles.

(b) Gas phase aromatics immediately before the onset of sooting [371].

Figure 1.3 Primary particles and gas phase aromatic molecules. Used with permissions from Elsevier CC BY 4.0.

Figure 1.3a also reveals a disordered core 2–5 nm in size containing smaller aromatic species with no clear fringes, which are often observed in aromatic fuels [415]. These are thought to be sub-primary particles 2–6 nm in size. Other techniques reveal two distinct sub-primary particles, one with the aromatics connected via their edges and the other made up of aromatic molecular stacks [438]. We will return to the sub-primary particles, but for

now will consider the gas phase molecules present just before the formation of the first nanoparticles.

These molecules have recently been imaged using non-contact high resolution atomic force microscopy (HR-AFM) [371]. This technique allows the bonding network to be directly imaged in planar aromatics, providing the first insights into the variety of arrangement of rings within these disc-shaped molecules. Hexagonal arrangements of carbon atoms bonded to three other carbon atoms are seen with their edges terminated by hydrogen – a molecular "chicken wire". Different reactive radicals were also seen, suggesting the possibility of reactions between these aromatic species.

Pentagonal arrangements of carbon atoms were also seen, predominantly on the edge of the molecules but also as partially embedded pentagonal rings, where >2 of the pentagon's edges are bordered by hexagonal rings. Curved polycyclic aromatic hydrocarbons (cPAH) can be formed from complete enclosure of a partially embedded pentagonal ring by acetylene addition [130].
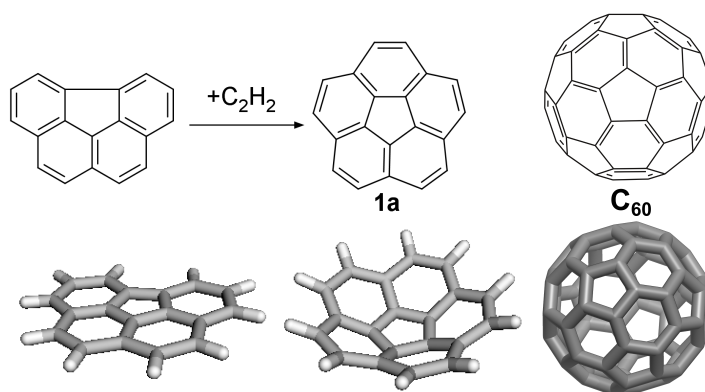
This cPAH, corannulene **1a**, is actually found in small concentrations in flames [238]. Evidence also exists for significantly curved larger aromatic molecules, which are currently unable to be imaged at the bond resolution with HR-AFM [371]. Bent fringes in electron micrographs, e.g. Figure 1.3a, have long been seen as an indication of species with multiple embedded pentagonal rings [153, 147, 437]. Low pressure flames are even able to produce molecules with 12 pentagons, allowing for complete closure of the bowl into a molecular cage of carbon, **C_{60}** fullerene [142].

Returning to sub-primaries or nanoparticles, surprisingly, their formation mechanism from the gas phase aromatic molecules is the least well understood aspect of carbon particulate formation [438]. To put it plainly, the transformation from molecules to nanoparticles is still not understood. One of the goals of this thesis is to explore the impact of curved species clustering and reactivity on nanoparticle formation.

Further transformations await the nanoparticles as they grow and are heated by the flame. The thermal treatment drives off hydrogen at the edge of the aromatic molecules, allowing them to crosslink. These crosslinks are unable to be imaged in electron micrographs such as Figure 1.3a. However, from hardness measurements using a technique called nanoindentation it is clear that most molecules within soot are highly crosslinked hard carbon resembling charcoal [32] (see Table 3.2). These properties inhibit the breakdown of soot by oxidation in engine exhaust after-treatment systems. This thermal transformation is also critical for making the most extensively produced nanoparticles in the world – combustion synthesised carbon black.

A flame provides a certain degree of thermal treatment, leading to a low level of carbonisation. On the other hand, extreme thermal treatment (>2000 K) of soot, carbon black, coal and practically any biomass gives rise to an interesting puzzle – these materials cannot convert into graphite (are non-graphitisable), instead forming glassy carbon. Figure 1.4a shows a complex tangle of layered graphene ribbons within this glassy carbon produced from carbon black. The bends and polyhedral shapes found in these micrographs were one of the early indicators that the nanostructure of carbon black contained curved fullerene-like structures [174, 167]. However, how the curves and layers of this nanostructure coexist in glassy carbon remains unknown.
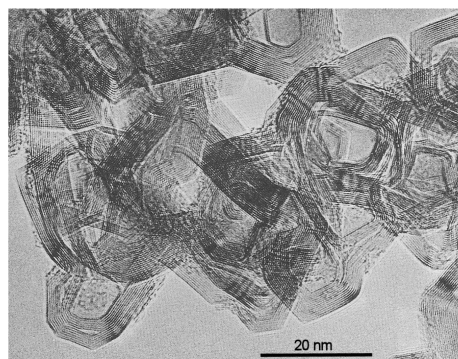
(a) Phase contrast transmission electron microscopy of thermally treated carbon black (2600 °C) showing ribbon-like structures [21].
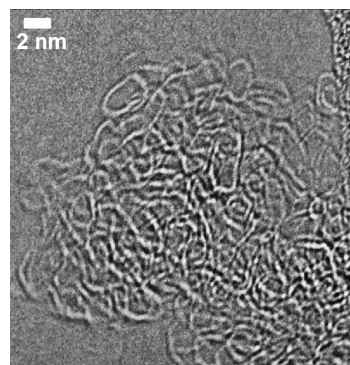
(b) Porous carbon foam produced from activation of a soot particle with oxygen at 900 °C [416].

Figure 1.4 Thermally annealed carbon black and activated soot particulates. Used with permission from the Royal Society of Chemistry © and Elsevier CC BY 4.0.

A recent experiment observing the thermal annealing of soot, while also oxidising the structure to reduce its density, produced a porous carbon foam otherwise known as an activated carbon [416] (see Figure 1.4b). As with glassy carbon, this nanostructure is unknown.

In this thesis, the impact of curved aromatic species on the formation of combustion nanoparticles will be explored, as well as the transformation under heating of carbons into glassy or porous carbon. However, before we explore these questions we need to understand why answering them is of pressing importance.

1.2   Motivation

Two main motivations can be detailed for understanding carbon particulate formation in flames: materials and environmental pollutants. Firstly, a variety of industrially useful carbon particles can be synthesised in flames, such as carbon blacks and more recently carbon nanomaterials. Secondly, soot pollution poses significant environmental hazards related to human health and its impact on the global climate.

1.2.1   Materials

Carbon particulates in flames continue to be used for a variety of applications, which requires an understanding of how to tune their nanostructural ordering during formation.

The oldest use of combustion carbons was as black pigments for inks [149, 81, 311]. Prehistoric cave paintings used carbon particulates [81] (see Figure 1.5) as well as the oldest known tattoos preserved on a 5,300-year-old caveman [314]. Egyptians used carbon ink for writing on papyrus 4,600 years ago [67]. Recent analysis of papyrus from Egypt and Greece has found copper and lead compounds in these carbon inks indicating that their synthesis occurred alongside metallurgy [67] and pottery glazes [92] (Figure 1.5). Chinese inks were produced from the particularly resin-rich pine [149]. The carbon was then mixed with an animal glue as a binder and formed into a dry stick that could be rubbed with water on an inkstone to produce ink. This technology was transferred to India where it was then exported to Europe and became known as Indian ink. Sheng Kuo (1031–1095) suggested the production of Chinese ink sticks from petroleum as deforestation was beginning to limit pine supplies during the Song Dynasty due to the expansion of the iron industry [392]. The Greeks and Romans significantly increased the production of carbon black for decoration. Between 30 and 15 BC, the architect Vitruvius wrote a description for the building of brick-lined rooms inside which resins were burnt to produce carbon black that collected on the walls. This was mixed with gum arabic to produce black ink [152]. The 15th century Gutenberg press made use of an oil-based carbon ink [66]. The printing of many thousands of books in Europe rapidly increased the need for combustion carbons, which relied primarily on the pine resins from Germany's Black Forest [66].
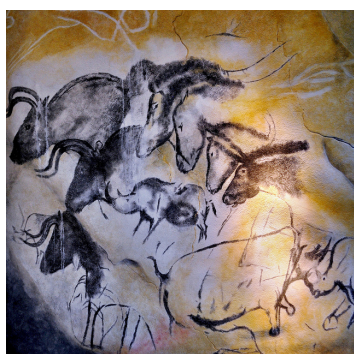
(a) Prehistoric animal drawing in charcoal and soot date 35 kya in Chauvet's cave, France.
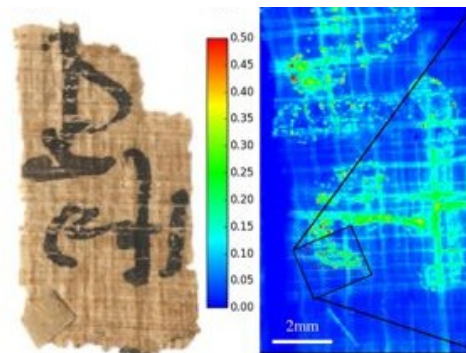
(b) Black ink [67].

Figure 1.5 Ancient uses of carbon materials. Photo credit: CC BY-SA 2.0 T. Thomas Flicker CC BY 4.0 and Elsevier ©.

Since the industrial revolution, production of carbon black has become a large scale industry with an estimated 13.9 million metric tons of carbon black being produced in 2016, predominantly from fossil fuels. This makes it the most extensively produced nanomaterial in the world [195]. These industrial/technical carbons, not to be confused with black carbon as used in climate science terminology, are produced in reactors that provide sufficient temperatures and residence times to carbonise the material to a higher degree than soot from an engine or candle flame. Carbon black therefore does not contain the harmful extractable aromatics found in many soot samples and can be produced at food grade for consumption without carcinogenic activity [265].

The majority of carbon black becomes fillers in rubber tires or inks for printers. More recently, applications include conductive carbon black for circuits and battery applications, such as in lithium ion batteries. Some applications that have yet to become widely used include electrodes in dye sensitised solar cells [294], fluorescent carbon dots for biological staining [252] and coherent spin systems for quantum computing [295].

Understanding the mechanisms of particulate formation and being able to tune their nanostructure will help to improve the material properties of carbon black for current applications and open up new advanced applications, such as quantum bits [295].

Another aspect, mentioned in the previous section, is that carbon black and oxidised soot are non-graphitising carbons that produce glassy carbons and activated carbons respectively [265]. There is considerable interest in understanding these nanostructures. Activated carbons are important for many industrial applications such as gas storage, supercapacitors, gas/water filtration and catalytic supports to name a few [265]. Glassy carbons, unlike

activated carbon, are impervious to chemicals and are therefore used in electrodes for electrochemical sensing, high temperature ceramics (such as in nuclear fusion tokamaks) and in prosthetic limbs [167]. Nanostructural understanding could provide novel carbons for these applications.

Much effort has also been put into untangling the ribbon structure of glassy carbon to produce graphite [302, 168]. Currently, graphite must be mined at high cost and is used in many electronic applications such as lithium ion batteries, 2D graphene synthesis and fuels to name a few [306]. Understanding the nanostructure of glassy carbons is then critical for stopping these structures forming. If common materials such as biomass and coal could be made to graphitise, this would greatly reduce the cost of these technologies, which is critical for addressing concerns surrounding the environment.

1.2.2   Environmental pollutants

The harmful effects of soot were first detailed in large cities where the burning of wood and coal produced significant amounts of soot. In 1774, the surgeon Percivall Pott reported a connection between soot and skin cancer in chimney sweeps [332]. This carcinogenicity is now known to be due to the small aromatic molecules that are present in or on soot that has not been sufficiently heat-treated [360] (such as napthalene, acenaphthylene, acenaphthene, fluorene, phenanthrene, anthracene, pyrene and the particularly active benzo(a)pyrene). Most studies ascribe this activity to the interactions of aromatic molecules with DNA [17]. Significant understanding of benzo(a)pyrene has been gained due to its particularly strong carcinogenic activity in humans. This molecular species is metabolised to the diol and is able to slot in between the DNA base pairs and react with guanine bases [333]. This disrupts the reading of the DNA into RNA and should then lead to cell death, however, occasionally this leads to cancerous cells instead. There is also evidence that benzo(a)pyrene can inactivate the gene that encodes for the p53 protein that functions as a tumour suppressor [326]. Thus, exposure to soot in the skin or lungs means exposure to harmful, small molecular carcinogens.

While the links between molecular species and cancer are the most well studied, there are also strong connections now being made with soot and many other diseases [183, 241, 368]. In cardiovascular disease it is thought that the smallest soot particles, <2.5 μm (PM2.5), can pass through the lungs into the blood stream triggering an immune response. This creates plaque that can potentially lead to heart attacks or strokes [162]. The issue is not restricted to cities, with the majority of the world population still cooking over open fires in rural settings [309]. In 2012, the World Health Organisation estimated that 3.3 million people die prematurely due to indoor smoke inhalation from cooking on open fires. Including the outdoor air pollution, this increases to 7 million premature deaths (including contributions

from nitrous oxides), making air pollution the cause of one in eight deaths worldwide. One recent study finds these particles are able to make their way into the fetal side of the human placenta with unknown consequences of such exposure on development [45].

Soot emissions have also been implicated in changes in the climate (in this context, the soot is often referred to as "black carbon" by climate scientists, which should not be confused with the material carbon black). There are many factors leading to the warming of the climate, which are shown in Figure 1.6. The greatest radiative forcing is due to the build-up of greenhouse gases CO_2 and CH_4 [123].
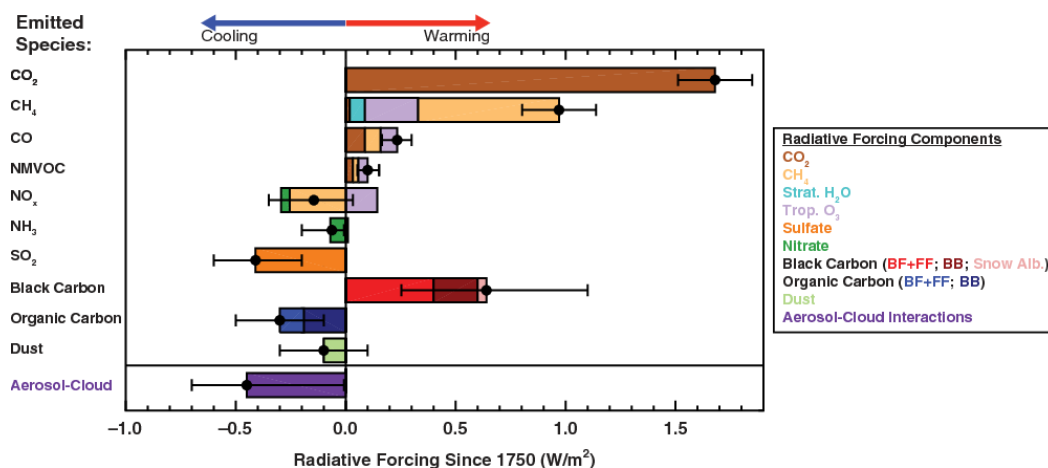
Figure 1.6 Radiative forcing of a variety of factors form 1750 to 2011 [123]. Used with permission from Taylor & Francis ©.

The second biggest contributor after these gases is black carbon (Figure 1.6 [123]). This includes the soot produced from biofuel and fossil fuel combustion (BF+FF) and from biomass burning (BB). More recent estimates place the radiative forcing of black carbon closer to +1.1 W/m^2 [39]. There is also a contribution from black carbon deposited on snow and ice (snow albedo). Soot combines with dust to provide an environment where microbes can grow. This mixture blackens the ice and reduces the amount of light normally reflected off the white ice, thus increasing the radiative forcing effect on the climate. This heat is absorbed by the blackened glaciers and sea ice, speeding up their melting [355].

One reason to aim at reducing black carbon is the rapid reduction in heating it could provide to the climate. Black carbon is persistent in the atmosphere for days to weeks and removal of soot from the atmosphere would remove a significant contributor to the global warming in weeks, whereas removal of carbon dioxide and methane from the atmosphere present a significant challenge. Black carbon emissions associated with open fires, smog formation from nitrous oxide emissions and some coal combustion also emit aerosols of ash, which cool the atmosphere by a similar degree to the radiative forcing effective [39].

However, the majority of the emitted carbon black does not emit aerosols and would therefore have a direct impact on climate change.

The combined impact of soot emissions on human health and changes in the climate require rapid reduction in soot emissions from human activities from a fundamental understanding of the processes involved.

1.3   Aim

The main aim of this dissertation is to understand the properties, formation and thermal transformation of curved pericondensed aromatic molecules in carbonaceous nanoparticles formed in hydrocarbon flames.

1.4   Novel contributions of the thesis

This dissertation presents the following novel contributions:

- A comprehensive review of soot nanoparticle formation mechanisms and experiments allowed for an updated plot of H/C ratio versus the molecular mass.

- The flexoelectric effect was found to be significant in hydrogen terminated curved aromatic molecules [267].

- Curved aromatic molecules were found to be present in early soot nanoparticles using high resolution transmission electron microscopy [270]. A minimum of six aromatic rings was found for initial curvature integration [270]. Cyclic fuels with 5-membered rings were found to integrate pentagonal rings and curvature into soot. Soot formation also was enhanced indicating a strong correlation between pentagonal rings and soot formation.

- Homogeneous nucleation of curved aromatics was explored using electronic structure calculations [270]. Flexoelectricity was found to be important, however, reduced dispersion interactions due to steric issues reduced the binding energy so that curved aromatics with one or two pentagonal rings have similar intermolecular interactions to planar aromatics of a similar mass, which are known to be unable to condense at temperatures in the flame where soot forms. Polarity was found to be persistent at flame temperatures for large cPAH [273].

- Heterogeneous nucleation of curved aromatics with chemi-ions was then found to be capable of stabilising small clusters [269, 46].

- No physical nucleation mechanism presented strong enough interactions to allow for soot growth past small nanoparticles.

- Chemical inception was then explored using chemical reactivity theory [272]. Reactive sites were calculated on recently experimentally imaged aromatic species. Curved aromatics were found to have an enhanced reactivity towards phenyl-type radicals, as were a variety of other edges.

- A new type of localised π-radical on a partially saturated rim-based pentagonal ring was also found that allowed for physical condensation and covalent bonding to occur simultaneously [272]. Electrostatic and dispersion interactions could then improve the collision efficiency of crosslinking reactions for such species.

- Finally, a nanostructure for thermally annealed disordered carbons was presented [271]. A mesh-based decomposition of computationally self-assembled disordered 3D graphenes allowed the net Gaussian curvature to be determined for the first time to be net-negative. New screw defects were found to allow for the curved network to become layered and form a 3D network of ribbons.

1.5 Structure

This document is organised into ten chapters. After some necessary background, Chapters 3–7 focus on the potential physical nucleation mechanisms of cPAH. Chapter 8 then considers the chemical bonding possible between cPAH and aromatic radicals. Chapter 9 explores how this curvature develops as hydrogen is removed and soot is fully carbonised and then graphitised materials are formed. The final chapter summarises the work and proposes further studies.

- Chapter 1 – *Introduction*

- Chapter 2 – *Background* gives a theoretical background and introduces some carbon physics and chemistry.

- Chapter 3 – *Review of carbonaceous nanoparticle formation in flames* provides an introduction to the formation of aromatic soot precursors and nanoparticles in flames as well as mapping from the available models to the experimental data to frame the results of this thesis.

- Chapter 4 – *Polarisation of PAH curved by pentagon incorporation* considers the electric field produced in an aromatic molecule when a pentagonal ring is incorporated. We find a significant dipole moment at each pentagonal disinclination and consider how to integrate such an effect into the forcefields using atom centred multipoles.

- Chapter 5 – *Quantifying and integrating curvature into soot* covers the evidence for curved aromatics in early soot including image analysis of electron micrographs. The smallest sized aromatics required to integrate curvature are then described and experimental work is detailed showing the introduction of curvature with the addition of cyclic fuels.

- Chapter 6 – *Physical nucleation of cPAH* considers the intermolecular forces driving nucleation between cPAH and also with chemi-ions in the flame. Some nucleation molecular dynamics studies are also described. Finally, the question of whether thermal fluctuations of the cPAH nullify the effect of the polarisation by rapidly changing its direction or reducing it is addressed.

- Chapter 7 – *Reactivity of cPAH and aromatic radicals* calculates the bond energies between the set of edge types, describing the increased reactivity in cPAH and the formation of localised π-radicals.

- Chapter 8 – *Curvature in thermally annealed soot* explores the curvatures within heated soot and chars where the removal of all heteroatoms, such as hydrogen, produces a layered 3D graphene. Non-sp^2 defects are found to be critical for resolving the topological complexities that arise from layered and curved carbon sp^2 networks.

- Chapter 9 – *Conclusions* provides a summary and considers future directions for the work.

Chapter 2

Background
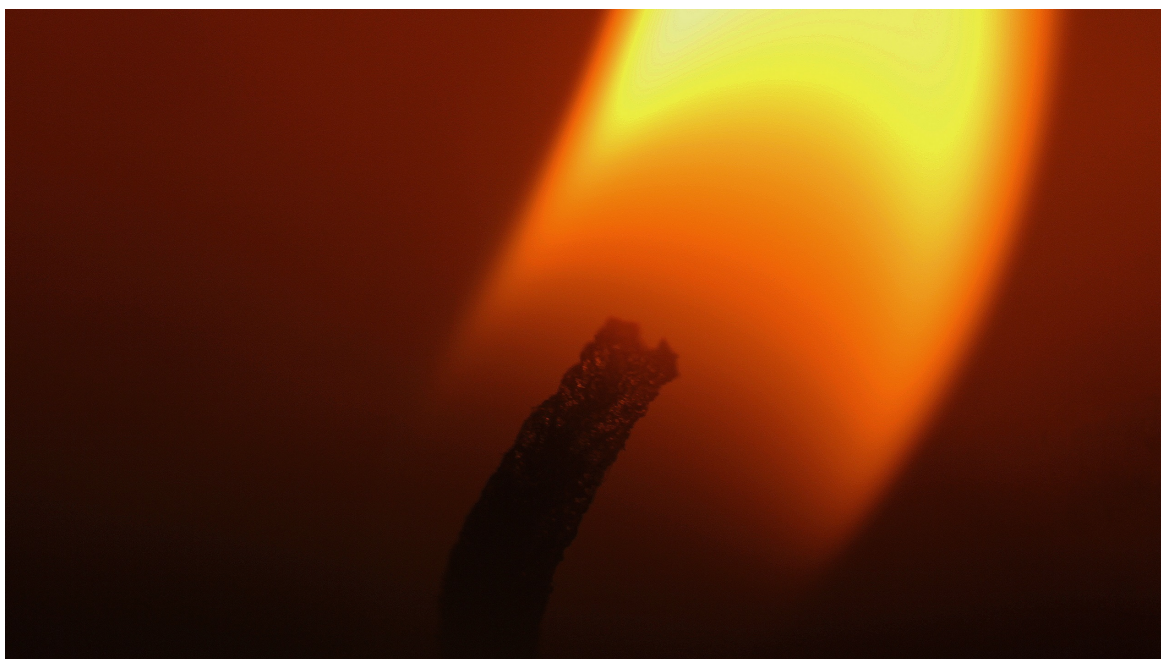
"There is not a law under which any part of this universe is governed which does not come into play, and is touched upon in these phenomena. There is no better, there is no more open door by which you can enter the study of natural philosophy, than by considering the physical phenomena of a candle."
– Michael Faraday, *The Chemical History of a Candle (1861), 13-4*

In this chapter, we begin with theoretical background. Much of this is found in physical chemistry texts. We have drawn heavily on the text from Szabo and Ostlund for electronic structure theory [408] and Leach's text on molecular modelling [245]. Particular attention will be paid to more recent theoretical descriptions, which will be used in this thesis. Finally, an introduction to carbon science will be given. This will outline the flexoelectric effect and the problem of graphitisability.

2.1   Theoretical background

2.1.1   Electronic structure theory

The goal of a molecular electronic structure problem is to mathematically describe the arrangement of charges (both electrons and nuclear cations) within a molecular system in order to attain physically measurable properties that provide predictive chemical understanding. As molecular properties are often independent of the nuclear masses and nuclear structure, this simplifies the problem to describing only the arrangement of electrons about a set of fixed nuclear cations. The decoupling of the nucleis' motion from that of the electrons is achieved due to their small sizes and the electrons' comparatively smaller mass. This is called the Born-Oppenheimer approximation. We will later see that this approximation does break down for certain molecular dynamics, such as proton systems, but we begin by posing the problem with a fixed set of nuclear charges and solving for the arrangement of electrons – the molecular electronic structure.

The first issue faced when describing the electronic arrangement is that classical mechanics is unable to describe the electron. As de Broglie postulated, and which has since been experimentally verified, matter waves are associated with the electron. For the energies of electrons bound to a nuclear charge and due to their small mass, the spacial extent of such a matter wave is on the scale of the atom-atom distances. This means that the using approximations of a point particle with a well defined position is inappropriate. Equally inappropriate would be a wave of infinite extent as the electrons are also localised in chemical systems. So how do we go about solving for the arrangement of the electrons' matter waves?

The electronic structure problem is solved in two main ways by making use of a many-body wavefunction or by considering the electrons' local density. The wavefunction approach considers the interactions between the electrons by solving the Schrödinger wave equation within the fixed potential of the atomic nuclei. For many electronic molecular systems the mean-field approximation is used with the many-body effects introduced through perturbation methods. The local density approach or density functional theory considers the local density,

comparing it to an ideal fermionic gas and computes an effective potential within which the electrons move to determine the electronic structure. In this work, the density functional approach will be combined with wavefunction methods to provide hybrid density functional methods, which provide the most accurate and economic calculation of the electronic structure. We will also use wavefunction methods that are formally able to approach the exact physical values for calibrating our more approximate theoretical methods.

Wavefunction approach

This approach makes use of a many-body complex wavefunction, $\Psi(\mathbf{r},t)$, to describe the electronic structure. The interpretation of the wavefunction is based on a probability density, which is the square of the wavefunction, and describes the likelihood of finding a particle at a certain position, otherwise known as the electron density.

$$\rho(\mathbf{r},t) = |\Psi(\mathbf{r},t)|^2 \tag{2.1}$$

By operating on the wavefunction with different quantum mechanical operators, all of the measurable physical properties can be determined from the complete wavefunction as it is an eigenvalue equation. One of the most important properties is the internal energy, which can be calculated using the Hamiltonian operator. The time independent, non-relativistic molecular Hamiltonian equation *Schrödinger equation* is written below for a fixed number of nuclei, I and electrons, i,

$$H(\mathbf{r}_i;\mathbf{R}_I)\Psi(\mathbf{r}_i;\mathbf{R}_I) = E(\mathbf{R}_I)\Psi(\mathbf{r}_i;\mathbf{R}_I) \tag{2.2}$$

$$H(\mathbf{r}_i;\mathbf{R}_I) = \underbrace{-\sum_i \frac{\nabla_i^2}{2}}_{\text{e kinetic energy}} - \underbrace{\sum_{i,I} \frac{Z_I}{|\mathbf{R}_I - \mathbf{r}_i|}}_{\text{e nuclear repulsion}} + \underbrace{\sum_{i \neq j} \frac{1}{|\mathbf{r_i} - \mathbf{r_j}|}}_{\text{e-e repulsion}} - \underbrace{\sum_{I,J} \frac{Z_I Z_J}{|\mathbf{R_I} - \mathbf{R_J}|}}_{\text{nuclear repulsion}} \tag{2.3}$$

where $\mathbf{R}_I$ are the nuclei positions and $\mathbf{r}_i$ are the electrons' positions.

The energy is then determined by left multiplying the complex conjugate of the wavefunction and performing an integration over all space,

$$E = \frac{\int \Psi^* H \Psi dr}{\int \Psi^* \Psi dr} = \frac{\langle \Psi | H | \Psi \rangle}{\langle \Psi | \Psi \rangle}. \tag{2.4}$$

written with integral and Dirac notation, both of which will be used.

This equation is only exactly solvable for one-electron systems, such as the hydrogen atom. However, for most systems the Schrödinger equation is unsolvable due to the three-body

terms introduced by the electron-electron repulsion term. How do we go about approximating such an equation?

The variational principle suggests that the wavefunction can be approximated and improved by approaching the ground state energy. The variational principle states that any approximate ground state wavefunction ϕ_0 used to describe the real ground state wavefunction Ψ_0 (which is usually unknown in many electron molecular systems) will be higher in energy. This can be shown by considering an approximate wavefunction, ϕ_0. The approximate wavefunction can be represented as a superposition of the actual eigenstates of the Hamiltonian equation, i.e. the real ground state ψ_0 and excited n states, ψ_n. The real ground and excited wavefunctions form a complete basis set of orthonormal functions and therefore will be able to reproduce any approximate ground state as a linear expansion over all excited states.

$$\phi_0 = c_0 \psi_0 + c_1 \psi_1 \ldots \tag{2.5}$$

Making use of Eq. 2.4 the energy is then,

$$\tilde{E} = |c_0|^2 E_0 + |c_0|^2 E_1 \ldots. \tag{2.6}$$

As all the excited state energies are higher than the ground state energy and the coefficients are positive, the approximate wavefunction will always be higher in energy than the real wavefunction as,

$$\tilde{E} = |c_0|^2 E_0 + |c_1|^2 E_1 \cdots \geq E_0. \tag{2.7}$$

This allows us to improve our approximate wavefunction by minimising the energy.

The first approximation is to consider combinations of the atomic orbitals of hydrogen, ϕ_{nlm}^H. These functions can be computed exactly for the hydrogen atom and are therefore a good starting point for constructing molecular wavefunctions. In spherical coordinates they have the solution,

$$\phi_{nlm}^H(r, \theta, \phi) = R_{nl}^{LF}(r) Y_{lm}(\theta, \phi), \tag{2.8}$$

which is the product of a radial function $R_{nl}^{LF}(r)$ and the spherical harmonics $Y_{lm}(\theta, \phi)$. The radial part contains the Laguerre functions multiplied by a decaying exponential in r. The Laguerre functions results in $n - l - 1$ radial nodes in the wavefunction and are inappropriate for combining into molecular orbitals. Slater was the first to consider an atomic orbital appropriate by expansion of the Laguerre functions and only keeping the highest power of r in the expansion,

$$R_{nl}^{STO}(r) = \frac{(2\zeta)^{3/2}}{\sqrt{\Gamma(2n+1)}} (2\zeta r)^{n-1} exp(-\zeta r), \tag{2.9}$$

where ζ is the Slater coefficient and Γ is the gamma function. While these describe the electronic density accurately, the numerical costs of evaluating the decaying exponential term in r are prohibitive to their usefulness. For these reasons Gaussian-type functions present a preferable alternative,

$$R_{nl}^{GTO}(r) = \frac{2(2\alpha_{nl})^{3/4}}{\pi^{1/4}} \sqrt{\frac{2^{2n-l-2}}{(4n-2l-3)!)}} (\sqrt{2\alpha_{nl}}r)^{2n-l-2} exp(-\alpha_{nl}r^2), \qquad (2.10)$$

where α_{nl} is the Gaussian coefficient. The significant difference with this function compared with the Slater-type function is that the exponential contains the square of the radius providing a zero gradient at zero radius. This leads to the incorrect behaviour of the wavefunction near the atomic nuclei. Where a non-zero gradient should exist, the function should come to a point or cusp, however multiple Gaussian type orbitals can be summed together to approach this cusp using a contracted Gaussian type orbital,

$$R_{nl}^{CGTO}(r) = \sum_{i=1}^{n} c_i R_{nl}^{GTO}(r). \qquad (2.11)$$

Two reasons that a sum of Gaussian functions is used instead of one that is more physically correct, such as a Slater-type function, is due to numerics and the approximation being accurate enough to describe bonding. Numerically, Gaussians are simple to integrate. The product of two Gaussians is another Gaussian centred at a point in between the original Gaussian functions, which can be readily integrated using tabulated values from the error function. The breakdown of the approximation near the cusp is not usually necessary to describe bonding as it is the interactions far from the nuclei that contribute most significantly to the bonding. Far from the nuclei, this approximation accurately describes the decaying exponential of the Slater-type function. In this paper each basis function will be considered a contracted Gaussian-type function (CGTO).

As mentioned, the accuracy of the wavefunction at long distances is more important than at short distances. This leads to a variety of approximations that use more detailed descriptions of the valence orbitals than the core orbitals, allowing for accurate and low-cost computation of molecular properties. These come in two families, the Pople-type basis sets and the Dunning and coworkers basis sets. The Pople-type basis set is a split-valence where the core and valence electrons are treated with a different number of contracted Gaussian basis functions. The form of this basis set is X-YZW+g** or X-YZW+g(d,p), where X is the number of Gaussians describing the core atomic orbitals, and Y and Z (and possibly W) describe the valence orbitals. These in turn are described by two (or three) orbitals, where the first is composed of Y primitive Gaussians and the second of Z primitive Gaussians. This is

called a double zeta with W giving the triple zeta. Polarisation functions can be added with *
being only a d orbital on non-hydrogen atoms and ** being a d orbital on non-hydrogen atoms
and a p orbital on hydrogen atoms [also denoted by (d,p) etc.]. For example, a commonly
used basis set 6-31G(d) for carbon, which has an electronic structure of $1s,2s,2p_x,2p_y,2p_z$,
uses one CGTO with six Gaussian functions to describe the 1s orbital, two CGTO where the
first uses three Gaussian functions and the second uses only one Gaussian function. A set of
six d functions are then added to each of these functions (we normally consider that there are
five d-orbitals, $d_{x^2-y^2}$, d_{z^2}, d_{xy}, d_{xz} but for numerical reasons six d functions are used, d_{x^2}, d_{y^2},
d_{z^2}, d_{xy}, d_{xz}, d_{yz}). This gives a total of 15 basis functions that describe nine CGTO functions
and six d functions. The + denotes diffuse s and p functions for non-hydrogen atoms and ++
denotes diffuse s and p functions for all atoms. These diffuse functions have small α values
meaning they decay slowly, are spread out and are important to include when considering
ions. The Dunning-type basis sets are similar to Pople's but are designed to converge to
the basis set limit (where addition of further basis functions does not improve the result).
Dunning-type sets are correlation consistent polarised valence X zeta basis sets (cc-pVXZ),
where X can be D,T,Q,5,6,7 (double split, triple split, etc.). The aug- prefix is included to
denote diffuse function (e.g. aug-cc-pVXZ). It should be mentioned that these functions are
optimised for the basis set limit of the wavefunction methods with higher order perturbations
[CCSD(T)], however, they are also used in density functional methods where the validity of
such a basis set convergence does not hold.

While Gaussian orbitals are optimal for the small molecular systems treated here they are
by no means the best option for all electronic structure problems. For experiments involving
core shell electrons, Gaussian functions are unable to describe the cusp with high enough
accuracy and either Slater-type orbitals or numerical orbitals are required. For simulations
of periodic crystals or plane wave basis functions, periodic functions such as sinusoids
are preferable. They have numerical advantages as the basis set can be constructed to be
orthogonal with respect to the unit cell, avoiding a set of matrix diagonalisation operations.
However, many more basis sets are required to describe the system, in particular at the cusp,
that often offsets the advantage of avoiding the matrix diagonalisation.

Combining the atomic orbitals into bonding orbitals requires the same conditions for
determining the atomic orbitals of hydrogen, such as the indistinguishability of fermions,
orthogonality and normalisation, and various schemes have been developed to create com-
binations that achieve these constraints. We will focus on two main methods. One takes a
local approach, *valence bond theory*, and the other a delocalised approach, *molecular orbital
theory*.

Valence bond theory

Valence bond theory considers a localised bonding approach where atomic orbitals are combined into hybrid orbitals and then a superposition of molecular Lewis structures (or spin configurations) is used to consider the interatomic bonding interactions. We will make use of this method to describe the local polarisation of curved aromatics but not for large scale calculation, for reasons provided below.

Heitler and London developed the first atomic orbital combination scheme called valence bond (VB) theory that led to the correct description of covalent contributions to bonding for hydrogen molecules in the singlet ground state (spin paired electrons),

$$\Psi_{HL-VB}(\uparrow\downarrow) = N\left[\phi_A(\uparrow)\phi_B(\downarrow) + \phi_A(\downarrow)\phi_B(\uparrow)\right], \tag{2.12}$$

where $N = \left[2(1 + S_{AB}^2)\right]^{-1/2}$ is the normalisation constant and $S_{AB} = <\phi_A|\phi_B>$ is the overlap integral, ϕ_A is an atomic orbital function centred on atom A and vice versa for B. Spin is indicated by the up and down arrows and can take one of two states $|1> = \uparrow$ or $|0> = \downarrow$. Due to the indistinguishability of electrons (Fermionic statistics) Heitler and London realised that an averaged sum of each configuration is required to correctly describe the electronic configuration. Solutions are trivially attained from making use of this wavefunction in Eq. 2.4 and will not be shown here for brevity. However, this construction can only be applied to homodimers that dissociate homolytically, i.e. into two radicals.

Pauling, in 1931, extended this treatment. Considering molecules that dissociate into ions, he realised an ionic wavefunction must also exist,

$$\Psi_{ion}(\uparrow\downarrow) = N\left[\phi_A(\uparrow)\phi_A(\downarrow) + \phi_B(\uparrow)\phi_B(\downarrow)\right]. \tag{2.13}$$

The superposition is set up with both electrons on either one or the other atom. In this situation the hydrogen molecule would dissociate into H^+ and H^-. Noting that the Heitler-London VB wavefunction is simply the covalent bonding interactions, $\Psi_{HL} = \Psi_{cov}$, allows us to consider superposition of the two. For the hydrogen molecules this gives,

$$\Psi_{P-MVB}(\uparrow\downarrow) = N\left[\lambda\Psi_{cov} + \sqrt{1 - \lambda^2}\Psi_{ion}\right], \tag{2.14}$$

where λ is optimised at each nuclear distance to provide the lowest energy structure and describes the proportion of covalent character to the bonding. This provided the first and most basic implementation of modern valence bond theory for the singlet state of hydrogen. For an optimised solution to the hydrogen problem the covalent contribution is dominant and contributes 75% while the ionic contributes 25%.

What does it mean for the covalent and ionic states to be in a superposition? A more informative construction was provided by Coulson and Fischer in 1949 who realised the problem could be rewritten in a semilocalised form,

$$\Psi_{MVB-CF}(\uparrow\downarrow) = N' \left[\Phi_A(\uparrow)\Phi_B(\downarrow) + \Phi_A(\downarrow)\Phi_B(\uparrow)\right], \tag{2.15}$$

where $\Phi_A = \phi_A + \varepsilon\phi_B$ and $\Phi_B = \phi_B + \varepsilon\phi_A$ are the new semilocalised wavefunctions with a contribution from the neighbouring atomic orbital given by a coupling parameter ε. Expanding out the solution we arrive back at a similar form as Eq. 2.14,

$$\Psi_{MVB-CF}(\uparrow\downarrow) = N' \left[\Psi_{cov} + \frac{2\varepsilon}{1+\varepsilon^2}\Psi_{ion}\right]. \tag{2.16}$$

Therefore the contribution of the ionic interactions can be considered to "distort" the orbitals in this truly localised valence bond picture.

Going beyond homodimers, such as the hydrogen molecule we just discussed, requires the concept of hybridisation and Lewis structure resonance. Hybridisation is a helpful construction for understanding carbon's bonding geometries and describes how superpositions of atomic orbitals can produce hybrid orbitals and geometries not otherwise possible. In the case of carbon the electronic structure is $1s^2 2s^2 2p_x{}^1 2p_y{}^1$. In this configuration we would expect two covalent bonds to form with carbon, however, carbon is also known to bond tetrahedrally to four neighbours in diamond and to three neighbours in graphite and graphene. This raises two issues: how the number of bonds is increased and how orbitals oriented in the x, y and z directions allow for a tetrahedral geometry. The first issue, to do with increasing the number of bonding electrons, was explained by Pauling as an excitation of one of the 2s orbitals into the higher energy $2p_z{}^1$ orbital giving $1s^2 2s^1 2p_x{}^1 2p_y{}^1 2p_z{}^1$, with this energy being recovered due to the bonds formed. The orientation of the bonds was rationalised due to hybridisation, which is the observation that an orthogonal superposition (linear combination) of hydrogen-like atomic orbitals is an equivalent basis set that can then be used for bonding. Diamond, for example, was explained as the promotion of one of the 2s electrons into the 2p orbitals and the linear combination of these four orbitals into four new hybrid orbitals with angles between them of $109.5°$ given by the orbitals,

$$\begin{aligned}
\phi_{h_1} &= \tfrac{1}{2}\left(\phi_{2s} + \phi_{2p_x} + \phi_{2p_y} + \phi_{2p_z}\right) \\
\phi_{h_2} &= \tfrac{1}{2}\left(\phi_{2s} - \phi_{2p_x} - \phi_{2p_y} + \phi_{2p_z}\right) \\
\phi_{h_3} &= \tfrac{1}{2}\left(\phi_{2s} + \phi_{2p_x} - \phi_{2p_y} - \phi_{2p_z}\right) \\
\phi_{h_4} &= \tfrac{1}{2}\left(\phi_{2s} - \phi_{2p_x} + \phi_{2p_y} - \phi_{2p_z}\right).
\end{aligned} \tag{2.17}$$

The hexagonal arrangement of carbon in graphite was explained by the formation of three hybrids,

$$\phi_{h_1} = \frac{1}{\sqrt{3}}\phi_{2s} + \frac{\sqrt{2}}{\sqrt{3}}\phi_{2p_x}$$
$$\phi_{h_2} = \frac{1}{\sqrt{3}}\phi_{2s} - \frac{1}{\sqrt{6}}\phi_{2p_x} + \frac{1}{\sqrt{2}}\phi_{2p_y}$$
$$\phi_{h_3} = \frac{1}{\sqrt{3}}\phi_{2s} - \frac{1}{\sqrt{6}}\phi_{2p_x} - \frac{1}{\sqrt{2}}\phi_{2p_y}$$
$$\phi_{h_\pi} = \phi_{2p_z}.$$

(2.18)

The sp^2 hybridisation provides a spare orbital ϕ_{2p_z} that can be involved in aromatic bonding as will be discussed below. Figure 2.1 schematically shows the three hybrid orbitals found for carbon in grey with the unhybridised orbitals shown in blue.
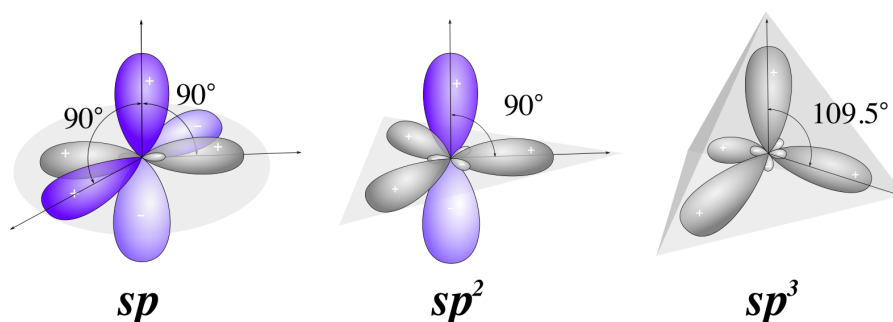
Figure 2.1 Three hybridisation states of carbon that can be constructed from a combination of the s and p orbitals. The hybrid orbitals formed are shown in grey and those not involved in hybridisation are shown in blue.

The second aspect of valence bond theory is the use of Lewis bonding structures that are in superposition or resonance. Lewis, in 1916, proposed that a bond could be described by pairings of the valence electrons in a molecule. Pauling realised that the atomic or hybrid orbitals could be paired into bonds matching those of their Lewis structures. These Lewis structures were then placed into superposition to provide the molecular electronic configuration. Confusingly the term resonance is also used to describe the covalent bonding interaction when two atomic orbitals combine as in Eq. 2.13. Therefore, we will refer to the superposition of bonding configurations as Lewis resonance. Radicals that can exist in many Lewis resonance structures are said to be resonantly stabilised radicals (or in the molecular orbital approach below, delocalised π-radicals).

Early application of valence bond theory to chemical problems by Pauling and others led to incorrect predictions that have recently been remedied with modern valence bond theory methods [379]. Examples such as the spin configuration of oxygen, the photochemistry of C_2 and the electronic configuration of benzene have been incorrectly described by valence bond theoretical methods. Many of these errors arose due to either too few Lewis structures being

considered in their molecular electronic configuration or the constraint of only considering 2-centre, 2-electron bonds. Modern valence bond theory methods such as generalised valence bond (GVB) and spin coupled valence bond theory (SC-VB) are able to accurately reproduce the results of multiconfiguration molecular orbital theory, which we will discuss next. The challenge of using valence bond theory for large structures is the steep increase in computational cost of considering all spin configurations.

We will make use of orbital hybridisation in this work to describe strained carbon nanostructures but will not make use of Lewis resonance to describe the molecular systems as the molecules explored are too large to make this practical. We will therefore turn to an approximation that works surprisingly well for molecules at their equilibrium distances – molecular orbital theory.

Molecular orbital theory

Molecular orbital theory is a non-local description of bonding within molecular systems as it considers delocalised molecular orbitals. We will again use the hydrogen molecule to introduce this theory. A molecular orbital is constructed from a linear combination of atomic orbitals in this manner,

$$\phi_\sigma = N(\phi_A + \phi_B). \tag{2.19}$$

The wavefunction is written as a product of the molecular orbitals. We can rewrite this with the different spin configurations in an expanded form,

$$\Psi_{MO}(\uparrow\downarrow) = \phi_\sigma(\uparrow)\phi_\sigma(\downarrow) \tag{2.20}$$
$$= N^2 \left[\phi_A(\uparrow) + \phi_B(\uparrow)\right]\left[\phi_A(\downarrow) + \phi_B(\downarrow)\right] \tag{2.21}$$
$$= N^2 \left[\phi_A(\uparrow)\phi_B(\downarrow) + \phi_A(\downarrow)\phi_B(\uparrow) + \phi_A(\uparrow)\phi_A(\downarrow) + \phi_B(\downarrow)\phi_B(\uparrow)\right]. \tag{2.22}$$

This equation can be compared with valence bond theory where the first two terms are the covalent wavefunction from Eq. 2.12 and the last two terms are the ionic wavefunction from Eq. 2.13. This shows that the molecular orbital approach is similar to modern valence bond theory for hydrogen except that there are equal ionic and covalent contributions. These fixed, equal contributions provide a useful approximation of a molecule's electronic structure at equilibrium distances, but lead to incorrect electronic structure at non-equilibrium distances such as during homolytic bond breaking where ionic contributions should tend to zero.

Generalising the molecular orbital theory to many-electron systems will highlight the reason this approximation is helpful for calculating the electronic structure of larger molecules. Focusing for now on closed shell molecules, each molecular orbital, ϕ_j^{MO}, will be described as a linear combination of atomic orbitals,

$$\phi_j^{MO} = \sum_i^n c_{ij} \phi_i^{AO},$$

(2.23)

where the sum is over all n electrons, which are described by an atomic orbital function, ϕ_i^{AO}, multiplied by a coefficient, c_{ij}, that is optimised to provide a set of molecular orbitals giving the lowest internal energy.

We can then construct a spin orbital, e.g. $\chi_\sigma(\uparrow) = \phi_\sigma^{MO}(\uparrow)$. Unlike for hydrogen, the many-electron system requires the antisymmetry properties of the electrons to be enforced. A Slater determinant can be constructed that contains the correct properties.

$$\Psi_{MO} = \frac{1}{\sqrt{N!}} \begin{vmatrix} \chi_1(1) & \chi_2(1) & \cdots & \chi_n(1) \\ \chi_1(2) & \chi_2(2) & \cdots & \chi_n(2) \\ \vdots & \vdots & \ddots & \vdots \\ \chi_1(N) & \chi_2(N) & \cdots & \chi_n(N) \end{vmatrix}$$

(2.24)

Expansion of this determinant automatically constructs the required spin symmetries between the molecular orbitals, although the ionic and covalent contributions have equal weighting as mentioned. Now that we have a good description of the wavefunction we can consider the approximations for the Hamiltonian operator that allow it to become solvable.

The Hartree-Fock method is an effective way to calculate a molecule's electronic structure. This involves an iterative solution to the molecular Schrödinger equation by approximating the electron-electron interactions within the Hamiltonian operator using a mean-field approximation where the electrons are considered to be only influenced by an average interaction with the other electrons. The Hartree-Fock approximation also only considers a single arrangement of the electrons in the molecule, meaning only one Slater determinant is used. The Hartree-Fock equations are written as,

$$[h_a(1) + v^{HF}(1)]\chi_a(1) = \varepsilon_a \chi_a(1)(f(1))\chi_a(1) = \varepsilon_a \chi_a(1),$$

(2.25)

where $h_a(1)$ is the one-electron kinetic energy and potential energy for attraction to the nuclei. The second term describes the interaction that the electron has with the other electrons and is called the Hartree-Fock potential $v^{HF}(1)$. This is the mean field approximation where the electrons move in the mean field of the other electrons $v^{HF}(1) = \sum_{j \neq i} \int |\chi_j|^2 \frac{1}{|\mathbf{r}_j - \mathbf{r}_i|} d\mathbf{r}_j$. This

integral is further broken into two parts: the coulomb integral J_b, which averages the coulomb repulsion between each electron with all the other electrons, and the exchange integral K_b, which comes from the antisymmetric condition. By expanding the wavefunction this can be written as,

$$f(1)\sum_i^n c_{ia}\chi_i = \varepsilon_a \sum_i^n c_{ia}\chi_i. \tag{2.26}$$

Left multiplying by the atomic orbital χ_j and integrating gives,

$$\sum_i^n c_{ia}\int \chi_j f(1)\chi_i = \varepsilon_a \sum_i^n c_{ia}\int \chi_j\chi_i. \tag{2.27}$$

This is further simplified into matrix notation. The first integral becomes the Fock term F_{ji} and the second integral is the overlap integral S_{ji}. This equation can easily be solved in the computer and is called the Hartree-Fock-Roothaan equation.

$$\mathbf{FC} = \mathbf{SC}\varepsilon \tag{2.28}$$

As the Fock operator depends on its own solutions to solve the set of equations the solution must iteratively improve until the eigenequation is self-consistent. It is therefore referred to as the self-consistent field approach.

Appendix A contains a short Hartree-Fock calculation written in Python. While this is informative we have made use of the Gaussian software package throughout this manuscript to perform large scale electronic structure calculations.

The Hartree-Fock method only uses a single Slater determinant. This allows for the bonding in many-electron systems to be computed readily, in contrast to valence bond theory, but it comes with a caveat: it considers equal amounts of covalent and ionic contributions to bonding which underestimates the bond strength at the equilibrium and is completely unable to describe bond dissociation. However, this method does compute the electron-electron kinetic energy contribution exactly, which will be useful for improving another method discussed later (density functional theory).

Extending the Hartree-Fock method

For computing the electronic structure of molecules, the Hartree-Fock method always falls short of the true ground state energy. This difference is called the correlation energy as it relates to the mean field approximation that does not consider correlated electron dynamics. Post-Hartree-Fock methods have been developed to compute the correlation energy. They use either perturbation methods or many Slater determinants (different spin configurations).

This correlation energy is also of great importance to this work as dispersion interactions, which contribute significantly to intermolecular interactions, are due to electron correlation.

Perturbation methods make use of a known solution (such as the Hartree-Fock solution) and add a small perturbation to the equation to account for the undescribed physics. The Möller-Plesset (MP) method adds a fluctuation potential W to the Hamiltonian,

$$H = H_0 + \lambda W. \tag{2.29}$$

This is the difference between the true electron-electron correlation and the Hartree-Fock approximation,

$$W = H_0 - H = \sum_{i<j}^{n} r_{ij}^{-1} - \sum_{i<j}^{N} v^{HF}. \tag{2.30}$$

Different expansion orders of this fluctuation potential can be used with the first non-zero term being the second order expansion [MP(2,3,4,5 etc.)]. MP2 is often the highest order used as it scales as $\mathscr{O}(N^4)$ and gives rise to an improvement in the electronic structure. MP2 can be thought of as perturbing the ground state with all doubly excited determinants. This series unfortunately does not converge meaning that the variational principle breaks down and the estimated energy can be lower than the actual energy. It is also found that MP2 overbinds dispersion interactions [409].

The second method to describe the correlation energy is the configuration interaction method, where multiple spin configurations are brought into superposition. This will be illustrated for the hydrogen atom again. A linear combination of the bonding molecular orbital ϕ_σ and the antibonding orbital $\phi_{\sigma*}$ given by $\phi_{\sigma*} = N(\phi_A - \phi_B)$ are taken,

$$\Psi_{MO-CI} = c_1 \phi_\sigma(\uparrow)\phi_\sigma(\downarrow) + c_2 \phi_{\sigma*}(\uparrow)\phi_{\sigma*}(\downarrow). \tag{2.31}$$

The contribution of each configuration, c_1 and c_2, is optimised to produce the lowest energy. The optimisation can be performed as the variational principle applies and will converge towards the actual energy of the many-body electronic structure.

Expanding the two molecular orbitals within Eq. 2.31, the coefficients produce the correct weighting of ionic and covalent contributions. In this way it can be shown that the configuration interaction wavefunction is equivalent to the modern valence bond methods (Eq. 2.14), i.e. $\Psi_{MO-CI} = \Psi_{MVB}$.

The configuration interaction method is found to be an inefficient expansion as it is not size consistent. Instead, a different expansion named the coupled cluster method is more often used. This method uses an exponential excitation operator to expand the single Slater

determinant into higher excited states,

$$He^T\Psi = Ee^T\Psi. \tag{2.32}$$

By considering the contributions from these higher excited states, almost all of the correlation energy can be recovered. The inclusion of all single and double excitations, with triple excitation only considered via a perturbation [referred to as CCSD(T)], provides chemically accurate energies and geometries. However, the cost of the calculation scales as $\mathscr{O}(N^7)$ which makes only small molecules able to be described using this theory. The plot below (Figure 2.2) shows the convergence of wavefunction methods as the level of theory and the basis set size are increased [175].
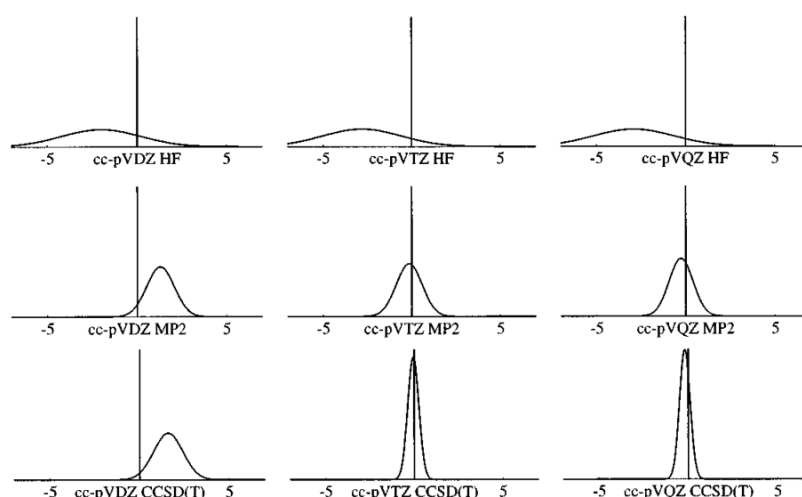
Figure 2.2 Error in the equilibrium bond lengths (in pm) compared with experimental X-ray structures [175].

We will make use of CCSD(T) calculation results as standard calculations for intermolecular interactions. These are able to describe the dispersion interactions to a high level of accuracy given a significant sized basis set. Table 2.1 considers the scaling of such calculations.

This scaling shows that wavefunction based calculations that provide chemical accuracy [CCSD(T)] are only possible for small molecules < 30 atoms. Therefore, other methods have been developed for computing the electronic structure of large molecules.

Density functional theory (DFT)

While wavefunction methods are variational and therefore able to converge upon the exact solution for a multi-reference infinite basis set calculation, they are very computationally

Table 2.1 Scaling of electronic structure calculations

Method	Scaling[†]
DFT(pure)[*]	$\mathcal{O}(N^3)$
HF, DFT(hybrid)[*]	$\mathcal{O}(N^{3-4})$
MP2, DFT(double hybrid)	$\mathcal{O}(N^4)$
CCSD	$\mathcal{O}(N^6)$
CCSD(T)	$\mathcal{O}(N^7)$

[†] where N is a measure of the system size including number of electrons and/or number of basis functions.
[*] DFT pure functionals and hybrid functionals will be described below.

costly. This is due primarily to the difficulty in calculating the electron-electron interactions, which demands two electron integrals to be performed and many excited Slater determinants to be considered. Instead, efforts to reframe the electronic structure problem in terms of the local electron density has been found to be an attractive alternative for large systems. However, it took some time before it could become a useful theory.

Early attempts to achieve such a mapping from the electron density to the ground state energy led to the development of the Thomas-Fermi model in 1927. The total energy was calculated solely as a functional of the electron density $\rho(r)$,

$$E[\rho(\mathbf{r})] = T_{TF}[\rho(\mathbf{r})] + U_{eN}[\rho(\mathbf{r})] + U_{ee}[\rho(\mathbf{r})] + V_N, \quad (2.33)$$

$$E[\rho(\mathbf{r})] = C_F \int [\rho(\mathbf{r})]^{5/3} d^3r + \int \rho(\mathbf{r}) V_N(\mathbf{r}) d^3r + \frac{1}{2} e^2 \int \frac{\rho(\mathbf{r}) \rho(\mathbf{r}')}{|\mathbf{r} - \mathbf{r}'|} d^3r \, d^3r' + V_N(\mathbf{r}), \quad (2.34)$$

where $T_{TF}[\rho(\mathbf{r})]$ is the classical kinetic energy of an electron gas with $C_F = \frac{3h^2}{10m_e} \left(\frac{3}{8\pi}\right)^{2/3}$, $U_{eN}[\rho(\mathbf{r})]$ is the electron nuclei potential energy, $U_{ee}[\rho(\mathbf{r})]$ is the electron-electron repulsion and V_N is the potential energy between the nuclei. Importantly, the energy is only a function of the atomic coordinates and the electron density $\rho(r)$. The model does not include any exchange energy, which was added by Dirac in 1928 (Thomas-Fermi-Dirac model). Sheldon in 1955 showed for calculations on N_2 that no stable bonding configuration would be formed [380], which was proved to be the case for all molecular systems by Teller in 1962 [410].

Improving the kinetic energy operator $T[\rho(\mathbf{r})]$ by including quantum mechanical effects meant that bonding within molecules could be achieved, for example that of Weizsäcker [445],

$$T_W[\rho(\mathbf{r})] = \frac{1}{8} \frac{\hbar^2}{m} \int \frac{|\nabla \rho(\vec{r})|^2}{\rho(\mathbf{r})} dr. \quad (2.35)$$

Balàzs in 1967 was able to show that the addition of this term to the Thomas-Fermi-Dirac equation allowed stable diatomic molecules to form [20]. This highlighted the importance of a quantum mechanical treatment of the kinetic energy in allowing molecular bonding to be stable and renewed interest in using density functional methods.

Up until this point, many had doubted whether density functional theory would be able to derive the actual ground state energy of a molecular system as wavefunction methods can. Hohenberg and Kohn put DFT on a more solid footing in 1964 by proving that the energy of a molecular system is a functional of the electron density to within an additive constant [184]. It was thought that physical quantities could only be determined from the quantum mechanical operators acting on the wavefunction. This proof suggested that all of the physically determinable quantities could be calculated from only the electron density – if an exact functional could be determined. The advantage to be gained was being able to determine the electronic structure using only the electron density in three spatial coordinates instead of computing the many-body wavefunction with configuration interaction, which is costly.

Around this time Kohn and Sham showed a different way of calculating the kinetic energy term by using a similar method from molecular orbital theory. They considered a fictitious system of non-reacting electrons within Kohn-Sham orbitals $\phi_i(r)$ that computes the kinetic energy term in a similar manner to Hartree-Fock theory [225] and is exact. This is written as,

$$T_{KS} = \sum_{i=1}^{N} \int d\mathbf{r} \; \phi_i^*(\mathbf{r}) \left(-\frac{\hbar^2}{2m} \nabla^2 \right) \phi_i(\mathbf{r}).$$ (2.36)

As well as the kinetic energy term, the two electron terms were also improved by Kohn and Sham to include exchange and correlation using a local density approximation [225]. This can be written as,

$$E_{xc}^{LDA} = \int d\mathbf{r} \varepsilon_{xc}^{uni.}(\rho(\mathbf{r}))\rho(\mathbf{r}),$$ (2.37)

where the exchange correlation energy for a uniform electron gas is $\varepsilon_{xc}^{uni.} = \varepsilon_x + \varepsilon_c$, with the exchange term, ε_x, by Slater (LSDA) and the correlation term, ε_c, by Vosko, Wilk and Nusair (VWM) becoming the most widely used. These local density approaches were found to be able to describe systems with slowly varying density such as periodic crystals but underestimated exchange energy and overestimated correlation energy. Improvements to the correlation energy were also gained by using quantum Monte Carlo methods [61]. However, the energy was still poorly described for many molecules.

The density functional method was further improved by including the local generalised gradient approximation (GGA) of the electron density in the computation of ε_{xc}. Becke, in

1988, produced one of the most well-known descriptions of the local gradient of the electron density to compute the exchange (B88) [25]. This combined with Lee, Yang and Parr's correlation energy (LYP) produced the most widely-used GGA, called BLYP,

$$E_{xc}^{BLYP} = E_x^{B88} + E_c^{LYP}. \tag{2.38}$$

In Table 2.1 the scaling of the GGA's [DFT(pure)] computational cost is shown to scale with $\mathscr{O}(N^3)$, a significant improvement over wavefunction methods.

While the GGA functionals provided significantly improved results compared with LDA, it was found that the electron exchange was not well described. Hartree-Fock theory, however, provides an exact description of electron exchange so combining it with GGA was suggested – a hybrid DFT. These combination schemes were challenging. The first, most popular version was called B3LYP,

$$E_{xc}^{B3LYP} = (1 - a_0)E_x^{LSDA} + a_0 E_x^{HF} + a_x E_x^{B88} + E_c^{LYP} + (1 - a_c)E_c^{VWM}, \tag{2.39}$$

where $a_0 = 0.20$, $a_x = 0.72$ and $a_c = 0.81$. Looking again at Table 2.1 the scaling of DFT(hybrid) computational cost is shown to scale with $\mathscr{O}(N^{3-4})$. This is similar scaling to the Hartree-Fock method, however, unlike Hartree-Fock the electron correlation is included in DFT(hybrid), which significantly improves the quality of the electronic structure.

Perdew noticed that there is a hierarchy in DFT approximations with each level of approximation including more information about the electron distribution. Table 2.2 shows the classes of approximations, some popular functionals, the parameters that need to be computed to determine the exchange-correlation energy at each level and the error from each class.

Table 2.2 Hierarchy of DFT approximations proposed by Perdew with average errors in energy

Classes	Functionals	Parameters	Error[†]
double hybrids	ωB97X-2, B2PLYP	$E_{xc}\left[\rho, \nabla\rho, \nabla^2\rho, \psi_{occ.}, \psi_{vir.}\right]$	1.8
hybrid meta-GGA	M06-2X, M11	$E_{xc}\left[\rho, \nabla\rho, \nabla^2\rho, \psi_{occ.}\right]$	~2.5
hybrid GGA	B3LYP, B97, PBE0, HSE	$E_{xc}\left[\rho, \nabla\rho, \psi_{occ.}\right]$	3.3
meta-GGA	TPSS M06-L	$E_{xc}\left[\rho, \nabla\rho, \nabla^2\rho\right]$	4.4
GGA	PBE, BLYP	$E_{xc}\left[\rho, \nabla\rho\right]$	5.3
LDA	VWN, GPW92	$E_{xc}\left[\rho\right]$	12.0

† weighted total mean absolute deviation (WTMAD) (kcal/mol) compared with GMTKN30 benchmark database for general main group thermochemistry, kinetics and noncovalent interactions [148].

Along with the hybrid density functionals mentioned which only include the occupied KS orbitals $\psi_{occ.}$ there are also meta-GGA methods that include the second derivative of the electron density – $\nabla^2 \rho$. These have been found to contain similar information as the kinetic energy of the electrons and is also called the Laplacian of the electron density (we will later use the Laplacian to look for regions of electron localisation).

Mixing the Laplacian and the Hartree-Fock exchange constructs the hybrid meta-GGA functional. One example of this is the Minnesota functional M06-2X. This has been found to provide highly accurate energies and kinetics and is widely used in combustion for computing reaction pathways (in benchmark calculations having WTMAD=2.2 kcal/mol [148]). We will make use of M06-2X to determine accurate bond energies in Chapter 8.

Finally, the correlation energy can be improved by incorporating the MP2 method into DFT (otherwise known as PT2) to give double hybrid functionals. These include information about the virtual orbitals $\psi_{vir.}$ through this perturbation approach. Table 2.2 also shows the weighted total mean absolute deviation (WTMAD) calculated from each class of functional showing the decrease in error as the description becomes more complete [148].

While intramolecular physics are well described by the hybrid meta-GGA and double hybrid functionals they are unable to capture all of the long range electron correlations. These correlations are critical for describing the intermolecular or van der Waals interactions between molecules. The simplest way to incorporate these effects is to add a pair-wise empirical forcefield to the energy computation $E_{DFT-D} = E_{KS-DFT} + E_{disp}$. Grimme and coworkers developed the widely used B97D functional [155] where the correction is a damped attractive potential of the form,

$$E_{disp} = -s_6 \sum_{i=1}^{N_{at}-1} \sum_{j=i+1}^{N_{at}} \frac{C_6^{ij}}{R_{ij}^6} f_{dmp}(R_{ij}), \qquad (2.40)$$

where N_{at} is the number of atoms in the system and energy is computed as the sum of the binary interaction energies of all atomic pairs; s_6 is a scaling factor that depends on the DFT method used (we used B97 with a s_6 value of 1.25). It should also be noted that the spin dependent components of the exact exchange integrated into the B97 hybrid were also modified as they were linearly dependent on this scaling coefficient. C_6^{ij} are the dispersion coefficients for the atomic pair ij and R_{ij} is the respective intermolecular distance. A damping constant is used to ensure stability in the calculations for overlapping geometries,

$$f_{dmp}(R_{ij}) = \frac{1}{1 + e^{-d(R_{ij}/R_r - 1)}}, \qquad (2.41)$$

where R_r are the vdW radii and $d = 20$. The dispersion coefficients and vdW radii for carbon and hydrogen used are $C_6^C = 1.75$, $R_r^C = 1.452$ Å and $C_6^H = 0.14$, $R_r^H = 1.001$ Å respectively with the coefficient between two different atoms being determined using the geometric mean $C_6^{ij} = \sqrt{C_6^i C_6^j}$.

More advanced methods compute the dispersion interactions through atom-centred distributed polarisabilities such as exchange-hole dipole moment (XDM) theory and many-body dispersion (MBD) theory. They can provide <2 kJ/mol of error compared with CCSD(T) methods. However, for most cases, as long as the DFT-D method has correctly fitted the C_6 parameters for a given system, energies with errors <4 kJ/mol can be attained [51]. SAPT(DFT) is another method that will also be used as a benchmark providing similar accuracies to CCSD(T) but with considerably fewer computational resources. In this method the dispersion is computed using coupled Kohn-Sham theory or time dependent DFT, a perturbation method that allows the computation of the polarisabilities and dispersion energy.

When computing the intermolecular interactions between two species it is important to also consider the basis set superposition error (BSSE). This is an error that comes about from having an incomplete basis set. A monomer's energy is expected to lower with increasing basis set size and this should converge to the basis set limit. When two species are brought together the basis set from one monomer can improve the description of the electronic structure on the other monomer, converging the whole system to the basis set limit more rapidly. This has the effect of lowering the energy and appearing as a fictitious binding energy. In order to correct for this (known as counterpoise correction) the monomer energy is computed with the basis sets from the other species present but without the nuclear charges. It can also be practically eliminated by performing the calculations with large basis sets.

Ab initio molecular dynamics

Ab initio molecular dynamics (AIMD) techniques are used in Chapter 7 to study the thermal fluctuation of the cPAH. These methods have been used previously in combustion to study the dimer lifetimes of pyrene using semi-empirical quantum theory [369]. In Born-Oppenheimer molecular dynamics (BOMD) nuclei are approximated as classical ions with the forces on these ions computed from the electronic structure,

$$\partial E / \partial \mathbf{R} = \langle \Psi | \partial H / \partial \mathbf{R} | \Psi \rangle + \langle \partial \Psi / \partial \mathbf{R} | H | \Psi \rangle + \langle \Psi | H | \partial \Psi / \partial \mathbf{R} \rangle, \qquad (2.42)$$

with the first term being the Hellmann-Feynman force and the other two being the Pulay forces [365]. BOMD performs a self-consistent field calculation to iteratively determine the electronic structure at each time step, which is prohibitively expensive. One successful

approximation is the atom-centred density matrix propagation (ADMP), which propagates the electronic structure using an extended Lagrangian coupled to the nuclear positions via a fictitious mass. This significantly reduces the computational cost of such calculations. This is similar to the Car-Parrinello method, however for ADMP, the density matrix is used instead of the Kohn-Sham orbitals and atom-centred Gaussian basis functions are used instead of plane wave basis functions [365]. These features of ADMP allow the use of any hybrid density functional theory to generate the density matrix and provide a better separation between the electronic and nuclear degrees of freedom. With small timesteps ($<$0.5 fs) it has been found to accurately follow the fully converged Born-Oppenheimer MD with vibrations and energy being independent of the fictitious mass used [365, 199, 366, 250]. Since ADMP was implemented in the software Gaussian 03 it has seen applications in describing gas interactions with aromatic macrocycles [87] and has recently been used to model the formation of covalent bonds between pyrene dimers [303]. A similar method using converged semi-empirical PM3 simulations has also been employed in combustion to study PAH dimerisation at flame temperatures by Schuetz and Frenklach [369] and Wong et al. [449].

2.1.2 Nucleation

Physical condensation of molecules can often be adequately described by classical nucleation theory and will aid our discussions of whether curved aromatics are able to physically condense into soot in Chapters 6 and 7. In describing classical nucleation theory we will make use of the description in "Nucleation - Basis theory with applications" by Kashchiev [212]. Classical nucleation theory provides many of the important ideas needed in a theory of nucleation, however, it is a macroscopic theory (not built from an atomic foundation) and so there is a limit to its usefulness in describing small clusters with only a few molecules. The first concept which is helpful to consider is a first order phase transition in a van der Waals (VDW) solution. The equation of state for a van der Waals solution is,

$$\left(P + M^2 a'/V^2\right)\left(V - Mb'\right) = Mk_B T. \tag{2.43}$$

Typical values for water are a = 4.47×10^{-1} Pa m^3 and b = 30.52×10^{-6}. We can define critical values for each variable where they are equal to unity, $P_{cr} = a'/27b'^2$,$V_{cr} = 3Mb'$ and $T_{cr} = 8a'/27kb'$, with reduced coordinates defined as the reciprocal of the critical value with the current value $P' = P/P_{cr}$, $V' = T/T_{cr}$ and $T' = T/T_{cr}$. This leads to the reduced

VDW fluid at constant temperature and pressure as,

$$\left(P' + 3/V'^2\right)\left(3V' - 1\right) = 8T'.$$ (2.44)

Rewriting in terms of P the constant temperature,

$$P = \frac{8T'}{(3V' - 1)} - \frac{3}{V^2}.$$ (2.45)

Isotherms of Eq. 2.45 are plotted as a function of the reduced volume in Figure 2.3.
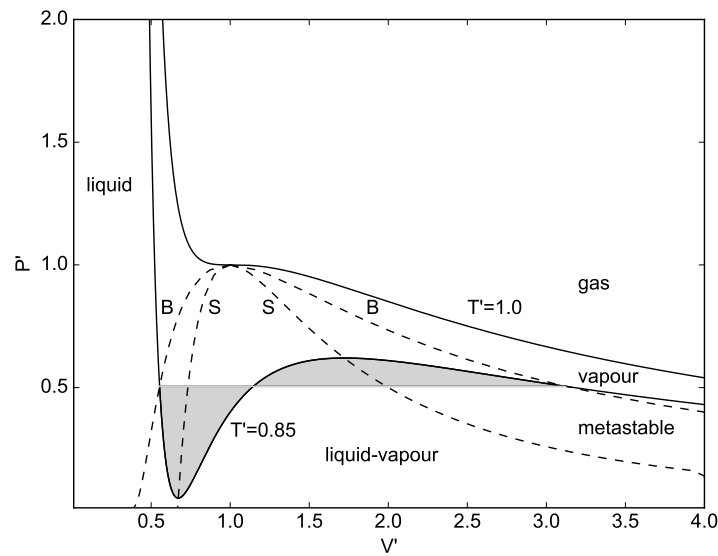
Figure 2.3 Dependence of the reduced pressure on the reduced volume of a Van der Waals gas. The area under the T'=0.85 curve leads to the binodal construction. The spinodal points come from the stationary points of the isotherms.

Unlike an ideal gas where the pressure varies with $1/V$ we see a dip in the phase diagram due to interactions. Below the critical temperature $T' < 1$ the gas is considered a vapour. Upon reducing the volume, the fluid coexists as a vapour and a liquid until it becomes entirely a liquid. Following the $T' = 0.85$ isotherm from the right tracks the metastable and liquid-vapour states. For this isotherm the fluid is in the vapour phase at large volume. As the volume is reduced the vapour moves to the metastable state. This transition into the metastable state is determined by the Maxwell construction where a line is drawn across the isotherm connecting the binodal points.

To consider when these phase transitions will occur the Gibbs free energy must be determined as the system will spontaneously move towards the state with the lowest Gibbs

free energy. The Gibbs free energy is equal to $G = F + pV$, where F is the Helmholtz free energy and is given by $F = -P(V)dV$. This leads to;

$$G(V', T') = G_{ref}(T') + Mk_B T_{cr} \left[\frac{3P'V'}{8} - \frac{9}{8V'} - T' log\left(3V' - 1\right) \right], \qquad (2.46)$$

where G_{ref} is the reference Gibbs free energy. Looking at Figure 2.4 the $P' = 0.540$
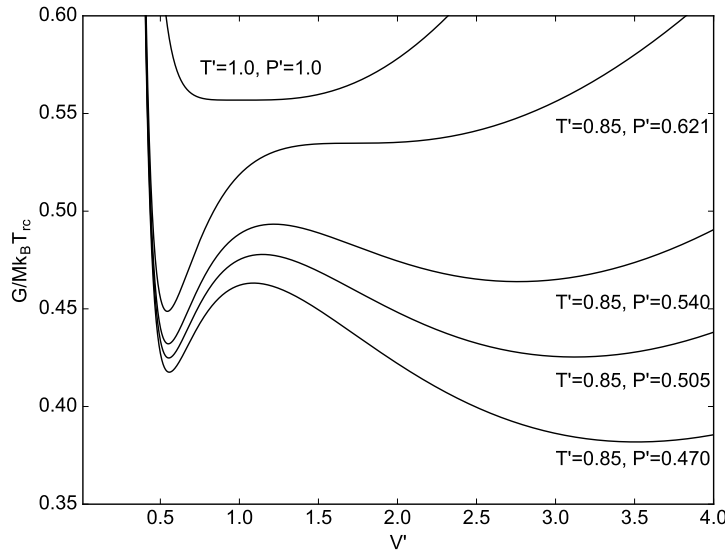
Figure 2.4 Dependence of the chemical potential on the reduced pressure and temperature of a Van der Waals gas.

isobar for $T' = 0.85$ shows that there are two minima, one for a liquid (left) and the other for a gas (right). Both have the same chemical potential. This pressure for each temperature can be plotted as the binodal points (denoted by the B in Figure 2.3). Increasing the pressure (Figure 2.4) past the binodal pressure given by Maxwell's construction leads to the liquid phase becoming lower in energy than the gas phase. However, there is a barrier between the gas and the liquid phases. This means that the transition is not always possible.

The next point of interest is when the slope of the *PV* isotherm becomes zero. This corresponds to the local maximum and minimum on the $T' = 0.85$ isotherm, called the spinodal point. In relation to the free energy (Figure 2.4) this corresponds to the $P' = 0.621$ isobar. At this point there is no barrier to the phase transformation and the gas will spontaneously change phase. This makes the region between the spinodal points unphysical and liquids are known to proceed along the Maxwell construction, a constant pressure isotherm between the binodal points. The important points to draw out of this example for soot formation is that in order for a phase transition to occur, the new phase must first and

foremost have a lower free energy than the previous phase. Also, if the supersaturation pressure is in between the binodal and spinodal points the system is not guaranteed to change phase as there is a barrier to transformation; however, if the saturation pressure surpasses the spinodal pressure then the transformation is instant and barrierless. This is assuming early soot is a liquid and is described by a physical condensation and not a chemical inception from gas to solid which has no spinodal region.

We turn now to the creation of nuclei in a metastable phase. From where does this barrier originate and how much energy is required to overcome it? From this free energy description the rate of nucleation can be determined. Classical nucleation theory states that there are two free energy contributions: a positive contribution (which resists formation of nuclei) from the creation of a new surface and a negative contribution (which drives nuclei formation) from the decrease in the free energy for the new phase due to the lower chemical potential. The latter is called the bulk contribution. For a spherical droplet this is given by,

$$\Delta W(n) = -n\Delta\mu + a\sigma n^{2/3}, \tag{2.47}$$

where the first term is the bulk term which drives the transformation and the second term is the energy to form a new surface given by the surface tension σ. a is a geometric factor and for spherical droplets is given as $a = (36\pi v_0^2)^{1/3}$, where v_0 is the molar volume. The change in chemical potential $\Delta\mu$ can be written in terms of the supersaturation of the vapour, $\Delta\mu = k_B T \ln S$, where $S = p_V/p_{sat}$, which is the ratio of the vapour pressure to the vapour saturation pressure. The dependence for water at a supersaturation of $S = 4$ is shown in Figure 2.5. What can be seen is a critical cluster size at the maximum of $\Delta W(n)$. In classical
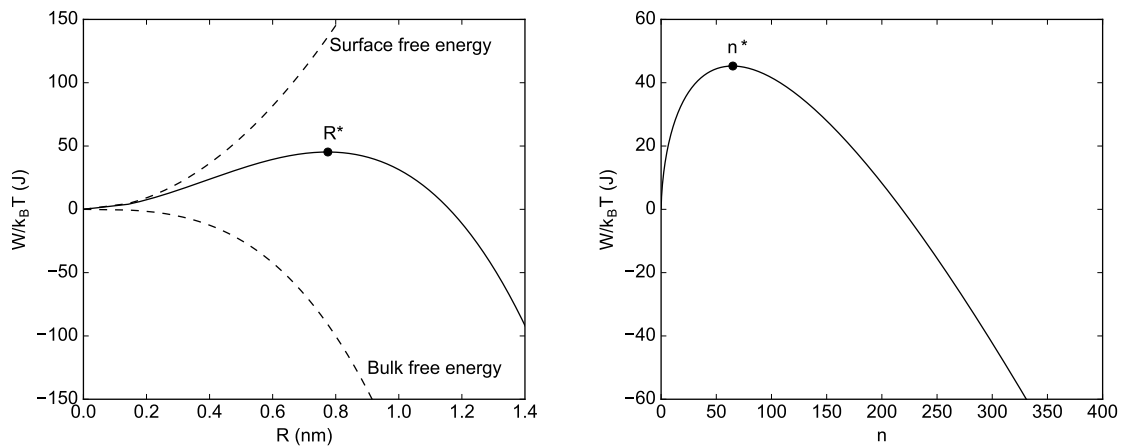
Figure 2.5 Work of cluster formation as a function of cluster size and radius for water droplets forming in a vapour at a supersaturation of 4 at $T = 293$ K.

nucleation theory, this is the energy barrier that must be overcome to allow for spontaneous growth of a cluster and can be determined from the derivative of the work of cluster formation to be,

$$n^* = 8c^3 v_0^2 \sigma^3 / 27\Delta\mu^3, \tag{2.48}$$

$$W^* = 4c^3 v_0^2 \sigma^3 / 27\Delta\mu^2. \tag{2.49}$$

At these conditions, the critical nuclei size is only 78 molecules for water. One critique of the theory is whether bulk properties like surface area are physically meaningful at clusters of fewer than 100 molecules where a large proportion of the molecules are surface species. However, for the purpose of understanding soot formation it is seen as an adequate place to begin the discussion.

Ion-induced nucleation

Ions are often required to overcome the nucleation barrier. For example, salt spray from the sea is required for cloud formation. The contribution to the Gibbs free energy from an applied electric field can be considered as such,

$$\Phi_{el}(n) = (1/2) \int [\mathbf{E}_2(\mathbf{r}) \cdot \mathbf{D}_2(\mathbf{r}) - \mathbf{E}_1(\mathbf{r}) \cdot \mathbf{D}_1(\mathbf{r})] d\mathbf{r}, \tag{2.50}$$

where the displacement field is due to the electrical properties of each medium and is given as $\mathbf{D}(\mathbf{r}) = \varepsilon \mathbf{E}$, where ε is the electric permittivity. Making use of the electric permittivity of the cluster and medium $\varepsilon_{c/m}$ and assuming they are r independent we can write,

$$\Phi_{el}(n) = -(\varepsilon_0/2)(\varepsilon_m - \varepsilon_c) \int_{V_n} \mathbf{E}_1(\mathbf{r}) \cdot \mathbf{E}_2(\mathbf{r})] d\mathbf{r}. \tag{2.51}$$

The electric field around a point charge before and after cluster formation is given as,

$$E_{r,1} = Q/4\pi\varepsilon_0\varepsilon_m r^2, \tag{2.52}$$

$$E_{r,2} = Q/4\pi\varepsilon_0\varepsilon_c r^2. \tag{2.53}$$

Making use of $n = (4\pi/3v_0)(R^3 - R_i^3)$ where R_i is the radius of the ion and integrating from R_i to R gives,

$$\Phi_{el}(R) = (1/\varepsilon_c - 1/\varepsilon_m)(Q^2/8\pi\varepsilon_0)(1/R_i - 1/R). \tag{2.54}$$

This suggests that for ions to improve nucleation $\varepsilon_c > \varepsilon_m$. Considering water nucleation, at a point charge we can plot the impact on the work of nucleation (Figure 2.6). The first interesting feature is a minimum n_{min} which arises from the short range interactions with the

molecules of water and the ion of interest. It is interesting that these ionic nuclei can exist even if the supersaturation is lower than one. If the supersaturation is greater than one then the cluster can, if it overcomes the barrier n^*, grow in size. On the right of Figure 2.6 the free energy barrier for the ion-induced and ion-free classical nucleation are compared.
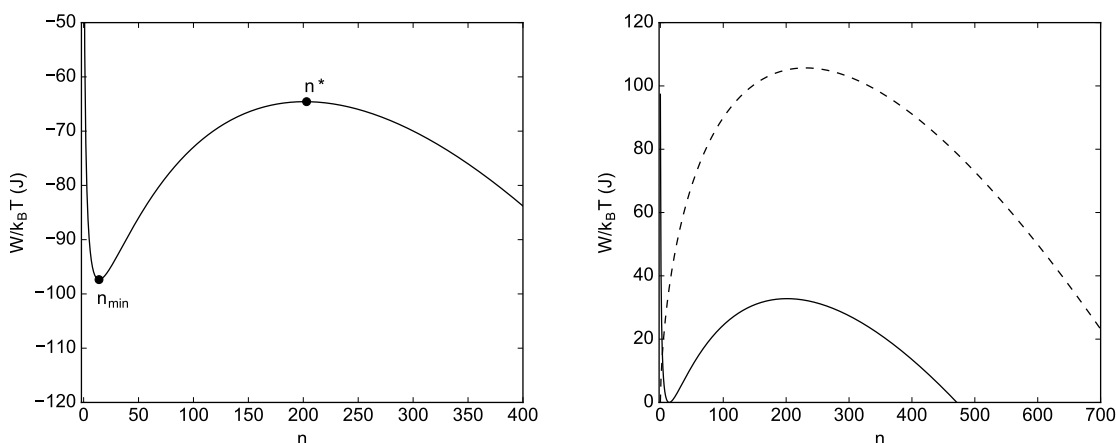
Figure 2.6 Work of cluster formation as a function of cluster size and radius for water droplets forming on ions in a vapour at a supersaturation of 2.5 at $T = 293$ K (left). The free energy curve is shifted so that n_{min} is at zero and the barrier for cluster formation is shown also for nucleation without an ion (right).

The barrier of cluster formation is significantly reduced in the presence of the ion for water. As the rate of cluster formation is proportional to the exponential of the barrier divided by the thermal energy, this reduced barrier makes a large difference, significantly increasing the rate of nucleation.

In summary, these are the conditions under which a supersaturated mixture will nucleate. This is not spontaneous and most often requires some nuclei to begin the process by lowering the barrier for cluster formation. These ideas will be important when discussing the nucleation of soot.

2.2 Carbon chemistry and physics

A parallel field to combustion is that of carbon materials science and nanotechnology, which will be heavily discussed in this thesis. We will briefly introduce the different carbon nanoforms, defect structures that are possible in sp^2 carbons, flexoelectricity, graphitisability of carbon materials and the synthesis of fullerenes.

2.2.1   Carbon molecules and allotropes

Figure 2.7 shows a range of carbon nanostructures. Linear chains of carbon include acetylene (C_2H_2), polyacetylenes and hydrocarbon chains, some of which are often fuels in combustion. Forming a network of carbon atoms, sp^2 bonded, are the polycyclic aromatic hydrocarbons (PAH). These are the most stable structures, with hexagonal arrangements of carbon atoms in roughly circular geometries, which maximise aromaticity. If extending PAH to infinity and stacking these layers, the bulk material graphite is constructed. A single layer of graphite is called graphene and has recently attracted significant interest due to the 2D nature of the electron system providing unique coherent electronic states [301]. Amorphous carbons are defined as those materials containing $>30\%$ sp^3 but no long range crystalline ordering. These materials form diamond-like coatings, which have been extensively used as coatings with extreme abrasion resistance [348]. Diamond is a tetrahedrally bonded carbon that forms an extended lattice of sp^3 bonded carbon atoms. Graphitic structures with sp^2 bonded carbon are more thermodynamically stabilised compared with diamond at atmospheric pressure and therefore the amount of sp^3 bonded carbon in nascent soot is 84% sp^2 bonded with mature soot approaching $>95\%$ [12]. Introducing curvature into carbon nanoforms allows a graphene layer to be curled into a carbon nanotube.
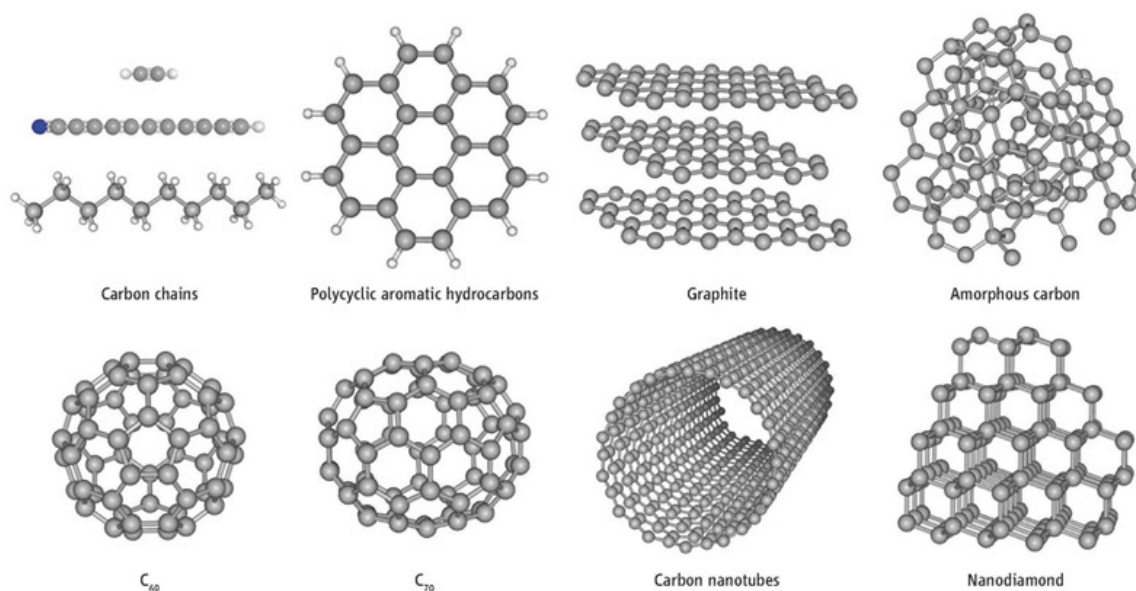
Figure 2.7 Different carbon allotropes are shown based on different hybridisations. Carbon chains are in sp and sp^3 hydridisations. Polycyclic aromatic hydrocarbons, graphite, the C_{60} fullerene, the C_{70} fullerene and carbon nanotubes with sp^2 hydridisation. Diamond and amorphous carbon with sp^3 hydridisation [111]. Used with permission from Zan Peeters.

Fullerenes were discovered in 1985 by laser ablation of a graphite target that was found to produce magic number carbon clusters C_{60} and C_{70} [234], which were later confirmed to be closed icosahedrons of carbon. Fullerenes are highly symmetric molecules containing 12 pentagonal rings that curve the hexagonal net into a closed network. These non-hexagonal rings are critical defects for warping the graphene network and forming a variety of carbon nanoforms.

2.2.2   Defects and curvature in carbon materials

We can discuss the integration of non-hexagonal rings using the language of crystallographic defects in graphene structures. Figure 2.8 shows the common topological defects in graphene. For example, the pentagonal rings in C_{60} fullerene can be characterised as defects with positive disclination. Also shown are negative disclinations that arise from the integration of a heptagonal ring within the graphene network. Combining these two disclinations provides a 5–7 dislocation. Dislocations can be assembled into lines providing grain boundaries between two misaligned graphene crystallites.

5-Disclination	7-Disclination	5-7 Dislocation	Grain boundary
$s = 60°$	$s = -60°$	$\mathbf{b} = (1,0)$	$\theta = 21.8°$
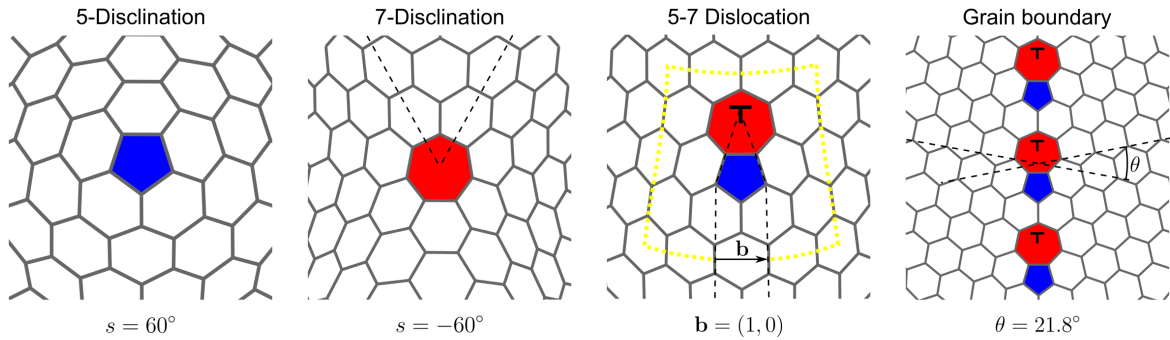
Figure 2.8 Topological defects in sp^2 carbons.

Many other defects exist in graphitic materials such as vacancies, screw dislocations, interstitial atoms and edge dislocations. These will be discussed in more detail in Chapters 4 and 8. In order to introduce this we will compare defects using the language of differential geometry on continuous surfaces. Curvature can be defined on a continuous surface by constructing two principal axes of curvature. Figure 2.9 shows the construction of the surface curvature. Firstly, the surface normal is found at a particular point. The first normal plane is formed parallel to this normal so as to produce a section of the surface. This produces a curved line from which the radius of curvature can be computed using the derivative of the tangent $\mathbf{X}_1$ along the segment $d\mathbf{s}$,

$$\kappa_1 = \frac{d\mathbf{X}_1}{d\mathbf{s}}, \tag{2.55}$$

where $\kappa = 1/R$, with R being the radius of curvature of the section at a particular point. Importantly, κ is signed which will become apparent when defining curvatures. A second normal plane perpendicular to the first tangent $\mathbf{X}_1$ is also defined with a second tangent vector $\mathbf{X}_2$, which provides a second curvature κ_2. The principal axes of curvature occur along the directions where κ_1 is maximised and κ_2 is minimised and lie along the planes of greatest and smallest curvatures, respectively.
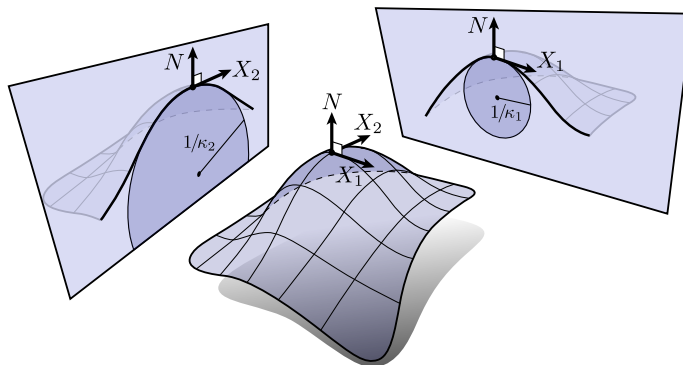
Figure 2.9 Construction of the principal axes of curvature on a surface. The two normal sections through the surface are shown. Credit: Peter Schröder CC-BY-NC-ND.

Surface curvatures can then be defined. The Gaussian curvature is the product of the principal curvatures,
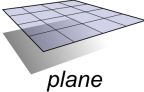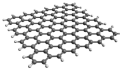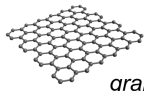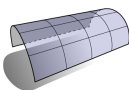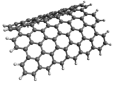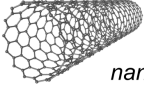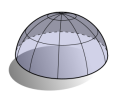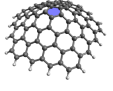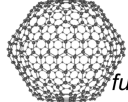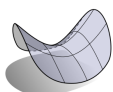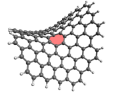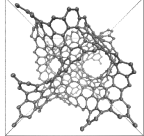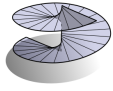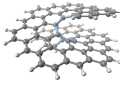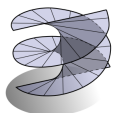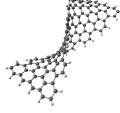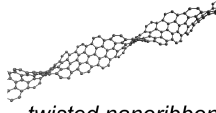
$$K = \kappa_1 \kappa_2. \tag{2.56}$$

The Gaussian curvature provides the out-of-plane warping of the network (also known as "double curvature"). Surfaces that have a non-zero Gaussian curvature are non-developable, meaning they are unable to be flattened into a plane without distortion. These are non-Euclidean geometries which are common in carbon materials. Table 2.3 shows the geometrical surfaces with their corresponding Gaussian curvatures and associated nanocarbons.

2D graphene is a developable surface that can be flattened and as such is Gauss flat. A section of a nanotube is also Gauss flat. Fullerenes contain positive disclinations providing an ellipsoidal or bowl-shaped geometry with a positive Gaussian curvature. Periodic carbon schwarzites contain hyperbolic or saddle-shaped geometry with negative Gaussian curvature. Two other defects, screw dislocations and twisted nanoribbons, are described by half or full helicoid geometries respectively, with negative Gaussian curvature (also making them hyperboloids) [221]. Screw dislocations are well known defects in graphites [176] and twisted nanoribbons have been synthesised and imaged inside nanotubes [71].

Table 2.3 Geometrical surfaces and their corresponding defects within carbon networks, curvatures and nanocarbon.

Surface	Carbon network	Principal curvatures	Gaussian curvature	Nanocarbon
plane		$\kappa_1 = 0, \kappa_2 = 0$	$K = 0$	graphene
parabaloid		$\kappa_1 > 0, \kappa_2 = 0$	$K = 0$	nanotube
ellipsoid		$\kappa_1 > 0, \kappa_2 > 0$	$K > 0$	fullerene
hyperboliod		$\kappa_1 > 0, \kappa_2 < 0$	$K < 0$	schwarzite
half-helicoid		$\kappa_1 > 0, \kappa_2 < 0$	$K < 0$	screw dislocation
full-helicoid		$\kappa_1 > 0, \kappa_2 < 0$	$K < 0$	twisted nanoribbon

For closed carbon networks, those with only sp^2 carbon atoms, the net of bonds forms a closed polyhedron, which allows the networks to be treated as closed topological manifolds [372]. One of these relationships is the Gauss-Bonnet theorem which allows Euler's polyhedron formula to be related to topological properties,

$$V - E + F = \chi = 2(1 - g), \tag{2.57}$$

where V, E and F are the number of vertices, edges and faces, respectively. χ is the Euler characteristic and for closed surfaces this becomes $\chi = 2(1 - g)$ where g is the genus or number of "holes" or "handles" (these holes are not associated with any edges but are continuous punctures formed within a continuous manifold, e.g. a torus). For polyhedra, these equations hold: $F = \sum_n F_n$, $V = \sum_r V_r$ and $2E = \sum_n nF_n = \sum_r rV_r$, where n is the

cycle number of the face and r is the connectivity or degree of the vertex. For sp^2-bonded carbon the vertices are always degree three ($r = 3$, $V = V_3$). Combining these relations with Equation 8.1 gives the Euler-Poincaré polyhedral equation,

$$\sum_n^{+\infty} (6 - n) F_n = 12 (1 - g).$$ (2.58)

Eq. 2.58 then relates the sum of rings or faces, F_n, to the genus, g, of the network (i.e. a heptagonal ring would be denoted as F_7 in this notation) [372, 160]. For example, to connect a periodic carbon schwarzite in 3D, the network must possess at least three holes, $g \geq 3$. This sets the requirement from Eq. 2.58 for an excess of non-hexagonal rings, F_n, with $n \geq 7$ providing a negatively Gaussian curved network in schwarzites. Figure 2.10 shows some types of schwarzites [285]. It is important to note that these are unit cells of a periodic crystal so the structures have no edges but are made entirely of sp^2-bonded carbon atoms. We will be examining periodic carbon networks in Chapter 8.
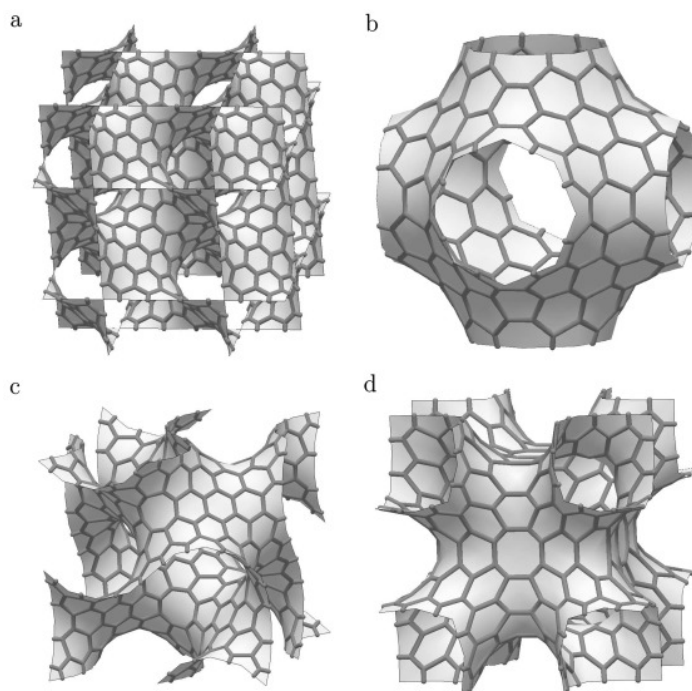
Figure 2.10 a) primitive, b) diamond, c) gyroid and d) I-graph periodic surfaces. The surfaces and the carbon bonding network are shown. Used with permission from Elsevier © [285].

The reason for the schwarzites being considered minimal surfaces is due to another metric of the surface curvature: the mean curvature $H = 1/2(\kappa_1 + \kappa_2)$. This is an extrinsic metric with units of inverse length. Systems that minimise surface area (such as soap films) are often found to contain zero mean curvature and are given the name minimal surfaces. However,

unlike soap films sp^2 carbon networks are not driven by a decrease in surface area but by reduction in the bending energy as the planar configuration has optimal π-bonding as earlier discussed. The bending energy of a surface can be defined as [158],

$$E_B = \frac{1}{2}D \int_S dA \left[2H^2 - (1-\nu)K\right],\tag{2.59}$$

where D is the flexural rigidity and ν is the Poisson ratio. For graphene, calculations suggest $D = 1.41$ eV and $\nu = 0.165$, making it remarkably stiff and providing a strong driver for reducing the bending energy and for planar graphene geometries.

The sp^2 carbon networks, however, do not describe a discrete surface, as the polyhedron's vertices are not necessarily in the same plane, therefore to define this sort of bending energy the networks need to be converted into a discrete mesh such as a triangular mesh. Often the dual of the network is used to construct this triangular mesh [158], however, this is somewhat arbitrary and found to fail for some instances. Therefore, often another geometrical construction is used based on the atom-centred pyramidalisation angle and misalignment angle that allows for a direct link with the electronic structure [299]. We will make use of a new mesh-based approach to consider the topology of disordered 3D graphene networks in Chapter 8 and will consider electric polarisation using the pyramidalisation angle, which will be introduced in the following section.

2.2.3 Flexoelectricity in carbon materials

One interesting aspect of pentagonal ring integration in sp^2 carbons is the introduction of strain. This strain leads to a pyramidalisation of the carbon atoms, particularly those associated with pentagonal rings. When this occurs the hybridisation is modified and becomes sp^3-like (see Figure 2.11).
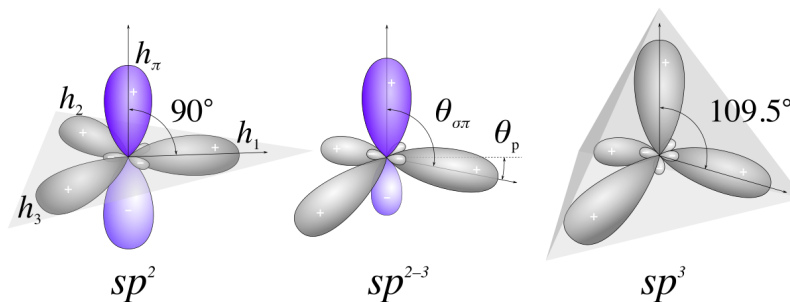
Figure 2.11 Partial hybridisation.

Haddon developed a valence bond model to describe this rehybridisation of strained carbon structures [161], which will be used in the analysis of flexoelectricity in curved PAH

molecules. Returning to the hybrid orbitals introduced earlier in Eq. 2.18, pyramidalisation then modifies the h_π orbital to contain some 2s character,

$$\phi_{h_\pi} = \frac{1}{\sqrt{1 + \lambda_\pi^2}} \left(\phi_{2s} + \lambda_\pi \phi_{2p_z} \right), \tag{2.60}$$

where the parameter λ_π determines the mixing and therefore depends on the curvature through the angle $\theta_{\sigma\pi}$ between the hybrid π-orbital, h_π, and the hybrids directed along the carbon bonds, $h_{1,2,3}$, shown in Figure 2.11,

$$\lambda_\pi^2 = \frac{1 - \cos^2 \theta_{\sigma\pi}}{2\cos^2 \theta_{\sigma\pi}}. \tag{2.61}$$

The direction of the h_π-bond's unit vector, $\mathbf{v}_\pi$, can then be determined from solving the set of orthogonality constraints $1 + \lambda_i \lambda_j \mathbf{v_i} \cdot \mathbf{v_j} = 0$, where $i, j = 1, 2, 3, \pi$, allowing $\mathbf{v}_\pi$ to be expressed as a linear combination of unit vectors along the C–C bond unit vectors $\mathbf{v}_{1,2,3}$. The pyramidalisation angle, θ_p, is often used instead, which is the angle the bonds deviate from planarity, $\theta_p = \pi/2 - \theta_{\sigma\pi}$.

This rehybridisation polarises the electronic structure giving rise to a dipole moment, μ_p [107]. Using the tight binding approach this is computed as,

$$\mu_p = e \int z h_\pi^2 d\mathbf{r} = \frac{2e\lambda_\pi}{1 + \lambda_\pi^2} \int z \phi_{2s} \phi_{2p_z} d\mathbf{r}. \tag{2.62}$$

Given that the overlap integral between the 2s and $2p_z$ orbitals is close to constant, the dipole moment is therefore linearly dependent on λ_π and in turn on the pyramidalisation angle.

The more classical definition of flexoelectricity is where a local mechanical stress (strain gradient) leads to an electric polarisation [469]. To consider its relation to piezoelectricity the electric polarisation for a dielectric material can be written as,

$$P_i = d_{ijk}\sigma_{jk} + \gamma_{ijkl}\frac{\partial \varepsilon_{jk}}{\partial x_l}. \tag{2.63}$$

The first term corresponds with the piezoelectric effect, where a bulk stress, σ_{jk}, leads to an electric polarisation with proportionality constant, d_{ijk}, being a third rank tensor. The second term corresponds with the flexoelectric effect where a strain gradient, $\frac{\partial \varepsilon_{jk}}{\partial x_l}$, leads to an electric polarisation with a flexoelectric coefficient, γ_{ijkl}, being a fourth rank polar tensor [236]. The flexoelectric effect, unlike the piezoelectric effect, does not rely on a non-centrosymmetric crystal. However, as flexoelectricity is a second order term in the expansion of stress-induced electric polarisation, a significant local strain gradient is required to produce an effect comparable with piezoelectricity. Two dimensional systems are able to

achieve these significant strain gradients and therefore many 2D systems such as graphene, boron nitride and lipid bilayers are being explored for flexoelectric responses [209, 4]. In our discussions we will use the flexoelectric constant, $f_{\theta \mathrm{p}}$, which is defined in relation to the pyramidalisation angle,

$$\mu_{\mathrm{p}} = f_{\theta \mathrm{p}} \theta_{\mathrm{p}}. \tag{2.64}$$

γ_{ijkl} and $f_{\theta \mathrm{p}}$ are interchangeable with the first being a bulk term while the latter is a molecular term [237]. Flexoelectricity in hydrogen-terminated curved PAH molecules will be discussed in detail in Chapter 4.

Pyramidalisation also decreases the overlap between π-orbitals leading to a reduction in aromatic delocalisation and an increase in reactivity. The high resistance to bending explains the low reactivity of graphene, which would have to become pyramidalised to sp^3 bond and react with a species [318]. A direct relationship has been found between pyramidalisation angle and the stability of oxygen-containing complexes [386]. The increase in reactivity has been experimentally demonstrated with carbon nanotube ends being more pyramidalised and therefore easily oxidised compared with the cylindrical surface [6]. Colleagues and I also showed that the gas phase coalescence of fullerenes could be accurately modelled by considering the strain at pentagonal rings in small fullerenes [266].

The reduction in aromaticity caused by pyramidalisation has been quantified computationally using error-cancelling balanced homodesmotic reactions. These found an aromatic stabilisation energy of 44.5 kcal/mol for the bowl shaped molecule containing a single integrated pentagon (corannulene), compared with 58.4 kcal/mol for the planar coronene [101]. Upon planarisation the aromaticity increases for corannulene providing an energy reduction of 10.7 kcal/mol. This helps to explain the low barrier for inversion found experimentally for corannulene $\approx$11 kcal/mol [373], when a higher value of 24 kcal/mol is expected if considering only the strain energy [406]. This will be important when discussing inversion of curved PAH in flames in Chapter 6.

This decreased delocalisation in curved PAH increases the localisation of charge around their edges, increasing their reactivity. In the combustion context this will impact the growth process. Raj [336] computationally determined an increased growth of curved aromatics for HACA growth, which will be described later. Raj et al. [338] also found decreased barriers for the reaction of oxygen with the curved corannulene compared with the planar pyrene. Thermo-gravimetric experiments also showed that curved carbons are more readily oxidised compared with more planar graphitic carbons [338, 143]. However, in these experiments it is unclear whether the effect is due to oxidation at the rim or at the hub of the materials. This will be important when discussing reactivity of curved PAH in flames in Chapter 7.

2.2.4 Graphitisability

Graphitisability is the ability of a carbon material to transform into graphite upon intense heating (>2500 K). In the Introduction it was stated that most combustion carbons are non-graphitising. In this section we will discuss the thermodynamics of stable and metastable phases (or allotropes), review the experimental finding of non-graphitisability and compare modern models for the nanostructure of non-graphitising carbons. This will introduce the background required for Chapter 8.

Figure 2.12 shows the pressure temperature phase diagram for carbon. Graphite is the most stable phase of carbon at atmospheric pressure (101.3 kPa). Graphite has a high melting point of >5000 K. High pressures (> 1 − 10 GPa) are required to provide the high density diamond allotrope of carbon [50].
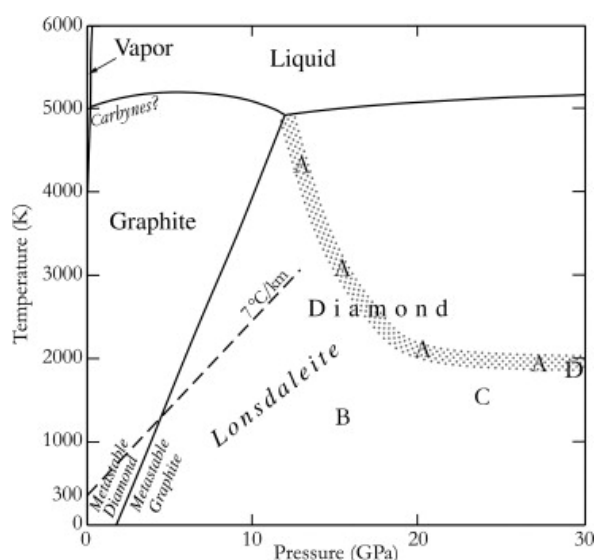
Figure 2.12 Phase diagram for elemental carbon based on data from [50]. Used with permission from [146] Elsevier ©.

Metastable phases of carbon are well known with diamond being metastable at atmospheric pressure and room temperature for many thousands of years. Lonsdaleite is another metastable phase of diamond that matches the lattice of graphite but is sp^3 bonded. Ion impregnation can be used to produce tetrahedral amorphous carbon where >50% of the bonding is sp^3. These metastable phases can be "frozen" at room temperature and stabilised for hundreds or thousands of years, however, heating above room temperature rapidly transforms diamond and amorphous carbon materials into graphite-like sp^2-bonded carbons at atmospheric pressure. Graphite, however, due to its extreme anisotropy – being covalently bonded in two dimensions but van der Waals solid in the other dimension – can readily form a variety of complex allotropes such as carbon fullerenes and nanotubes without the layering.

The development of graphitic structures during heating was first carefully studied by Rosalind Franklin in the 1940s. She tracked the emergence of stacked graphitic crystallites during high temperature treatment of carbons with X-ray diffraction. In isotropic or non-graphitising carbons these crystallites did not align and could not grow into large graphitic crystals, being restricted in their size and degree of stacking. Figure 2.13 shows the electron micrographs of the graphitising material anthracene compared with the non-graphitising material sucrose before and after strong heating. Layers of graphene are formed in the case of anthracene while sucrose develops small regions of ordered stacking connected together into a 3D structure.
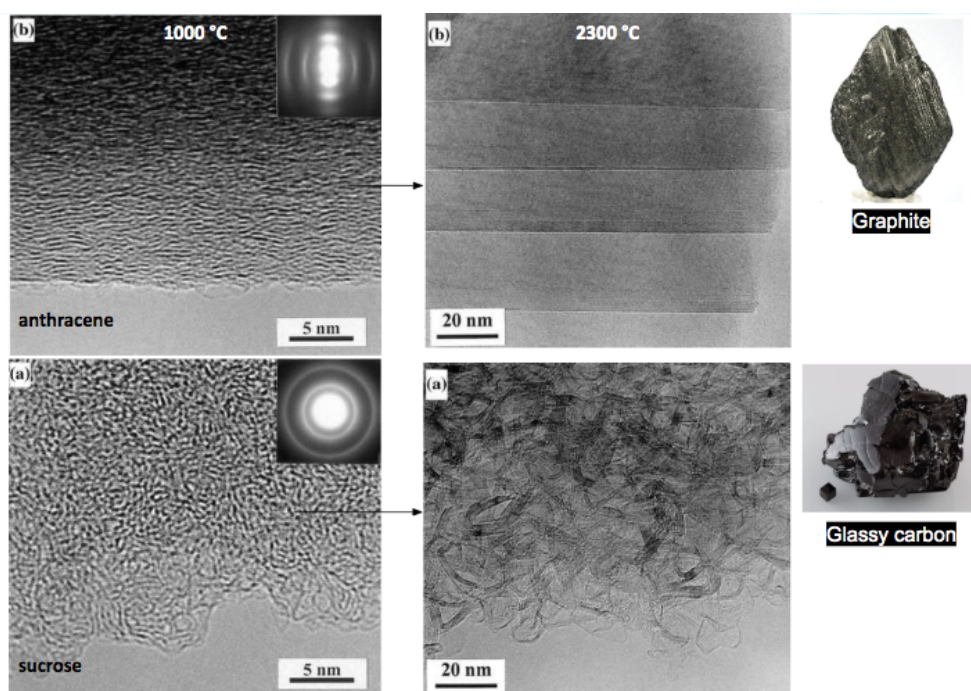
Figure 2.13 HRTEM images of the transformation of anthracene and sucrose under thermal treatment forming graphite or glassy carbon [166]. Used with permission from Taylor & Francis ©.

Many models were proposed to describe the connectivity of non-graphitising carbon (see Figure 2.14). In 1951, Franklin proposed that crosslinks between the misaligned crystallites maintain their 3D connectivity and inhibited alignment [126]. In the 1960s, high resolution transmission electron microscopy (HRTEM) of heated carbon blacks showed the crosslinks between crystallites to be curved ribbon structures. The well-known model of Ban, Jenkins and Kawamura proposed a knotted ribbon model containing branches and forks [202, 21]. Using the language of differential geometry, such structures could be described as locally Gauss flat, i.e. curvature $K \approx 0$, with only one non-zero principal axis of curvature [160].

More recent ribbon models of 3D graphenes by Zhang Zhang et al. [466], Wu et al. [452] show pores or holes in the network. However, in these ribbon-like models the significantly branched topology creates high porosity and large fractions of reactive edges, inconsistent with experiments [168].
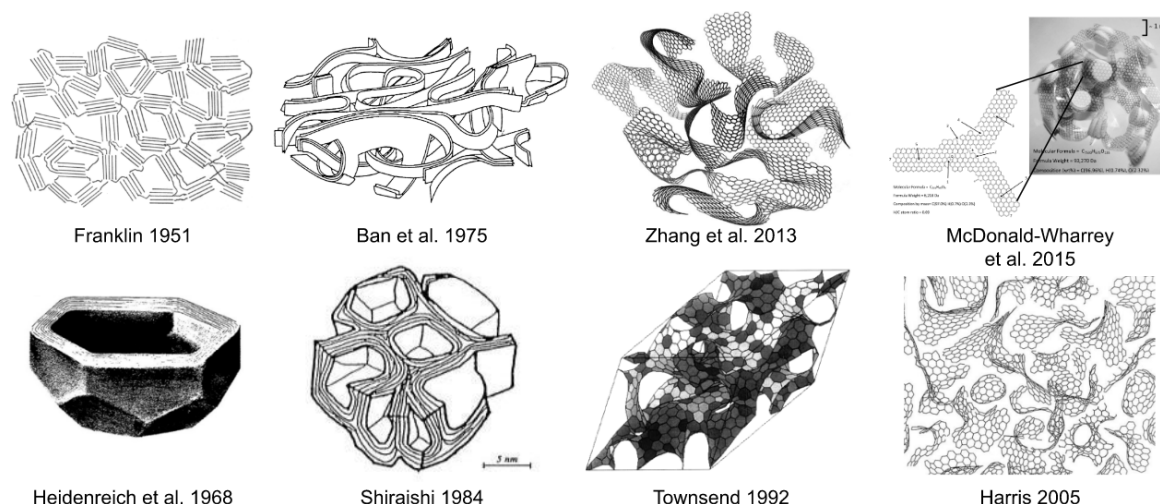
Figure 2.14 Models of non-graphitising carbon broken into ribbon-like models [126, 21, 466, 278] (top) and fullerene-like or schwarzite-like models [174, 420, 166] (bottom).

Models have also been presented that involve non-zero Gaussian curvature. For example Heidenreich, Hess and Ban were the first to find evidence for curvature in carbon particulates in 1968 [174]. By heating of carbon black particles to 2600 °C and using the first phase contrast imaging transmission mode of the electron microscope they were able to observe the fringes arising from the aromatic planes. They proposed a closed polyhedral structure indicative of a bowl-shaped topology ($K > 0$). Shiraishi and Oberlin also independently presented models containing spherical micropores in low density carbons <1.5 g/cc [302]. Inspired by Schwartz's study of triply periodic minimal surfaces, Mackay and Terrones proposed 3D carbon networks warped by $\geq$7-membered rings, providing saddle-shaped or Gauss negative curvature, $K < 0$ [259]. These schwarzite structures are theoretically purely sp^2, low reactivity nanoforms that form a continuous solid. Figure 2.14 shows a disordered schwarzite proposed by Townsend [420]. Layered schwarzites have been computationally explored but the connectivity requires highly symmetric structures [324], contrary to the low-symmetry structures found in electron microscopy experiments [168].

The 1985 discovery of fullerenes provided new geometrical possibilities within graphene networks [234]. Harris, in 1997, was the first to suggest fullerene-like structures in isotropic carbons, evidenced from his electron micrographs of polygonalised structures in glassy carbons and imaging of single pentagonal rings in microporous carbons [168] (previously

seen by Heidenreich in heated carbon blacks [174]). Pentagonal rings within a hexagonal network introduce bowl-shaped or Gauss positive curvature, $K > 0$, as mentioned previously. While fullerene-like graphenes help to resolve many structural features of carbons [168], the positive curvature of fullerenes cannot create three-dimensional (3D) connected networks. Schwarzites do allow for 3D connectivity but have yet to be synthesised.

Another topological element that has found recent experimental [15, 198] and theoretical [18] support are Y-shaped or T-shaped junctions. These defects connect graphene fragments via a line defect of sp^3 bonds. Although these junctions create porosity, they require high symmetry and many more sp^3 bonds than are observed experimentally [382].

Recent evidence has shown that there are both curved and ribbon-like structures (see Figure 2.15). As well as these results, recent diamond anvil work has found that uniaxial pressures of >35 GPa are required to partially graphitise glassy carbon [382]. They also found that the sp^2 fraction increased after compression indicating there are also non-sp^2 atoms within these non-graphitising materials.
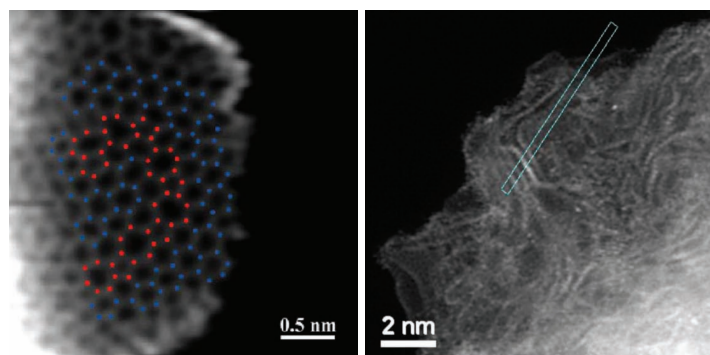
Figure 2.15 Annular dark-field images from the edge of nanoporous carbons, showing topological defects and ribbon-like structures. Used with permission from Wiley © [159].

Understanding this nanostructure of nongraphitising carbons is important for combustion generated nanoparticles as it will impact the destruction of soot and provide insights into value-adding industrial processes of carbon blacks such as activation. As mentioned in the introduction the oxidation of soot has been directly imaged at high resolution [416]. At 900 °C the ribbon-like structures were consumed and rearranged into a microporous carbon, which has different oxidation characteristics than the layered soot nanoparticles (see Figure 1.4). For carbon blacks this process of activation is important for preparing carbon adsorbents [265]. Also of industrial significance is the possibility of graphitising biomass or coal to produce high quality graphite. This would help to meet the need for battery graphite, which is currently mined and therefore costly. Therefore, the nanostructure of low density

porous and high density glassy non-graphitising carbons is important for eliminating soot, producing better adsorbents and for learning how materials can be graphitised.

2.2.5   Gas phase synthesis of fullerenes

Fullerenes were found to be produced in flames with aromatic fuels [142, 345] and even in candle soot [177]. Therefore the historical discussions of soot formation were intimately connected with those of how highly symmetric fullerenes self-assemble in combustion systems. We will therefore consider the mechanisms proposed for fullerene formation outside of the flame environment as knowledge of these will be required to fully appreciate the review in the next chapter.

Fullerenes are most often produced in carbon plasmas formed from laser ablation or arcs made with pure graphitic samples [234, 230]. This means that most of the mechanisms proposed focus primarily on conversion of a carbon vapour (C^+, C_2, etc.) into the magic number fullerenes like C_{60} and C_{70}, which are found in excess in comparison with other smaller cages. This is significantly different from conditions within hydrocarbon flames, as will be explored in the next section, where considerable amounts of hydrogen are present which passivate the surface of graphene molecules [357].

Early analysis in the 1990s showed that C_{60} and C_{70} fullerenes are more stable than smaller, caged carbon structures due to their high symmetry and it was suggested that they arise as the end product of a series of bottom-up reactions [104]. A variety of bottom-up mechanisms are presented in Figure 2.16 ([455]) such as the pentagon road mechanism where C_2 species grow the edge of a curved carbon network until closure into a magic number fullerene. This is similar to a mechanism of fullerene formation in flames proposed by Pope et al. [330], where acetylene addition to fluoranthene curves a PAH until closure into a fullerene cage is achieved with the loss of hydrogen. However, in carbon plasmas it has been found that after C_{20} all of the carbon is found in cage-like structures [455]. In the fullerene road mechanism a closed cage C_n, $n > 20$, forms and C_2 is ingested into the small cage [455]. Closed network growth of cages has been demonstrated using mass spectrometry of metal confined endohedrally (inside the fullerene) [109]. This was demonstrated by ingestion of C_2 while the metal stayed confined inside the fullerene indicating the fullerene road can occur.

Curl et al. [80] raised a difficulty with the bottom-up mechanisms based on thermodynamics considerations and suggested top-down mechanisms must also be in operation. Figure 2.17 shows the energy for a selection of the most stable fullerene isomers from C_{20} to C_{100}. What can be seen is that C_{60} and C_{70} lie below the trendline for the energy of the other fullerene isomers due to their uniquely high symmetry. However, this reduction is not as marked are previously thought and to reduce the enthalpy of the system larger fullerenes

Pentagon Road
(1) Haufler et al. (1991)

(2) Wakabayashi & Achiba (1992)

Chain
$C_n(n<10)$

Ring
$C_n(10<n<20)$

Fullerene Road
(3) Heath (1992)

C_2 addition

Folding
(4) Helden et al. (1993)

(5) Lagow et al. (1995)

Others
(6) Robertson et al. (1992)

Graphite —

(7) Dravid et al. (1993)
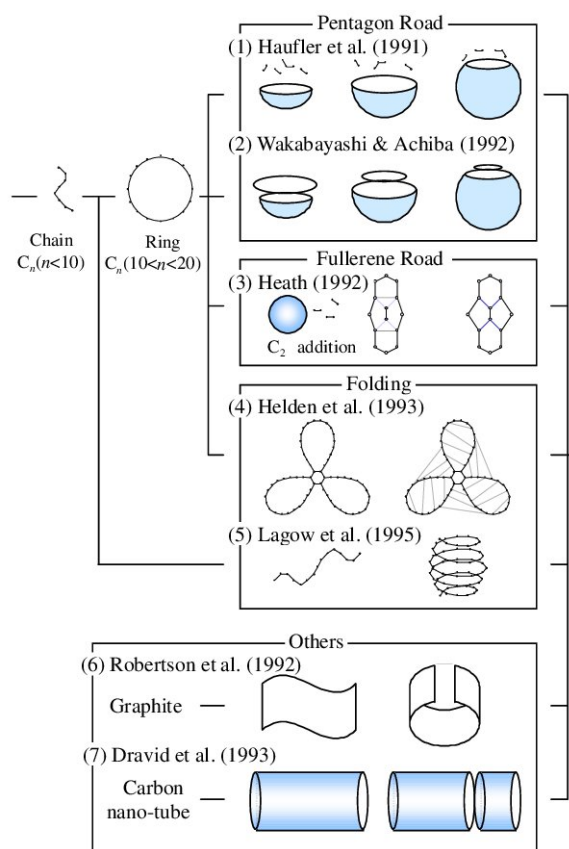
Carbon
nano-tube

Figure 2.16 Bottom up formation mechanisms for fullerenes from a carbon vapour [455].

are expected instead of the magic number fullerenes. Curl et al. [80] then showed that if C_2 is lost as well as gained by the fullerenes an increasing concentration of magic number fullerenes arises.

This top-down mechanism was experimentally observed where a giant fullerene was seen to shrink under heating [192]. Another example is the fragmentation of graphite to small graphene flakes that then close into cages, shrinking to form magic number fullerenes [347, 70]. Computationally, density functional tight binding (a DFT version of the wavefunction based tight binding methods) molecular dynamics simulations were used to describe the C_2 ejection that occurs alongside C_2 ingestion [197, 358].

Fullerenes are also known to coalesce with one another. Coalescence is seen experimentally in laser desorption ionisation mass spectrometry of C_{60} with species formed at $(C_{60})_n$ $n = 2 - 3$ that were found to be chemically fused [459]. Another indicator that coalescence is occurring is the distribution of higher fullerenes (C_n, $n > 100$) possessing a log-normal distribution found in the laser ablation synthesis [276] and in arc synthesised carbons by the author [266] (see Figure 2.18). The thermal treatment of this arc carbon, by the author,
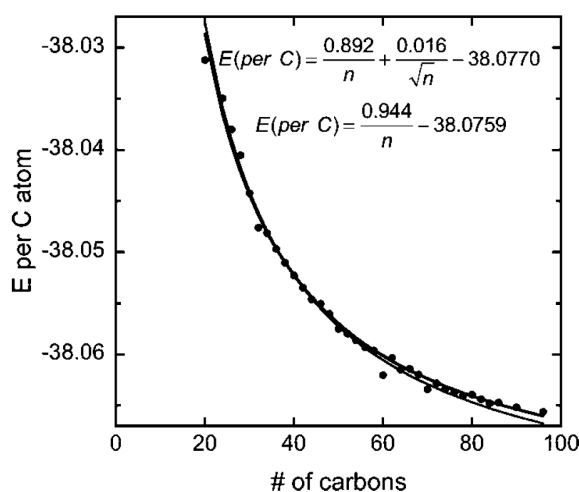
Figure 2.17 Energy per carbon atom for fullerenes calculated at the PBE1PBE/6-31G(d,p) level of theory (Hartree) [80]. For reference, graphite is significantly lower at -38.07704961.

lead to the consumption of C_{60} and C_{70} converting them into higher fullerenes [266]. This suggests that coalescence is thermodynamically preferred and that unique conditions are required for magic number fullerenes to form.

Irle et al. proposed that these unique conditions require continuous energy input into the system and significant carbon concentration gradients. This provides non-equilibrium conditions that allow for cage formation, C_2 ingestion, C_2 ejection and fullerene coalescence [350]. Under these conditions Ahmad [3] demonstrated, using an information-theoretic model, the emergence of significant concentrations of C_{60} with a net increase in entropy. Once a cluster has reached 60 or 70 carbon atoms it has been found to rapidly rearrange into the most stable icosahedral form due to the funnel-like potential energy surface [434]. As the most stable form of C_{60} and C_{70} are at local energy minima, ingestion or ejection of C_2 is less effective for these species and they accumulate in concentration. Therefore, the entropy penalty for the highly symmetric C_{60} produced is gained from significant amounts of C_2 ejected from the higher fullerenes [3].

Comparing these conditions to those commonly found in hydrocarbon combustion it is easy to see why fullerene formation is not forthcoming in most flames. Firstly, as will be discussed later, there is insufficient time for curved aromatic molecules to grow to the size needed to close into higher fullerenes [130]. Homann also showed that there is not a direct growth path from PAH to fullerenes and suggested a single crosslink between two PAH leads to pentagon integration and closure of the fragments, which will be discussed later. Ejection of carbon from curved nanostructures requires significant energy – 11.0 and 12.7 eV for C_2 and C evaporation at a pentagon site respectively – compared with 14.0 and
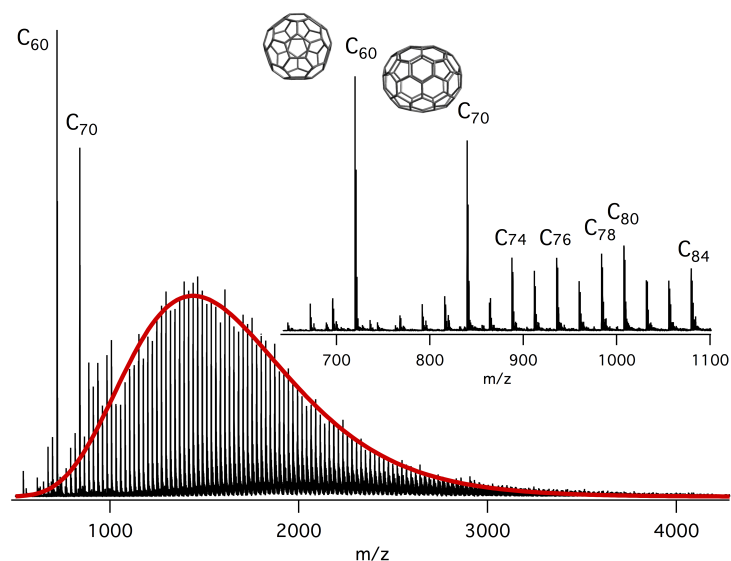
Figure 2.18 Distribution of fullerenes produced from arc plasma. Inset shows the magic number fullerenes with an increased intensity compared with the broad distribution of non-symmetric neighbours [266].

15.3 eV for hexagon sites [192]. These high barriers require >2500 K to compete with soot nucleation, which is often why high temperature benzene-oxygen flames are used to produce fullerenes. Annealing is also required within fullerenes via Stone-Wales transformations which range from 5–10 eV depending on the environment [100]. Low pressures are used in a benzene-oxygen flame to increase residence time to allow larger yield of magic number fullerenes [142, 345]. All together these considerations explain the low amount of fullerenes in atmospheric air-hydrocarbon flames [177].

Chapter 3

Review of carbonaceous nanoparticle formation in flames
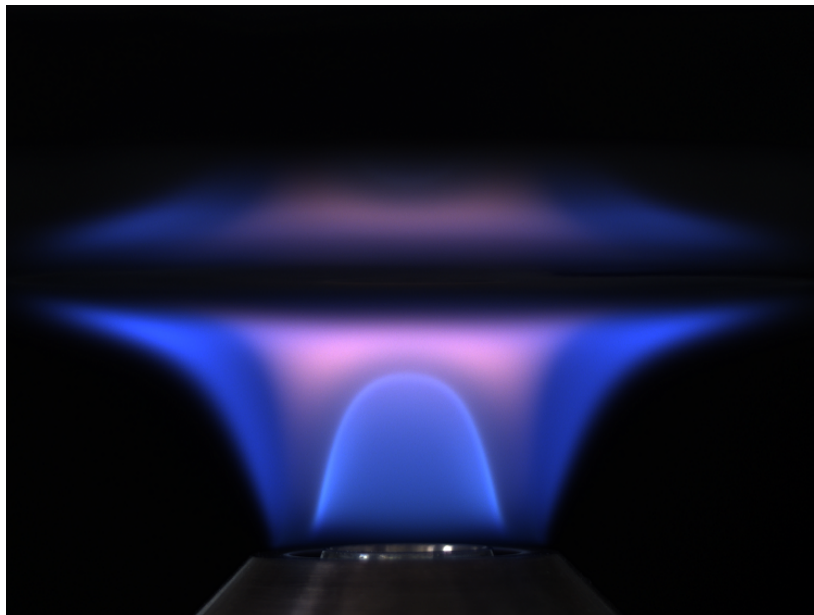
Credit: Jochen Dreyer © (used with permission)

"A major breakthrough in understanding carbon formation will have been achieved when it becomes possible in at least one case to account for the entire course of nucleation and growth of carbon on the basis of a fundamental knowledge of reaction rates and mechanisms."

– Palmer and Cullis (1965)

In this chapter, a brief review of carbonaceous nanoparticle formation in flames is provided. The formation of aromatic soot precursors is detailed along with the importance of the HACA growth process, aromers and the formation of curved aromatics. The many mechanisms for the formation of soot nanoparticles are then critically reviewed with a focus on chemical and physical mechanisms and those that combine both. Finally, the various mechanisms are compared with the nanoparticles experimentally observed in mass spectrometry. This provides the needed background for the main thesis of this dissertation: that curved aromatics influence soot formation.

What are the mechanisms by which carbonaceous particles form in flames and how can they be controlled or eliminated? This problem was most clearly articulated in the above quote from one of the first systematic reviews by Palmer and Cullis in 1965. In this section, we will discuss the current experimental observations and mechanistic models that address this problem. The transition from molecules to a condensed carbonaceous nanoparticle is of particular interest as no mechanism can currently explain this rapid and important process. We will draw from the most recent reviews on the topic by Richter and Howard in 2000 [344], Frenklach in 2002 [129], the book edited by Bockhorn, D'Anna, Sarofim and Wang in 2009 [37], D'Anna in 2009 [83], Wang in 2011 [438], Desgroux et al. in 2013 [96], Niessner in 2014 [298], Michelsen in 2017 [284] and Wang and Chung in 2019 [443].

Soot formation can be broken into four main steps:

1. Polycyclic aromatic hydrocarbon formation (molecular zone)

2. Nanoparticle formation (particle zone)

3. Primary particle formation

4. Aggregate formation

These steps are not strictly distinct but overlap and influence each other. Also throughout these steps oxidation competes with the formation of each of these products, indicating that soot can be eliminated or its properties modified through the control of each of these transformations. From these transformations, arguably the least understood process is the formation of nanoparticles from molecular species: the so-called molecule-to-particle transition [36]. As this thesis focuses on this transition we will review only these aspects.

3.1 Polycyclic aromatic hydrocarbon (PAH) formation

While many molecular species have been suggested to be the precursors of soot, the class of compounds that has received the most attention is the pericondensed aromatic species. Faraday, in 1825, was the first to implicate aromatics in soot formation even as he discovered them [117]. On extracting a condensate of benzene and aromatics from the illumination gas, produced from coal, he was able to show the critical role of benzene in generating vast amounts of soot and therefore providing the illuminating power of the gas. As the expanding petroleum industry developed standards to assess the sooting propensities of different liquid fuel mixes it became clear that larger aromatics produced more soot [216]. This led Rummel and Veh, in 1941, to suggest PAH as soot precursors [353].

The structure of diffusion flames also suggested that aromatics more readily produce soot [138]. Figure 3.1a shows the difference between benzene and hexane diffusion pool flames. For the benzene fuel, soot is rapidly formed at low heights above the burner, but for the aliphatic fuel hexane, a "dark zone" is observed that indicates a delay in soot formation. This "dark zone" implies that the aliphatic fuels require transformations before the onset of sooting. This begins with pyrolysis of the fuel to break it into C1–C5 compounds, including acetylene C_2H_2, through radical-induced fragmentation. A variety of chemical pathways then assemble the first aromatic ring from these fragments as shown in Figure 3.1b [164].

(a) Diffusion pool flame benzene and hexane fuels [224].

(b) First aromatic ring formation [164].
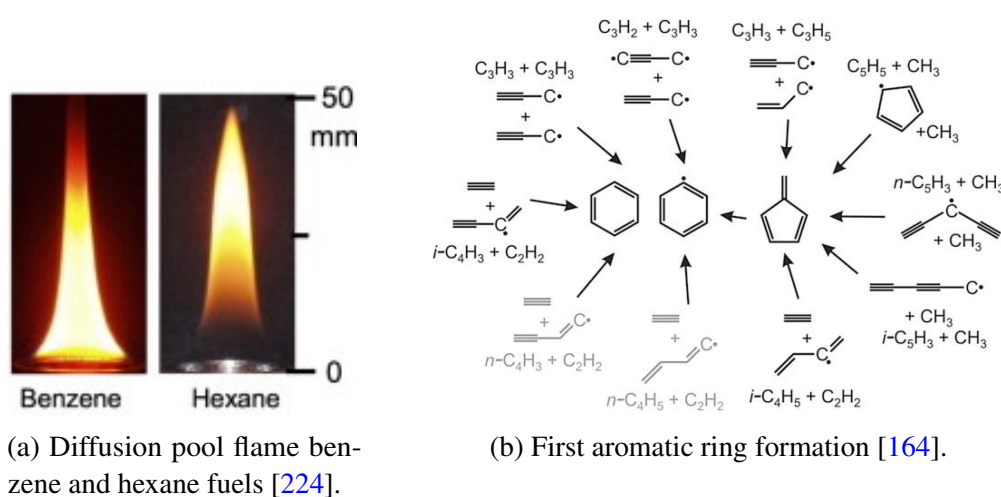
Figure 3.1 Benzene in soot formation.

3.1.1 Hydrogen abstraction carbon addition (HACA)

Further growth of the aromatics proceeds by a radical mechanism where a colliding hydrogen radical (or other radical) abstracts an aromatic hydrogen atom, providing a reactive site

where acetylene can attach – the so-called hydrogen abstraction carbon (acetylene) addition (HACA) mechanism [132, 129]. Figure 3.2 shows one pathway that highlights the HACA mechanism, plotting the change in the free energy (at $T = 1800$ K, $P = 1$ atm) and showing a table of species consumed or produced. The process is seen to be energetically downhill and spontaneous. This is primarily due to the generation of hydrogen gas which entropically drives the aromatic growth [438].

C$_2$H$_2$	5	5	4	4	3	2	2	1	0
H	1	0	1	0	0	1	0	0	1
H$_2$	0	1	1	2	2	2	3	3	3
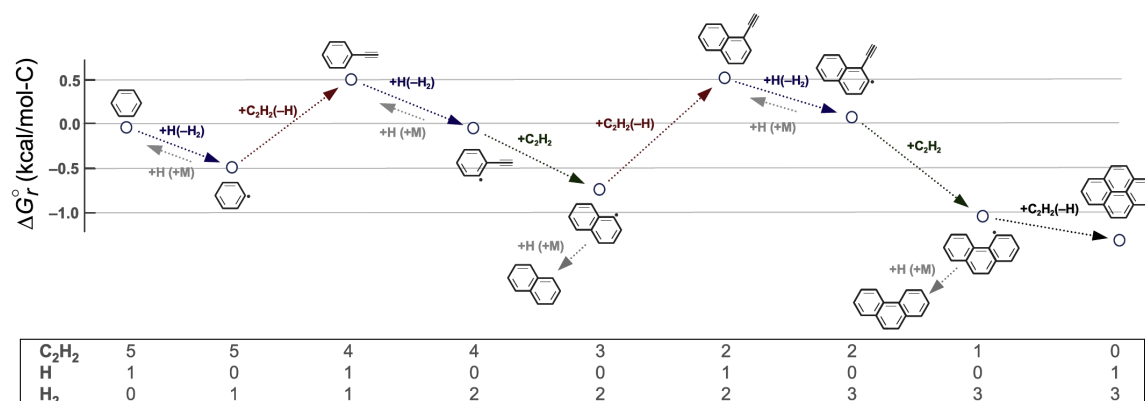
Figure 3.2 HACA mechanism with energetics of the intermediates and species count highlighting the release of H$_2$ [438]. Used with permission from Elsevier ©.

As the PAH grows, a variety of complex arrangements of fused aromatic rings are produced. Mass spectrometry allowed the ratio of carbon to hydrogen (H/C ratio) in the PAH to be measured as H/C =0.3–0.5 [186]. The reason for the presence of these species was explained by considering the thermodynamic stability of pericondensed polyaromatic hydrocarbons (PCAH), revealing an "island of stability" or the "stabilomers" as described by Stein and Fahr, where aromatic rings are fused in a roughly circular fashion [398]. A lower H/C ratio was found than that from PAH with only hexagonal pericondensed rings (maximally pericondensed structures) and explained by the presence of pentagonal rings, at this stage placed on the periphery or edge of the aromatic molecules. The concentration of these small aromatics drops exponentially so that these species only extend to ∼300 Da [438].

Direct imaging of soot precursor pericondensed PAH was recently achieved using non-contact or high resolution atomic force microscopy (nc/HR-AFM) from a nearly sooting premixed ethylene flame [371, 78]. Figure 3.3a shows three small species imaged to reveal highly pericondensed PAH molecules with rim-based pentagonal rings. Figure 3.4 shows the H/C ratio for a collection of these directly imaged molecules. The species were found to contain a higher concentration of hydrogen than that of maximally pericondensed species (the most condensed a set of hexagonal rings can be in an aromatic), due to methyl groups and the hydrogenation of the rim-based pentagonal rings. This technique was limited to small

flat aromatics (mean size of 372 Da [78]) sampled from nearly sooting flames and could not adequately image the 3D aromatic molecules produced in a sooting flame. However, recent advances in HR-AFM have been developed to image bonds within 3D aromatics [274].

(a) Bonding network resolution [371].

(b) Stoichiometry of aromatics in nearly sooting flames [78].
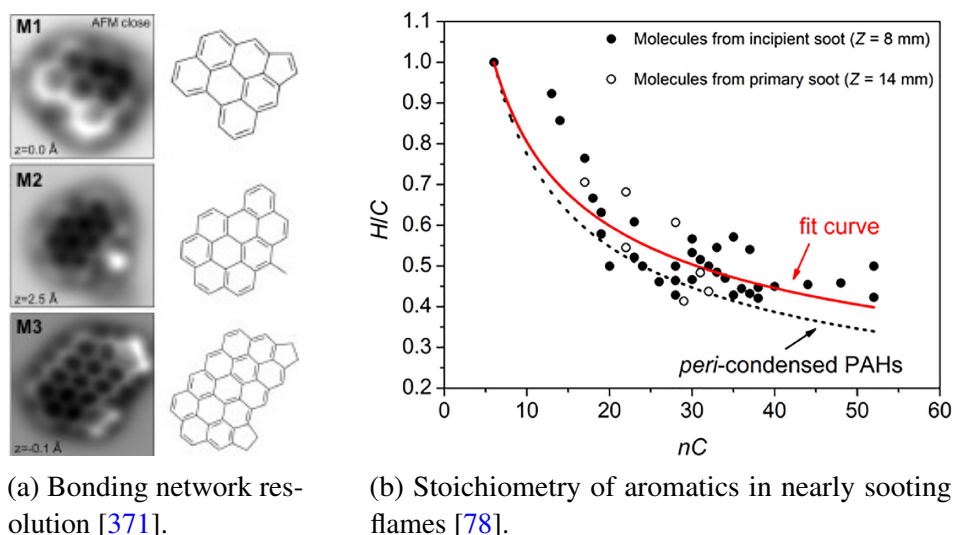
Figure 3.3 HR-AFM results of aromatic soot precursors.

3.1.2 Aromers and curved aromatics

Evidence also exists for a class of larger PAH species, so-called reactive aromatics or aromers, from 300–2000 Da [185, 213, 186]. Homann demonstrated in low pressure benzene/oxygen rich premixed flames that the concentration of aromatics does not exponentially decrease monotonically but increases from 300 Da to ∼620 Da. This has also been further demonstrated in methane/O_2/N_2 [115] and n-butane/O_2/N_2 premixed flames (peak at ∼500 Da)[97], an ethylene/O_2/N_2 premixed flame (peak at ∼700 Da)[11] and an ethylene diffusion flame (peak 400–600 Da)[196].

Homann interpreted these larger PAH as curved PAH (cPAH) [186]. The evidence for this curvature came from these larger PAH readily forming negative ions. Fullerenes and curved aromatics are known to have a high electron affinity and easily form negative ions [93]. The type of curvature he was referring to is due to the complete enclosure of a pentagonal ring within the aromatic network that causes the aromatic molecule to be bent out of plane and curved like a bowl. More direct evidence came from the extraction of corannulene and completely closed cages of carbon – C_{60} fullerenes – from flames and soot [238, 142].

The location of these larger PAH in the flame before the formation of fullerenes, as well as their loss of hydrogen, suggested they were fullerene precursors [14]. Recently, hydrogenated
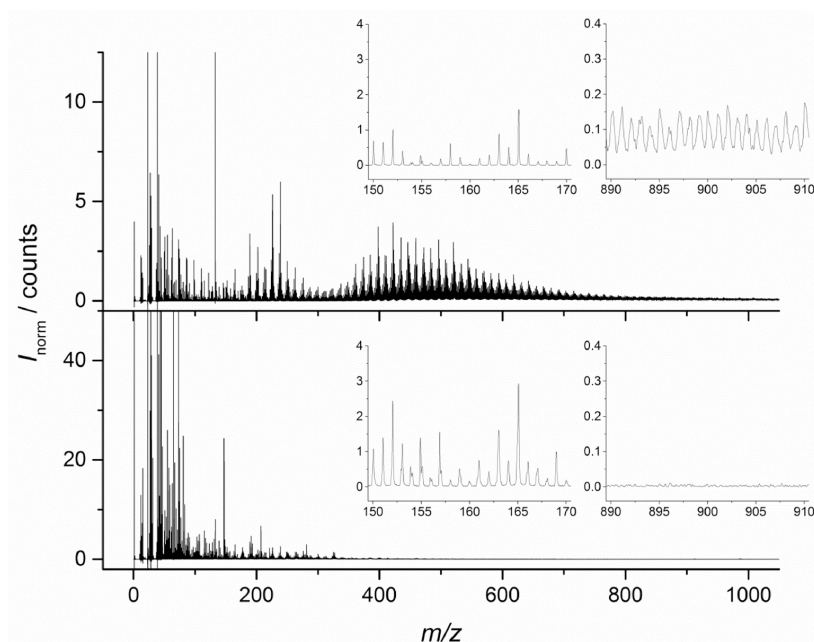
Figure 3.4 Secondary ion time-of-flight mass spectrum (SIMS-TOF) of premixed sooting $\phi = 2.32$ (top) and nucleation $\phi = 1.95$ (bottom) $CH_4/N_2/O_2$ flames [97]. Used with permission from Elsevier ©.

fullerenes have been extracted and crystallised from low pressure flames showing closure can occur before loss of hydrogen [413]. However, in most atmospheric flames the conditions for fullerene formation are unfavourable. They therefore have a low concentration [177] and are unable to contribute to a soot formation mechanism.

Figure 3.5 compiles the various mechanisms that have been experimentally proposed or computationally explored for curvature integration due to pentagonal ring embedding. These can be broadly separated into the corannulene pathway and the planar or flat PAH (fPAH) pathways. The corannulene pathway was suggested by Pope and Howard [330]. It involves small PAH and goes through the intermediate corannulene, which is the most well known curved aromatic. Starting from benzene, a series of HACA reactions generate a variety of fPAH, as well as precursors for the cPAH. Recently, evidence has been found for a HACA pathway starting from cyclopentadiene either with acetylene [204] or methyl addition [452] that generates a variety of fPAH, some with an odd number of π-electrons giving resonantly stabilised π-radicals. As with the growth from benzene, the same precursors for cPAH are also generated.

The corannulene pathways contain most of the pentagonal embedding reactions and will be used to introduce them. The first pentagon integrating reaction is shown in Figure 3.5 i) where an aryl crosslink reaction between benzene and napthalene is followed by cyclodehy-
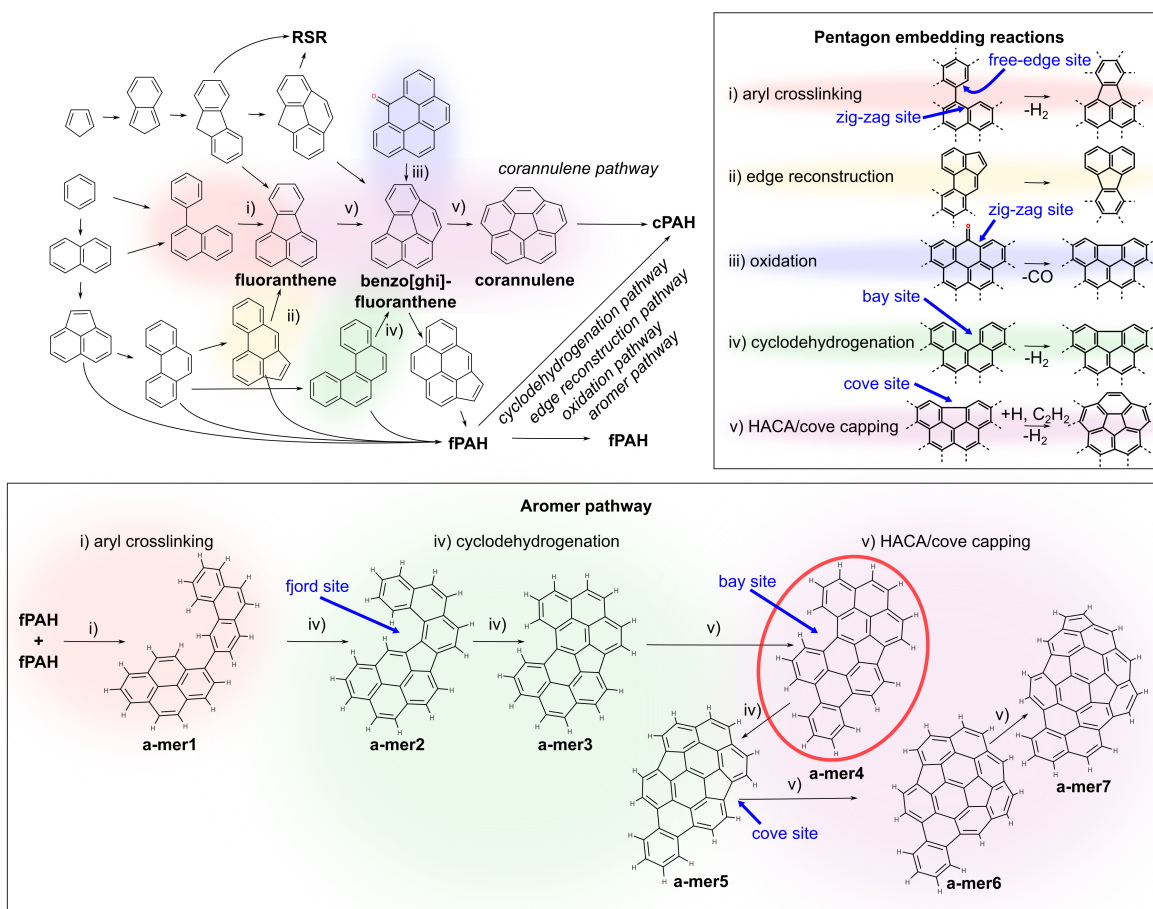
Figure 3.5 Curvature integration mechanisms. Insets show the pentagon embedding reactions (top right colour coded) and an aromer pathway (bottom). The structure circled in red is based on the structure imaged in HR-AFM [78]. Site types are shown with blue arrows to aid the discussion.

drogenation to form fluoranthene. Aryl crosslinks twist the aromatic species relative to one another so that there is an angle between the two aromatic planes, due to the steric hindrance of the hydrogens neighbouring the crosslink. The π-bonding is optimal when the two aromatic planes are colinear and therefore at flame temperatures these species rapidly transform into planar structures in a process of cyclodehydrogenation or ring condensation [161]. Experimentally, this reaction is well known [308] and is used in many modern mechanisms of soot PAH chemistry [424]. Pope and Howard suggested a mechanism where fluoranthene can also be generated from a thermal edge reconstruction or rearrangement with an edge pentagon becoming embedded and surrounded three hexagonal rings [330, 374] (Figure 3.5 ii)). HACA growth then can generate the next intermediate, benzo[ghi]fluoranthene, with a partially embedded pentagon enclosed by four hexagonal rings. This intermediate has also been suggested to arise from oxidation of a zig-zag edge [376, 388] or cyclodehydrogenation of

the bay edge site of benzo[c]phenanthrene [427] (Figure 3.5 iii) and iv)). Figure 3.5 v) shows the final enclosure of the pentagonal ring through HACA growth onto benzo[ghi]fluoranthene, also referred to as a bay capping reaction. This forms corannulene, the most well known curved aromatic with five hexagonal rings enclosing a pentagonal ring [130]. Before this bay capping reaction the aromatic is flat, however, afterwards the aromatic is bent into a bowl shape due to the considerable strain the enclosed pentagon creates. This step is critical as the benzo[ghi]fluoranthene is still able to thermally rearrange into a flat aromatic with an edge-based pentagonal ring. However, once the pentagon has become embedded through a HACA reaction the mechanisms for pentagon migration are unlikely to occur. The mechanisms involve C_2 rotations (Stone-Thrower-Wales transformations) with significant energetic barriers that kinetically "lock" the less stable pentagonal ring within the hexagonal network, which has been demonstrated experimentally from flash pyrolysis studies [374]. Lafleur et al. [238], however, found corannulene to be in low concentrations in benzene flames [(mass corannulene)/(mass pyrene) from 0.8 to 6.3%]. This pathway therefore appears to not be a primary formation mechanism of cPAH. Given that corannulene is the smallest cPAH known to date this suggests species <300 Da are expected to be predominantly flat with rim-based pentagonal rings and partially embedded pentagons present in planar aromatics.

The other curvature integration pathways mirror the reactions seen in the corannulene pathway, however, they become more likely as the aromatic grows in size. Cyclodehydrogenation of a bay site followed by HACA growth has been studied using Kinetic Monte Carlo simulations of growing aromatics and has been found to enclose pentagonal rings [431, 446, 457]. However, these reactions are slow as they require a bay site, which is not readily generated for PAH ∼500 Da in size. This pathway is therefore unlikely to provide the curvatures required to explain the significant curvature integration in flame or fullerene formation [130]. An oxidation pathway is also more likely for larger aromatics [376, 388]. Experimentally it has been found that partially premixed diffusion flames (Bunsen-type) have structures with increasing curvature as a function of oxygen concentration [191] and another recent study using *in situ* high resolution TEM imaging showed curling of graphene flakes into curved fragments at the surface of a soot particle during oxidation [416]. It is unclear how oxidation contributes to overall curvature integration, however, the low amount of oxygen found in early soot particles [77] and the prevalence of these larger species in diffusion flames with much lower oxygen concentrations indicates it is also not a primary curvature integration mechanism.

Thermal rearrangements have also been found to provide partially embedded pentagonal rings that with further HACA growth produce cPAH. These can be classified into peri-condensation and edge rearrangements. Pericondensation involves the rearrangements of

orthocondensed (otherwise known as catacondensed) PAH into pericondensed structures with the loss of hydrogen. This has been extensively explored as a synthesis route for buckybowls and graphene. Edges of aromatics are highly mobile above 1300 K and rapidly rearrange into partially and fully embedded pentagonal rings [374]. Some example schemes from buckybowl synthesis are;
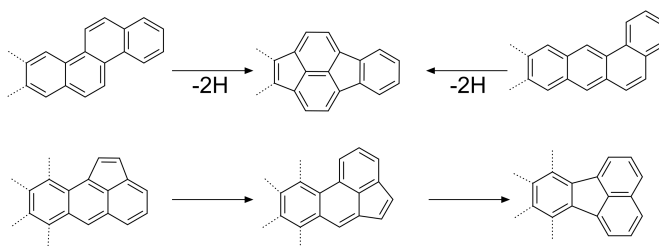
Another recent experimental work on the transformation of ethylene into graphene on an Rh(111) surface using scanning tunnelling microscopy found some interesting thermal transformation of PAH [435]. Long acenes were formed at 470 K, however, heating to 670 K led to the breakup of these long acenes and the formation of pericondensed species, which then grow and fuse into polycrystalline graphene. While in this study the surface likely catalysed the rapid rearrangement reaction, flash pyrolysis experiments demonstrate that past 1300 K aromatics also rapidly rearrange into pericondensed species in the gas phase [374]. However, edge rearrangement competes with the embedding of pentagonal rings by allowing the migration of the ring to an edge (as it does not involve hydrogen loss and is therefore highly reversible). This inhibits the formation of long acenes and was the initial reason curvature integration was not explored in the combustion community for a long time – the edge rearrangements were thought to provide more thermodynamically stable planar PAH [130].

Homann suggested the aromer pathway, which is a combination of the aryl crosslinking, cyclodehydrogenation and HACA/bay capping reactions, which can be seen in the inset of Figure 3.5. The experimental evidence for the aryl crosslinking of two fPAH arises from the presence of a separate distribution of larger PAH as mentioned, suggesting a separate mechanism from HACA, which can explain the distribution of the smaller PAH [213]. Recent tandem mass spectrometry has also been used with collision-induced dissociation to show the fragmentation of this mode at 500 Da Adamson et al. [2]. The possible radical sites for aryl crosslinking are shown in Figure 3.6.

Howard considered σ-radicals produced from hydrogen abstraction from the edges of hexagonal and pentagonal rings and computed that molecules $\sim$600 Da in size would contain 5–6 of these radical sites per molecule [189]. σ-radicals are considered to be the most reactive radicals in the flame, reacting readily with acetylene in the HACA mechanism [129].
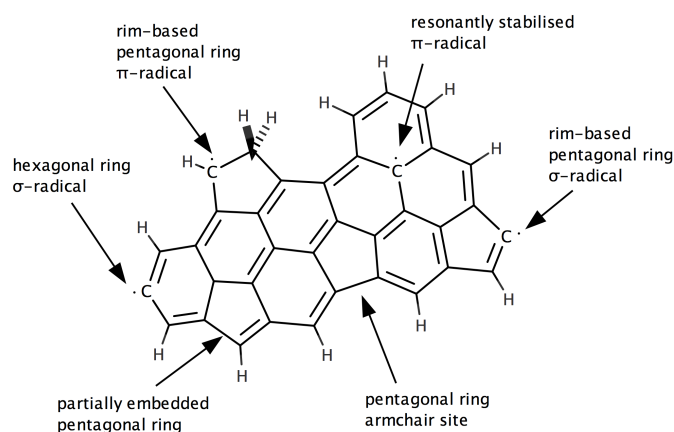
Figure 3.6 Reactive edges of soot precursors.

Homann mentioned the odd number of carbon molecules and suggested a non-bonding π-radical that is delocalised [213] and has also been imaged in HR-AFM [370]. These resonantly stabilised π-radicals are important in benzene formation – being less reactive than σ-radicals, they have longer lifetimes in the flame [164]. Frenklach also suggested a partially protonated rim-based pentagonal ring that forms a π-radical, showing it impacts surface rearrangements and growth processes but did not explore the reactivity with other aromatic species [128, 446].

Subsequent cyclisation of these aryl crosslinked species has been experimentally found to favour the partial embedding of a pentagonal ring as opposed to a hexagonal ring [293, 362] (e.g. the free edge is found to preferentially react with the zig-zag edge in pyrene pyrolysis, forming a pentagonal ring). Evidence for the crosslinking and partial embedding of pentagonal rings has also been found in HR-AFM with species found containing two aromatic segments with predominantly hexagonal rings linked via pentagonal rings [78]. These species are then highly orthocondensed and will thermally rearrange and cyclodehydrogenate to further embed the pentagonal rings, with HACA growth also contributing to pentagon enclosure. **a-mer4** from Figure 3.5 is highlighted as this aromatic network was experimentally observed in HR-AFM experiments [78]. This species can rapidly cyclodehydrogenate or have HACA growth to form the curved species. Evidence for this suggestion comes from the slightly higher concentration of hydrogen rich species in the 300 to 700 Da range and the fact that dehydrogenation rapidly gives way to species in the region with H/C ratios suggesting pericondensed structures [14]. Similar crosslinking schemes have long been used in the synthesis of buckybowls and C_{60} molecules [9, 374] (see Figure 3.7).
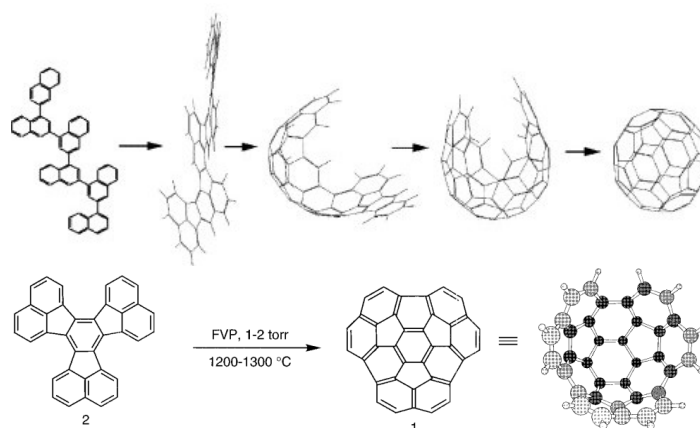
Figure 3.7 Buckybowl and fullerene formation [9, 374]. Used with permission from Elsevier ©.

Aryl crosslinks and further thermal rearrangements are known to integrate curvature and close cage structures completely [344]. However, it appears that multiple crosslinks are required for the integration of sufficient curvature to allow for complete formation into fullerenes. This is not possible in most atmospheric sooting flames but is possible in some low pressure flames [186, 431]. It is interesting to note that Homann originally suggested that this process was enhanced by the physical interactions holding PAH dimers together while the edge zipped up [24, 186]. This was based on an early model of fullerene formation called the zipper mechanism [197]. The summarised synthesis work on buckybowls highlights that no such physical interactions are required and that thermal rearrangements are sufficient to integrate curvature. However, in this dissertation I will explore the idea of how physical interactions could impact reactivity [344].

What unique properties do these cPAH possess that are interesting for nanoparticle formation in flames?

- High electron affinity [93], which allows them to be detected with mass spectrometers in negative ion mode [186].

- They are geometrically curved due to the bonding network, which competes with the π-bonding to drive planarity.

- Electrically polarised – the flexoelectric effect – due to the rehybridisation of their π-electrons giving the molecules a permanent dipole moment, which will impact their self-assembly with other polar species and ions.

- cPAH possess an increased reactivity due to a decrease in aromaticity, which has been shown to increase the HACA growth mechanism [336] and the oxidation of these species [402, 338].

The growth of curved or planar pericondensed PAH is generally not found to extend past 1000 Da. We will therefore consider any species above 1000 Da to be nanoparticles. This cutoff is somewhat arbitrary but in the context of soot formation is consistent with how the term nanoparticle is used in literature. There are some exceptions to this definition that are worth mentioning. PAH growth can extend further than 1000 Da in some low pressure flames [444, 213, 186] and inverse diffusion flames [354]. Another exception is the formation of giant fullerenes that can extend to 6000 Da within low pressure flames [24]. However, at atmospheric pressure fullerenes are not readily produced in hydrocarbon flames and do not contribute to soot formation [130, 186].

3.2   Nanoparticle formation

Before exploring soot nanoparticle formation some nomenclature must be discussed. There is much controversy around the language of soot nanoparticles. They are variously described as nanodroplets, microparticles, soot nuclei, ultrafine particles, precursor nanoparticles, nanoorganic carbon, incipient soot and nascent soot. This confusion is unsurprising, given that there is still significant uncertainty surrounding how soot forms. Without understanding the possible mechanisms for soot formation and which are operating under different conditions, naming conventions will remain undecided. For the sake of clarity we will make a distinction between chemical and physical soot nanoparticle formation referring to chemical mechanisms as *soot inception* and physical mechanisms as *soot nucleation*. Mechanisms involving both chemical and physical interactions will be referred to as *covalently stabilised soot nucleation*.

Table 3.1 lists the many mechanisms that have been proposed for the formation of carbonaceous nanoparticles in hydrocarbon flames. The main strengths and weaknesses that have been discussed in the literature are consolidated. We will focus only on a collection of these mechanisms applicable to the main thesis, which are shown in Figure 3.8. The mechanisms with black borders are the novel mechanisms suggested in this dissertation.

Table 3.1 Formation mechanisms for soot nanoparticles

Mechanisms	Scheme	Strengths	Weaknesses	Possible
(I) Disproportionation				
(a) acetylene	$C_2H_2 \rightarrow C_2(g) + H_2 \rightarrow C(s)$	Location of C_2 [395]	Cyanogen (C_2N_2)-oxygen flame sootless [341]. Soot contains hydrogen [411]	N
(b) CO	$2CO \rightarrow C(s) + CO_2$	Boudouard reaction well known on surfaces low T [28]	Thermodynamics do not support this past 1000 K [181]	N
(II) Acetylene inception				
(c) amorphous	$-HC_2\bullet + C_2H_2 \rightarrow -C_2HC\bullet$	Suggested from photolysis of acetylene [331]	Too slow, does not explain aromatic sooting propensity [315]	N
(d) C_2, acetylene	$C_2 + C_2H_2 \rightarrow 2C_2H + 2C_2H_2 \rightarrow 2C_4H_3 + C_2 \rightarrow 2C_4H_2 + C_2H$	Location of C_2 [395], reactivity of C_2H_2 [137]	Insufficient C_2 at flame T [315]	N
(e) chemi-ion	$C_3H_3^+ + C_2H_2 \rightarrow PAH^+$	Ion-neutral reactions are fast. Ions and soot correlated [56].	Reactions are not much faster [440]. Neutral PAH grow at same rate [444].	N
(f) graphene	$PAH(\sigma\bullet) + C_2H_2 \rightarrow PAH$	Acetylene rapidly forms PAH [132, 129]	Too slow for nanoparticle formation [129]	N
(g) icospiral	$PAH(\sigma\bullet) + C_2H_2 \rightarrow cPAH \rightarrow$ icospiral	PAH integrate curvature [239, 153], fullerenes present in flames [142], templated growth is fast [233], spirals and onions observed in HRTEM [194, 422]	Too slow [130], closure into fullerenes is more likely [186]	N
(III) Polyyne inception				
(h) ring condensation	$C_2H_2 \rightarrow C_nH_2 \rightarrow PAH \rightarrow C(s)$	Many polyynes in the flame [185] thermodynamically stable at high T [231]	Rigid unlikely to cyclise [254], Radical-induced fragmentation limits growth [141]	N

Mechanisms	Scheme	Strengths	Weaknesses	Possible
(i) fullerene-like	$C_2H_2 \rightarrow C_nH_2 \rightarrow$ cage (+ PAH)	Fullerenes present in flames [142], high pressure acetylene pyrolysis simulations [463]	Radical-induced fragmentation limits growth [141], fullerenes are formed from aromatic species in flames [186]	N
(IV) Polyaromatic inception				
(j) PAH, PAH	PAH + PAH $\rightarrow$ PAH–PAH	PAH most stable, resistant to radical-induced fragmentation, so high conc. [398, 129], curved PAH were also suggested [5]	Edges are unreactive in peri-condensed PAH [369]	N
(k) aryl, PAH	PAH($\sigma\bullet$) + PAH $\rightarrow$ PAH–PAH	Hydrogen abstraction generates many σ radicals [189]	Requires large number of radicals for creating σ-radicals [438], prone to radical-induced fragmentation [129]. Low collision efficiency [263].	Y
(l) aryl, aryl	PAH($\sigma\bullet$) + PAH($\sigma\bullet$) $\rightarrow$ PAH–PAH	Hydrogen abstraction generates many σ radicals [189], strong bonds formed [263]	Requires large number of radicals for creating σ-radicals [438] low conc. and collision efficiency [263].	Y
(m) cyclodehydrogenation	PAH–PAH $\rightarrow$ PAH	Ring condensation rapid at flame temperature [362] reduces impact of radical-induced fragmentation	Slow as relies on the initial crosslinking of aryl radicals (see above)	N
(n) pentaring, pentaring	(5)PAH + (5)PAH $\rightarrow$ PAH(5)=(5)PAH	Pentaring more reactive than 6-membered ring [361]	Symmetry forbidden [2+2] pericyclic reaction unstable [361]	N

Mechanisms	Scheme	Strengths	Weaknesses	Possible
(o) aryl, pentaring	(6)PAH($\sigma\bullet$) + (5)PAH $\rightarrow$ PAH(6)–(5)PAH	Pentaring more reactive than 6-membered ring [85]	Requires large number of radicals for creating σ-radicals [438]. Prone to radical-induced fragmentation.	Y
(p) carbyne diradicals	PAH($\sigma\bullet$) $\rightarrow$ PAH(2$\sigma\bullet$) + PAH $\rightarrow$ PAH–PAH	Strong binding energy to PAH [75, 179]	Requires two H-abstractions, the second having a significant barrier [188], unlikely due to concentrations of H and PAH($\sigma\bullet$) [189], no split EPR carbon signal [433].	N
(q) O furan	PAH($\sigma\bullet$) + O$\bullet$ + PAH $\rightarrow$ Furan	Furan-like PAH found in some flames [205]. Oxygen can enhance soot formation [113].	Large oxygen rich PAH not found in most flames [186, 467]. Insignificant oxygen content has been found in early soot particles [77]. Prone to thermal and radical-induced fragmentation [425].	Y
(r) delocalised-π, aryl	(6)PAH($\pi\bullet$) + PAH($\sigma\bullet$) $\rightarrow$ PAH–PAH($\pi\bullet$)	Delocalised-π and σ-radicals are present in flames [189, 213]. Reaction easily lose H to regenerate delocalised-π [204].	Conc. of odd number PAH (likely to be delocalised-π) not reduced [213]. Radical-induced fragmentation likely to compete.	Y
(s) pentaring aryl, pentaring	(5)PAH($\sigma\bullet$) + (5)PAH $\rightarrow$ PAH(5)=(5)PAH	Imaged HR-AFM [371], provides planar species [321]	Unlikely for (5)PAH($\sigma\bullet$) to react with pentaring, prone to radical-induced fragmentation	Y
(V) physical nucleation				

Mechanisms	Scheme	Strengths	Weaknesses	Possible
(t) aliphatic polymer	Fuel $\rightarrow$ polymer $\rightarrow$ [polymer]$_n$	Some vapours are light emitting [125]. Condensible tar is seen in thermophoretic samples from diffusion flames [340, 217].	Aliphatics are found to increase later in the flame [305, 53]. Prone to radical-induced fragmentation [339], condensible tar can be removed with fast sampling [44].	N
(u) aromatic polymer	Fuel $\rightarrow$ aromatics $\rightarrow$ polymer $\rightarrow$ [polymer]$_n$	Large polymers are able to condense [240, 84]. Large polymer can cluster more effectively [193]. Extension of polyaromatic routes.	Prone to radical-induced fragmentation, aromatically linked PAH have lower dimerisation propensity than fPAH [193, 114]	Y
(v) fPAH	fPAH $\rightarrow$ [fPAH]$_n$	Irreversible dimerisation describes soot particle no. [439]. Internal rotors improve stability [369].	Dimerisation not possible <650 Da [438, 419, 356]	N
(w) aliphatic chains	PAH + aliphatic $\rightarrow\sim$PAH$\sim\rightarrow$ [$\sim$PAH$\sim$]$_n$	Evidence from IR spectroscopy [279]. Seen in HR-AFM [371]. Improves clustering [112]	Enhancement is minor $\approx$2.5 kcal/mol [112]	N
(x) cPAH	cPAH $\rightarrow$ [cPAH]$_n$	van der Waals interactions [24]. Dipole-dipole interactions improve clustering [270, 269]	Dimerisation energy similar to fPAH i.e. too low [270]	N
(y) ion, fPAH	fPAH + C$_3$H$_3^+$ $\rightarrow$ [PAH]$_n^+$	Long range interactions [226]	Low binding energies [62]	N
(z) ion, cPAH	fPAH $\rightarrow$ cPAH + C$_3$H$_3^+$ $\rightarrow$ [cPAH]$_n^+$	Long range strong interactions [270, 269]	Limited to small clusters [269]	Y
(VI) Covalently stabilised soot nucleation				
(aa) zipper mechanism	fPAH–fPAH $\rightarrow$ cPAH	Suggested for fullerene formation [24, 5, 186]	Very low reactivity edges	N

Mechanisms	Scheme	Strengths	Weaknesses	Possible
(bb) aliphatic bridge	$2PAH(\sigma\bullet)$ + aliphatic $\rightarrow$ $PAH–(CH_2)_m–PAH$	Allows stacking and bonding [84, 112]. Mass spectrometric evidence in some flames [2].	Prone to radical-induced fragmentation [339] high H/C ratio	Y
(cc) acetylene bridge	$PAH(\pi\bullet)$ + $PAH(\sigma\bullet)$ + C_2H_2 $\rightarrow$ $PAH–C_2H_2–PAH$	Acetylene is abundant and π-radicals have also been detected [371], stable complex [144]	Prone to radical-induced fragmentation [339], polymerisation mechanism unclear	Y
(dd) O_2, bridge	$PAH(\pi\bullet)$ + O_2 + PAH $\rightarrow$ $PAH–O_2–PAH$	Oxygen is found to enhance soot formation [113], binding energies are strong [264]	Insignificant oxygen content has been found in early soot nanoparticles [77]. Prone to radical-induced fragmentation [339], polymerisation mechanism unclear.	N
(ee) excimer stack	PAH^* + PAH $\rightarrow$ $(PAH,PAH)^*$	Presence of fluorescence in soot forming region [289], excimers formed with stacked PAH [288]. LIF gives long duration fluorescence supporting excimers [391, 282].	Weak interactions over nanoseconds [282], can only stabilise a dimer, trimers weakly bound [86]	N
(ff) pancake bond	$(6)PAH(\pi\bullet)$ + $(6)PAH(\pi\bullet)\rightarrow$ $PAH\equiv PAH$	Many π-radicals present [433, 371], multicentre bonds allowing stacking [394, 215]	Low interaction energy [79, 215, 270], polymerisation mechanism unclear	N
(gg) zig-zag diradicals	acene $\rightarrow$ diacene + acene $\rightarrow$	Long acenes have large dimerisation energies [438, 227], large PAH with zig-zag edges can be open-shell singlet multitiradicals [327, 464]	Acenes fragment or rearrange into PCAH [438, 435]	N

Mechanisms	Scheme	Strengths	Weaknesses	Possible
(hh) localised π-radicals	PAH($\pi\bullet$)/(5)PAH + (5)PAH($\pi\bullet$)$\rightarrow$ PAH(5)–(5)PAH	Many π-radicals present [433, 371]. Strong bonding and less prone to radical-induced fragmentation [270].	Prone to radical-induced fragmentation, unknown concentrations of this radicals type	Y
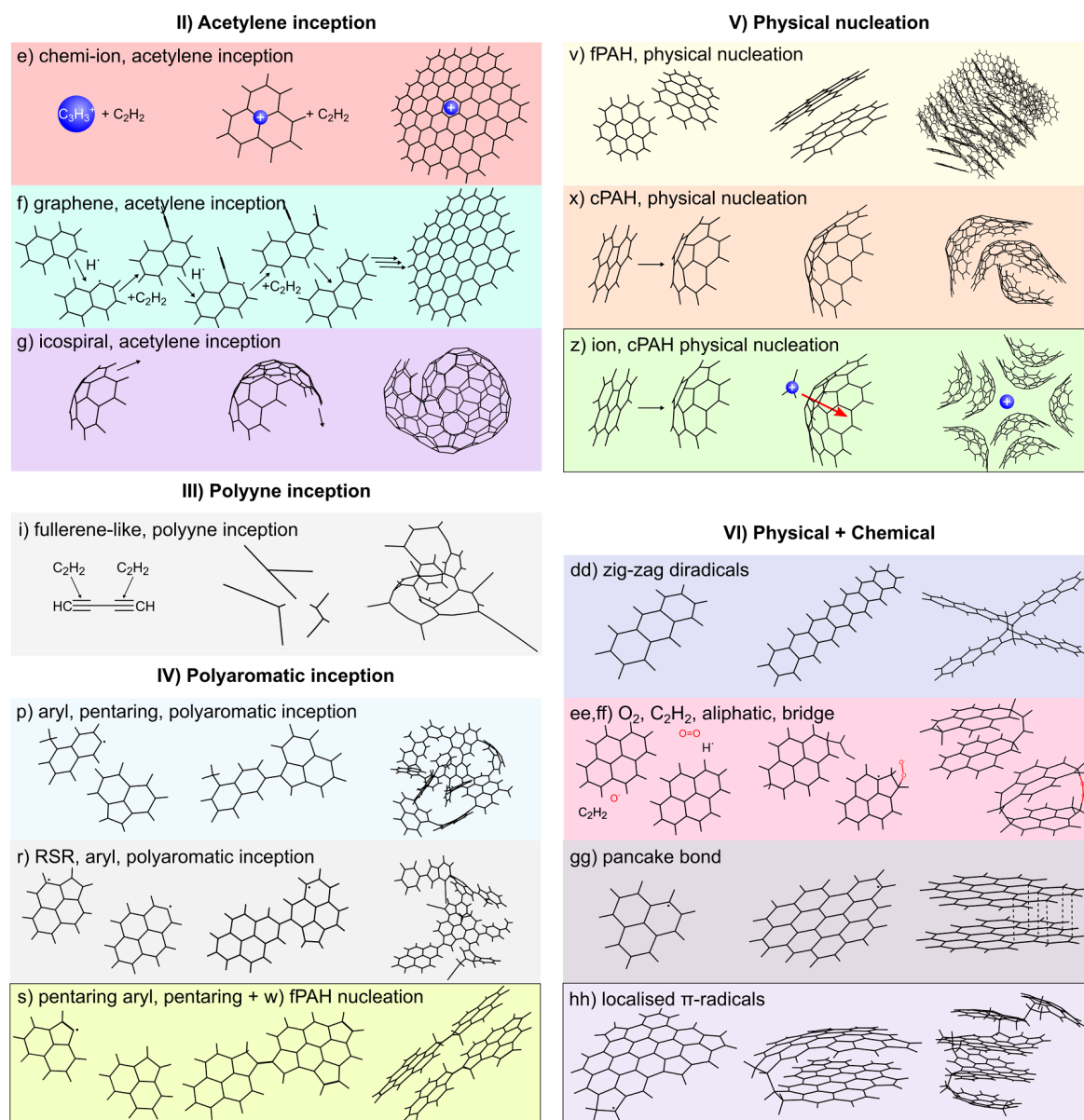
Figure 3.8 Schematics for a collection of mechanisms from Table 3.1. Mechanisms with black borders are the novel contributions from this work.

3.2.1 Acetylene inception

Acetylene inception is the chemical polymerisation of acetylene forming soot nanoparticles. Calcote provided one of the first detailed reviews of various pathways and kinetics involved in acetylene inception [55]. He showed that none of the chemical mechanisms up to the 1980s were rapid enough to explain nanoparticle formation. Instead he proposed an ionic

mechanism based on two observations: the correlation between soot and charged species in the flame and the more rapid reactions between neutral species and hydrocarbon ions.

The correlations between soot and charged species are well known and have been thoroughly reviewed by [242] and more recently by [121]. Briefly, significant concentrations of charged species are found in flames ($10^{15} - 10^{17} ions$ m^{-3}) [56]. This significant charge concentration was found to be due to chemi-ionisation reactions and not thermal ionisation [54]. Chemi-ionisation reactions rely on the ejection of an electron in a high energy reaction between an electronically excited molecule and a neutral species. The main reactions are [171],

$$CH^* + O^\bullet \longrightarrow CHO^+ + e^- \tag{3.1}$$

$$CHO^+ + H_2O \longrightarrow CO + H_3O^+ \tag{3.2}$$

$$CHO^+ + neutral \longrightarrow protonated^+ + CO, \tag{3.3}$$
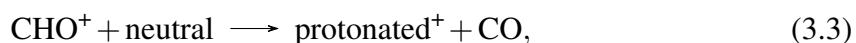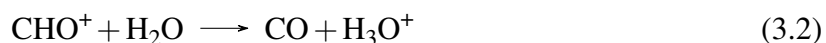
where the electronically excited carbyne (CH*) reacts with an oxygen radical (O$^\bullet$) to form the cation radical formyl (CHO$^+$) (Eq. 3.1). This is a short lived radical that reacts rapidly with water to form the hydronium ion (H$_3$O$^+$) (Eq. 3.2). Many other small positively charged hydrocarbons are produced through protontation with the formyl cation (Eq. 3.3).

Under rich flame conditions the primary ion-producing reactions become,

$$CH^* + C_2H_2 \longrightarrow C_3H_3^+ + e^- \tag{3.4}$$

$$PAH + C_3H_3^+ \longrightarrow PAH^+ + C_3H_2 \tag{3.5}$$

$$PAH + CHO^+ \longrightarrow PAH^+ + CO \tag{3.6}$$

$$C_3H_3^+ + C_2H_2 \longrightarrow PAH^+ \tag{3.7}$$

$$soot \longrightarrow soot^+ + e^- \tag{3.8}$$

where excited carbyne reacts with acetylene (C$_2$H$_2$) to form propenyl radicals (C$_3$H$_3^+$), which are longer lived as they can cyclise into cyclopropenyl (Eq. 3.4) [121]. PAH are known to become charged as they grow through reactions with chemi-ions (Eq. 3.5 and 3.6) allowing them to be detected in molecular beam mass spectrometry [186]. Soot can also be charged due to thermoionisation (Eq. 3.8), which is most effective for larger soot particles that are sufficiently carbonised to have a low ionisation potential [121].

Why are these positive species not neutralised by negative charges? The primary negative species are electrons, however, low concentrations of negatively charged species are able to be formed i.e. being in equilibrium with the electrons.

$$e^- + H_2O \rightleftharpoons H + OH^- \tag{3.9}$$

$$e^- + C_2H_2 \rightleftharpoons H + C_2H^- \tag{3.10}$$

$$e^- + cPAH \rightleftharpoons cPAH^- \tag{3.11}$$

$$e^- + soot \rightleftharpoons soot^- \tag{3.12}$$

Formation of negative ions is through electron attachment. However, the electron affinity of most flame species is low, with most electron ion collisions leading to elastic scattering and the majority of negative charge being carried by the electrons [171, 121]. One exception is curved PAH that easily become negatively charged by electron attachment (Eq. 3.11) as shown by Homann [186]. Soot is also able to become negatively charged through electron attachment. Electron attachment (Eq. 3.12) and thermoionisation (Eq. 3.8) provide a charge equilibrium for primary and aggregate soot particles that is in thermal equilibrium and is described by the Saha equation [121]. This list of flame ion reactions is not comprehensive and more complete mechanisms exist for flame ion chemistry [7].

Returning to soot formation, Calcote also drew attention to the location of the ions directly preceding the formation of soot nanoparticles (with concentrations of a similar order of magnitude to the ionic concentrations $10^{14} - 10^{16}$ ions m^{-3}) was also suggested to indicate a causative link [56]. It is well known in atmospheric chemistry that reactions involving charged species and neutral molecules can be significantly faster than neutral-neutral reactions due to the ion-induced dipole forces. Calcote's reaction mechanism was then based on the chemical polymerisation of $C_3H_3^+$ with acetylene (Eq. 3.5) [see Figure 3.8 (e)) [56]. Charged molecules were suggested to polymerise by acetylene addition at a rate sufficient to explain the rapid growth of soot nanoparticles. Preliminary studies supported such a mechanism with positive nanoparticles up to 8×10^3 Da being found using mass spectrometry in acetylene flames [24, 141] (see Figure 3.9). Experiments involving electric fields and easily ionised metals were used to explore such a mechanism.

Electric fields have long been seen as evidence for an ionic mechanism. Brande in 1814 showed that a diffusion flame can be deflected towards a negative plate within an electric field, suggesting positive ion carriers [47]. The influence on soot inception is complicated by the production of an ionic wind. The accelerated chemi-ions in the flame entrain air in such a way that the flame is aerated, increasing oxidation and thereby reducing soot formation. Weinberg
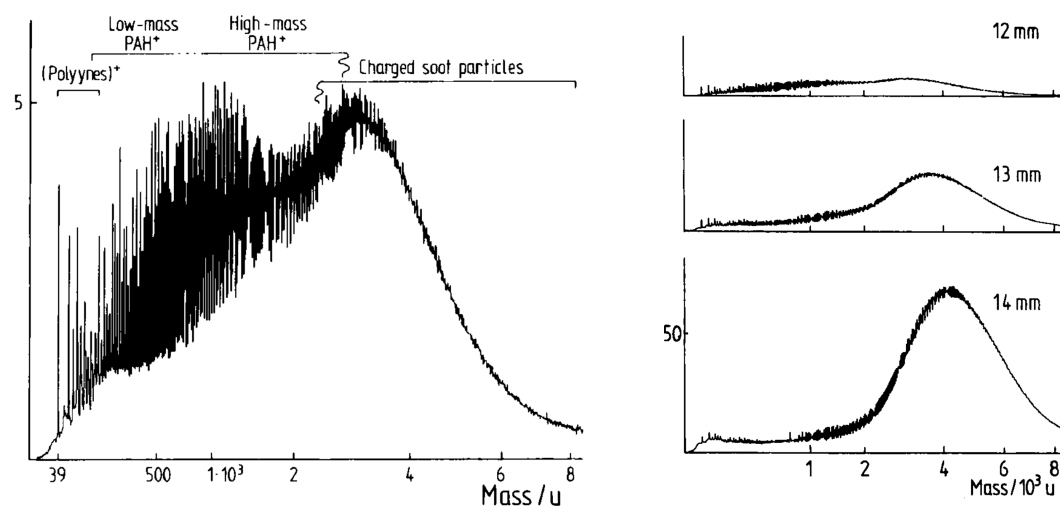
(a) Positive mass spectrum at 12 mm.

(b) Scaled mass spectrum for 12 mm as seen in (a) as well as mass spectra at 13 and 14 mm.

Figure 3.9 Positive ion mass spectrometry of an C_2H_2/O_2 low pressure flame $p = 2.7$ kPa at various heights above the burner [24]. Used with permission from John Wiley and Sons ©.

and Place were the first to realise that a counterflow diffusion flame would allow for the ionic wind to have no impact on the aeration of the flame [328]. Counterflow flames provide a flame front nearly perpendicular to the flow field. An electric field applied across the burner provides an ionic wind which merely shifts the stagnation surface. Soot's residence time in the flame was found to be reduced and the size of the primary particles was significantly reduced. Figure 3.10 shows the significant impact of the electric field on the formation of soot, recently measured using laser induced incandescence (LII) and the aromatic species and the hydroxyl radical using laser induced fluorescence (LIF) [316].

The application of the electric field shifts the reaction zone, providing some quenching of the production of aromatics, however, the impact on soot formation is more pronounced with a complete removal of soot. This effect is most pronounced when the electric field is established in such a way that shifts the chemi-ions formed in the chemiluminescence zone of the flame into the soot-forming region, increasing the charge present during soot formation [121]. Weinberg suggested that this reduces soot formation through the attachment of cations to soot particles;

$$\text{soot} + C_3H_3^+ \longrightarrow \text{soot}^+ + C_2H_2 + \text{H.} \tag{3.13}$$
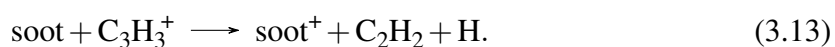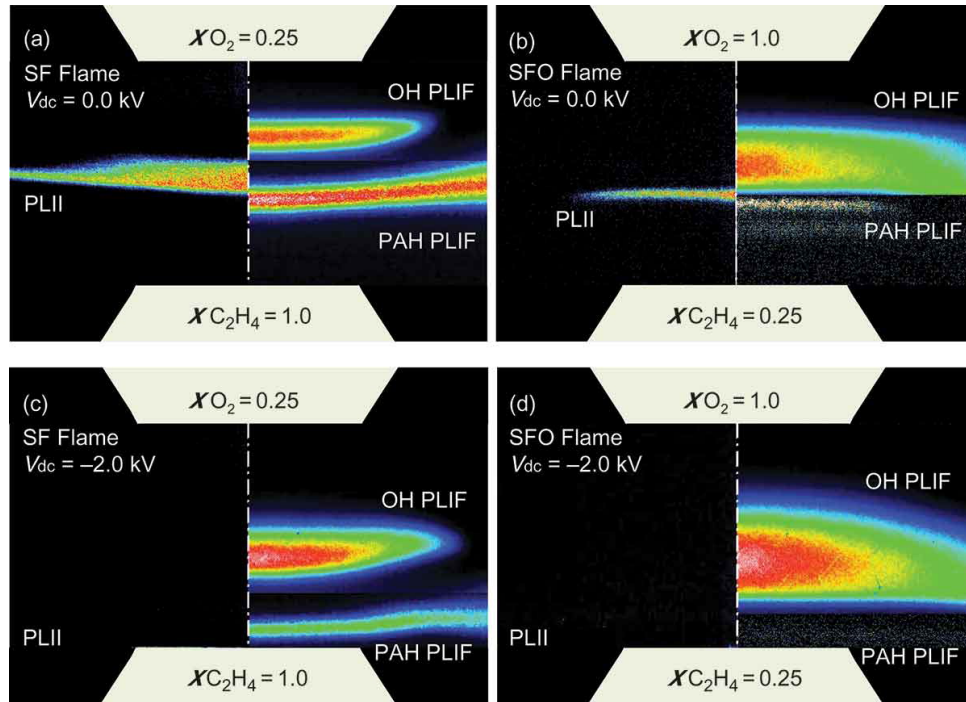
Figure 3.10 Counterflow $C_2H_4/O_2/N_2$ diffusion flame without (top) and with (bottom) an electric potential difference of 1 kV applied. Luminous carbon particulates measured with LII disappear from the flame upon application of the field (from Park et al. [316] used with permission from Taylor & Francis ©).

This charge attachment reduces the coagulation efficiency of soot as an excess of positive charge increases the repulsion between soot primary particles. The reduction in size was then initially attributed to a reduction in the residence time of the charged soot in the flame. By tuning the direct current (DC) electric field strength, these positively charged soot particles were held in the soot forming region allowing them to grow to hundreds of nanometres in size. Weinberg suggested that only soot particles larger than 9 nm are able to become charged due to charge attachment as in Eq. 3.17 [242]. However, as has been mentioned, smaller charged soot particles were also able to be observed as the resolution of particle mass analysers improved [24]. Furthermore, the electric field uniformly reduces all soot primary particles' diameters, not only the charged soot, indicating that charged and neutral soot formation is linked [121]. Using DC electric fields to explore the impact of ionic soot mechanisms is challenging. The flow fields can be modified through ionic winds and chemi-ions can shift within the flame, which makes distinguishing the impact on soot nanoparticle formation and soot aggregation difficult to decouple. Alternating current electric fields have also shown an impact on soot nanoparticle formation, causing soot emissions to increase or decrease

depending on the frequency and voltages used [228]. These results were interpreted as primarily impacting soot nanoparticle formation.

Addition of easily ionised metals to flames provides an opportunity to further explore ionic aspects of soot formation. They have long been studied as anti-smoke additives to diesel engines [261] and in polystyrene combustion have been shown to reduce soot emissions by 50–90% [69]. These metals increase the ionic concentrations through a variety of processes and reactions:

$$M \rightleftharpoons M^+ + e^- \tag{3.14}$$

$$H_3O^+ + M \longrightarrow H_2O + M^+ + H \tag{3.15}$$

$$C_3H_3^+ + M \longrightarrow H_2O + M^+ + H \tag{3.16}$$

$$soot + M^+ \longrightarrow soot^+ + M \tag{3.17}$$

$$M + OH^* \longrightarrow MOH^+ + e^- \tag{3.18}$$

$$\tag{3.19}$$
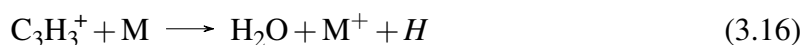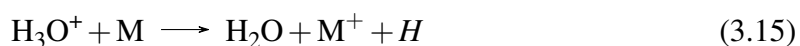
Thermal ionisation (Eq. 3.14) is the first mechanism considered for alkali metals as they possess a low ionisation potential. The rate of thermoionisation can be determined from the Saha equation and has been shown in a hydrogen flame by Ashton and Hayhurst to be $k = (9.9 \pm 2.7) \times 10^{-9} T^{1/2} \exp{-E_I/RT}$, where E_I is the ionisation energy [13], with the ionisation energy decreasing down the periodic table. Therefore, larger alkali metals are expected to more completely ionise in flames. Experimentally, the ionisation effect can be less pronounced as can be seen in Figure 3.11 where ionic concentrations are measured in a premixed flame aspirated with water and alkali metal salts [151].

The delayed increase in the charge concentration for most alkali metals in this flame was explained as being due to the high ionisation potential of these species. The charging later in the flame when the temperature is lower was suggested to be due to charge transfer from hydronium (Eq. 3.15). This late charging is thought to primarily influence coagulation. In this case charge transfer to soot increases the fraction of positively charged soot primary particles (Eq. 3.17). This reduces the coagulation efficiency due to electrostatic repulsion, producing less aggregated primary particles that are more easily oxidised. A partially premixed coflow ethylene flame ($\phi = 2.27$) probed by small angle X-ray diffraction indicates that the size of primary particles does not change significantly for potassium addition [98]. However, in a different flame (premixed ethylene/air flame on a modified PerkinElmer burner $\phi = 2.6$) potassium has been found to reduce the size of the primary particles, indicating a possible role in soot nanoparticle formation [387]. Another complication in interpreting these results is the catalytic effects of alkali metals. Potassium has been found to catalytically reduce the
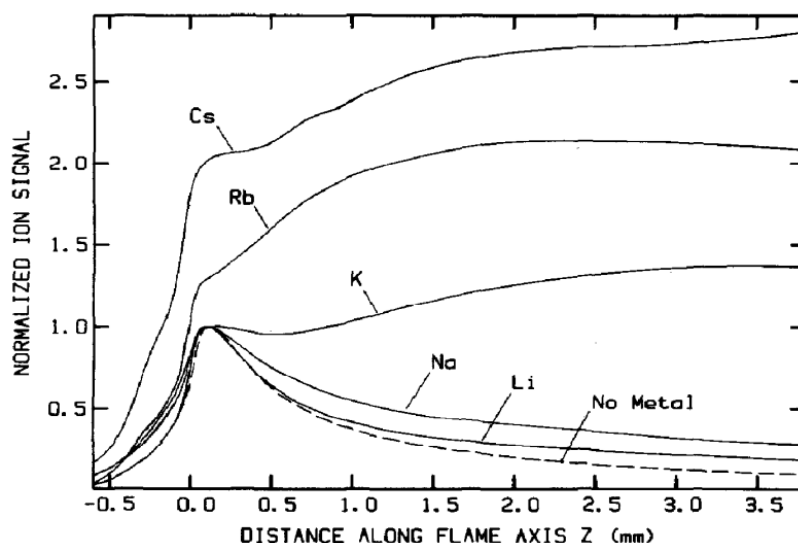
Figure 3.11 Ionisation signal with different metals addition to a flame [151]. Used with permission from Elsevier ©.

mass of soot as demonstrated by experiments that added the potassium further downstream where coagulation has already occurred, finding a decrease in soot emissions from improved oxidation [346]. Similar challenges exist for interpreting the role of alkaline metals such as Ba, Ca, etc. which are known to form cations with excited hydroxyl (Eq. 3.18) and catalytically produce the aggressive hydroxyl oxidant [121].

Cesium provided the most insight on the impact of ions on soot formation. It has a low ionisation potential and is the only metal to provide a considerable increase in the ionic concentration in the soot-forming region of most flames, as seen in Figure 3.11. In the mentioned study, a decrease in the chemi-ion corresponding to $C_3H_3^+$ was found, indicating that the metal was able to be charged through charge transfer according to Eq. 3.16, and was suggested to support a chemical mechanism for soot formation (Eq. 3.7). The reduction in soot was then explained as being due to the reduction in the number of nuclei chemically grown from $C_3H_3^+$. However, *in situ* small angle X-ray diffraction using synchrotron light sources has recently found that addition of cesium into an ethylene flame doubles the concentration of the smallest carbon nanoparticles [98], which suggests cesium promotes soot nanoparticle formation. This would suggest a different mechanism for the metal ions suggested by Howard and Bonczyk [190, 38], where the ions play a stabilising role for nuclei, producing large numbers of smaller carbon particles with increased surface area, allowing for their rapid oxidation and destruction and leading to less soot.

Other significant critiques arose for the chemical ionic mechanism. Firstly, there are a number of soot-producing systems that have insufficient ion concentration such as benzene

flames, shocktube studies and pyrolysis experiments [344]. Secondly, the molecular beam mass spectrometry of larger PAH found that the growth rates of charged and neutral aromatic molecules were similar [444]. While reaction rates can be enhanced in atmospheric chemistry for ions at room temperature, the high temperatures found in flames provide thermal energies that overwhelm any ion induced-dipole enhancement [440]. Finally, the HACA mechanism was able to explain the growth of pericondensed aromatic molecules under flame conditions [129].

Therefore while HACA and other PAH growth mechanisms can explain the formation of PAH they are unable to explain the rapid formation of soot nanoparticles [129]. There is an exception for low pressure acetylene flames in which the conditions can be tuned to produce large flat graphene structures [444]. However, this requires sooting to be eliminated and in most sooting flames the PAH growth from acetylene ends before 1000 Da.

The discovery of fullerenes in 1985 by Kroto, Curl and Smalley [234] led to a number of new proposed mechanisms for soot formation. In this landmark paper, the authors also suggested that this C_{60} species could act as the nuclei for soot formation. Fullerenes were subsequently found to be formed in many flames [142]. The concentration of C_{60} was then found to be too low in atmospheric flames to be critical for soot formation [177, 186]. A second suggestion was that an aromatic species was formed that then curved onto itself like a nautilus shell. This geometry (the icospiral) is geometrically achieved by two screw dislocations allowing for the fullerene layers to be wound together [233]. The geometry was suggested to allow for a templated growth process, which is known to be rapid and the predominant growth mechanism in crystals [212]. Further evidence came from electron micrographs of soot and carbon black particles where closed and spiral fringes indicated such a fullerene-like seed [194, 422]. These early electron micrographs were often formed from strong electron annealing that allowed for the fringes to be clearly imaged. Such annealing is known to convert many zero-dimensional carbon materials such as nanodiamond into fullerene-like carbon onions [423], suggesting these structures were formed during the electron irradiation. Some recent work has shown that HACA type growth of PAH can be enhanced due to curvature integration [336]. While this is of considerable interest, curvature has also been found to modify the rate of oxidation, in most cases increasing it [338, 388]. Therefore, more work is required to determine the impact that curvature has on PAH growth. Nevertheless, the fraction of hydrogen in soot and the molecular beam mass spectrometry support the view that PAH growth does not extend past 1000 Da in most sooting flames, which would be required for an icospiral.

In summary, acetylene is critical for PAH formation and therefore indirectly contributes to soot nanoparticle formation. However, HACA mechanism is too slow to explain soot

nanoparticle formation. Enhancements due to ionic effects or curvature are also unable to lead to a significantly increased growth of PAH into soot nanoparticles.

3.2.2 Polyyne inception

The first molecular beam mass spectrometry from within flames revealed significant concentrations of polyynes, suggesting them as a potential precursor to soot nanoparticles [185]. Recent molecular beam Raman analysis also confirms the significant concentration of polyynes present in soot forming flames [244]. However, the growth of these species was not found to extend past 150 Da using mass spectrometry [185, 186]. While many have pointed to the increased stability of polyynes at high temperatures compared with pericondensed aromatic molecules [231], they are prone to degrade in flame environments. Hydrogen addition to growing polyynes leads to radical-induced fragmentation such as,

$$H-C\equiv C-C\equiv C-H + H \longrightarrow H-\bullet C=CH-C\equiv C-H \longrightarrow H-C\equiv C-H + \bullet C\equiv C-H,$$
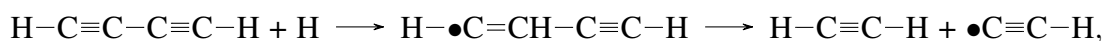
where the hydrogen addition leads to a radical that fragments through a β-scission – breaking up the chain. Analysis of polyynes in partial equilibrium with hydrogen radicals and H_2 supported a limit to polyyne growth of C_mH_2, m < 16 [283, 141]. Long polyynes are unlikely to cyclise into PAH due to their high rigidity [254] and are more likely to degrade to acetylene and C4 species that are able to cyclise into aromatics [164].

Recently a range of reactive molecular dynamics simulations have suggested a polyyne mechanism [463, 163, 253] reminiscent of fullerene cage formation that was explored using similar methods [334]. In simulations involving highly concentrated mixtures of acetylene and other fuels (0.1 g/cc) and extreme temperatures (2000–3000 K) large fullerene-like structures were observed [463, 163, 253]. These extreme temperatures led to breaking of the C−H bonds and a large number of radicals which readily react due to the high density forming long polyyne chains that condense into cage structures. As mentioned, such growth of long polyynes is not observed in most flame systems. The H/C ratio of early soot particles of 0.3–0.5 is also too high compared with what would be expected from a fullerene-like polyyne mechanism. Careful reactive molecular dynamics of benzene pyrolysis showed the initial formation of aromatic species [357, 358] and only after loss of all hydrogen atoms were fullerene-like cages able to form. This result matches what is observed in the negative mass spectrum during aromatic to fullerene transformations [14, 186, 413].

The discussion of polyynes leads us to recall the comment from Bansal and Donnet from 1993 [102],

"...the presence of a particular species is not sufficient proof that it is involved in soot formation. A species may be present because it is not reactive."

It also reminds us that a soot mechanism must consider not only the construction towards soot nanoparticles (forward reactions) but also the destruction of the growing species (reverse reactions).

3.2.3   Polyaromatic inception

Polyaromatic inception is a chemical polymerisation between PAH that forms nanoparticles. It is important to note that crosslinks and acetylene growth mechanisms often occur simultaneously, as discussed in the previous section describing PAH formation. Nonetheless, the growth into nanoparticles is distinct from PAH formation as we are exploring rapid formation mechanisms past 1000 Da that provide three-dimensional growth. The first to suggest a polyaromatic inception was perhaps Rummel and Veh [353] when they suggested that moderately sized PAH molecules react to form soot. These species had by then been extracted from sooting flames [411]. We have also mentioned that as PAH grow in the harsh environment within flames they form and fragment with only stabilomers (highly pericondensed aromatics) being formed [398], which have low reactivity towards each other.

Palmer and Cullis suggested that the abstraction of an edge-based hydrogen from a PAH produces an aryl-type σ-radical able to react with a closed shell PAH – called aryl/PAH polyaromatic inception [see Table 3.1 (k)]. This follows the well known pyrolysis reactions of aromatics. Benzene pyrolysis, for example, will yield biphenyl with subsequent phenyl additions giving triphenylene, which involves cyclodehydrogenation [see Table 3.1 (m)] [293]. Unless subsequent cyclodehydrogenation takes place the phenyl addition of an aromatic ring is prone to radical-induced fragmentation [116]; for example, C–C aryl bond energies of only -20 to -23 kcal/mol are found for the hydrogenated biphenyl/phenyl-benzene complex [317, 385]. Therefore, soot mechanisms involving the reaction between σ-radicals and highly aromatic PAH were not considered to be thermally stable in the flame under radical-induced fragmentation [129]. However, in pyrolysis systems operating at lower temperatures the aryl/PAH inception appears to be critical for the formation of PAH and possibly carbonaceous nanoparticles [74, 384].

As the aromatic network increases in size, so does the concentration of σ-radicals. This in turn heightens the chance of the aryl/aryl polyaromatic inception mechanism occurring [see Table 3.1 (l)]. Howard calculated that PAH $\approx$600 Da in partial equilibrium with $H^{\bullet}/H_2$ would each possess 5–6 σ-radicals [189]. A radical termination reaction was considered as a chemical soot inception mechanism. The rate for such a mechanism can be described as,

$$R_{C_{a,b}} = C_E \times \beta_{a,b} \times C_a \times C_b, \tag{3.20}$$

where the reaction rate of molecules a and b is the product of the collision efficiency, C_E (other authors use α [438], β [110] or γ [218]); the free molecular collision coagulation kernel, $\beta_{a,b}$; the concentration of molecules a, C_a; and b, C_b (in Kraft notation; Raj et al. [337]). The collision efficiency is often further split to separately consider the van der Waals enhancement, E_F. It was found that aromatic species would need to react with a collision efficiency of $C_E = 0.1 - 1.0$ to produce the concentration of particles found during soot formation [344]. However, a reactive molecular dynamics study of colliding aryl/aryl PAH found efficiencies one to two orders of magnitude lower than those required (closer to $C_E = 0.001$) [263]. Some other reactive molecular dynamics studies have suggested rapid clustering of PAH radicals with close to unity C_E [461, 214]. However, the high densities used, 0.2 g/cc, significantly enhanced the clustering, overshadowing the importance of fragmentation in flames where PAH densities are closer to 10^{-6} g/cc [121]. Furthermore, high temperatures (2000–2500 K) have often been used to speed up these simulations, leading to direct hydrogen loss from PAH edges. This does not occur at any significant rate at flame temperatures without a radical abstraction, which means that the number of radicals in these simulations is much higher than in the flame itself [461, 214]. Mao et al. demonstrated the importance of temperature in reactive molecular dynamics [262]. No clustering was seen at 2000 K for PAH such as coronene, however increasing the temperature to 2500 K led to hydrogen loss and chemical inception [262]. Chemical inception could be effective at 2000 K if nickel is added, however catalytic effects will not be considered in this review [378].

Less reactive but more abundant edges on PAH molecules were also suggested to contribute to polyaromatic inception, such as rim-based pentagonal rings on acenaphalene or the 9, 10 low aromaticity free edge on phenanthrene [85]. While these edges are not able to crosslink with one another e.g. [2+2] pericyclic reactions are symmetry forbidden [361], they have significant reactivity with aryl σ-radical PAH. Significant bond energies of -44 kcal/mol have been calculated between phenyl radicals and acenapthalene crosslinks, suggesting flame stability [429]. However, hydrogen addition to the unsaturated carbon part of the crosslink would lead to its breakdown. This could be overcome if hydrogen abstraction from the saturated carbon formed a closed shell C–C bond, which is highly stable [430] forming aromatic aryl-linked hydrocarbons (AALH) (see Figure 3.12a). As with the other aryl crosslinks a similar low collision efficiency would be expected as was determined for aryl/aryl crosslinks [263].

Within an aromatic molecule π-electrons are able to form aromatically stabilised bonding, providing significant thermal stability within PAH. An odd number of π-electrons within

(a) Aliphatically/aromatic linked hydrocarbons nanoparticle [428].   Used with permission from AIP ©

.

(b) Clustering of hydrocarbons by radical-chain reactions (CHRCR) from RSR and σ-radical [204].   Used with permission from Science AAAS ©

.
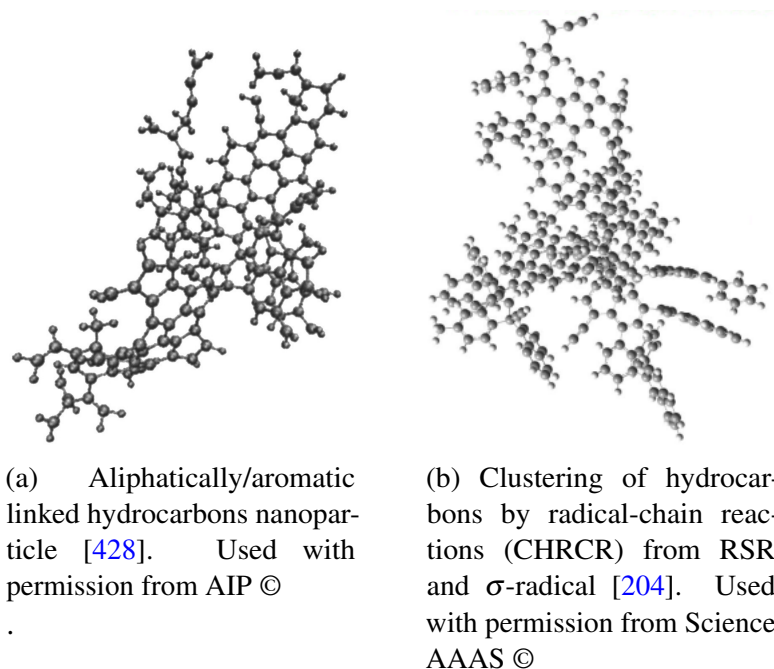
Figure 3.12 Nanoparticles from chemical inception mechanisms.

such networks gives rise to a delocalised or resonance-stabilised π-radical (RSR). These stabilised π-radicals are critical for the formation of the first aromatic ring as, for example, propargyl can rise to significant concentrations and cyclise into benzene [286]. A mechanism where RSR crosslinks with aryl radicals forms a strong bond (80 kcal/mol). Critically, this is rapidly further stabilised by a unimolecular loss of hydrogen with a barrier of only 4.5 kcal/mol [204]. This regenerates the RSR and further reactions with aryl radicals can occur. The ability to regenerate the reactive radical led to the naming of the mechanism as clustering of hydrocarbons by radical-chain reactions (CHRCR) [see Table 3.1 (r)] and Figure 3.12b]. Unlike the mechanism between aryl and pentarings [see Table 3.1 (p)] CHRCR does not require a subsequent hydrogen abstraction to produce a stable single bond as hydrogen is instead easily lost, restoring aromaticity to the π-radical.

However, such an increased reactivity for odd numbers of carbon atoms, most likely to be RSR, was not seen experimentally [213]. For this reason Homann suggested that RSR were not very reactive. While it is true that aromatic RSR are less reactive for recombination with themselves, reactions with σ-radicals were calculated to form strong bonds even more so than with pentaring polyaromatic inception [204]. A possible answer to the similar concentration of even and odd carbon fragments in flames could be inferred from the recent HR-AFM analysis of aromatic soot precursors [78]. Many regions of aromatic molecules with an odd number of carbon atoms, where one would anticipate an RSR to form, contained a hydrogen

saturated edge carbon (most often on a zig-zag site). Therefore, while aromatic σ-radicals can react with RSR, it is unclear how hydrogen radicals could terminate these chain reactions. Hydrogen addition across the crosslink at the unsaturated carbon atom, or neighbouring site, could also lead to fragmentation. Therefore, experimental evidence for this pathway is required as well as a full reaction mechanism that includes all pathways. A low collision efficiency would also be expected for this mechanism, as with other polyaromatic inception mechanisms.

Compared with the single-site σ-radicals discussed above, diradicals such as carbynes or carbenes can have a greater reactivity and provide an alternative means of crosslinking PAH [73, 75, 313]. Carbyne is formed when two hydrogen abstractions occur along the same free edge (the simplest example being benzyne, where benzene loses two neighbouring hydrogen atoms) [75, 179]. Phenyl – produced by one hydrogen abstraction – is able to undergo a unimolecular decomposition to benzyne with a barrier of some 80 kcal/mol. This large barrier makes phenyl concentrations significantly greater than benzyne in flames [260]. It was also found that above 1500 K, the benzyne ring is found to break open and a linear form of $l-C_6H_4$ becomes dominant [260]. For larger PAH, hydrogen abstraction is unlikely to provide two neighbouring sites given the average 5–6 σ-radical sites per 600 Da species as mentioned [189]. The other option for carbyne creation is the decomposition pathway of the neighbouring hydrogen from larger σ-radical PAH. This has not been explored in detail but if similar barriers are seen as in phenyl this option is less likely. Indirect insight can be provided by a recent exploration of the pyrolysis of coronene and dibenzo[a,e]pyrene [307]. These two species have the same number of carbon atoms but significantly different edges: coronene possesses a more condensed structure with six zig-zag and six free edges while dibenzo[a,e]pyrene possesses nine free edges, three armchair edges and two zig-zag edges. If the carbyne route was dominant, the species with more free edges would be expected to dimerise more readily, forming more soot. However, dibenzo[a,e]pyrene, with its numerous free edges, inhibits soot formation compared to coronene (with more zig-zag edges than free). This suggests a more significant impact of aryl/PAH as opposed to carbyne-like polyaromatic inception.

Carbenes are diradicals where a hydrogen atom has been abstracted from a zig-zag edge to form a σ-radical. They also have an odd number of carbon atoms, forming a π-radical. While both radicals are localised for small carbenes such as methylene (H_2C:, with a spin density of 2 at the carbon site), calculations for large PAH have shown that the π-radical becomes delocalised [313]. Strong bonds were formed between carbenes and large PAH. However, it is unclear whether these are any stronger than what would be expected from σ-radicals (with spin density of 1 at the carbon site) and PAH. Given that the spin density

of the carbene site on a large PAH was found to be only slightly greater than one, at 1.1 electrons, it is clear that larger carbenes are more similar to σ-radicals than they are to methylene. This does pose the question of how reactive π-radicals are in comparison with σ-radicals as PAH grow in size.

In summary, many polyaromatic inception mechanisms have been suggested. Some have been integrated into kinetic Monte Carlo simulations and have shown the ability to grow nanoparticles ≈ 2 nm in size [428] (see Figure 3.12a). These nanoparticles have only slow, first-order growth due to their radical-induced fragmentation and the low collisional efficiencies of PAH. As a result, these mechanisms are not a contender for primary particle formation.

3.2.4   Physical nucleation

Frankland was the first to consider a physical nucleation or condensation mechanism for soot formation. Upon lighting a candle at the summit of Mont Blanc (a picture of which begins Chapter 6) he noticed a significant reduction in flame luminosity [124]. Back at the Royal Society he made use of air pumps to operate a candle above atmospheric pressure, finding an increased flame luminosity which indicated that soot formation was being enhanced. Frankland's initial suggestion that the emission of light from flames was not from solid particles but from a dense vapour has since been disproved [247]. However, the strong pressure dependence of soot formation has long been seen as evidence for physical nucleation of hydrocarbons in flames.

Recent experiments on sooting flames within high pressure chambers further highlights the influence of pressure on soot formation [8]. Figure 3.13 reveals the increase in primary particle size of soot aggregates, sampled from within the pressure vessel, as the pressure was increased. Such a strong dependence is not anticipated for chemical routes as kinetically controlled pathways in soot formation, for example HACA growth, are characterised by reaction rates, which are first order in monomer concentration [438]. However, the significant increase in particle size and non-linear increase in soot volume with pressure [277] suggest condensation, which depends on the square of the monomer concentration [129, 438].

Polymerisation of fuel into an aliphatic polymer that condenses [see Table 3.1 (t)] can be quickly dismissed given the rapid radical-induced fragmentation of aliphatic fuels in flames and that no large liquid particles are detected with laser scattering [173, 339]. However, aromatic polymerisation [see Table 3.1 (u)] has been considered in detail as mentioned in the previous section. After the influential paper of Rummel and Veh [353] suggesting that larger polycyclic molecules precipitate soot particles, Parker and Wolfhard suggested such a mechanism [319]. In their 1950 review they state,
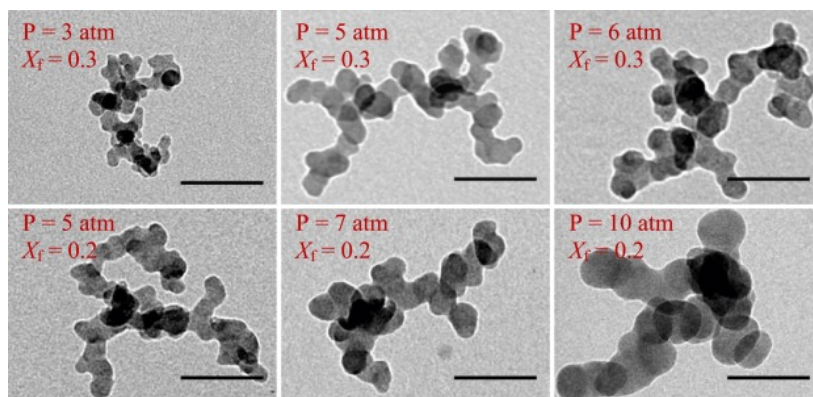
Figure 3.13 Soot sampled from a counterflow diffusion flame over a variety of pressures [8]. Used with permission from Elsevier ©.

> "Higher hydrocarbons are formed by pyrolysis. The molecular weight and concentration of these increase until the saturation vapour pressure is exceeded, whereupon condensation occurs and fine droplets are formed."

The higher hydrocarbons they discussed are crosslinked PAH that form an aromatic polymer which then condenses into a liquid droplet [see Table 3.1 (u)]. The reverse rate due to thermal breakdown was proposed to be counteracted by carbonisation reactions. This mechanism represents a combination of many mechanisms already discussed, where PAH grow through the HACA mechanism, polymerise according to a polyaromatic inception mechanism and then physically nucleate. Such a proposal relies therefore on the mechanisms preceding condensation and is subject to their limitations.

The condensation of polyaromatic clusters has recently been explored using molecular dynamics simulations [193]. Aromatically-linked PAH were found to cluster with greater propensity than their monomeric components, however, these species were highly contorted which significantly reduced physical interactions compared with similar sized pericondensed PAH. It is unclear then how large a polyaromatic would need to be for physical nucleation to occur and whether such growth processes were possible given the radical-induced thermal degradations occuring within the flame.

Direct physical nucleation of pericondensed aromatic species [see Table 3.1 (v)] has been, arguably, the most widely explored mechanism in soot nanoparticle formation. This suggestion had been considered unlikely by Haynes and Wagner in 1981 given the low boiling/sublimation temperatures for PAH molecules [173]. PAH species would need to be 2000–3000 Da in weight to have boiling points high enough to provide a supersaturated vapour required for condensation within the flame. Miller turned to the formation of molecular clusters and considered the dimerisation of PAH in flames using intermolecular

potentials [290, 287]. As discussed in the section on PAH formation, the HACA mechanism provides small PAH ≈250 Da of a sufficient concentration to form soot [438]. These species were found to be unable to dimerise at flame temperatures. Large species (circumcoronene $C_{54}H_{18}$ 667 Da or larger) were required to provide a significant concentration of dimers at flame temperatures, however their concentrations were too low to predict the number of soot nuclei [438, 419].

While condensation was seen as unlikely, the evidence for stacked aromatic species grew due to the discovery of a green fluorescence signal in flames. Figure 3.14 shows this fluorescence in an image from the 1980s when UV lasers were able to provide such a signal [136]. Initially, this was seen as a response from the individual molecules as PAH are known to fluoresce. However, the signal was of a high enough wavelength to suggest an excimer origin. Excimers are long-lived optical states that are formed from the delocalisation of the $\pi-\pi^*$ state across two stacked aromatic species, and are present in the fluorescence spectra of PAH dissolved in liquids [35, 182]. Figure 3.14 also shows the potential energy surface for such a state and the molecular orbitals of the HOMO and LUMO showing the bonding present in the LUMO as calculated with DFT by Miller [288].

Time resolved laser induced fluorescence (LIF) experiments have established that this green fluorescence signal belongs to excimers [282, 391]. Excimer states are long-lived (tens of nanoseconds) and time resolved LIF confirmed such long lived states for signals in the range 500–600 nm. Critically, the excimer signal reveals that physically bound, stacked aromatic species are present during soot formation as these signals are unable to be produced from polyaromatic linkages.

Mass spectrometric evidence began to emerge in the 2000s that clustering was occurring with a periodicity of 500 Da [165], using soft ionisation laser desorption ionisation techniques. Figure 3.15 shows this series of peaks with a periodicity of 500 Da.

As has been mentioned in the section on PAH formation, these species require a combination of HACA and PAH crosslinks to form. This size of species is also found to be present in soot particles (see Figure 3.4) [97].

Other suggestions were made for the stabilisation of moderately sized PAH clustering through internal rotations or aliphatic chains. In molecular dynamics simulations of colliding PAH species, Miller observed orbiting of the PAH [287]. Schultz and Frenklach explored this effect using a quantum molecular dynamics approach and found evidence for internal rotors [369].

This stimulated research into performing highly accurate calculations of intermolecular energies between PAH and providing new descriptions of the free energy. Making use of the SAPT(DFT) method, high accuracy binding energies were calculated between PAH [418].
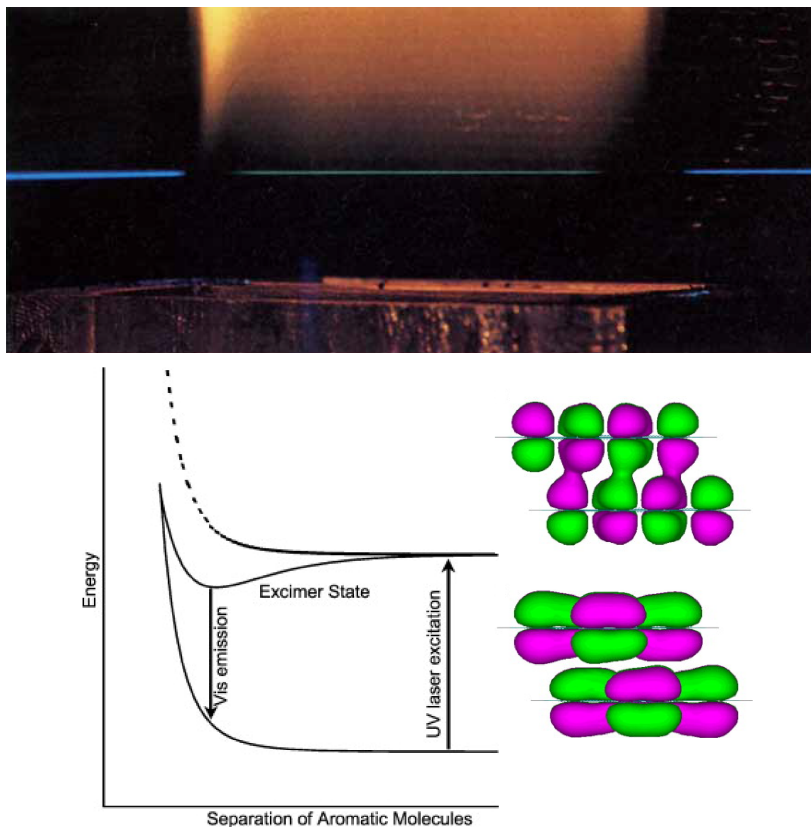
Figure 3.14 Green fluorescence from UV laser excitation (top) [136]. Energy landscape for excimer state [288]. Used with permission from Springer Nature America and Elsevier ©.
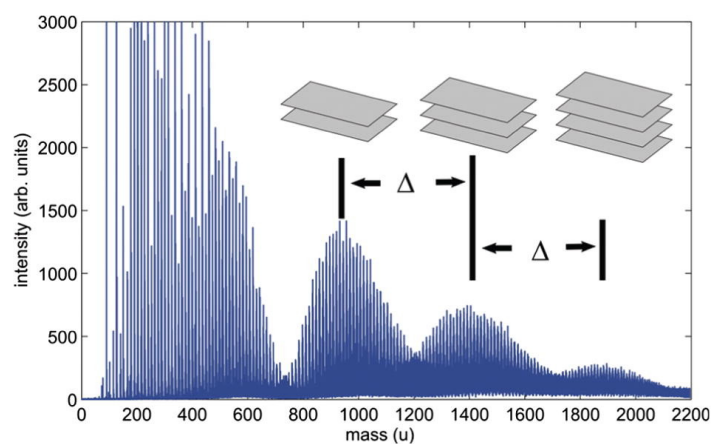
Figure 3.15 Mass spectrum of high-molecular weight species extracted from a 13 kPa acetylene–oxygen flame (ϕ = 3.25) by molecular beam mass spectrometry with 193 nm laser ionisation [165].

Molecular dynamics simulations were used to show the clustering of the species, with species smaller than circumcoronene unable to cluster at >1500 K [419]. Experiments confirmed the

accuracy of the forcefield in describing both the virial coefficient for benzene, the exfoliation energy of graphene [418] and more recently, scanning tunnelling microscopy of coronene clusters (see Figure 3.16). Experiments on supersonic jets of pyrene also confirm its lack of stability past boiling point [356].
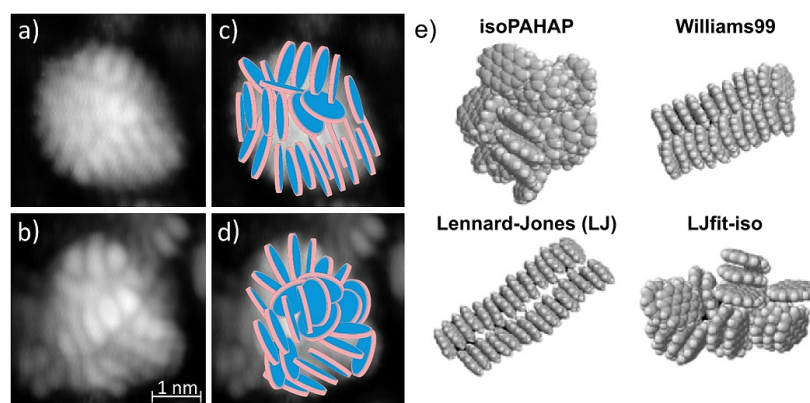
Figure 3.16 a-b) Scanning tunneling microscopy imaged clusters of coronene molecules. c-d) Potential orientations of the coronene molecules in these clusters [441]. e) The computational results from clusters formed during a molecular dynamics simulation of coronene with different forcefields used [320]. Used with permission from Elsevier ©.

A full description of homodimerisation of PAH using statistical mechanics introduced by Wang [438] and Totton et al. [418] showed that the intermolecular interactions and internal modes developed were insufficient to overcome the entropic penalty of reducing the number of species in the gas phase. Metadynamics simulations were also employed that allowed the free energy to be directly and economically computed from molecular dynamics simulations with guided dynamics [68, 112]. Again, similar results were found for pericondensed PAH but soft modes could be included from aliphatic chains. They were found to improve clustering of the species but the collision efficiencies were similar to the pericondensed sub-structure, indicating it is the van der Waals interactions of the pericondensed structure that still govern the ability to form complexes at high temperature. These chains have been observed in HR-AFM of PAH [78]. However, for 500 Da species the chains are still unable to provide the increased intermolecular forces required to allow for clustering at >1500 K.

Frenklach and Wang in 1991 were among the first to suggest an ion-induced physical nucleation mechanism in soot formation [131]. Experimental work on cationic benzene dimers had found an enhanced binding energy increasing from 0.5–3 to 17 kcal/mol (the neutral to the cationic dimer, respectively [255, 381]). More recently, computational work on larger PAH cationic dimers found binding energies in the range 15–20 kcal/mol for PAH with 4–5 rings [MP2/6-31G(d)] [342]. Larger clusters were recently explored using basin hopping and density functional tight binding methods [103]. More compact clusters were

formed with a positively charged dimer or trimer in the centre, indicating that the enhanced binding energy is only reserved for a few molecules in the cluster. Cation-π interactions are more significant with small cations such as metals or flame ions. Binding energies to benzene of 108 and 151 kcal/mol were found for Mg^{2+} and Fe^{2+}, respectively [226], while the 1+ cation Na^{1+} was found to be weakly bound with 21 kcal/mol. Binding energies of larger PAH (1–4 rings) with more flame relevant chemi-ions were recently computed [62]. Binding energies of 30–60, 18–27 and 26–32 kcal/mol were found between CHO^+, $c-C_3H_3^+$ and H_3O^+, respectively. Chen and Wang noted;

> "...the cation-enhanced binding remains to be too weak to impact the gas-phase
> PAH chemistry or the clustering of PAHs leading to soot nucleation."

However, curved PAH, unlike planar PAH, should have a more considerable interaction given the polar nature of these species, which will be explored in Chapter 6.

In summary, physical nucleation provides a rapid soot formation pathway, given that sufficiently strong intermolecular interactions allow for a supersaturated vapour to form. However, the clustering species in flames of mass 500 Da are found instead to have interactions too weak to explain soot formation.

3.2.5 Physical + Chemical

The crux of the soot formation problem is that the physical and electrical condensation of precursor molecules is rapid but too weak to hold soot together, while most chemical bonds are strong but mechanisms proposed to date are too slow to account for soot's rapid growth as observed in experiments. A mechanism that combines both aspects, condensation and chemical bonds, is required. One of the first clear articulations of such a proposal is from Harris and Weiner in 1989 [170];

> "Once coagulated they will quickly become chemically knit together since a
> significant fraction of the aromatic species are radicals."

Miller followed with a similar suggestion in 1991 that;

> "...if individual PAH or their dimers undergo rapid, irreversible reactions, the net
> rate of production of the soot nuclei may be sufficiently high so that the concen-
> tration of the nuclei far exceeds the concentrations of the reacting, intermediate
> species."

This irreversible dimerisation, that was assumed to be facilitated by some sort of chemical or non-equilibrium process, was the basis for the first successful kinetic model of soot formation that captured the particle number as well as the volume fraction [131].

Many different options have been suggested for a species that is both physically bound and chemically crosslinked. However, aryl/aryl bonds can be immediately ruled out given their bonding parallel to the aromatic plane that does not allow folding over of the species into a physically bound complex. Homann suggested that the bound PAH dimer could spontaneously react at the rim, releasing hydrogen and becoming a curved PAH or a fullerene – the zipper mechanism [24, 5, 186] [see Table 3.1 (aa)]. The strong aromaticity of the sp^2 network resists this zipper mechanism. It has been found instead, for fullerene formation, that near-complete loss of hydrogen is required before the carbon will curl and close into a fullerene [357].

Aliphatic bridges between stacked PAH have also been discussed in detail since the 1990s [see Table 3.1 (bb)]. In relation to the formation of interstellar dust, a mechanism was proposed by which a "cross-linked structure of aliphatic and aromatic hydrocarbons" formed and was suggested to explain soot formation under certain flame conditions [292]. Aliphatic bridges were also included in the early models of stacked species from Homann et al. [24], which showed the first stacked complex that was stabilised by a covalent link. This mechanism was suggested as part of the formation of some of the smallest nanoparticles in flames with D'Alessio commenting, during the 1994 Heidelberg soot workshop [84];

> "We think of two-ring structures connected together with some non-aromatic,
> some aliphatic bridges. You may also think about oxygen bridges..."

We will come back to the oxygen bridges. This description would later become known as aromatic aliphatic-linked hydrocarbons (AALH) [128] with aryl-linked pentagon containing species being introduced later [85].

Molecular dynamics revealed that aliphatic bridged ([CH$_2$]$_n$, $n = 2$) aromatics of mass ~250 Da were found to stack below the boiling point of the aromatic species. However, at flame temperatures (above the boiling point) these physical interactions were overcome and clustering of these species was at a significantly lower rate compared with pericondensed PAH [449, 68]. Therefore, for nucleation and soot formation from aliphatically-linked chemical mechanisms at least two [CH$_2$]$_n$, $n = 1$, would be required per PAH. This would lead to an H/C ratio greater than one, when most early soot nanoparticles are $H/C = 0.5$. However, the rapid carbonisation processes that occur in flames could rapidly decrease the H/C ratio, so this is less conclusive and requires more exploration.

Detailed kinetic mechanisms of how these aliphatic crosslinks form and fragment have also not been explored in significant detail. Some kinetic Monte Carlo codes do include such aliphatic crosslinks allowing comparison with other chemical pathways [430, 431, 428]. However, the aryl/aryl bonds continue to dominate, suggesting these aliphatic links are a

minor chemical pathway. More recently, for a $[CH_2]_n$, $n = 2$ aliphatic crosslink, one conceivable option is the reaction between two methyl resonantly stabilised π-radicals. Simulations and experiments have recently been performed using free electron laser IR radiation and mass spectrometry to probe the pyrolysis products of benzyl and indenyl [389, 390, 180]. Bibenzyl, a crosslinked species was found and shown to rapidly cyclodehydrogenate into pericondensed structures in a similar manner to the aryl-linked species discussed previously. These methyl radical sites could form from hydrogen abstraction of a methyl group. Methyl radical sites $-C^•H_2$ have not been directly imaged using HR-AFM, however, the precursor $-CH_3$ group has been imaged in soot precursor molecules using HR-AFM [78]. Another possible mechanism by Chen and Wang [62] involves $C_3H_3^+$ reacting with the edge to provide acetylene and a methyl radical group. It is also conceivable that for larger PAH the rearrangement reactions could be less important.

For these aliphatically bridged species, Krueger and Blanquart [235] were able to show that the excimer signal was still produced, indicating that stacked, non-conducting bridges also possess the excimer signal (see Figure 3.17).

(a)   (b)   (c)
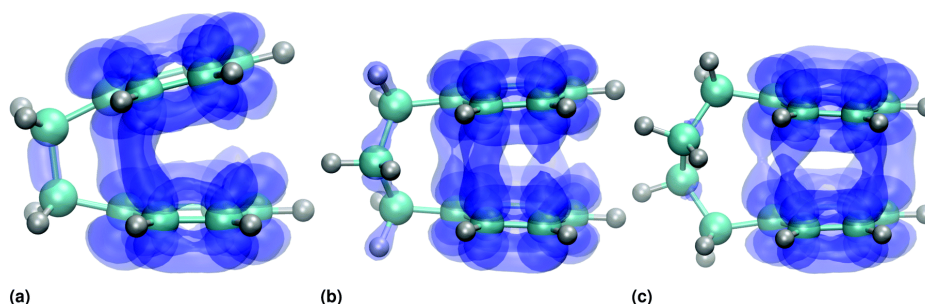
Figure 3.17 Isosurfaces (± 0.05) of the orbitals involved in the $S_0 \longrightarrow S_1$ optical transition for aliphatically bridged bezene dimers [235]. Used with permission from the Royal Society of Chemistry ©.

Acetylene groups attached to the edge of PAH have also been suggested to crosslink the PAH, reacting either with an RSR [144] or PAH σ-radical [461] [see Table 3.1 (cc)]. Double crosslinking is found for RSR crosslinked with molecular oxygen [264] [see Table 3.1 (dd)]. The impact of oxygen crosslinks can be considered minimal in most cases due to the lack of oxygen in soot nanoparticles [77] and the ability of pyrolysis reactors to produce soot without oxygen being present [344]. All aliphatic and acetylene bridges detailed to date are prone to significant radical-induced fragmentation [339].

Excimers have been discussed as evidence for stacking of aromatic species in the previous section but they also provide a bound state that has been suggested to stabilise soot nanoparticles [see Table 3.1 (ee)] [288]. A wide range of small PAH species have been calculated with binding energies of <20 kcal/mol found, too low to provide significant

stabilisation at flame temperatures [282]. The stabilisation is also only appreciable between pairs of species; the trimer is found to be weakly bound indicating the excimer is only able to delocalise effectively across two species [86]. Time resolved studies have found lifetimes of tens of nanoseconds [282], which are too short to provide stability over the hundreds of nanoseconds to milliseconds required for soot nanoparticle formation. Finally, insufficient UV light is produced in the flame to maintain a sufficient concentration of these species. This is evidenced by no spontaneous emission of the excimer signal. These excimers therefore require external, often laser, illumination to maintain and produce the fluorescence response.

Multicentre bonding, similar to the excimers, can be produced in the ground state for two PAH π-radicals – so-called pancake bonds [see Table 3.1 (ff)]. These form when AB stacking of two species, both with an odd number of π-electrons, allows for the singly occupied molecular orbitals to form a multicentre bonding molecular orbital [215]. The odd π-electron aromatics have been directly imaged in soot precursors using HR-AFM [78] and have been suggested to stabilise soot nanoparticles [394, 433]. However, the bonding is weak due to the strong Pauli replusion from the molecular orbitals not involved in the pancake bond. Therefore, poor overlap is found in these multicentre bonds with < 10 kcal/mol of additional interaction on top of the dispersion interactions [215]. They are also highly angle dependent, breaking after rotating by $30°$ [79].

Some PAH systems can possess an open-shell singlet or a multiradical character in their ground state – zig-zag diradicals [see Table 3.1 (gg)]. A good example is the acene series. As rings are linearly fused, the acene takes on a multiradical singlet ground state with significant reactivity with >5 rings spontaneously dimerising in solvent at room temperature [29]. Other PAH with significant zig-zag edges can also possess such a localised edge state [223, 220, 296] of higher reactivity and have been widely computationally explored [407]. They also possess an open-shell singlet with increasing radical character as the length of the zig-zag edge increases. Wang was the first to bring these species to the attention of the combustion community in 2010 [438] and since then considerable work has been undertaken to explore their impact on soot formation. Long acenes require considerable length of some five or six rings to attain the significant binding energy of 35 kcal/mol [227], which is nearing a value of importance for soot formation. Multiple [4+4] cyclisations were considered in a polymerisation to produce soot. Given the growth mechanisms found for PAH it is highly unlikely that a concentration of linear acenes with >5 rings will be present as evidenced by the species observed in the HR-AFM [78]. Another suggestion from the same work was to consider adding a circular pericondensed PAH to the end of the acene to combine stacked dispersion interactions and acene cycloaddition. However, as mentioned, this type of structure is highly unlikely to form in the flame.

Larger PAH, non-acenes, in roughly rectangular geometry were able to dimerise along their opposite zig-zag edges [464]. Species with five rings along the zig-zag edge were able to form strong complexes with binding energies of $\approx$50 kcal/mol. If we consider that in HR-AFM such symmetric species are not found and rarely are more than three adjacent zig-zag edges found (with a maximum of four zig-zag edges in a row observed) it is unlikely that this mechanism can explain the clustering of species of mass near 500 Da [78]. It is also not clear whether protonation could render such sites unreactive. For example, a pentacene-like species was directly observed in HR-AFM imaging. However, instead of a open-shell singlet ground state one of the zig-zag edges was protonated, forming a resonantly stabilised π-radical [78].

Finally, π-radicals can also be generated from protonation of rim-based pentagonal rings [see Table 3.1 (hh)]. The importance of these radicals in shuttling rim-based pentagons along zig-zag edges was first appreciated in calculations performed by Frenklach and Whitesides [133, 448]. These species have also recently been directly imaged in HR-AFM [78]. Given the non-aromaticity of the pentagonal rings, these radicals could have significant reactivity. Wang and coworkers found that this site reacted with the σ-radical phenyl forming a stable species that is unable to break open across the pentagonal ring (this is opposed to hexaphenylethane, which readily breaks to form free radicals) [82]. Given the location on the top of the aromatic species, potential stacked and bonded configurations could be possible. Further experimental evidence that edges with excess hydrogen are important clustering species comes from recent atmospheric pressure mass spectrometry [58].

In summary, soot mechanisms involving both covalent bonding and physical interactions provide the possibility of rapid irreversible nucleation with a variety of options proposed. The feasibility of these options has not received significant attention. This is partially due to the complex methodologies required to model nanoscale aromatic clusters with a variety of processes occurring on many different length and time scales, and partially due to the difficulty of experimentally probing this mass range.

3.3 Combining and mapping mechanisms and experiments

When exploring the various classes of mechanisms that have been proposed it is tempting to choose a primary mechanism. Instead, it is better to consider the conditions under which different mechanisms operate and how they interrelate. As has been noted by Frenklach when considering the PAH growth mechanisms [128];

"...it is pertinent to mention that the two nucleation models, AALH graphitization and PAH condensation, are not inconsistent with one another. On the contrary, they probably represent two possible extremes."

This was reiterated by D'Anna in his 2009 review stating that at low temperatures condensation is more likely to dominate, while at higher temperatures chemical mechanisms will dominate due to increased radical concentrations [83]. This requires a detailed computer simulation able to compare the various models, which is outside the scope of this review. A more manageable task is to map the various mechanisms onto the experimental results. I have therefore combined a variety of the most recent experimental results to update the H/C vs molecular mass graph initially plotted by Wagner and Homann in the 1970s (see Figure 3.18).
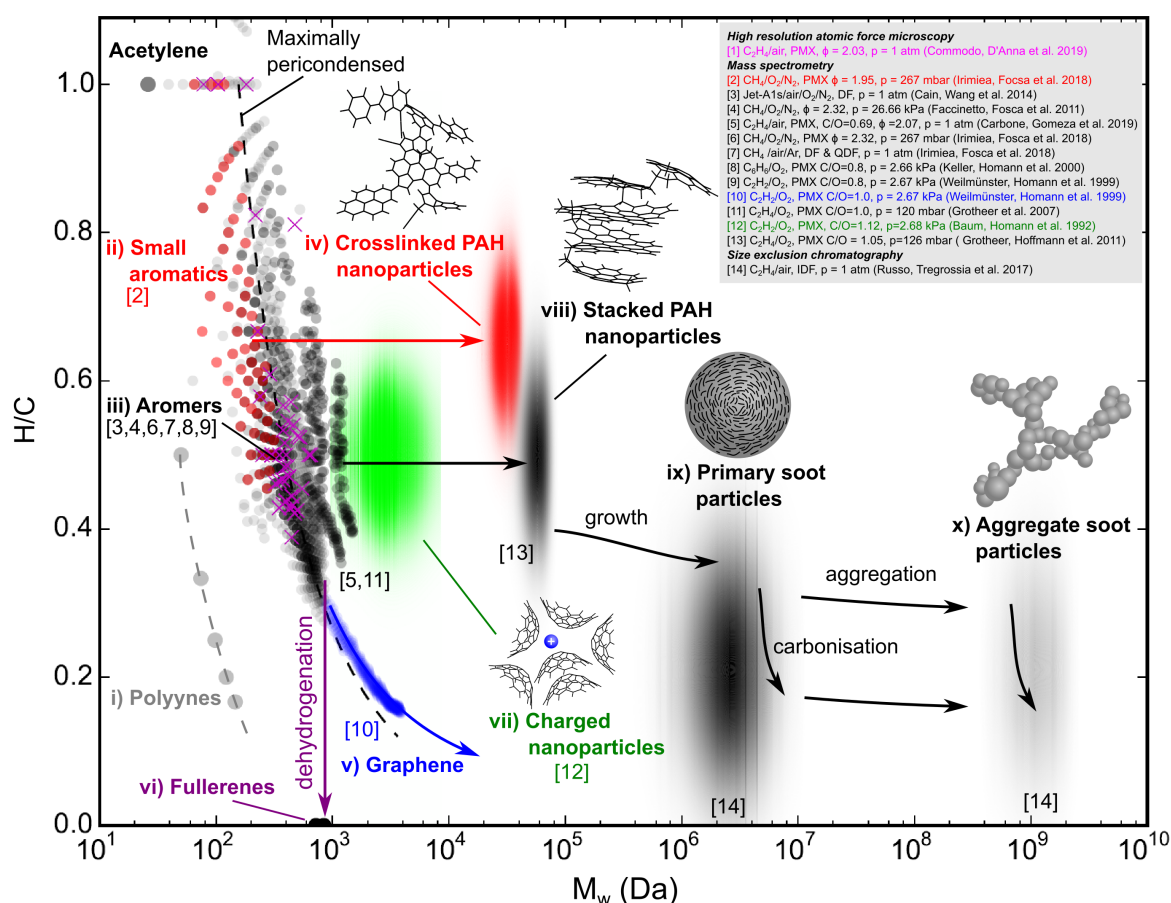
Figure 3.18 The variety of transformation of hydrocarbons towards soot formation.

The molecular masses of the different species are determined directly from either mass spectrometry data or from size exclusion chromatography from a variety of flames. In most modern mass spectrometers, the H/C ratio can be determined directly assuming only carbon

and hydrogen are present. The H/C ratio of the other nanoparticles, primary particles and aggregate particles are determined from elemental analysis with the ranges chosen to cover the observed values.

Looking at the figure, the first and most evident trend is a decrease in hydrogen content of the carbonaceous species as the mass increases. This follows from the entropically driven nature of soot formation from H_2 evolution [438]. Arrows show the pathways from precursors to particles for which experimental data or a correlation exists, unless otherwise mentioned below. I will now refer to each species within the figure in turn.

i) Polyynes are the first species to grow from polymerisation of acetylene, however due to radical-induced fragmentation these and acetylene are rapidly transformed into **ii) small aromatics**. **ii) Small aromatics** are formed from the HACA growth mechanism and have an exponentially decaying distribution of species with an average mass of 200–250 Da for slightly rich flames. For richer flames, aryl-crosslinking and cyclodehydrogenation are able to, alongside the HACA mechanism, produce the large distribution of **iii) aromers** centred at 450–550 Da [97]. Nucleation flames have demonstrated the presence of ≈2 nm nanoparticles in flames with only the initial distribution of **ii) small aromatics** [31, 97]. The photoionisation order indicates that these species are chemically **iv) crosslinked PAH nanoparticles** [157]. The small size of these nanoparticles could be due to radical-induced fragmentation that limits their growth. HACA growth can be continued only in low pressure acetylene flames to form large **v) graphene** structures [444].

iii) Aromers are suggested to form from aryl-crosslinking followed by cyclodehydrogenation. They are likely to be PAH curved by pentagon integration as they have been found to form negatively charged species in the flame that are able to dehydrogenate to form **vi) fullerenes**, but only significantly in low pressure benzene flames [186]. The fullerenes are suggested to form from three crosslinks of small aromatics, producing aromers large enough to be significantly curved to become fullerenes during dehydrogenation. **vii) Charged nanoparticles** are formed in acetylene flames. Homann found a correlation with the larger PAH species and the charged nanoparticle concentrations suggesting these particles are chemi-ion stabilised clusters of cPAH [187].

Clustering of PAH species weighing 450–550 Da has been demonstrated in low pressure and atmospheric flames [165, 58]. It is proposed in this dissertation that the aromers crosslink in a stacked configuration stabilised by localised π-bonds to form **viii) stacked PAH nanoparticles**. Evidence for this suggestion comes from mass spectrometry work. Firstly, in a low pressure flame clustering was seen preferentially for species with odd hydrogen numbers, suggesting that these species are localised π-radicals [165]. Secondly, in atmospheric flames it was found that species with an excess of hydrogen cluster, as de-

termined from the mass defect and the fact that only the positive mass spectrum showed clustering caused by protonation [58]. Compared with the crosslinked PAH nanoparticles, the larger stacked PAH nanoparticles, at 4–5 nm, are more easily fragmented by laser ablation and more easily photoionised. This indicates that they are more weakly bound [22].

The stacked PAH nanoparticle mode was shown to grow into the **ix) primary soot particles** using particle mass spectrometry [76]. HRTEM, Raman spectrometry and elemental analysis confirmed that ≈500 Da sized pericondensed PAH are present in early soot primary particles [96, 88]. It is unclear how the crosslinked PAH nanoparticles and charged nanoparticle modes influence the stacked PAH nanoparticles growth mode. HRTEM images show some soot particles contain less ordered cores, indicating heterogeneous nucleation (not amorphous but small aromatics). On the other hand, many soot particles also do not have such cores.

Another question surrounding charged nanoparticles was posed by Fialkov in 1997 [121];

> "The remarkable question remains: why is the number density of charged soot particles under nearly equal conditions (those which are important for thermoionization) in a benzene flame much smaller (or not registered at all) than in an acetylene flame?"

From preliminary results from premixed atmospheric flames it does, however, appear that species larger than 10^4 Da possess a charge distribution matching thermal equilibrium [377]. As mentioned, the speed at which these larger soot nanoparticles become charged indicates they arise from the aggregation of smaller charged soot nanoparticle clusters [121]. Therefore, these charged clusters are likely to contribute to growth into larger species. The soot nanoparticles ≈10 nm in size have between 1–2 orders of magnitude lower concentration of charged species while those at 2 nm have a slighter higher charge fraction – one order of magnitude lower – with a slight preference for positive ions.

Do charged mechanisms exist independently of neutral mechanisms? This appears not to be the case – as Fialkov mentioned, if neutral and charged species first exist separately and then later combine, the electric field would be expected to only influence the size of charged species while some unaffected, neutral primary particles remain. However, all primary particles are influenced [121]. It appears therefore that the relationship between the charged and non-charged nanoparticles is not as exclusive as previously thought. It is also unclear whether ionic interactions would enhance chemical mechanisms by holding species together long enough for them to react. However, the ability of other flame systems to form soot without significant chemi-ion concentrations makes this suggestion less likely to be of primary importance [344].

Primary soot particles then collide to form **x) aggregate soot particles**. Carbonisation also occurs, modifying soot's nanostructure to form an exterior shell and increasing the aromatic molecules' size [218]. The presence of significant crosslinking within mature soot particles, either from the soot formation process or from carbonisation, is evidenced by the hardness of soot particles measured using nanoindentation (see Table 3.2). Primary soot particles contain similar hardness values to charcoal, suggesting a highly crosslinked nanostructure, compared with nanocrystalline graphite which is largely uncrosslinked. Nanoin-

Table 3.2 Table of carbon-based materials hardness values from nanoindentation.

Material	Hardness (GPa)	Ref.
Fullerene (C_{60}) crystallite	0.21–0.24	[322]
Nanocrystalline graphite	0.1–0.4	[322]
Pyrolytic carbon HD	0.5–1.5	[397]
HOPG	2.4	[343]
Pyrolytic carbon LD	2–4	[397]
Carbon black	3–4	[32]
Ethylene soot	3–5	[32, 33]
Charcoal	3–5	[468]
Diesel soot	6–7	[32]
Polymerised C_{70}	30	[322]
Diamond	95–117	[343]

dentation of early soot nanoparticles would allow the degree of crosslinking to be found and help to determine whether the earliest soot nanoparticles are indeed crosslinked.

In conclusion, recent experimental and computational techniques have led to a flurry of new insights into soot formation. Soot aromatic precursor chemistry is becoming more complete with non-contact AFM providing the arrangement of rings within aromatics to reveal the importance of pentagonal rings and crosslinks. Small aromatics are formed from HACA growth with further growth to aromers made possible from PAH crosslinking and rearrangements. Soot nanoparticle formation mechanisms are becoming clearer, with many now being able to be ruled out through detailed computational and experimental results. Mechanisms involving both physical and chemical interactions, so-called covalently stabilised soot nucleation, are the most promising for explaining the rapid formation of soot in flames. Three nanoparticle modes have been experimentally observed and tentatively mapped to chemical, physical and chemical + physical mechanisms for the crosslinked, charged and stacked nanoparticles, respectively. Significant work is required to construct full and detailed models to refine the current mapping by determining how the mechanisms influence one another and how various mechanisms operate in different flame systems. Ultimately, as

experimental and computational techniques fill these knowledge gaps, opportunities will arise for significant reductions in soot emissions and for the control of carbonaceous nanoparticles in flames.

Chapter 4

Polarisation of PAH curved by pentagon incorporation
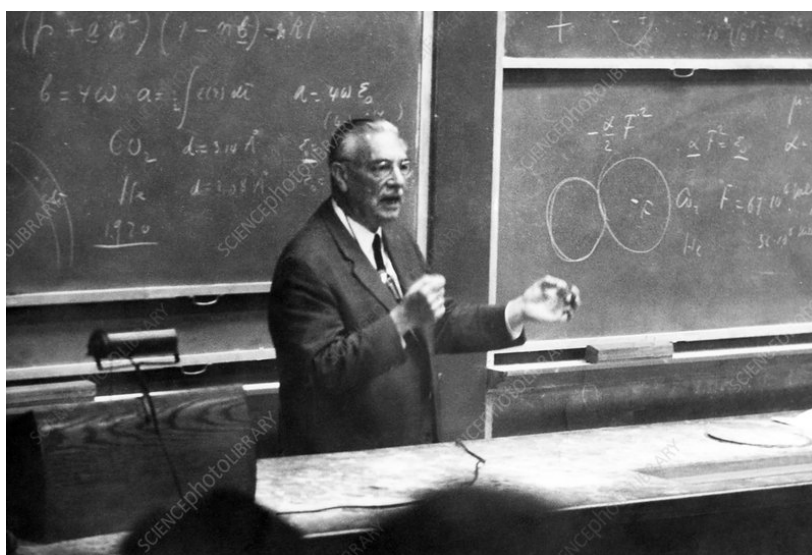
"I therefore conjectured that molecules in the state of equilibrium can also be carriers of a permanent electric moment and so the electric polarization in general must be attributed to two simultaneously effective causes, a deformation and an orientation."

– Peter Debye, Nobel lecture 1937

The work in this section was published as a paper in *The Journal of Physical Chemistry C* in collaboration with the Computational Modelling Group at the University of Cambridge. Contributions from this group included Dr Yapp providing a large kinetic Monte Carlo derived PAH **3f** for the analysis, while Dr Slavchov aided in the geometrical model derived and the other authors edited the manuscript. The calculations, analysis and writing were performed by the author.

In this chapter, electronic structure calculations were used to compute the electric polarisation of polycyclic aromatic hydrocarbons curved by pentagon incorporation. The origin of the dipole moment in these species was found to be solely due to the pyramidalisation of the carbon atoms and a geometrical model was found to accurately reproduce the dipole moment. Finally, the use of distributed multipoles was used to show the significant out-of-plane polarisation that cannot be captured with more commonly used atom-centred charge descriptions. This will aid in exploring the electrostatic interactions possible between cPAH in the flame and other species during soot formation, later in this dissertation.

The introduction of curvature into a hexagonal carbon lattice through a pentagonal disclination gives rise to a considerable molecular dipole moment. For example, corannulene (the first curved PAH to be synthesised [243]) was found experimentally to contain a dipole moment of 2.071 D [257] which is on the order of the dipole of water (1.85 D [383]). A range of indenocorannulenes have been synthesised [399] and electronic structure calculations suggested dipole moments from 3 to 4.5 D for PAH with eight to ten rings [122]. The nm-sized curved arenes known as nanocones, with curved nuclei that grow into large graphitic cones, have been fabricated with a clear number of pentagons integrated into the nucleus/tip of the nanocone [139, 232]. Electronic structure calculations of these nanocones showed a significant dipole for nanocones 0.5–4 nm in size ranging from ten to 35 D [237]. In another study, a nanotube cap (10,10) has been calculated to possess a dipole moment of 3.5 D [312].

Many applications are being explored for these molecules, centred around their dipole moment – for example, the flexoelectric response has been investigated for nanocones [237]. Large nanocones have been found to self-assemble into long filaments in an electric field, increasing the conductivity between the electrodes [222]. Some curved PAH, such as sumanene (Figure 4.1-**3a**), form crystal structures with 1D stacking [122] and have been suggested to possess a strong non-linear response for optical elements [249] and electronic transport properties for organic light emitting diodes [436]. The dipole moment is responsible for significant binding of curved PAH to metals which has been investigated as a method for electrical coupling between metals and organics in molecular electronics [23, 399] and could also improve ion capacity in lithium ion batteries [140]. However, the implications for such species in soot formation have yet to be considered.

The purpose of this chapter is to calculate the dipole moment for a range of curved PAH molecules, determine the origin of the dipole moment and develop an atom-centered distributed multipole model of the electrostatic potential controlling the intermolecular interactions. This is an initial step towards the parametrisation of force fields needed for molecular dynamics simulations of systems containing curved PAH, where the curvature-induced dipole produces the major long-range interaction and contributes significantly to the molecular interactions.

4.1   Computation of the charge distribution

A representative collection of known curved PAH were chosen to give a range of different geometries for analysis. Their curvature is due to pentagon integration and produces a dipole moment. Many structures were chosen in the size range of 6–20 rings, as these have been observed in non-graphitising carbon as determined from fringe analysis [460, 41, 169]. The set contains only molecules that fulfil the isolated pentagon rule formulated for fullerenes, according to which neighbouring pentagons are thermodynamically unstable and rearrange or expel C_2 to form pentagons isolated by hexagons [454]. Pericondensed PAH with high symmetry containing only sp^2 carbon atoms have been found to be stable due to π-delocalisation and are considered to be the primary species in high temperature combustion carbons [398], and comprise the main part of the list in Figure 4.1 accordingly. Sumanene (**3a**) and (**3b**) contain sp^3 carbons and were also considered as they have been previously synthesised [359, 450]. The terminating carbon atoms bonded to the hydrogen shall be referred to as *rim carbon* atoms and the central carbon atoms as *hub* atoms.

The calculation of the dipole moment of a molecule requires accurate molecular geometry and electron density. The hybrid density functional B3LYP [246, 26, 400] has been found to accurately describe both the geometry and the charge distribution of polyarenes and corannulene compared with experimentally determined values from synchrotron X-ray scattering [325, 150].

Once an accurate geometry and charge distribution has been calculated the dipole moment vector, μ_{tot}, can be calculated from the nuclear and electronic contributions,

$$\mu_{\text{tot}} = \mu_{\text{nuclear}} + \mu_{\text{electronic}}, \tag{4.1}$$

$$\mu_{\text{tot}} = \sum_{l=1}^{m} Z_l \mathbf{R}_l + \int \Phi^* \left(\sum_{i=1}^{n} -\mathbf{r}_i \right) \Phi, \tag{4.2}$$
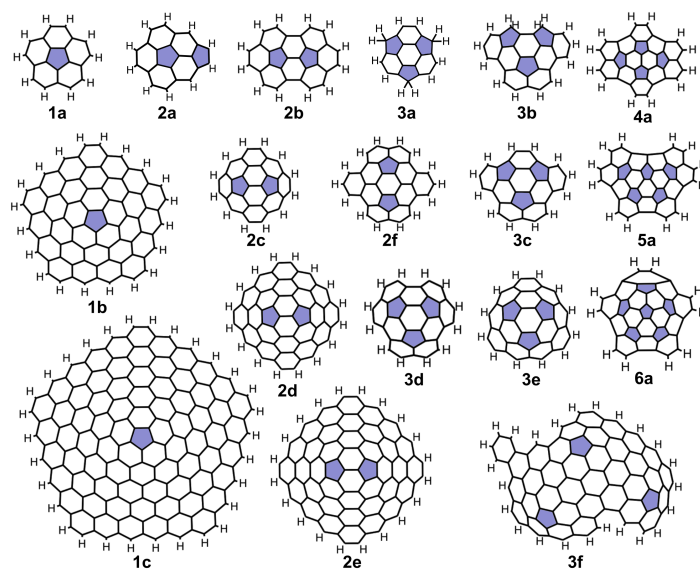
Figure 4.1 The list of curved arenes considered in this work: corannulene **1a** [243], dicircum-corannulene **1b** and tricircumcorannulene **1c** [99], acecorannulene **2a** [1], [5,5]circulene **2b** [335], sumanene **3a** [359], acenaphth[3,2,1,8-fghij]-as-indaceno-[3,2,1,8,7,6-pqrstuv]picene derivatives **3b**, **3c** and **2f** [450, 63], circumtrindene **3d** [374] and penta-benzocorannulene **6a** [363]. Other curved arenes **2c**, **2d**, **2e**, **2f**, **3e**, **4a** and **5a** were also studied. Pentagons are coloured for clarity.

where the nuclear contribution is considered for m atoms with nuclear charges Z_l and positions $\mathbf{R}_l$. The electronic contribution is determined from the wavefunction and the one-electron operator $\mathbf{r}_i$ for n electrons.

For a collection of 46 molecules it was found to predict the dipole to within 0.13 D of the experimental value (with the aug-cc-pVTZ basis set and B3LYP method) [178]. Table 4.1 shows the dipole moment of corannulene as calculated with this functional compared to the post-Hartree-Fock method MP2 [291]. All geometries were optimised with a variety of basis sets and calculated using the Gaussian 09 software [134]. The dipole moment of corannulene determined experimentally from the Stark effect is 2.071 D [257]. It was found that for B3LYP the dipole moment converged to 2.044 D for the largest basis set (1400 functions) used. As seen in Table 4.1, B3LYP yields a reasonably accurate dipole moment even with moderate sized basis sets where MP2 fails.

In order to tackle the geometry optimisation of the larger structures the B3LYP/6-311+G(d,p) level of theory was used to optimise the geometry of the structures in Figure 4.1, with the exception of the largest structures, **1c** and **3f**, where geometry optimisation was performed using the smaller basis set 3-21G. The electronic structure was then calculated at the B3LYP/cc-pVQZ level of theory for all of the geometry optimised structures. This

Table 4.1 Dipole moment of corannulene calculated with B3LYP and MP2 methods, using basis sets with a different number of basis functions, in debye with % deviation from the experimental value of 2.071 D [257].

Basis set	Function no.	B3LYP		MP2	
3-21G	200	2.414	(16.6%)	2.777	(34.1%)
6-31G(d)	320	1.722	(16.9%)	2.173	(4.9%)
6-311+G(d,p)	500	2.187	(5.6%)	2.667	(28.8%)
cc-pVTZ	740	1.994	(3.7%)	2.419	(16.8%)
cc-pVQZ	1400	2.044	(1.3%)	–	–

procedure (a B3LYP/6-311+G(d,p) geometry calculation used for the B3LYP/cc-pVQZ calculation of the electronic structure) led to a dipole moment for corannulene of 2.062 D, different by 0.45% from the experimental value. The coincidence is in part fortuitous, in view of the 1.3% deviation of the fully geometry-optimised corannulene structure at the cc-pVQZ level of theory from the experimental dipole, Table 4.1. The dipole moments can be found in Table 6.1.

4.2   Origin of the dipole moment

The dipole of curved arenes could originate from **(i)** a curvature-induced flexoelectric dipole from the polarisation of the π-bonds in direction normal to the C-skeleton [107, 209, 237]; **(ii)** the tilt angle of the C–H bonds [442]; **(iii)** charge transfer from the delocalised π-electrons in hexagonal sites to localised states on pentagonal sites [312, 59, 432, 10] or **(iv)** to localised states at the rim of the PAH [456]. To explore the importance of each of these factors, the correlation of the dipole moment to the size of the molecule and the number of pentagons in it was investigated first. Figure 4.2 shows the dipole moment as a function of the number of rings. The size dependency of the dipole for fragments of the C-skeleton of a nanocone has been found to be linear with the radius of the aromatic network [237]. A similar linear trend of the dipole as a function of the square root of the number of rings was found (which is proportional to the diameter of the fragment), i.e. the dipole moment of hydrogen-passivated curved PAH molecules also scales linearly with diameter (Figure 4.2, inset). The dipole moment increases with the number of pentagons in the PAH, but it soon saturates after two to three pentagonal rings have been incorporated, which was also found for nanocones [237]. Thus, for curved PAH with more than two pentagons, the dipole moment depends on the size but not predominantly on the number of pentagons.
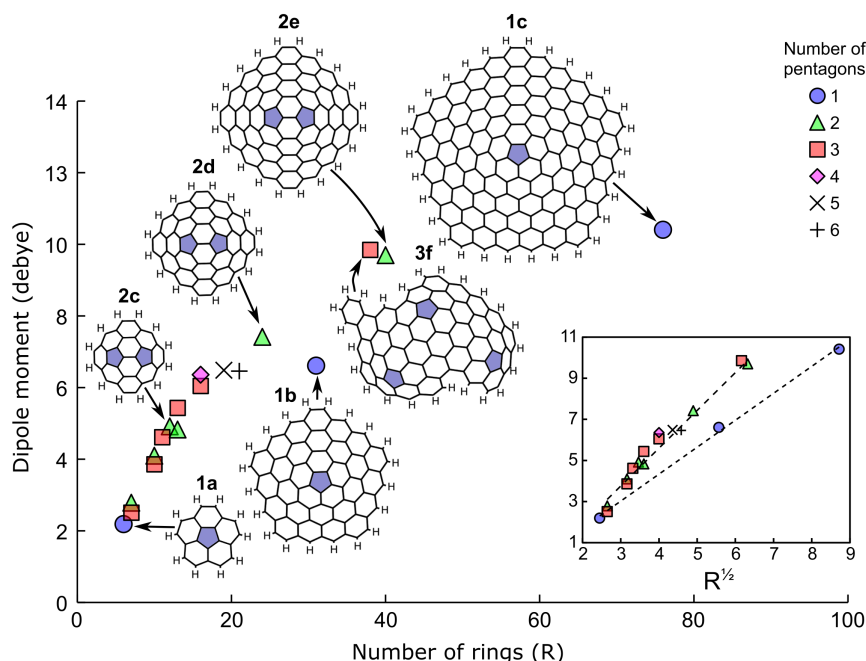
Figure 4.2 Dipole moment of curved PAH molecules as a function of the number of rings. Inset: Dipole moment as a function of size comparing different numbers of pentagons.

To illustrate the effect of the curvature on the electrostatic potential through the effects **(i-ii)**, flexoelectric effect and CH bonds, Figure 4.3 compares the potentials created by the flat PAH coronene with one of the curved PAH, corannulene (**1a**). In both cases, the excess positive charge is dominating the potential in the region of the hydrogen atoms and excess negative charge dominates above and below the plane of the aromatic system due to the π-electrons – this distribution provides the large quadrupole moment of these PAHs. A cross section along the z-y plane of the electrostatic potential demonstrates a significant difference between the flat and curved cases: a normal polarisation (relative to the aromatic plane) of the π-electron charge is apparent. The increased electron density on the convex face of the bowl leads to the large dipole moment of corannulene, as was observed earlier [156].

To illustrate the effects **(iii)** and **(iv)** from the localised states near the edge and at the pentagons, in Figure 4.4 the electron localisation function (ELF) was calculated for molecule **3f** – an analysis that has proved itself useful for curved PAH [280]. The ELF is a measure of the likelihood of finding two electrons of the same spin in a small region of space. It is defined as [27]

$$\text{ELF}(\mathbf{r}) = \left[1 + \frac{D(\mathbf{r})^2}{D_0(\mathbf{r})^2} \right]^{-1}, \tag{4.3}$$
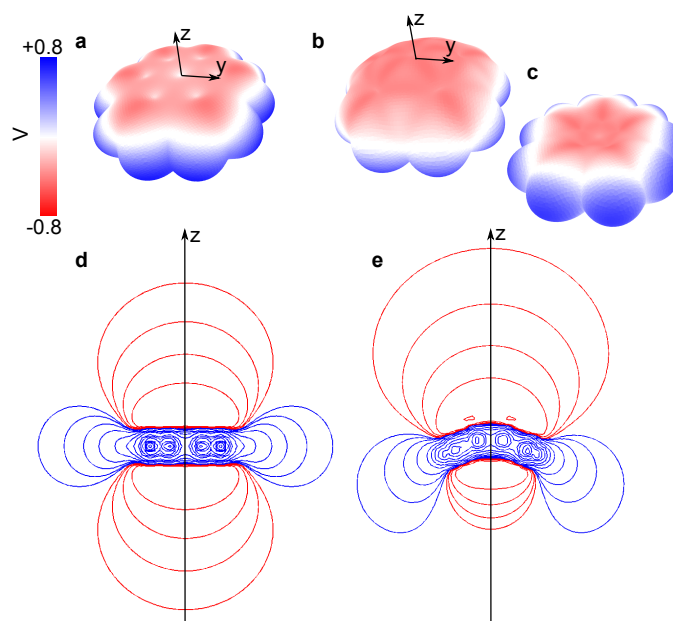
Figure 4.3 Coronene and corannulene are shown left (a,d) and right (b,c,e). The molecular electrostatic potential was mapped to an isosurface of the electron density (B3LYP/cc-pVQZ, with an isovalue of 0.001 e Å^{-3}) (a,b,c). A two dimensional contour plot of the electrostatic potential through the z-y plane is shown (d,e), with the outermost four contour lines being drawn at $\pm$ 0.03, 0.06, 0.1 and 0.2 V.

where $D(\mathbf{r}) = T_\sigma(\mathbf{r}) - |\nabla\rho_\sigma(\mathbf{r})|^2/4\rho_\sigma(\mathbf{r})$ is proportional to the first non-vanishing coefficient in the Taylor expansion (with respect to small $|\mathbf{r}|$) of the spherically averaged conditional pair probability to find a same-spin electron in the vicinity of an electron in the vector-position $\mathbf{r}$; $T_\sigma = \sum_i^\sigma |\nabla\psi_i|^2$ is the kinetic energy density, $\rho_\sigma = \sum_i^\sigma \psi_i^*\psi_i$ is the σ-spin probability density, and $D_0(\mathbf{r}) = 9.12\rho_\sigma^{5/3}(\mathbf{r})$ is the value for a uniform electron gas. A value of ELF = 1 corresponds to a perfectly localised electron and ELF = 1/2 to a uniform electron gas. Figure 4.4 shows the iso-ELF surface (iso = 0.66), calculated using the Multiwfn program [258], within which a region of localised electron pairing occurs. There appears greater localisation of the electrons (effect (iii)) at the pentagonal sites of **3f** compared to the hexagonal, cf. Figure 4.4b. This is a known effect that has been studied in relation to the energetic barrier for inversion of the bowl [101], where the transition from flattened structure to curved decreases the aromatic delocalisation energy. There is also increased localisation in the rim region, effect **(iv)**, Figure 4.4c, in relation to the increased bond order of the C–C bonds at the rim [456].

An additional example is given in Figure 4.5, where the π-electron localisation of artificially flattened and relaxed curved corannulene are compared. In the curved structure, the π-bonds at the hub of the molecule are visibly polarised in direction normal to the C
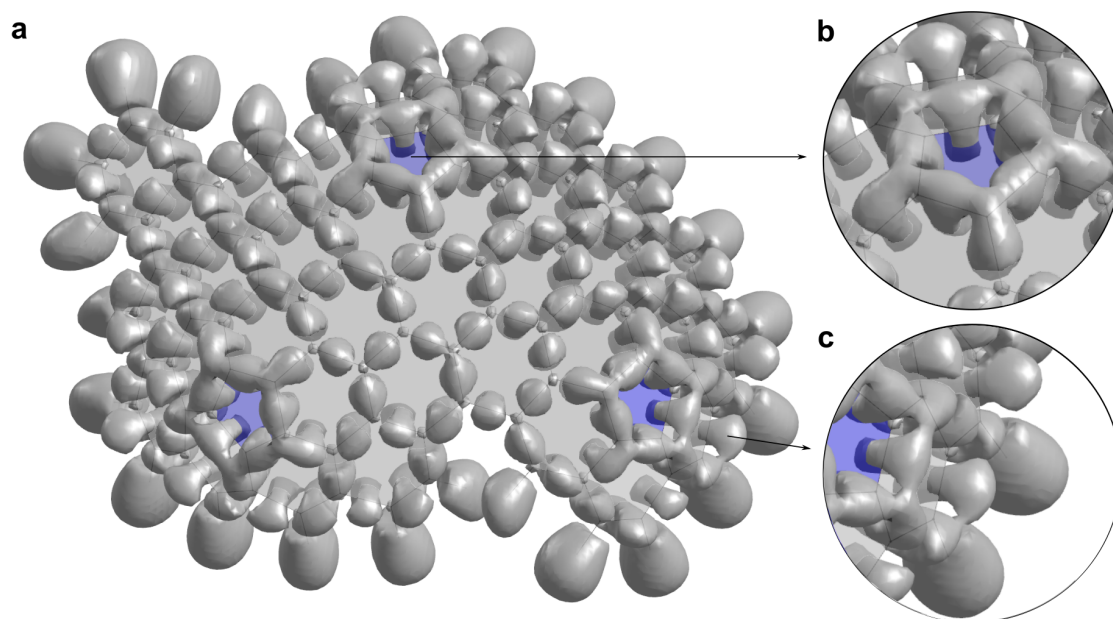
Figure 4.4 a) Plot of the iso-surfaces of the electron localisation function for molecule **3f** at iso=0.66. Pentagonal rings are coloured blue and hexagonal rings grey to allow the molecular geometry to be seen. Insets show the localisation at pentagonal rings b) and localisation at the rim c).

skeleton of the corannulene – the increase of the π-electron density on the concave side of the molecular bowl leads to a Pauli expulsion of electron density to the convex side, providing further evidence for effect **(i)**.

The local flexoelectric dipole μ_{flex} (per C-site) due to curvature-induced π-bond polarisation in direction normal to the C-skeleton has been analysed using a tight binding rehybridisation model [107]; linear dependence with Haddon's pyramidalisation angle [161] has been demonstrated:

$$\mu_{\text{flex}} = f_{\theta_{\text{p}}} \theta_{\text{p}} \mathbf{v}_{\pi}. \tag{4.4}$$

Here, $\mathbf{v}_{\pi}$ is the unit vector collinear with the axis of the π-orbital and pointing toward the concave side of the PAH, and θ_{p} the pyramidalisation angle, a characteristic of the deformation of the carbon skeleton (at each atom centre, a plane can be constructed that makes three equal angles θ_{p} with the adjacent C-C bonds; this plane is referred to as the *pyramidalisation plane*). The value of the flexoelectric constant $f_{\theta_{\text{p}}}$ of a π-orbital next to a sp^2 carbon atom between three hexagons has been calculated using electronic structure methods for fullerenes and nanotubes as $f_{\theta_{\text{p}}} = 2.34$ D/rad [237]. Using the approach of these authors, a similar value of $f_{\theta_{\text{p}}} = 2.35$ D/rad for a (5,5) nanotube was found with the
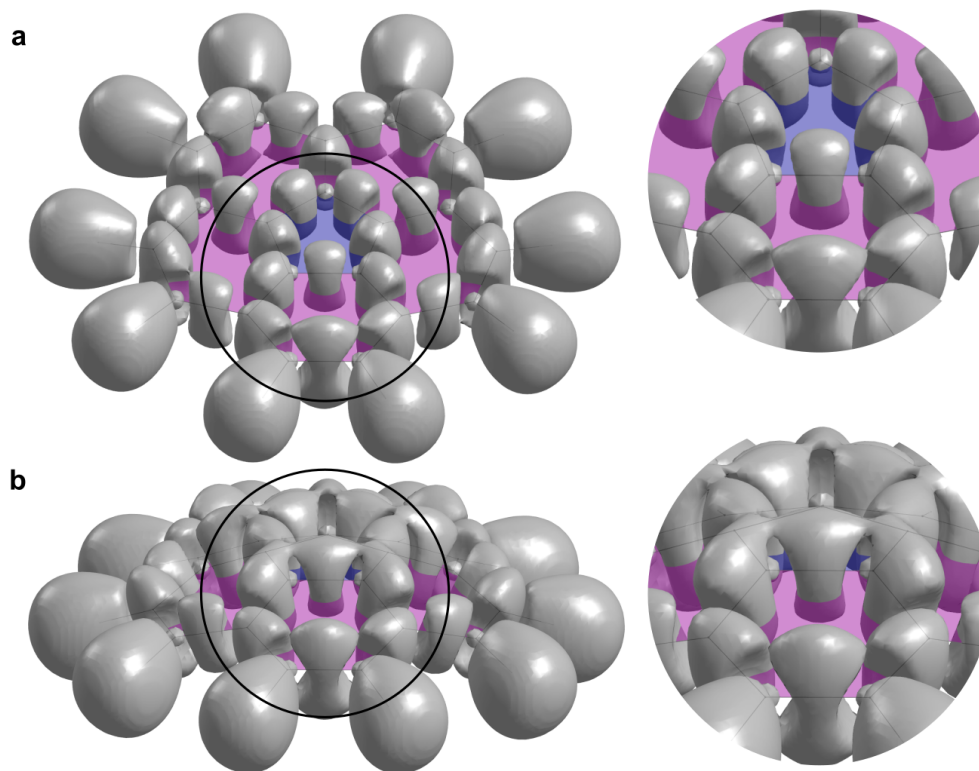
Figure 4.5 Plot of the iso-surfaces of the electron localisation function for corannulene **1a** at iso=0.66 for a) flattened and b) relaxed corannulene. Insets on the right are expanded views near the π-bonding region at the hub showing the asymmetry of the bond.

B3LYP/cc-pVQZ method used. This flexoelectric coefficient is obviously unrelated to the localisation effects or the CH bond tilt.

The flexoelectric effect dominates the dipole moment of the curved PAH considered. This can be shown by neglecting the other three effects leading to polarisation. The summation of μ_{flex}, Eq. 4.4, over all C_{hub}-sites gives for the total dipole moment μ of the molecule,

$$\mu \approx \sum_{C_{\text{hub}}} \mu_{\text{flex}} = f_{\theta_{\text{p}}} \theta_{\text{tot}}, \tag{4.5}$$

where the vector is referred to as $\theta_{\text{tot}} = \sum_{C_{\text{hub}}} \theta_{\text{p}} \mathbf{v}_{\pi}$ as to the *total pyramidalisation* of the molecule. It is a geometric characteristic of the molecular structure (Figure 4.6b); for small pyramidalisation, it can be expressed as $\theta_{\text{tot}} \approx L N_{C_{\text{hub}}} \overline{H \mathbf{v}_{\pi}}/4$, where $N_{C_{\text{hub}}}$ is the number of hub atoms. Thus, θ_{tot} is a *global* measure of the curvature of the molecule as a whole, equal within a coefficient to the average mean curvature vector $H \mathbf{v}_{\pi}$ of the sp^2-skeleton. The rim C-atoms (bonded to hydrogen) are neglected in the sum (Eq. 4.5), with the assumption

that the π-electron repulsion leading to the polarisation is less effective for the two adjacent π-orbitals next to a rim C compared to three π-orbitals next to a hub C. The sp^3 carbon atoms (having no π-orbitals) in structures **3a** and **3b** were also excluded. To determine the vector $\mathbf{v}_\pi$, the POAV2 approach of Haddon [161] introduced in the Background chapter was used. Note that this $\mathbf{v}_\pi$ can be quite different from the normal vector to the pyramidalisation plane (which is used often as an approximation of $\mathbf{v}_\pi$ within the POAV1 approach [161]). If the contributions to μ of the localisation effects and the CH bond tilt are small, the dipole moment of all molecules investigated must be proportional to θ_{tot}, with proportionality coefficient f_{θ_p}. This is indeed the case, as demonstrated in Figure 4.6a; the linear relationship (Eq. 4.5) holds with $R^2 = 0.995$ and the value of the linear coefficient is $f_{\theta_p} = 2.24 \pm 0.03$ D/rad (all errors are 2σ). This value differs by 4.7% from the one calculated for a nanotube, i.e. more than 95% of the dipole of the curved PAHs considered here is of flexoelectric origin.
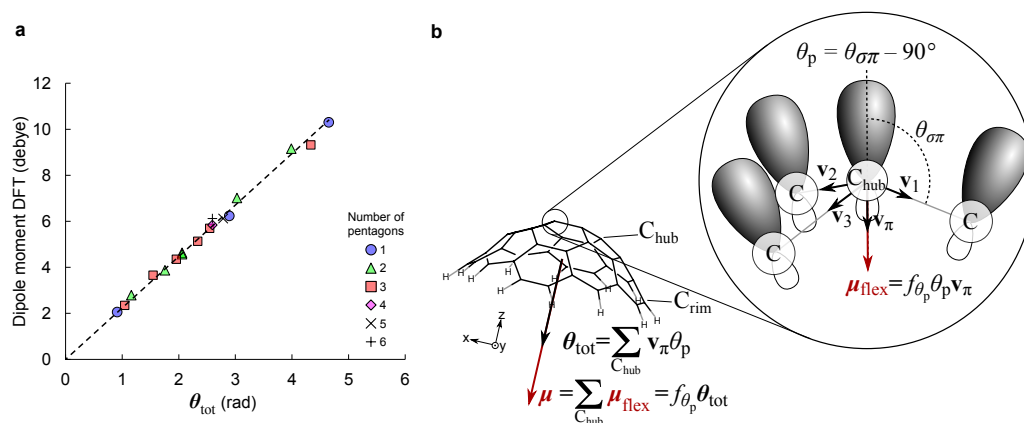
Figure 4.6 **a)** Values of θ_{tot} from Eq. 4.5 (dashed line) compared with the calculated DFT dipole moments for the set of molecules in Figure 4.1, cf. Table 6.1. The number of pentagons for each fragment is also indicated. **b)** Illustration of the relation of θ_{tot} and θ_p to the geometry of the molecule. At each sp^2 carbon, a *pyramidalisation plane* can be constructed that makes equal angles (θ_p) with the three adjacent C–C bonds. The normal to this plane is approximately colinear with the π-orbital axis. The angle $\theta_{\sigma\pi}$ in the figure is the one between the C–C bonds and the normal to the pyramidalisation plane.

The contribution of the other three effects is surprisingly small. An attempt to elaborate the geometrical model Eq. 4.5 was made by including the contribution of the C–H bond dipole **(ii)** and the rim localisation **(iv)**, and also by allowing for different values of f_{θ_p} for carbon in pentagons and at the rim. However, due to the complete domination of the flexoelectric effect and to efficient compensation of the other polarisation sources, the respective effects cannot be decoupled in this manner. Qualitatively, by considering the direction of the effects **(ii-iv)**

relative to the flexoelectric dipole **(i)**, one can conclude that the observed 4.7% reduction of the flexoelectric coefficient is mostly due to the neglected rim localisation effect **(iv)**. (The dipoles due to the C–H bond tilt **(ii)** and to the pentagon localisation **(iii)** are in the same direction as the flexoelectric dipole – plus pole towards the concave side – and would lead to a larger effective f_{θ_p} value in Eq. 4.5.) However, even this conclusion is uncertain as the error in the calculation of the π-electron flexoelectric effect is probably of the same order of magnitude as the combined result of all other effects: a small additional π-electron flexoelectric effect can be expected from **(i)** the rim atoms were neglected, and from **(ii)** the asymmetric deformation at the pentagon C-atoms (where torsional misalignment of the π-orbitals is present, similar to the one studied by Nikiforov et al. [299] in relation to nanotube strain energy – it may affect μ_{flex}).

The simulations of flattened corannulene confirm that the linear flexoelectric effect dominates the polarisation, and also indicate that the success of Eq. 4.5 is due to fortuitous cancellation of effects. These simulations' constrained variable was the internal dihedral angle ϕ between the pentagonal and the hexagonal rings (as shown in Figure 4.7). All other coordinates were optimised for geometries of varying ϕ ranging from 180° to 140° in 2° increments. Three of the constrained and optimised structures are shown in Figure 4.7. The total pyramidalisation angle, $\theta_{\text{tot}} = \sum_{\text{C}_{\text{hub}}} \theta_p \mathbf{v}_\pi$, was then computed (compare to Eq. 4.5). The magnitude of the dipole moment μ was calculated at the B3LYP/cc-pVQZ level of theory using the Gaussian 09 software [134]. The dependence of μ on θ_{tot} is shown in Figure 4.7. The linear model Eq. 4.5 is shown for comparison, with slope $f_{\theta_p} = 2.24$ D/rad, as determined in Figure 4.6. As seen, the dependence of μ on θ_{tot} shows non-linearity even at rather small values of the angle, and the success of Eq. 4.5 seems to be due to fortuitous cancellation of effects at larger pyramidalisation.

To conclude, Eq. 4.5 allows the calculation of the dipole moment of a curved arene from our list with an average error of 2.3±1.9%, which is a satisfactory accuracy in view of the expected error of the DFT values (cf. Table 6.1). A component-by-component comparison between the DFT dipole with the one calculated via Eq. 4.5 is given in Table 4.3 for the large asymmetric structure **3f** (showing the worst match to Eq. 4.5 from those in Table 6.1): the difference in magnitude is 4% and the difference in direction is 6°.
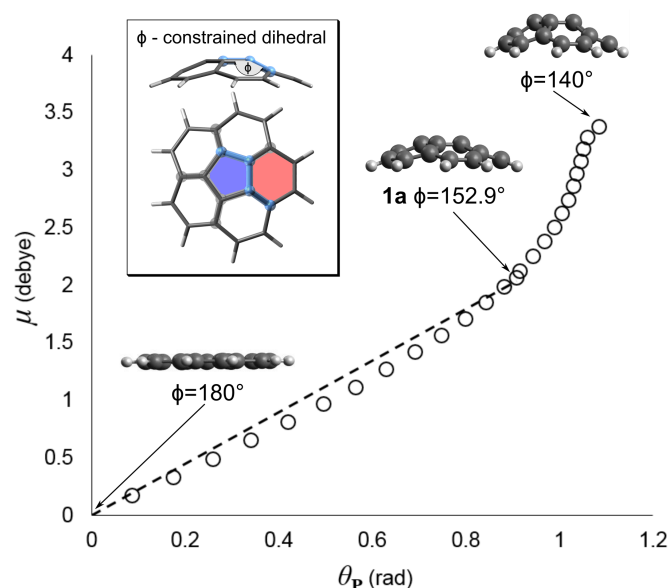
Figure 4.7 The magnitude of the dipole moment of the strained corannulene geometries are plotted versus the total pyramidalisation angle θ_{tot}. The dihedral angle which is constrained in the geometry optimisation is shown in the boxed inset. Three of the geometries with their corresponding dihedral angles are inset. The dashed line corresponds to Eq. 4.5.

4.3   Distributed multipole description

Curved aromatic structures play a role in numerous technologically relevant processes, and the interest towards modelling the interactions within these materials is growing. One such process of interest to us is the role of the curved PAHs' dipole in soot formation. A strong correlation is known to exist between soot formation and chemi-ions in a flame [56], but Chen and Wang recently calculated binding energies between flat PAH and flame chemi-ions that are not strong enough to stabilise anything larger than a dimer [62]. One can expect the situation to be qualitatively different with curved PAH due to strong long-range ion-dipole interaction, which might be involved in stabilising clusters of PAHs, but an appropriate force field is required to study this case. A second example is the adsorption in microporous carbon. The effect of the curvature has been explored, e.g. for hydrogen absorption, which is enhanced on corannulene due to a dipole-induced dipole interaction [364] modelled with molecular dynamics via modification of the van der Waals parameters of the force field. Obviously, in cases of adsorption of polar molecules on microporous carbon, a strong directional solid dipole-solid dipole interaction will control the process – in this case, an effective van der Waals model of the flexoelectric dipole is inapplicable. The strained pentagon presents a binding site for ions as well [426] (which is probably the reason why corannulene allows for

Table 4.2 Dipole moment and pyramidalisation of the curved aromatic hydrocarbons in Figure 4.1: DFT dipole values (B3LYP method) compared with the model Eq. 4.5, and total and maximum pyramidalisation angles.

Molecule	DFT dipole μ [D]	max. pyr. angle $\max(\theta_p)$ [°]	total pyr. $\theta_{tot} = \sum_{C_{hub}} \theta_p \mathbf{v}_\pi$ [rad]	flexoel. dipole $\sum_{C_{hub}} \mu_{flex}$ [D]
1a	2.06	8.34	0.909	2.03
1b	6.24	10.48	2.89	6.46
1c	10.30	10.59	4.65	10.39
2a	2.79	10.99	1.16	2.59
2b	3.87	11.23	1.75	3.92
2c	4.63	11.63	2.06	4.60
2d	7.01	11.91	3.03	6.76
2e	9.15	11.59	3.99	8.92
2f	4.57	10.65	2.06	4.60
3a	2.34	8.85	1.04	2.33
3b	3.66	12.51	1.54	3.45
3c	4.35	12.35	1.96	4.37
3d	5.13	12.08	2.33	5.21
3e	5.70	12.17	2.54	5.69
3f	9.32	10.64	4.33	9.69
4a	5.84	12.52	2.59	5.80
5a	6.12	12.28	2.78	6.22
6a	6.12	12.09	2.59	5.80

supercharging of lithium in battery applications [462]), and force fields are also required for this case.

The most common representation of the charge distribution in a molecule used in force fields is an ensemble of atom-centred point charges. However, this model is unsuitable for curved PAHs, where the most long-ranged interaction is due to the flexoelectric dipole that cannot be represented with atom-centred point charges. Therefore, the capability of a distributed multipole [401] description of the electrostatic potential of curved PAHs will now be investigated.

The expansion of the electrostatic potential in an ensemble of multipole centres (a set of atom-centered charge, dipole, quadrupole, etc.) is not unique – different sets of values of the multipoles at each centre can produce the same total potential, and all decomposition methods are based on heuristic assumptions of how the electron density is separated between the atoms; therefore, no strict physical meaning should be ascribed to the values of the multipoles in a distributed multipole expansion. Nevertheless, a decomposition was sought

that not only describes the electrostatic potential outside the van der Waals surface correctly, but is also physically reasonable. Two methods were tested which are commonly employed for the decomposition: the Gaussian distributed multipole analysis (GDMA) [401] and the atoms-in-molecules (AIM) approach [16]. The advantage of the AIM approach is that the electron density itself is partitioned and then integrated to yield the multipoles in the atomic basins, making the decomposition independent of the basis set of molecular orbitals used and of the system size [275]. On the other hand, GDMA computes the multipoles directly from the Gaussian basis functions, is fast even for the largest structures studied, and is more widely used (GDMA point multipoles have been integrated into molecular dynamics packages such as AMOEBA, CHARMM and DL_MULTI). Two variants of GDMA were employed: one with rank 2 multipoles (point charge-dipole-quadrupole) on every atom, which are referred to as $GDMA(C_2H_2)$, and another with rank 2 multipoles on every carbon but only a point charge (rank 0 restriction) on every hydrogen, $GDMA(C_2H_0)$, which will be named the cPAHAP forcefield. For the PAHs in Figure 4.1, both methods produce a total dipole moment of magnitude within ± 0.002 D of the exact μ that follows from the electronic structure calculations. An example is given in Table 4.3 for the asymmetric PAH **3f**: the component-by-component comparison of the total dipole for the $GDMA(C_2H_0)$ multipole expansion and the DFT shows that the GDMA method reproduces all components effectively. $GDMA(C_2H_0)$ and AIM agreed well in all cases. However, the larger structures had significant divergence between $GDMA(C_2H_2)$ and AIM.

Table 4.3 Dipole moment components (in debye) of molecule **3f** calculated with DFT, Eq. 4.5 and $GDMA(C_2H_0)$.

	μ_x	μ_y	μ_z
DFT	-1.183	-0.763	-9.211
Eq. 4.5	-0.181	-0.742	-9.660
$GDMA(C_2H_0)$	-1.085	-0.789	-9.219

Further insights into the divergence between AIM and $GDMA(C_2H_2)$ can be gained by discussing in more detail how they are determined. The AIM approach partitions the atoms into volumes with the condition $\nabla\rho(\mathbf{r}) = 0$ defining the interfaces between them; ρ is the electron density. The AIM analysis was performed on corannulene and dicircumcorannulene using the Multiwfn program [258] with a grid spacing of 0.06 Bohr. Figure 4.8 shows an *xy* cross section through the molecules. The blue lines show the interface of the two atomic volumes in cross section.

By integration of the charge density (electron density along with the nuclei) over the atomic volume, the AIM analysis allows the calculation of the atom-centred multipoles up to
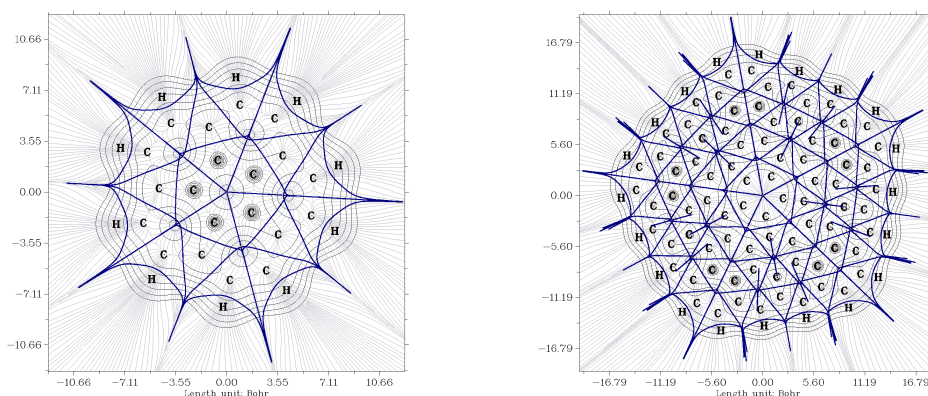
Figure 4.8 Cross section of the molecular volumes/basins calculated using the atoms in molecules approach for the molecules **1a** and **1b**.

quadrupole moments. This method produces reasonable values of the atom-centred multipole moments, which are size extensible and independent of the basis set [275] as the decomposition uses the electron density directly as provided by the electronic structure calculation. However, the partitioning and numerical integration are computationally expensive and could not be applied to the largest carbon structures studied. The GDMA method is of lower computational cost as it provides the atom-centred multipoles directly from the optimised molecular orbital calculations.

As the flexoelectric dipole moment has been found in this study to be important, the atom-centered dipoles were compared between the GDMA(C_2H_2) method and the AIM method as the benchmark. For the molecule corannulene **1a**, the flexoelectric dipoles at the hub of the molecule were of similar magnitude (<10%) and direction for the different decompositions. Figure 4.9 shows a vector representation of the atomic centered dipole moments for dicircumcorannulene **1b** using the two variants of GDMA, where the length is proportional to the magnitude of the moment. The GDMA(C_2H_2) method produces dipoles at the hub C atoms that are 40-50% larger than the AIM method, Figure 4.9a. In addition, it produces a very high dipole moment at the hydrogen atoms (in addition to the positive point charge) that has no intuitive physical explanation. The second variant of the Gaussian distributed multipole decomposition, GDMA(C_2H_0), is with multipole rank at the H atoms set to 0 (point charges only). GDMA(C_2H_0) compares very well with the "benchmark" AIM multipoles, Figure 4.9b and produces intuitively reasonable values of the point charges and dipoles. One explanation could be that the GDMA method is ill-defined at the rim with linear combinations of point charge and dipole moments on the C–H atoms being able to describe the same charge polarisation. By constraining the hydrogen atoms to be point charges a boundary condition is provided giving a unique solution.
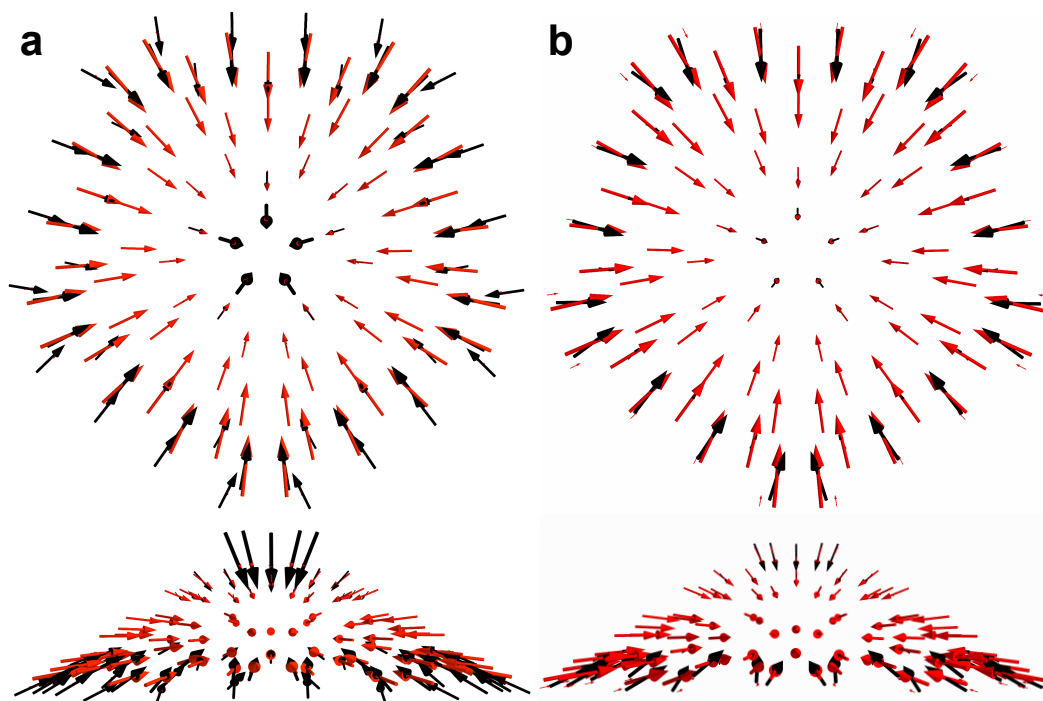
Figure 4.9 Atom-centred dipole moments plotted as vectors for circum-2-corannulene cal-
culated using the AIM approach (red arrows) and the GDMA method (black arrows). In
a), GDMA(C_2H_2) is shown with rank=2 multipoles on all atoms, hydrogens included. In
b), the GDMA(C_2H_0) dipoles are given, where restricted expansion (rank=0) of the atomic
multipoles on the hydrogen atoms is utilised.

Figure 4.10 shows the GDMA(C_2H_0) distributed point dipoles and monopoles for
molecule **3f**. The C-centred dipole moments range between 0.11–0.79 D in magnitude.
The procedure computes a large dipole at each rim carbon atom, in the direction of the C-H
bond with the positive pole pointing toward the hub. This polarisation reflects mostly the
localised states at the rim of the PAH (increased bond orders and electron density near the rim
compared to the hub [456], effect **(iv)**). In the GDMA(C_2H_0) decomposition, the polarisation
of the C-H bonds (and effect **(ii)**) is reflected by the partial charges at the C and H atoms.
From the dipole at each pyramidalised hub C-atom and the local θ_p, "local values" were
obtained for the flexoelectric coefficient f_{θ_p} in the range 2.24–2.27 D/rad, which coincide
with the "averaged" f_{θ_p} value in Eq. 4.5 and Figure 4.6. The largest contributors to the net
dipole moment are the pentagonal carbon atoms that are the most heavily pyramidalised. The
total dipole moment per pentagonal ring (defined as the vector sum of the GDMA(C_2H_0)
dipoles of all atoms in the pentagon) was found to be of magnitude 1.76$\pm$0.03 D. Finally, in
Figure 4.10c, the partial charges at the pentagonal carbon atoms are found to range between
-0.01 and -0.03 e, and each pentagon contains a total charge of -0.09$\pm$0.02 e (effect **(iii)**). This
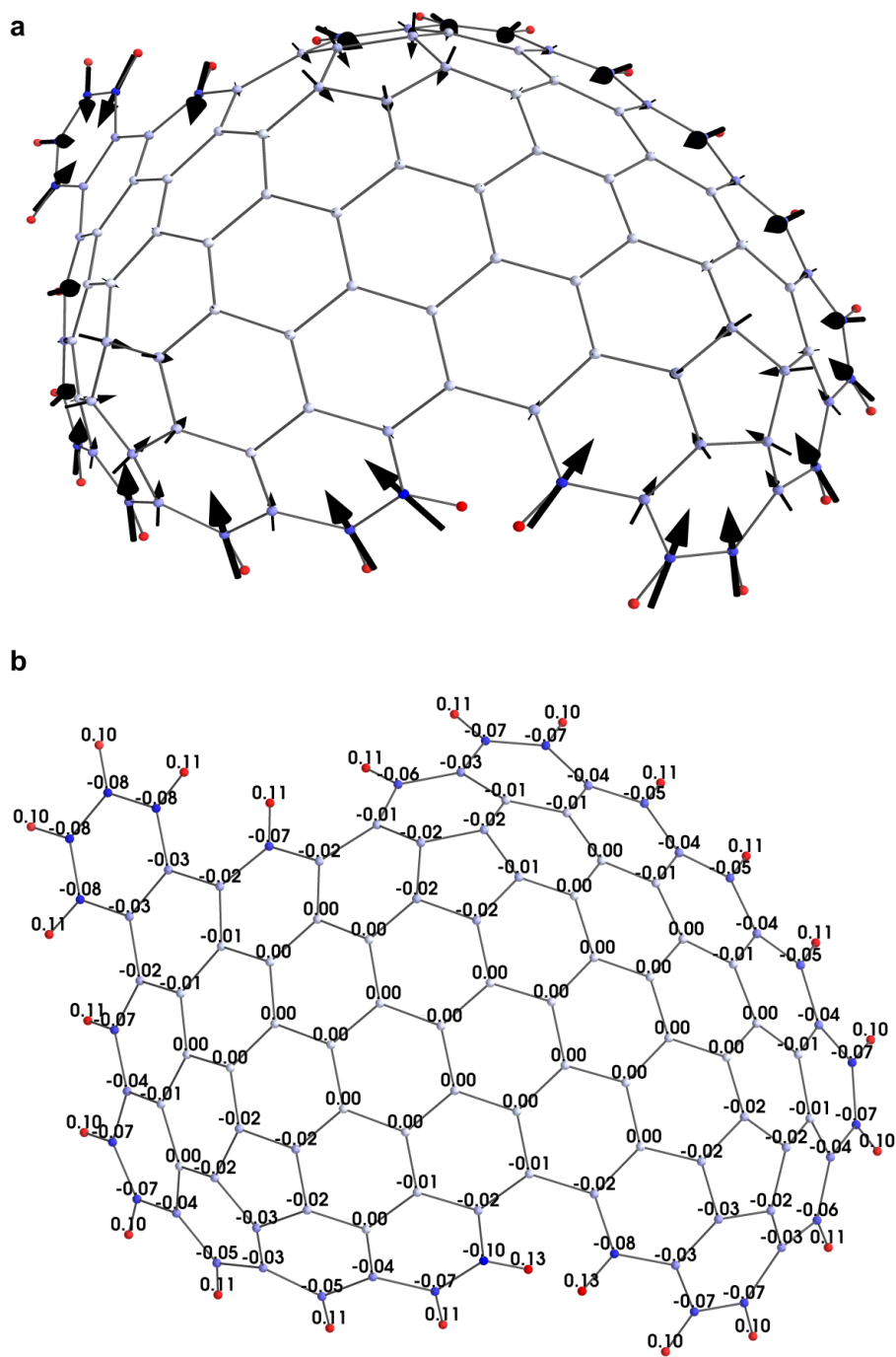
Figure 4.10 GDMA dipoles a) and partial charges b) for the molecule **3f** with the dipoles shown as vectors and partial charge values printed at the atomic sites.

value is similar to what has previously been predicted for the pentagonal charge accumulation in nanotube end caps, -0.013 e (calculated using the PBE density functional, with plane

wave basis functions up of 25 and 225 Ry for the valance and charge density, respectively) [432, 312]. Thus, all four polarisation effects are well represented by the GDMA(C_2H_0) distributed multipole expansion.
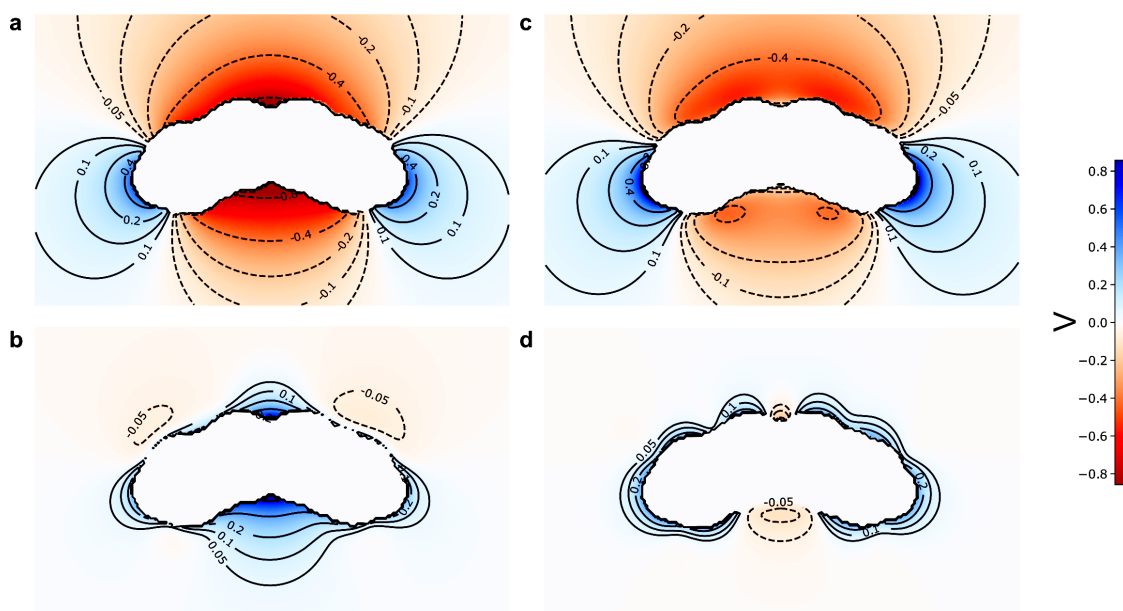
Figure 4.11 Electrostatic potential along the $z - y$ plane for corannulene (**1a**) calculated from a) the point charge model obtained by the MK scheme, and c) the GDMA(C_2H_0) multipole representation – cPAHAP. Potential maps of the difference between these potentials and the DFT result in Figure 4.3e are given in b-d) for the point charge b) and in d) for the multipole model.

Figure 4.11 shows the electrostatic potential on the $z - y$ plane outside the van der Waals surface of corannulene for two different multipole decompositions: c) is GDMA(C_2H_0) and a) is the standard point charge description as obtained by the Merz-Kollman (MK) scheme. In b) and d), the difference between these potentials and the exact DFT potential in Figure 4.3 is given (using the procedure of Kramer et al. [229]). A significant divergence between the point charge ensemble's potential and the DFT potential is evident, especially near the pentagonal carbon atoms where the flexoelectric dipole is large; on the other hand, the GDMA(C_2H_0) representation is accurate. In order to quantify the differences, the molecular electrostatic potential was calculated at the electron density isosurface 0.002 $e/Å^3$ (near the interaction surface of molecular pairs). For the point charge model, the average difference between the DFT and the model potentials at this surface was 36%. This error was reduced to 2.6% for the GDMA(C_2H_0) distributed multipole representation. An additional problem of the MK description is that the total dipole moment of the point charge ensemble is 1.73 D, a value

reduced by 21% compared with the DFT dipole. GDMA(C_2H_0) also produced reasonable total quadrupole moments (within 12% of the DFT results) which is not the case with the point charge model.

In summary, the dipole moment μ of 18 curved aromatic molecules has been computed and was shown to reach significant values (2-10 D). The main contribution to this moment was shown to stem from the π-orbital flexoelectric dipole moment: μ of all these molecules can be calculated with 95% accuracy using a standard linear model for the dependence of the flexoelectric polarisation on the pyramidalisation at each carbon atom. Gaussian distributed multipole expansion, restricted to rank 2 at the carbon atoms and rank 0 at the hydrogens – GDMA(C_2H_0) – has been shown to reproduce the electrostatic potential of the curved arenes with sufficient accuracy, which we will refer to as the cPAHAP forcefield. Previously our group has applied distributed multipole analysis to describe the potential of flat PAH molecules and found it improved on point charge models, allowing the reproduction of the second virial coefficient of benzene [418]. Yet, for dimers of flat PAH molecules, a point charge distribution is sufficient for developing an accurate force field (iso-PAHAP) [417, 418]. For curved PAHs, this is not the case. The common atom-centred point charge models fail to correctly reproduce the π-electron flexoelectric dipole moment, which controls the long range potential and contributes significantly to the short range interactions. Therefore, atom-centred point charge ensembles are inapplicable as a basis for force fields for molecular dynamic simulations of curved PAHs.

In conclusion, the dipole moments for a range of curved aromatic hydrocarbons were computed. Significant charge polarisations were determined for the size of species found in combustion and carbon materials. This was due to the flexoelectric effect and a geometric model allowed for the rapid computation of the dipole moment simply from the atomic arrangements. Finally, the atom-centred point charges, used in many forcefields for carbon, were found to be insufficient to describe the out-of-plane flexoelectric polarisation and a new forcefield, cPAHAP, was developed. These insights will become important when considering intermolecular interactions of cPAH with other species in the following chapters.

Chapter 5

Quantifying and integrating curvature into soot

"...the layer planes are shown bending from one facet to another rather than separate crystallites meeting at an angle. Bending appears more typical for this type (of carbon) black."
– Heidenreich, Hess and Ban, A Test Object and Criteria for High Resolution Electron Microscopy (1968), Journal of Applied Crystallography

The work in this chapter was published in *The Journal of Physical Chemistry C* and the *Proceedings of the Combustion Institute* as well as a preprint in collaboration with the Computational Modelling Group at the University of Cambridge. Contributions from the group included Dr Botero and Dr Salamanca being responsible for all of the experimental data including the sampling, performing the electron microscopy, experiments and image analysis. The experiments related to particle size, soot volume fraction and Raman spectroscopy measurements were performed by Dr Salamanca, as well as the data processing and analysis. Mr Menon contributed geometries for the calculations and the other authors edited the manuscripts. The electronic structure calculations, simulation of the electron micrographs and writing were performed by the author.

In this chapter, we will explore quantifying curvature and integrating curvature in soot nanoparticles. Experiments were undertaken with colleagues to quantify the degree of curvature in early soot nanoparticles. Computational work is then performed to determine the electronic effects driving curvature integration and the smallest aromatic species that can be curved by pentagon integration. Finally, cyclic fuels are used to seed curvature into soot nanoparticles and the impact on the Raman spectrum is explored using electronic structure theory.

5.1   Curvature within early soot nanoparticles

The first question that arises after determining that curved aromatic molecules contain a significant flexoelectric dipole moment is considering what fraction of species in soot nanoparticles are curved. In this section high resolution transmission electron microscopy and multislice electron micrograph simulations will be performed to provide an estimate for this in an ethylene laminar diffusion flame.

Robert Heidenreich was the first to develop the method of phase contrast transmission electron microscopy allowing for the carbon lattice to be imaged using an electron beam [174]. In this imaging mode the first order Bragg diffraction from the molecules is interfered with the zeroth order transmitted electron beam. Phase contrast high resolution TEM images are obtained from graphitic regions that are oriented so that their basal planes are at Bragg angles with the electron beam. These appear as dark fringes in the image and can be directly related to the nanostructure through fringe analysis. Fringe analysis involves processing the TEM image to convert each fringe into line of pixels (skeletonisation) from which statistics can be computed such as fringe length (L), end-to-end distance (C) and tortuosity ($\tau = L/C$).

The method used in this study has been previously benchmarked against simulated HRTEM images of planar PAHs [42].

Curvature was first noticed by Heidenreich et al. [174] looking at thermally annealed carbon black particles. They found, unlike in crystals where two crystallites will join at a sharp grain boundary, that the fringes instead curved continuously where two misaligned crystallites came together. As the resolution improved small fringes from soot nanoparticles could be imaged and were also found to be curved, however, it was difficult to eliminate other sources of tortuous fringes from imaging artifacts. Experimental work helped to solidify the presence of curvature. Firstly, low pressure benzene premixed flames were found to produce fullerenes and the fringes were found to be significantly curved [153, 147]. Secondly, large fPAH of hexabenzocoronene were prepared and HRTEM images were compared with soot nanoparticles. While the fPAH produced wavy fringes they did not curve to a similar degree as fringes seen in diesel soot [402]. More recently, bent fringes within soot were interpreted as being due to different 5- or 7-membered rings present in molecules with 28–49% of fringes suggesting pentagon integration in mature soot [437]. However, there is still contention about the presence of cPAH in soot particles particularly when observing mature soot particles, due to modifications from carbonisation. Other sources of curved fringes have suggested deformed aryl-linked PAH or bending of the aromatic plane. Therefore, simulated HRTEM images will be compared with early soot nanoparticle HRTEM images to see how much curvature can be inferred to arise from pentagonal ring integration.

Dr Botero performed the experiments in this section (with further details available in Botero et al. [43]). A 200 kV JEOL 2100F electron microscope was used to perform the imaging of the early soot particles with care taken to ensure low beam damage. Carbon particulates were sampled thermophoretically from an ethylene coflow diffusion flame using a rapid solenoid injector that holds a holey carbon TEM grid (Figure 5.1a and b). Grids were imaged beforehand to ensure no contamination. Particles were only imaged if they were suspended in the vacuum and therefore did not have any interference from the holey carbon support or other soot particles.

Dr Botero also employed fringe analysis software to analyse the fringes of 209 primary particles as a function of the radius from the centre of the particle and the sampling height above the burner. The earliest carbon nanoparticulates that could be sampled were at 10 mm above the burner. These early particles, ≈10 nm in diameter, provide insight into the aromatic content in the soot nuclei, which cannot be directly sampled thermophoretically and imaged due to their small size. Figure 5.1c and d show the skeletonised fringes from two representative primary particles – one early particle 10 mm above the burner, where luminosity has yet to develop, and another from the tip (at 49 mm above the burner) –
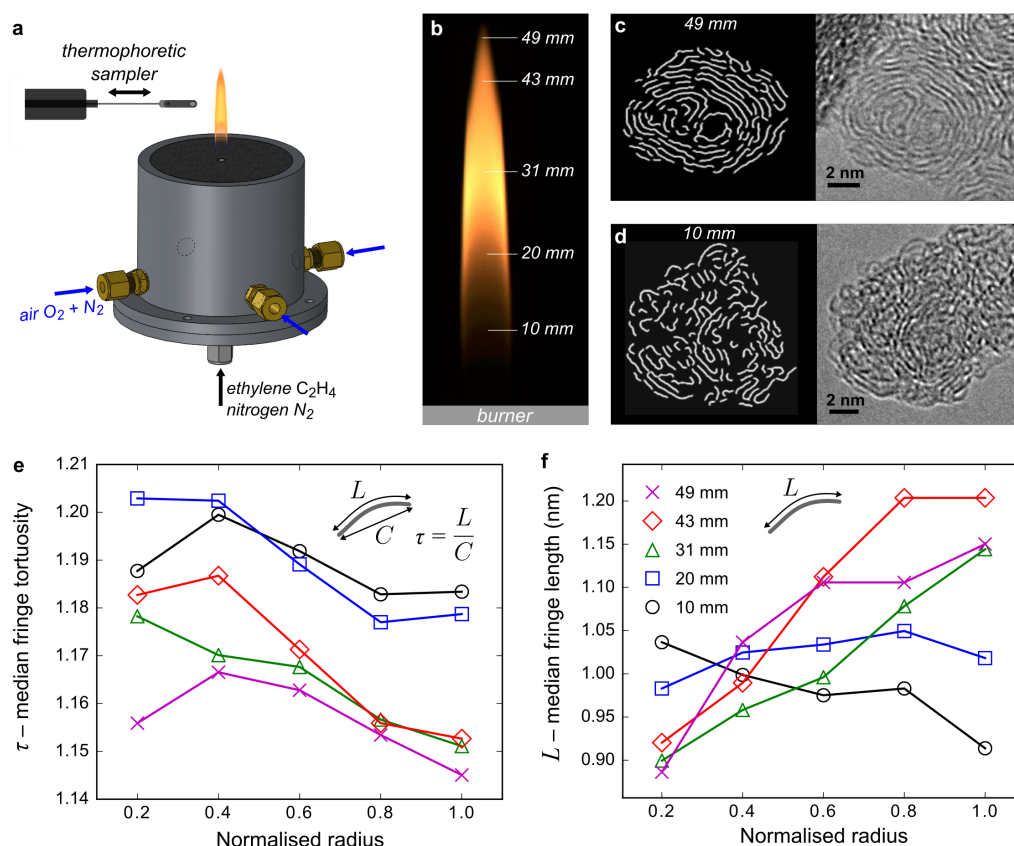
Figure 5.1 a) Schematic of the co-flow diffusion flame used and the rapid solenoid injector, and b) sampling positions. c-d) Skeletonised and unprocessed HRTEM images of primary carbon nanoparticulates for 10 and 49 mm heights above the burner (particles are not shown to scale but have radii of 9.5–10 and 8.5–10.2 nm; unprocessed images are also shown). e-f) Fringe median length and tortuosity as a function of the radial distance normalised to the size of the primary particles for various heights above the burner (standard errors ± 0.01 for τ, and ± 0.03 nm for L). Data provided by Dr Botero.

along with the electron micrographs of the particles before image processing. For the radial dependence, fringes were partitioned into five equal-radius concentric spherical shells and the fringe size and tortuosity distributions were calculated for each shell. The distributions were positively skewed towards longer fringes; therefore, the median length and tortuosity was preferred instead of the mean.

The size of the molecular fragments in the soot can be inferred from the fringe length. Figure 5.1f shows the fringe lengths across all heights above the burner. The fringes' median size ranges from 0.9–1.2 nm, corresponding to aromatics with 14–22 aromatic rings (assuming a circular pericondensed aromatic [42]). The results for the lowest height above the burner (10 mm) provide insight into the species present at nuclei formation; there,

$L = 0.9 - 1.05$ nm, corresponding to a size of 15 aromatic rings, consistent with optical band gap measurements [42] and mass spectrometry [251].

The amount of cPAHs in the soot particulates was quantified by analysing the tortuosity of the fringes. The tortuosity is a measure of the curvature, and therefore, of the polarity of the molecular fragments corresponding to a fringe. The majority of fringes in the soot at 10 mm above the burner contained a single peak in the curvature and no inflection, indicating the incorporation of pentagons, not heptagons, into the aromatic molecules at this low height (which was also observed by Wang et al. [437]). As seen in Figure 5.1e, the fringes became less tortuous as the carbon particulates progress through the flame, initially starting at $\tau = 1.18$–1.20 and finally leaving the flame with values of $\tau = 1.15$–1.17.

The author then established a correspondence between the tortuosity and number of pentagons by simulating HRTEM images of curved PAH with the similar number of aromatic rings (15) as seen in the early flame, with three, two and one enclosed pentagons (Figure 5.2a, b and c). The same fringe analysis software was applied to these simulated images and tortuosity values of 1.37, 1.20 and 1.13 were found. Small crosslinked PAH were also analysed as alternative species that could produce tortuous fringes [see Figure 5.2d]. The orientation with the maximum fringe tortuosity able to be produced for a non-pentagonal PAH crosslinked species was $\tau = 1.15$, a value similar to τ of a curved PAH with a single pentagonal ring. Fringes with tortuosity values >1.15 were therefore considered to be predominantly due to pentagon integration and not crosslinked species. This cutoff underestimates the amount of curved aromatics due to pentagon integration as it is not possible to distinguish them from crosslinked PAHs. Using this cutoff it was calculated that for the lowest sampled height, at least 62.5% of the fringes indicated pentagon integration. This amount of pentagon integration is higher than the values 28–49% found previously for mature carbon particulates [457, 437]. These lower values can be explained by the age of the particles; indeed, the fringe analysis for carbon particulates sampled from the late stages of the flame have considerably flatter and longer fringes. This indicates a carbonisation process leading to removal of embedded pentagonal rings.

The polarity of curved PAHs in the carbon particulates at 10 mm above the burner can be estimated based on the median fringe length ($L \approx 1$ nm) and tortuosity ($\tau \approx 1.2$) suggested from HRTEM image analysis of early soot particles, which correspond to the curved PAH containing two pentagons (Figure 6.7b). A dipole moment of 5.32 D was calculated for this species using the methodology developed previously in Chapter 4. Figure 6.7d shows the electrostatic potential perpendicular to the aromatic plane of the PAH and reveals significant charge polarisation due to the flexoelectric effect. The electrostatic potential indicates strong binding sites for cations on the convex and concave surfaces of the aromatic plane.
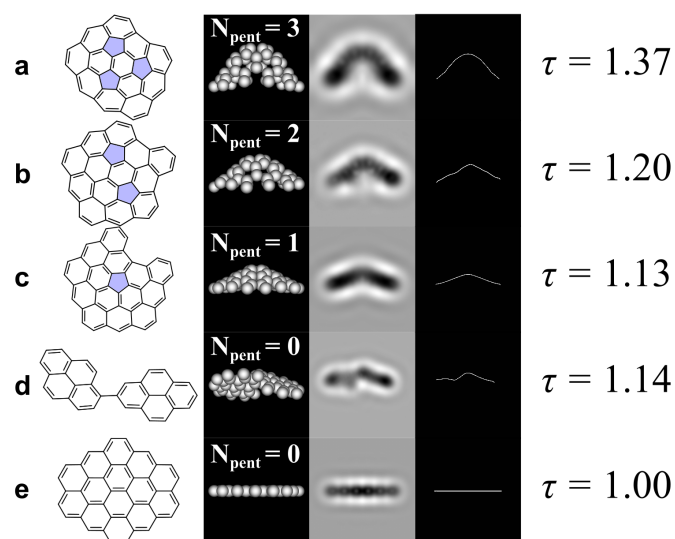
Figure 5.2 a-c) Curved aromatics with three, two and one pentagons, respectively, with simulated HRTEM images and fringe analysis (with their corresponding calculated tortuosity value).
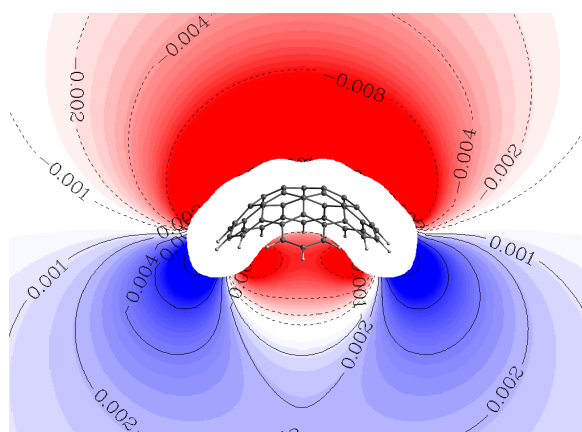
Figure 5.3 Electrostatic potential perpendicular to the aromatic plane for the curved PAH with two pentagons (isovalues of the potential are shown in a.u.).

In summary, a significant fraction of the molecules in early soot nanoparticles are curved. The lack of curvature in mature soot is suggested to be due to thermal transformations that soot undergoes.

5.2   Earliest inclusion of curvature

A more fundamental question arises after finding curvature in early soot nanoparticles – at which point during the growth of the PAH is curvature integrated? Answering such a question

experimentally would require the synthesis of many compounds, therefore, computational techniques will be used to consider how small an aromatic molecule can be before it becomes curved by pentagon integration. It is also interesting to consider which electronic features of aromatics cause or inhibit curvature integration.

For the curvature integration calculations, the hybrid density functional theory (DFT) method B3LYP with the 6-311G(d,p) basis set was used, which has been found to provide structures for small curved aromatics to the quality of those determined from X-ray crystallography [325, 150]. This level of theory provides molecular dipole moments to within 6% error compared with the experimental value for corannulene, as mentioned. Care was taken to ensure that geometry optimisations provided a structure not at a saddle point geometry (e.g. small cPAH can invert through a planar transition state geometry [373]). C_1 symmetry was enforced for all structures, initial geometries were purposely curved away from planar and frequency calculations ensured no negative frequencies indicating convex minima in the potential energy were found.

Small PAH have flat configurations even if pentagons are integrated. In order to predict at which stage of PAH formation in flames a significant flexoelectric dipole moment will occur, it is important to find the onset of curvature integration as a PAH grows. Various mechanisms for pentagon integration have been proposed, such as acetylene addition to fluoranthene [330], dehydrogenation of a five-member bay site [446, 447], oxidation of a zig-zag edge [388], dehydrogenation of aromers [186] or a C_1/C_2 mechanism [452], as discussed in Chapter 3. Our goal here is not to comment on which mechanisms are of most importance, but to determine the smallest PAH size that leads to curvature, and to expand the set of structures explored in Figure 4.1. Figure 5.4 shows the various strategies employed to increase the size.

The geometry of hexagonal and pentagonal nets should dictate that once two hexagonal rings border a pentagonal ring, curvature should be integrated. Considering the base structures, labelled **ac**, **fa**, **ph**, **be** and **1a** in Figure 5.4, no curvature is observed until the pentagon is entirely enclosed by five hexagonal rings. To understand the discrepancy between a geometrical net and that found in the calculated structures, the bonding must be considered. The σ-bonding of the sp^2 aromatic network containing pentagons favours curvature by limiting the bond lengths (1.3–1.6 Å) and providing an angle potential optimal at 120°, incompatible with pentagonal structure. The π-bonding network, however, resists bending (leading to a large elastic modulus of 21.5 eV/Å^2 [299]) and favours planarisation of the molecules. The π-bonding dominates for two to four bordering hexagons with the bond lengths and angles changing to accommodate the planar structure. The planarisation is only overcome for the structure with a pentagon completely enclosed by hexagons (**1a**).
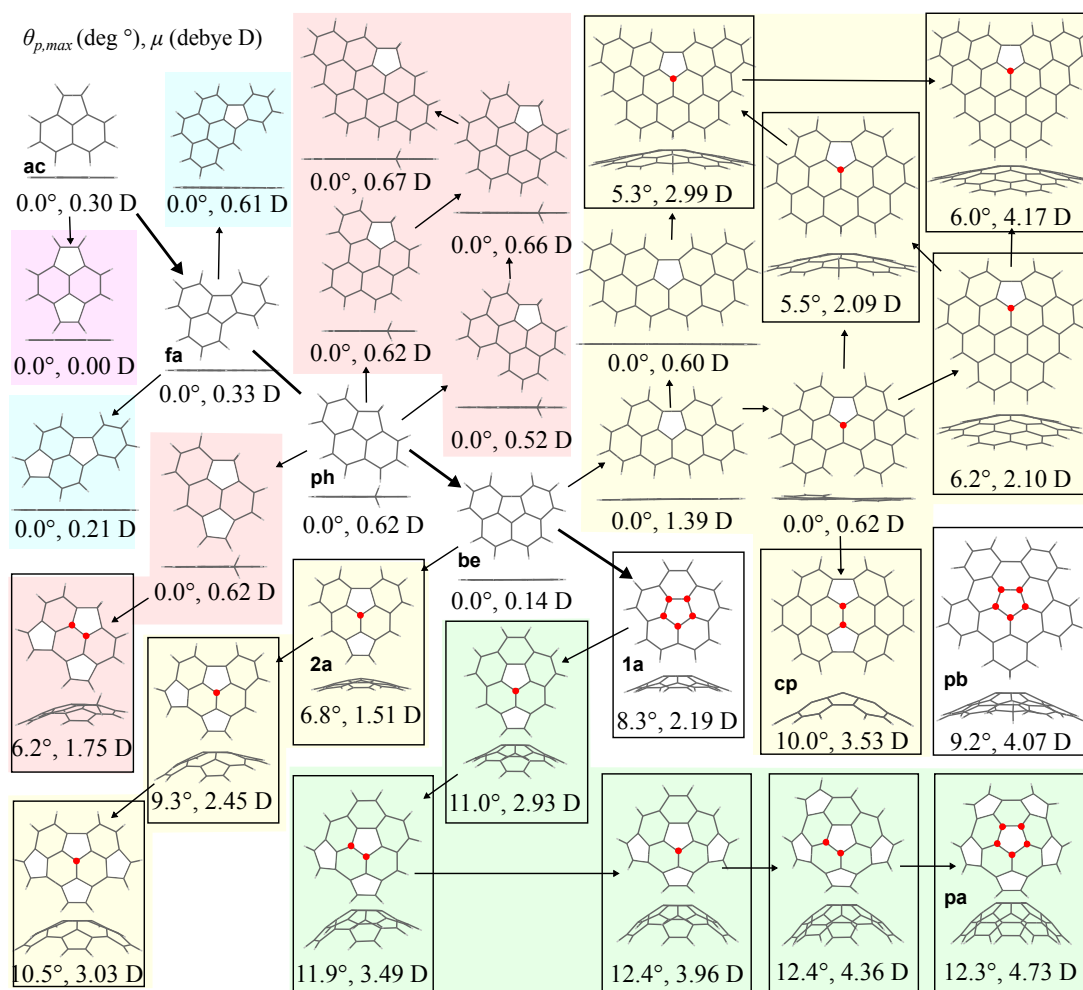
Figure 5.4 Optimised geometries are shown from above and side. The curved structures are framed. The most pyramidalised carbon atom of each structure is denoted by a red circle and its θ_p value is quoted underneath, along with the dipole moment calculated at the B3LYP/6-311G(d,p) level of theory. Base structures with single pentagons with two acenaphthylene **ac**, three fluoranthene **fa**, phenanthrindene **ph**, four benzo(ghi)fluoranthene **be** or five corannulene **1a** bordering hexagons are shown along the diagonal with hexagonal extension top right and acetylene addition bottom left.

The previous set of structures, from Figure 4.1, was extended to include more molecules containing pentagons incompletely enclosed by hexagons (containing sp^3 carbons). Curved geometries obtained via two pathways were analysed by increasing the hexagonal aromatic network around the structure or by acetylene addition to zig-zag edge site, as suggested by Pope and Howard [330]. For structures **fa** and **ph**, with a single pentagon and three bordering hexagons, additional hexagonal network growth did not give rise to curvature. However, for the structure **be** with four hexagonal rings enclosing the pentagonal ring, it was found

that hexagonal growth did lead to curvature and a flexoelectric dipole. However, substantial growth was required – the initial addition of hexagonal aromatic rings to the left and right of the pentagonal ring lead to planar structures. Significantly more hexagonal rings were required to curve the arenes containing a single non-enclosed pentagon ring. It was also found that substantial curvature could be induced by the geometry with two unenclosed pentagons joined by two hexagons (Figure 5.4 **cp**). An effective curvature integration mechanism was also found for the addition of acetylene to benzo(ghi)fluoranthene, **be**. This rapidly increased the maximal pyramidalisation angle ($\theta_{p,max} = 6.8, 9.3, 10.5°$ for one, two and three acetylene additions, respectively) and dipole moment of these structures ($\mu = 1.51, 2.45, 3.03$ D). This mechanism was also explored for corannulene and a substantial dipole moment was found with these non-integrated pentagonal rings giving dipole moments of 2.93, 3.49, 3.96, 4.36 to 4.73 D. The additional pentagonal rings around the edges produced curvature more effectively due to pentagonal rings' decreased internal angles compared with the hexagons, which provides more σ strain on the carbon network. This is further highlighted by comparing the curvature of pentacetylcorannulene (**pa**) and pentabenzocorannulene (**pb**). The former was found to be more pyramidalised, $\theta_{p,max} = 12.3°$, compared with the latter, $\theta_{p,max} = 9.2°$. Acetylene additions to zig-zag sites (producing edge-based peripheral pentagonal rings) are not persistent at high temperature and are prone to acetylene desorption, migration or rearrangement into hexagonal rings [446]. However, if further acetylene addition proceeds to enclose the pentagonal ring by hexagons, it would represent the most effective manner to integrate curvature, with the second most effective being acetylene addition to zig-zag edge sites.

Returning to the question of the critical size for the onset of curvature, Figure 5.5 shows the dipole moment as a function of ring number. It is seen that the onset of curvature occurs at 6 rings for the pentagon enclosure and acetylene curvature integration strategies. For the hexagonal extension strategy, the onset of curvature was found to be at 10 rings.

In summary, curvature integration is driven by the strain imposed on the carbon skeleton by the bond length and angle restrictions due to the σ-bonding, but it is resisted by the π-bonding which favors planar geometries. It turns out that the latter effect is dominant for small species, resulting in a relatively well defined critical size of the pentagon-containing structures that has to be overcome for curvature to occur. The onset size has been found to be six rings for growth by pentagon enclosure and rim based pentagonal rings and 10 rings for hexagonal extension for a pentagon that is not enclosed. Acetylene addition to a zig-zag edge providing rim based pentagonal rings was found to increase the curvature to a greater degree than the addition of hexagonal rings. It will now be considered whether curvature can be integrated experimentally using different fuels.
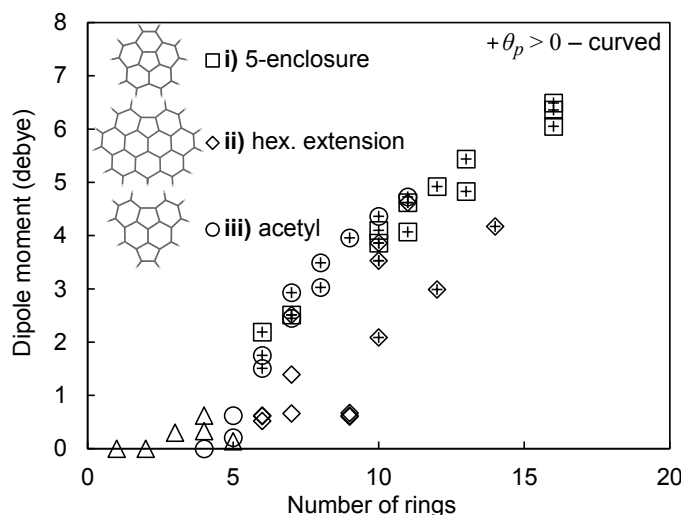
Figure 5.5 Dipole moment as a function of the number of rings for different curvature integration strategies. These strategies are also shown in Figure 5.4 with 5-enclosure being represented by **1a** as well as the structures previously calculated in Chapter 3, hex. extension in the upper right half and 5-rim in the bottom left of Figure 5.4. Curved structures are indicated by a plus symbol. The triangles correspond to **ac**, **fa**, **ph** and **be**.

5.3   Integrating curvature into soot

Thus far, the curvature of molecules within the earliest soot nanoparticles in an ethylene flame has been quantified and the size of aromatics needed to incorporate curvature explored. In this section the fraction of curved aromatics within soot will be modified by using a variety of cyclic fuels. This will help establish whether a correlation exists between pentagonal rings and sooting propensity.

Dr Salamanca performed the experimental work presented in this section (full details can be found online at https://como.ceb.cam.ac.uk/preprints/246/). I will briefly introduce the experiment to justify the analysis presented below. A similar coflow burner geometry is used as shown in Figure 5.1 but *n*-heptane is used as a base fuel instead of ethylene as it is closer to a real fuel surrogate. Doping of the cyclic fuels was achieved by mixing them within the *n*-heptane to have a 20% mol carbon substitution of the pure *n*-heptane fuel. The liquids were syringe fed and vapourised within a CEM evaporator (Bronkhorst), at 323 K and delivered to the burner via heated tubes at 423 K with flow rates from 6.98 to 7 gh^{-1} depending on the liquid mixture's mass density to ensure a constant carbon supply to the burner.

The soot volume fraction was determined using colour ratio pyrometry using the FLiPPID methodology developed and calibrated in the group [106]. Figure 5.6 shows the *n*-heptane and the three cyclic fuels cyclohexene, cyclopentene and methylcyclohexane. The maximum soot volume fraction for *n*-heptane is ≈1 ppm. The soot volume fraction increases for the

addition of the hexagonal fuels by 17% and 36% for MCHA and CHE, respectively. For cyclopentene, a significant increase of 80% is found, indicating an enhancement of soot formation.
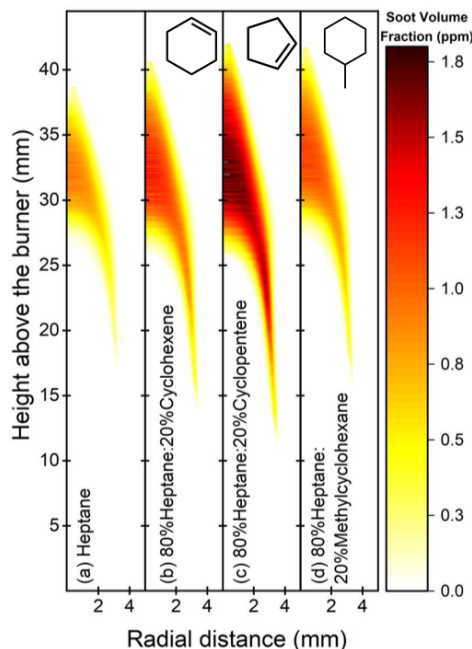
Figure 5.6 Soot volume fraction measured via colour ratio pyrometry. Courtesy of Dr Maurin Salamanca.

To explore the nucleation of particles the particle size distribution was measured. A quartz probe was used to sample from within the flame, allowing for rapid dilution and quenching of the gas mixture. A Differential Mobility Spectrometer from Cambustion Ltd. (DMS500) allowed for particle sizing down to 4 nm, however, only results down to 10 nm are shown. More details on the sampling can be found in a previous publication [105]. Figure 5.7 shows the particle size distribution as a function of height above the burner and fuel mixture. For all cyclic fuels added soot nucleation was found to occur earlier in the flame. The most significant effect is again found for cyclopentene at low heights above the burner. For >28 mm height above the burner bimodality is observed in the particle size distribution due to coagulation of primary particles into soot fractal aggregates. Less significant differences are observed at higher heights indicating the cyclopentene influences the particle formation primarily and coagulation is similar between the fuels.

The nanostructure of the soot nanoparticles doped with different cyclic fuels was explored using HRTEM and Raman spectroscopy. For this study, the FEI Tecnai FEG20 electron microscope was used. Figure 5.8 shows the nanostructure of soot from the *n*-heptane, *n*-heptane/cyclohexene and *n*-heptane/cyclopentene fuels sampled from $h = 32$ mm (methyl-
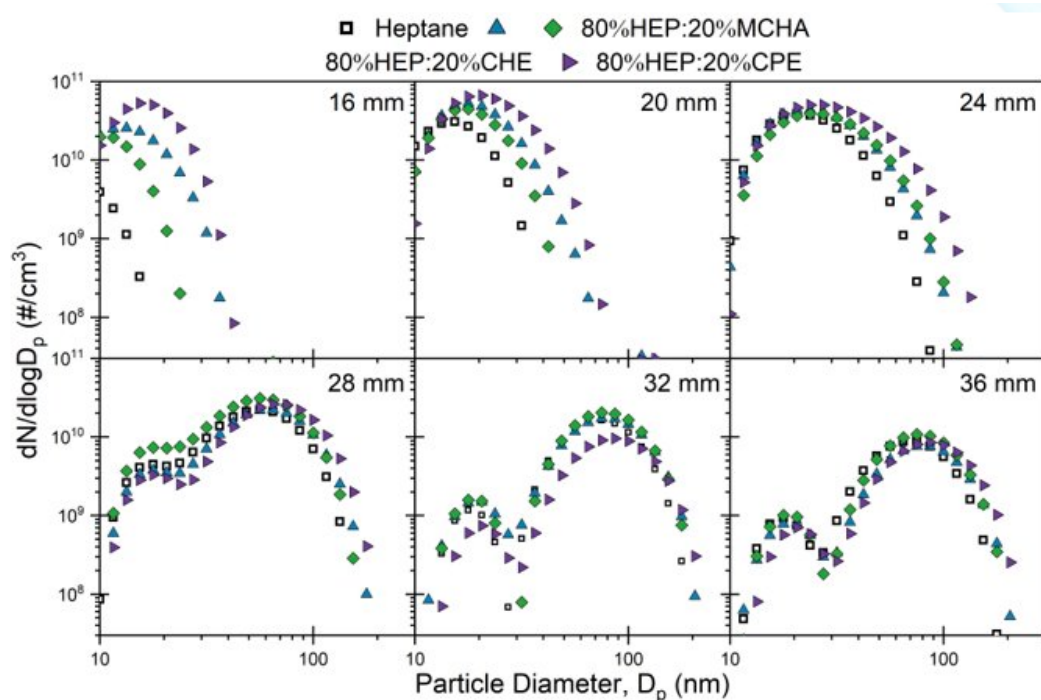
Figure 5.7 Particle size distributions for different heights above the burner and fuel mixtures in coflow diffusion flames. Courtesy of Dr Maurin Salamanca.

cyclohexane was found to have a similar nanostructure to *n*-heptane and is not reported for brevity). This height provides well formed primary particles that have not been exposed to significant oxidation. The core of the nanoparticles were found to be lacking in fringes indicating a more amorphous nanostructure. Fringes were found to be arranged in a concentric arrangement around the centre as is common in soot nanoparticles.
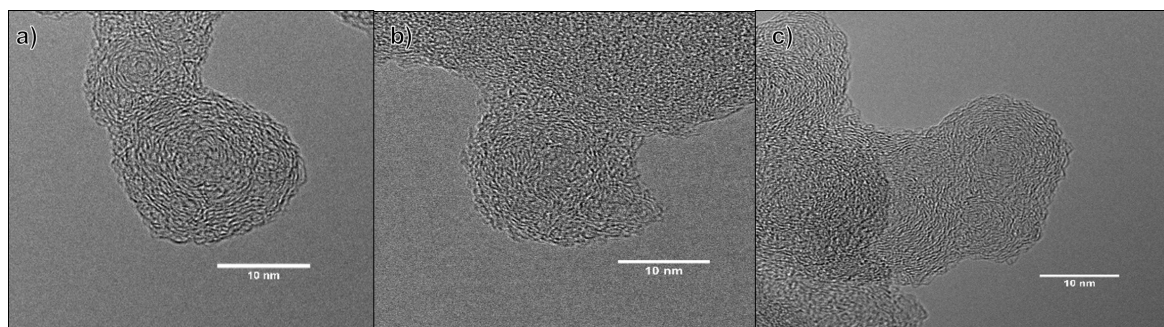
Figure 5.8 HRTEM images of soot from a) *n*-heptane as well as the b) cyclopentene and c) cyclohexene doped *n*-heptane fuels. Courtesy of Dr Maurin Salamanca.

To determine any difference in the nanostructure between the particles significant statistics needed to be captured. Therefore ten nanoparticles were analysed for each of the three fuels

and fringe analysis was performed on the set of all fringes collected according to the procedure previously published [42]. Table 5.1 shows the fringe statistics for the different fuels. The fringe length was found to be similar between the *n*-heptane and the cyclohexene doped fuel. Fringe length was slightly shorter for the cyclopentene doped fuel. Interlayer fringe spacing was slightly longer for cyclohexene fuel but still much longer than that from a fully graphitic material <0.34 nm. Tortuosity increases slightly for cyclohexene doped fuel but for the cyclopentene a significant increase is found. This is best illustrated by comparing ranges of τ previously determined for the early soot nanoparticles (while these ranges are only appropriate for non carbonised early soot particles they will nonetheless aid in the discussion). The cyclopentene fuel had a significantly higher fraction of strongly curved fringes.

Table 5.1 Mean fringe length (*L*), fringe spacing (*S*), tortuosity (τ) and percentages of fringes within certain tortuosity values for fringe analysis performed on particles collected at $h = 32$ mm. Courtesy of Dr Maurin Salamanca.

Flame	L (nm)	S (nm)	τ	$\tau < 1.15$ (%)	$1.15 < \tau < 1.35$ (%)	$\tau > 1.35$ (%)
n-hep.	0.936	0.418	1.19	52.8	34.9	12.3
hep.c-hexene	0.903	0.418	1.19	52.1	36.3	11.6
hep.c-pentene	0.834	0.421	1.25	40.6	40.7	18.7

Raman spectroscopy was also used to explore the nanostructure. This is an inelastic scattering method able to probe the vibrational modes within a material. Quantum mechanically Raman active modes significantly change the polarisability during the vibrational motion. This allows energy to transfer between the light and the molecular vibration, leading to emitted light downshifted in energy from the initial light (most commonly in Stokes shifted light). In carbon materials there are two main vibrational modes, the graphitic *G* band (at ≈ 1580 cm^{-1}) that arises in all sp^2 carbon materials due to an in-plane "scissor" motion of the atoms (E_{2g} symmetry). In carbon materials with edges, the disordered *D* band (at ≈ 1345 cm^{-1}) can also arise from an in-phase ring breathing vibration (A_{1g} symmetry) that cannot exist in graphite but becomes active near the edge of sp^2 carbon atoms. This has allowed the $I(D)/I(G)$ to be correlated with the size of the graphitic regions L_a within carbon materials,

$$I(D)/I(G) = C'(\lambda)L_a^2, \qquad (5.1)$$

where $C'(\lambda)$ is a wavelength dependent constant [120]. Significant photoluminescence was also found, an effect not related to Raman scattering, however, it has been correlated with

hydrogen content in carbon materials through the equation,

$$H[at\%] = 21.7 + 16.6 \log \left\{ \frac{m}{I(G)} [\mu m] \right\},\tag{5.2}$$

where m is the slope of the photoluminiscent background measured for the baseline between 1000 and 1800 cm^{-1} [60].

Returning to the analysis of the Raman spectrum, an area of Raman spectroscopy of carbon materials that has received less attention is the impact of curvature on the Raman vibrational modes. Recently, simulated Raman vibrational modes for corannulene with DFT found an upshifted D band relative to planar counterparts near 1450 cm^{-1} called the A band (or A_1 band), closely matching the experimental Raman spectrum for corannulene [352, 396].

Density functional theory is able to accurately capture molecular vibrations to within a few cm^{-1} after applying an anharmonic correction. Figure 5.9 shows the scaling factor used to correct for the anharmonicities and also shows the close agreement between the vibrational modes computed using B3LYP/6-311G(d,p) and the experimental Raman spectrum for corannulene [352].
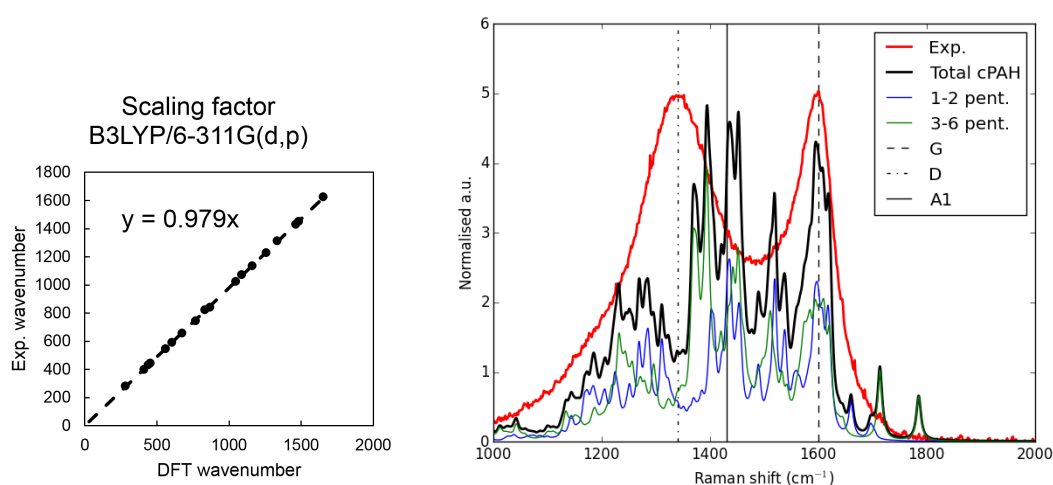
Figure 5.9 Experimental versus DFT derived Raman active modes and the anharmonic scaling factor (left). Simulated Raman spectrum from sum of curved PAH in Figure 4.1. Courtesy of Dr Maurin Salamanca.

The Raman spectrum was then calculated at the B3LYP/6-311G(d,p) level of theory for the species found in Figure 4.1. They were then grouped into those that had 1–2 pentagonal rings and more highly curved species with 3–6 pentagonal rings. For the entire set the spectra were normalised and their average taken. While this distorts the contribution from the smaller species that have small scattering cross sections it will help to illustrate the

regions where each class of species scatters. The Raman spectrum collected on soot from the cyclopentene doped *n*-heptane flame is also shown in an overlay. The *G* band was found to be overlapping between the low and high curvature cPAH and was not shifted from the frequency of flat PAH at $\approx$1580 cm^{-1}. The most significant difference is in the *D* band which is split in the cPAH species. There are a variety of defects that also lead to a downshifted signal so the upshifted signals from 1345 to 1500 cm^{-1} will be the focus. The highly curved species possess a vibrational mode at $\approx$1400 cm^{-1} due to a set of ring breathing mode vibrations. All cPAH possessed intensity at $\approx$1450 cm^{-1} due to the same vibrational mode. This suggests that considering the ratio of 1400 to 1450 cm^{-1} may be useful for comparing the fraction of slightly and highly curved PAH in carbon materials, however, due to the small separation between these bands it seems unlikely to be useful. Instead the ratio of the *A* band at 1450 cm^{-1} to the *G* band, which is similar for curved or planar PAH, seems to be the natural choice to quantify the number of curved species in carbon materials.

Figure 5.10 shows the construction of the different bands that will be used for comparing the different species. Given the large amount of photoluminescence in the early soot particles the *A* band was not computed due to the errors introduced from the baseline fitting. Table 5.2 shows the results from the fitting procedure. Sampling heights above the burner were chosen so that the mobility diameter measured using the DMS was either 25 nm or 80 nm, corresponding to height ranges of $H = 22 - 25$ mm and $H = 30 - 33$ mm, respectively. This ensured that the particles had similar residence times in the flame after nucleation – cyclopentene nucleation, for example, began earlier than the other fuels so could be collected at lower heights.
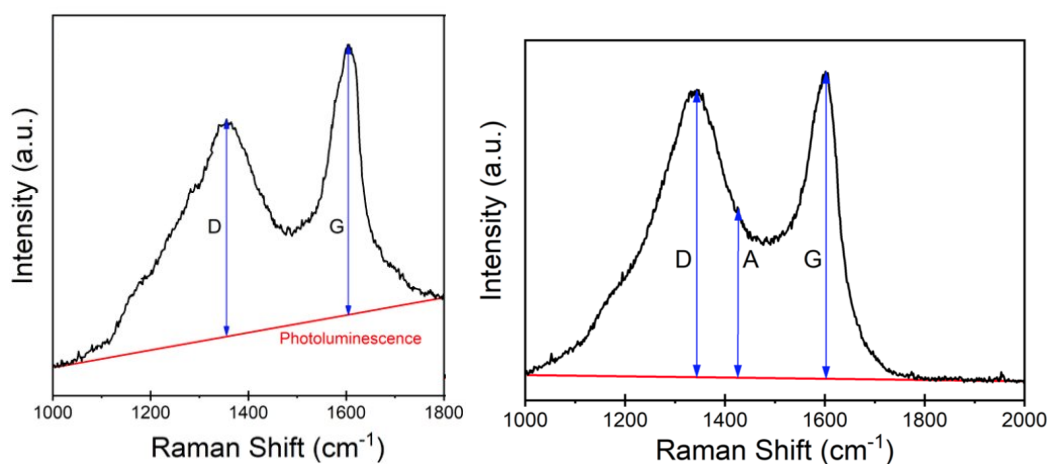
Figure 5.10 Raman spectra and the construction of the different metrics for the soot sampled at low (left) and high (right) heights above the burner for the cyclopentene doped *n*-heptane flame. Courtesy of Dr Maurin Salamanca.

Table 5.2 Results from Raman spectroscopy of particles from low height above the burner with particles of diameter $D = 25$ nm and high height above the burner with particles of diameter $D = 80$ nm. Hydrogen atom percentage H, crystallite size L_a determined from $I(D)/I(G)$ [120] and curvature is inferred from $I(A)/I(G)$. Courtesy of Dr Maurin Salamanca.

Flame	$D = 25$ nm		$D = 80$ nm	
	H (at%)	L_a (nm)	L_a (nm)	$I(A)/I(G)$
n-heptane	34±2	1.22±0.03	1.28±0.02	0.53
n-heptane/cyclohexene	35±1	1.24±0.01	1.25±0.01	0.51
n-heptane/cyclopentene	31±4	1.23±0.02	1.31±0.02	0.60

The hydrogen content inferred from the photoluminescence indicates an H/C ratio of 0.5 is expected for pericondensed aromatics with 10–15 rings. Slightly lower hydrogen content was found for the cyclopentene doped flame. Insignificant changes were found in the crystallite size between the low height samples. The Raman spectrum collected at the higher height above the burner allows the baseline to be more easily fitted and the crystallite size to be accurately determined from the $I(A)/I(G)$ ratio. Cyclopentene doped soot was found to have a significantly higher $I(A)/I(G)$ ratio than the n-heptane and cyclohexene doped soot. This was interpreted as being due to an increase in curvature in the cyclopentene doped soot as suggested from the simulated Raman scattering.

The larger crystallite size for cyclopentene compared with n-heptane or cyclohexene contradicts with the shorter fringes found in the HRTEM for the cyclopentene doped soot in Table 5.1. Considering again how the integration of curvature splits the D band, this could decrease the intensity at 1350 cm^{-1} providing a lower $I(D)/I(G)$ ratio. This would be interpreted as a larger crystallite size using Eq. 5.1 as the defect peak intensity (D band) would be lower compared with the graphitic peak (G band). However, more experimental work is needed to confirm this hypothesis. The HRTEM combined with the Raman spectroscopy results suggest that cyclopentene is able to provide more efficient pathways to pentagon integration followed by internal incorporation to form curved species as compared to hexagonal cyclic fuels.

In conclusion, curvature is quantified in early soot nanoparticles using HRTEM experiments and multislice image simulations. The majority of aromatic species were found to contain one or more pentagonal rings with, on average, two pentagonal rings within species with 15 rings providing a dipole moment of 5.32 D. Further computational work was undertaken to consider the earliest stages that curvature can become integrated into growing aromatic species. This was found to be six rings. At this size the carbon skeleton overcomes

the π-bonding that favours a planar geometry. Finally, cyclic fuels were added into *n*-heptane fuels. Cyclopentene doped *n*-heptane was found to provide a more curved nanostructure compared with cyclohexene. It appears that the growth of PAH from cyclopentene precursors provides a pathway to more pentagonal rings and curvature. This fuel also led to a significant increase in soot nucleation as measured via DMS and soot volume fraction, providing a correlation between curvature and soot formation. It is unclear experimentally whether there is a causative link between these two. Therefore, the following chapters will explore how cPAH could modify soot formation compared to fPAH; firstly, in terms of physical nucleation and secondly, in terms of chemical inception pathways.

Chapter 6

Physical nucleation of cPAH

Mont Blanc - Credit: Visavis Fickr CC BY-NC-ND 2.0

"In burning candles upon the summit of Mont Blanc, I was much struck by the comparatively small amount of light which they emitted."
 – Edward Frankland, *On the Influence of Atmospheric Pressure upon Some of the Phenomena of Combustion (1861), 629-653*

The work in this chapter was published as papers in *Proceedings of the Combustion Institute*, *Combustion and Flame* and *Combustion Science and Technology* in collaboration with the group at the University of Cambridge and Queen Mary University, London. Contributions from the team included Ms Bowal performing the molecular dynamics simulations, Mr Menon and Mr Lao performing the inversion rate calculations and the other authors editing the manuscript. Dr Alston Misquitta and Ms Bowal aided in the development of the curPAHIP forcefield. The calculations of the inversion barriers, quantum molecular dynamics and writing were performed by the author.

In this chapter, the possibility of cPAH physically nucleating in flames will be considered. Homogeneous nucleation will be explored with homodimer binding energies of cPAH. Ion-induced heterogeneous nucleation will then be considered using molecular dynamics simulations of corannulene and coronene clustering with and without ions present. Electronic structure calculations will be used to compute the binding energies between the cPAH with 15 rings, of which two are pentagonal, discussed in the previous chapter and the most common chemi-ion in sooting flames, $C_3H_3^+$. The question of whether curved PAH have a persistent dipole moment at temperatures at which soot forms in a flame will then be explored using electronic structure calculations. The rate of inversion is computed for a range of cPAH revealing the strain aromaticity relationships which make large cPAH unable to invert in a flame. Ab initio *molecular dynamics is then used to track the fluctuation of the dipole moment of a cPAH and study the dynamics of a chemi-ion interacting with the cPAH over two picoseconds. Finally, the role of cPAH in physical nucleation is discussed in the context of the presented results.*

6.1 Homogeneous nucleation

In this section, the ability of cPAH to homogeneously nucleate at flame temperatures will be explored using electronic structure calculations of homodimerisation energies. This dimerisation energy (defined as the minimum energy of all possible dimer conformations) has been used as a measure of the stability of clusters of flat PAH molecules previously [438, 418]. For example, Totton et al. [418] made use of symmetry-adapted perturbation theory DFT methods SAPT(DFT) that were found to accurately reproduce the exfoliation energies of graphene and the second virial coefficients of benzene [417, 418]. These energies have been compared with the temperature dependent equilibrium constants for dimerisation and clustering using molecular dynamics simulations of clustering. Energies above 40 kcal/mol

were found to be required to allow for molecules to cluster at temperatures within the flame where soot forms [418].

As already mentioned in Chapter 3 the suggestion of homogeneous nucleation of cPAH was first proposed by Baum et al. [24] in 1992. To date there has not been substantial work on this possibility. In the case of planar aromatics, the intermolecular potential energy was easily sampled by increasing the interplanar distance between the dimers and calculating the binding energy as a function of distance. However, for cPAH dimers, a more complex geometry can result from the symmetry breaking due to the curvature and full geometry-optimised structures were sought. This required a sufficiently rapid and scalable method in order to optimise the geometry of the largest structures. A hybrid DFT method with an empirical dispersion correction called B97D was used [155].

It must first be established whether B97D can accurately capture the dipole moment of the cPAH. Table 6.1 shows the absolute error of the dipole moment calculated using B97D, B3LYP and MP2 compared with the experimentally determined value for corannulene, 2.071 D.[257] Both B3LYP and B97D accurately predicted the dipole moment as the basis set size increased (which is not the case for MP2). Therefore, B97D is able to capture the dipole moment given a basis set the size of or larger than cc-pVTZ.

Table 6.1 Table of the difference of the dipole moments from the experimentally determined value 2.07 D [257] for corannulene at various levels of theory in debye with percentage errors in brackets.

Basis set	Func. no.	B3LYP		B97D		MP2	
6-31G(d)	320	0.35	(16.9%)	0.16	(7.8%)	0.10	(4.9%)
6-311+G(d,p)	500	0.12	(5.6%)	0.19	(9.1%)	0.60	(28.8%)
cc-pVTZ	740	0.08	(3.7%)	0.01	(0.6%)	0.35	(16.8%)
cc-pVQZ	1400	0.03	(1.3%)	0.05	(2.2%)	–	–

How about the dispersion interactions – how well does B97D perform compared with benchmark calculations? The B97D method has been found previously to accurately compute the intermolecular energy between dimers of corannulene **1a** and sumanene **3a** determining the interaction to within 2% of that calculated by CCSD(T) benchmark and symmetry adapted perturbation theory SAPT(DFT) methods [201, 52]. Planar PAH such as pyrene and coronene have been found to be overbound by B97D methods [418] and the B3LYP-D3 method was found to better describe these molecules [200]. Recently SAPT(DFT) simulations on curved arene dimers have been performed which allow the contributions of the intermolecular interaction to be decoupled. These are shown in Table 6.2 where the dispersion energies

calculated using the empirical correction in the B97D functional are compared for coronene and corannulene.

Table 6.2 Table of intermolecular energies (kJ mol^{-1}) determined using SAPT(DFT) and B97D methods. Equilibrium distances are also shown.

	Coronene		Corannulene	
	SAPT(DFT)[a]	B97D	SAPT(DFT)[b]	B97D
total	−65.7	−85.9	−65.9	−66.4
electrostatic	−27.5	–	−40.4	–
repulsion	145.5	–	118.6	–
induction	−38.9	–	−8.0	–
dispersion	−144.9	−154.9	−136.0	−121.1
R(Å)	3.58	3.51	3.62	3.62

^{a} *Taken from [329].* ^{b} *Taken from [52].*

The dispersion interactions are found to be overpredicted by B97D in the case of the flat PAH coronene and underpredicted for curved PAH corannulene, in comparison with the SAPT(DFT) benchmarks [329, 52]. Since the dipole moment was shown to be well described by B97D, see above, the electrostatic interactions are not expected to differ with that of SAPT(DFT) and, therefore, the underbinding of the dispersion interactions are compensated by an underprediction of the exchange repulsion providing a binding energy close to that of the benchmark calculations for corannulene. For coronene this compensation does not hold with an overprediction of the dispersion interaction leading to an overpredicted binding energy. It is well known for dispersion corrected hybrid density functional theory methods that the B3LYP-D3 method provides a better binding energy for coronene with a lower C_6^C dispersion coefficient [200]. This indicates corannulene has a larger dispersion interaction compared with coronene which would follow from the electrons being more easily polarised on pyramidalised carbon atoms. This has recently been shown to be the case for different carbon nanoforms [145]. Therefore, B97D is able to capture electrostatic and dispersion interactions to an acceptable level to provide a preliminary comparison.

Full geometry optimisations of the dimers were performed at this level of theory with basis set superposition error (BSSE) corrected for in the final electronic structure calculation (the BSSE error was not thought to impact the geometry optimisation substantially as it was found to be <2% in all cases). The results are shown in Table 6.3 as well as plotted as a function of molecular mass in Figure 6.2.

Table 6.3 Table of dipole moments, dimer binding energies, dimer equilibrium distances and molecular quadrupoles for PAH

	Dipole[a] (debye)	$\sum \theta_P \mathbf{v}_\pi$ (rad)	BE[b] (kJ mol^{-1})	D[d] (Å)	Tilt (degrees)
1a	2.06	1.269	-66	3.62	0.0
2a	2.79	1.697	-72	3.88	0.0
2b	4.10	2.309	-94	4.08	13.1
2c	4.92	2.723	-107	4.30	10.5
2d	7.42	3.778	-228	4.63	0.0
2f	4.83	2.598	-124	4.23	0.0
3a	2.51	1.524	-80	3.63	0.0
3c	4.62	2.579	-97	4.50	5.6
3d	5.44	2.953	-90	4.70	22.9
4a	6.36	3.257	-78	6.05	5.5
5a	6.49	3.274	-68	7.00	6.2
6a	6.46	3.205	-69	7.70	40.1
pyr	0.0	0.000	-42[c]	3.59	–
cor	0.0	0.000	-69[c]	3.58	–
ova	0.0	0.000	-98[c]	3.56	–
hbc	0.0	0.000	-140[c]	3.52	–
cir	0.0	0.000	-182[c]	3.46	–

[a] *Taken from [267].* [b] *Binding energy.* [c] *Taken from [419].* [d] *Equilibrium distance.*

Figure 7.4 shows the binding energies of cPAH compared with fPAH dimers of pyrene, coronene, ovalene, hexabenzocoronene and circumcoronene taken from [419]. For structures containing one to two pentagonal rings, it was found that similar binding energies for curved and planar PAH of similar masses. However, further increases in the number of pentagons destabilised the cPAH dimers significantly compared with flat PAH dimers.

To analyse the reasons for this behaviour, let us consider corannulene and coronene – small PAH whose similar binding energies allow the role of dispersion and dipole-dipole interactions to be analysed. SAPT(DFT) calculations showed a reduced dispersion interaction in corannulene dimers of -136 kJ/mol [52], compared with -145 kJ/mol [329] for coronene. This is also seen in the greater intermolecular distance between the two molecules centre of masses, in the dimer of corannulene, 3.62 Å compared with 3.58 Å for coronene (see Figure 6.2 for a more complete comparison). The role of the dipole can be evaluated via the electrostatic contribution, which for corannulene is 22% of the attractive potential compared with 13% for the coronene dimer. The dipole of the dimers increased in comparison with the
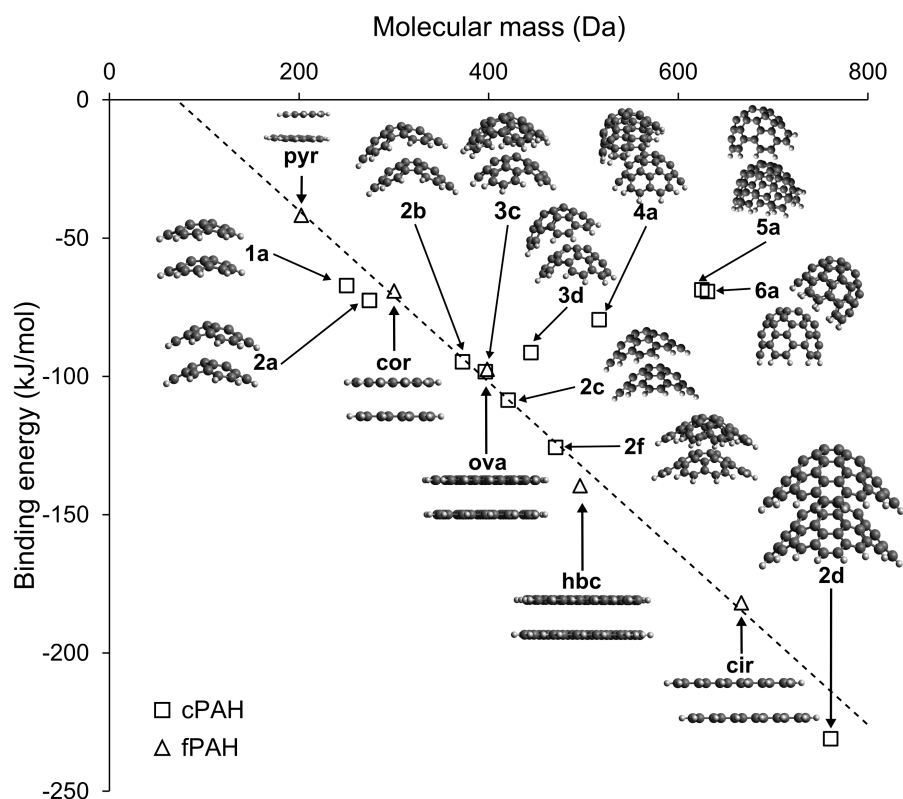
Figure 6.1 Binding energy of flat and curved PAH molecules as a function of molecular mass.

sum of the two static dipole moments, indicating a small contribution from induced dipoles (Debye interaction). SAPT(DFT) found induced polarisation to make up 4% of the attractive force in the case of corannulene [52].

Thus, while the dipole moment contributes to the binding energy, the molecule's curvature causes a decrease in the dispersion interactions due to steric effects. The intermolecular distance increases to 4.4–5 Å for one to three pentagons and 6–7 Å for four or more pentagons integrated (Figure 6.2). Due to the short range of the dispersion interactions (scaling as $\propto 1/r^6$) this significantly reduces the binding energy, most evidently for the structures with three or more pentagonal rings. For the highly strained structures a tilt towards a herringbone configuration was also found for the geometries. This is due to the positively charged hydrogen atoms interacting with the negative charge of the π-electron cloud around the carbon at the rim of the bowl; a similar effect has been observed in crystal structures [122].

Other dipole-dipole interactions with cPAH that could be important for soot formation can also be considered. Calculations have found significant interactions between water and corannulene, with similar binding strengths to water dimers, -12.0 kJ/mol [323] compared with -13.2 kJ/mol [349] respectively. In comparison, the water-graphite interaction energy
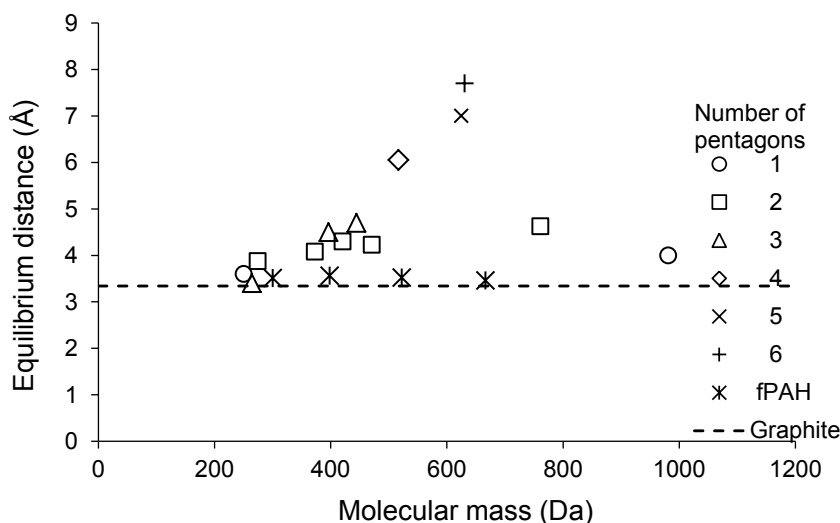
Figure 6.2 Intermolecular distances between homodimers computed using B97D for cPAH and SAPT(DFT) for fPAH.

is -9 kJ/mol [203]. These energies are of the order of RT at flame temperatures (12 kJ/mol 1500 K) and would therefore be insignificant for soot formation. Stronger interactions could be expected for heterodimers of cPAH, especially if the smaller molecule fits well in the concave side of the larger molecule. The order of magnitude of these interaction energies shows that, although they could contribute to nucleation, it is unlikely that they make a qualitative difference at flame temperature.

In summary, the similar binding energy of cPAH with one to two pentagonal rings to planar fPAH indicates that homogeneous nucleation of either species is unlikely to occur at flame temperatures [419]. Some preliminary molecular dynamics simulations have been performed on dimers **3c** by Chung and Violi [68] and a similar clustering behaviour was seen compared with planar fPAH. This is consistent with corannulene's sublimation temperature at standard conditions of 640 K [65]), which is similar to perylene 660 K at [304], a planar PAH with the same number of carbon atoms. The similar sublimation temperature indicates similar binding energies.

6.2 Ion-induced heterogeneous nucleation

6.2.1 Clustering of corannulene and coronene in the presence of ions

The impact of ionic species on the clustering behaviour of curved PAH was explored using molecular dynamics simulations. A new forcefield was developed for corannulene based on

dummy charges and SAPT(DFT) reference calculations [52]. The ion-induced clustering of corannulene and coronene was then compared using the new developed forcefield.

A significant interaction of cPAH will be with ions, as numerous examples from the literature show. Synthesised cPAH such as corannulene, **1a**, are known to bind small ions strongly (93–289 kJ/mol [108]). Anion binding is enhanced on the concave side by increased interaction with the positive hydrogen atoms and the increased dispersion interactions [62]. Cations can also bind to the concave face by interacting with the small excess negative charge present, but most significantly they bind via dispersion interactions in this configuration [108]. Binding on the convex face is favoured above the pentagonal ring but can also bind around the rim carbon atoms where charge is concentrated due to the C–H bond. Similar binding energies are found between ions and the cPAH corannulene/ions and the fPAH coronene [108, 62]. Yet, corannulene has increased capacity for lithium in battery applications (capacities of 372 and 602 mAh/g found for graphite and corannulene, respectively [462]). Chen and Wang recently considered the stabilisation of clusters of fPAH bound to a chemi-ion. A sandwich complex was found to have significant binding energies; however, the third fPAH added was weakly bound [62]. Curved aromatic molecules differ from planar fPAH most of all in their capacity for long-ranged interactions with ions (potential $\propto -1/r^2$); this means that larger clusters could be stabilised by ion-cPAH interactions. The only molecular dynamics simulation that has been conducted to date with a cPAH is a study of tri-acenaphtri-phenylene compared with planar PAH finding similar behaviour, however, the impact of clustering in the presence of ions has yet to be explored [68]. This work made use of atom-centred charges, however, in Chapter 4 it was made clear that atom-centred charges cannot reproduce the electrostatic field around a curved PAH. An atom-centred multipole description was shown to reproduce the electrostatics well. However, these descriptions are not able to be integrated into most molecular dynamics software at present. Therefore, another approach is required.

Colleague Kimberly Bowal, Dr Alston Misquitta and I developed an off-site point charge description for corannulene, which can be found in reference [46]. These massless dummy charges are used widely in multiple site models of water [30, 206]. In the case of corannulene we placed the virtual sites, seen as red spheres in Figure 6.3, above the pentagonal rings. Intramolecular bonds and angle potentials were used to keep these virtual sites fixed perpendicular to the plane made by the carbon atoms within the pentagonal ring. Ms Bowal then used the MULFIT program to fit the atomic charges, which uses the distributed multipoles to determine the best fitting of monopoles [119]. This provided a dipole moment of 2.14 D, a slight overestimation compared with the calculations performed in Chapter 4 (4%). Figure 6.4 compares the electrostatic potential making use of atom-centred point charges and using the off-site charge model, which is named the curved PAH isotropic

forcefield (curPAHIP). While it does contain some anisotropy with the dummy atoms it is not fully an anisotropic potential and therefore the name isotropic is used.
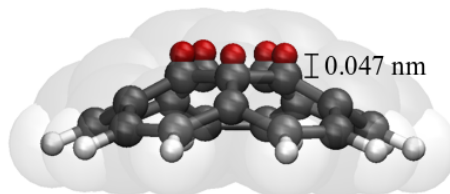
Figure 6.3 A charge is placed at each atom centre and off-site massless charges (red) are placed above the pentagonal ring.
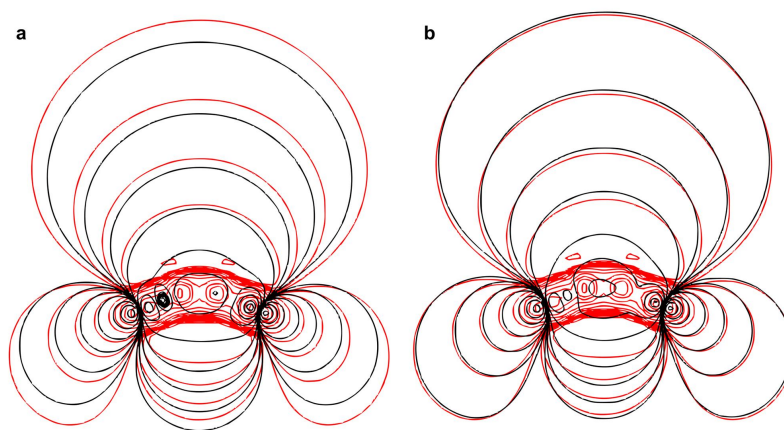
Figure 6.4 Electrostatic potential around corannulene calculated using DFT method (black) and with a) atom-centred point charges and b) off-site point charge description (red).

Ms Bowal, working with Dr Misquitta, completed the fitting procedure by using the benchmark SAPT(DFT) calculations for corannulene performed by others [52]. Figure 6.5 shows the fitting performed. The dispersion interactions were found to be enhanced compared with the fPAH dispersion fitted forcefield isoPAHAP. This enhanced dispersion interaction is well known for curved nanocarbons and is due to the polarisability and three-body effects being enhanced [145]. Further fitting was done to ensure the interactions between corannulene and the charged cation potassium for the following clustering simulations. More details on the forcefield can be found in Bowal et al. [46]. Potassium was chosen as it is readily ionised in a flame and has been shown to impact soot nucleation through the production of higher particle numbers and smaller particle sizes [172, 98, 387].

Ms Bowal then performed molecular dynamics simulations of one thousand PAH molecules (coronene or corannulene) with and without the same number of potassium ions randomly placed in a periodic box. High concentrations of 2×10^{18} cm^{-3} were used to increase the
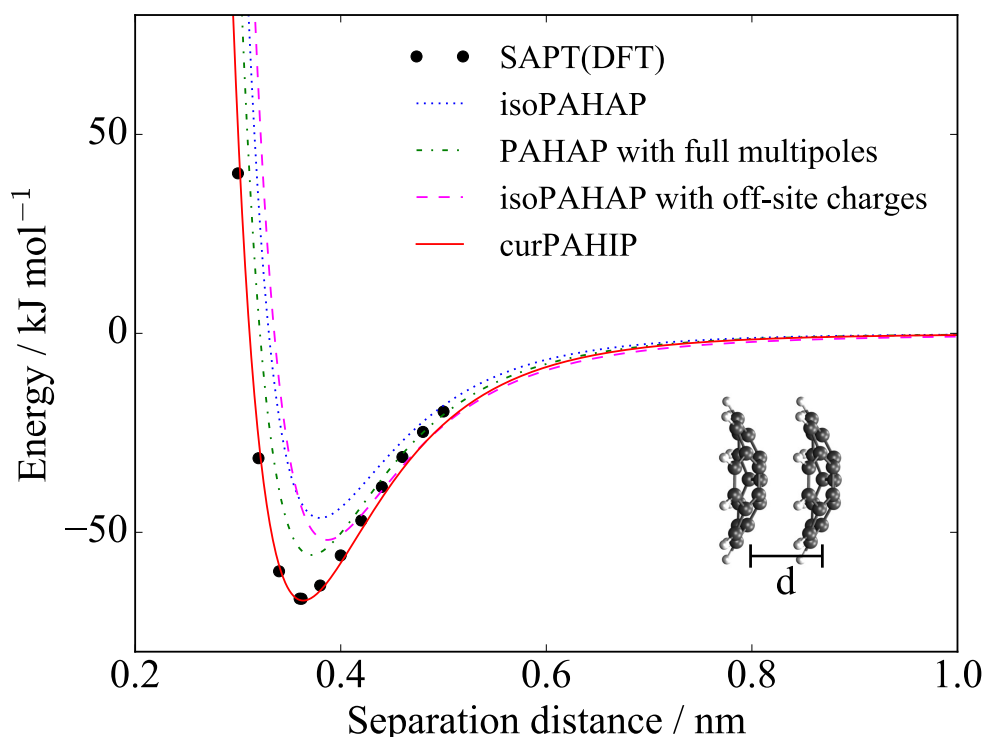
Figure 6.5 Intermolecular interactions between corannulene dimers using a range of different forcefields. With SAPT(DFT) calculations shown from [52]. Courtesy of Kimberly Bowal.

collision rate to provide insights into soot nucleation that occurs over microseconds, on the nanosecond simulation timescale as was employed previously by Totton et al. [419]. The NVT ensemble was ensured using a chain of Nosé-Hoover thermostats. Ewald summations were used to compute the periodic electrostatic interactions. Intramolecular interactions were described using the OPLS-AA forcefield [210]. The isoPAHAP and new curPAHIP forcefields were used to describe the intermolecular interactions between coronene and corannulene, respectively.

Figure 6.6 shows the molecular dynamics simulations at 500 K. Coronene and corannulene, both without ions, are found to cluster at similar rates. This was anticipated as coronene has a very similar interaction energy -65.7 kJ/mol compared with corannulene -65.9 kJ/mol. Addition of K^+ has little impact on the clustering of coronene as expected from the low charge-quadrupole interaction energies compared with the thermal energy. However, for corannulene a significant increase in the rate of cluster growth was observed. This was quantified as a collision efficiency using methodology developed previously [419]. At 500 K the collision efficiency of corannulene was doubled with the ions present, indicating that the strong, long-range ion-dipole interactions allow for more efficient cluster formation.
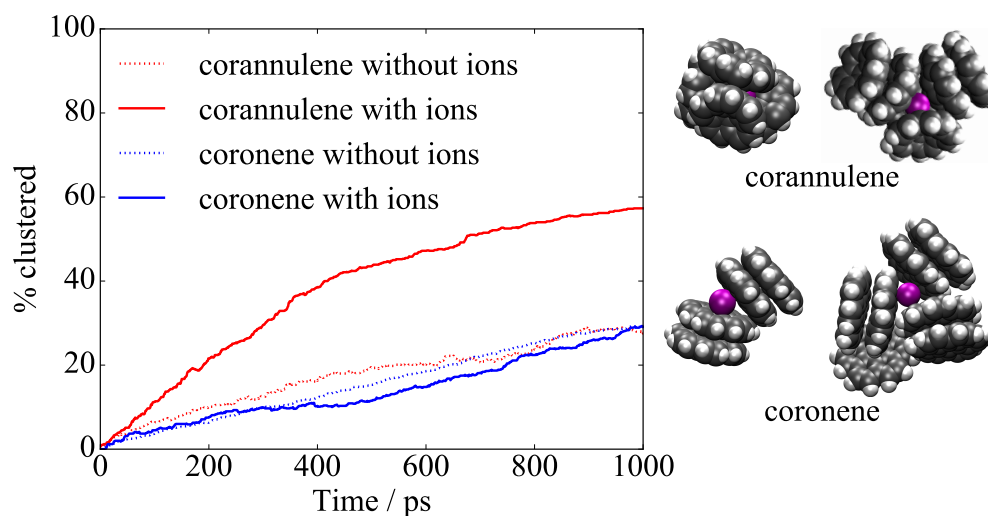
Figure 6.6 Percentage of clustered species in molecular dynamics simulations. Courtesy of Kimberly Bowal.

Clustering past 700 K was not possible for coronene or corannulene due to the low binding energy. Therefore, to explore whether ion-cPAH interactions could be stable at flame temperatures, calculations using cPAH of the size and curvature found in the flame are required.

6.2.2   Binding energy of cPAH with a flame chemi-ion

Binding energies between larger cPAH found in Chapter 5 and $C_3H_3^+$, the most abundant chemi-ions in sooting flames [171], were calculated using electronic structure theory. This assesses the possibility of an ion-induced nucleation occurring within the flame. For chemi-ions and curved PAHs to interact at flame temperatures where carbon nanoparticulates form (1300–1500 K) large intermolecular interaction energies are required to stabilise molecular clusters. For planar PAHs with 13–19 rings, Totton et al. [417] previously determined the dissociation energy required to stabilise clusters at these temperatures at $E_d = -140$– 180 kJ/mol (shown as the green range (i) in Figure 6.7e) [419]. The chemi-ion $C_3H_3^+$ is the most abundant cation in sooting flames and is a likely candidate for a nucleation centre in an ion-induced nucleation mechanism [171]. Chen and Wang recently used coupled cluster calculations to analyse the binding of $C_3H_3^+$ with planar PAHs [62]. They found that the stable configurations occurred when the cation bonded around the rim of the planar PAH, saturating for PAHs containing more than five aromatic rings at binding energies of

−60–112 kJ/mol (shown as the red range in Figure 6.7), which is insufficient to stabilise these complexes under flame-relevant temperatures.
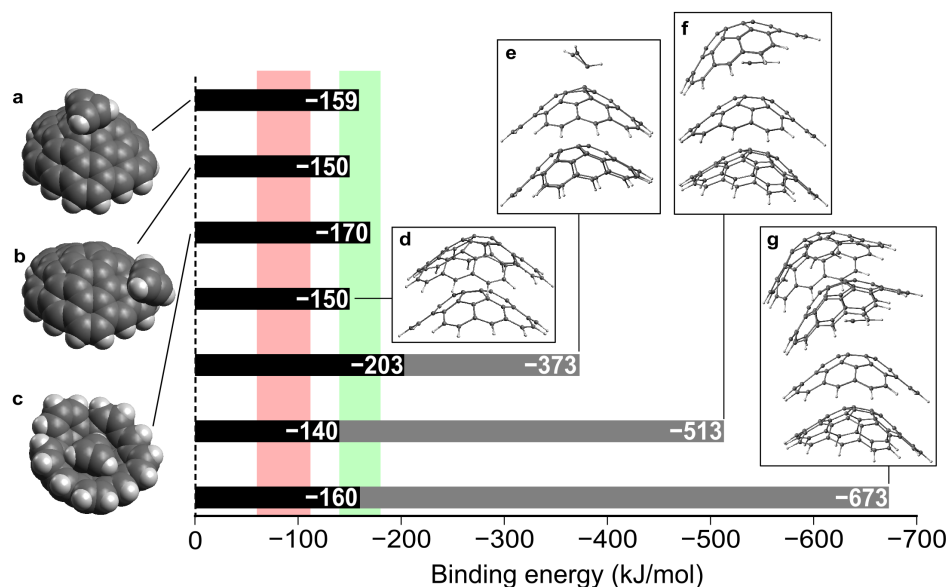
Figure 6.7 Binding energies for the cation-curved PAH complexes (black bar). The red region shows the range of binding energies calculated previously for planar PAHs binding to $C_3H_3^+$ [62]; the green shows the region of binding energies that were found to allow large planar PAHs to cluster at 1300–1500 K [419]. a-c) Optimised geometries of binding sites for the chemi-ion $C_3H_3^+$ on a large curved PAH. d) Geometries of the dimer of the curved PAH. e-f) Cluster geometries for the dimer, trimer and tetramer with the chemi-ion $C_3H_3^+$ (grey bars show complexes' total binding energies and black bars shows dissociation energy for a monomer).

The binding energies were computed between the curved PAH identified as a likely component in soot (Figure 6.7b) and $C_3H_3^+$ using hybrid density functional theory with a dispersion correction B97D/cc-pVTZ [155]. Figure 6.7a-c) shows the geometries of the three most stable binding sites of $C_3H_3^+$. A similar binding site to planar PAHs was found around the rim of the curved PAH, however, unlike the planar geometries, binding on the centre of the aromatic faces was stronger than on the rim. The binding site with the highest binding energy was found for the concave surface (Figure 6.7c), where the cupped geometry enhanced the dispersion interactions and the negative electric potential due to the π-orbitals. The binding site at the centre of the convex surface (Figure 6.7a) is dominated by the flexoelectric dipole-ion interaction: a classical electrostatic charge-dipole interaction at the intermolecular distance of 3 Å gives a similar binding energy of −171 kJ/mol using the dipole moment 5.32 D calculated earlier. Figure 6.7d shows the curved PAH homodimer

with an energy of $E_d = -150$ kJ/mol, which is comparable to a similarly sized planar PAH of -144 kJ/mol (interpolated from the Totton et al. benchmark calculations based on the number of carbon atoms [419]) indicating similar clustering behaviour to planar PAHs is expected for homogeneous nucleation of this curved PAH, as found earlier.

For larger clusters of the curved PAH stabilised by an ion, geometry optimisations were performed from different possible starting geometries to ensure stable energy minima were found for the dimer, trimer and tetramer (with the binding energies E_b shown in Figure 6.7 as grey bars). Unlike planar PAHs, which see a significant decrease in binding energy with a chemi-ion for subsequent additions after the dimer, the binding energies of clusters of curved PAHs stabilised with a chemi-ion continues to increase linearly towards that of the tetramer [62]. The stacking geometry of the curved PAH is stabilised by the dispersion and dipole-dipole interactions being further strengthened by the electrostatic and inductive interactions with the chemi-ion. The dissociation energies E_d were also computed as the energy required to remove a monomer from the complex (shown in Figure 6.7 as black bars). All of the dissociation energies calculated between the chemi-ion $C_3H_3^+$ with a representative polar curved PAH are found to be in the range to allow planar PAH to cluster at flame temperatures, suggesting these interactions play a role in stabilising carbon nanoparticulate nuclei.

6.3   Dynamic polarity of cPAH at flame temperatures

One significant issue raised at the 37th International Symposium on Combustion surrounding such an ionic route was how persistent the polarity of curved PAH is at the temperatures of sooting flames. Dynamic polarity presents two problems for interactions of cPAH with each other and chemi-ions: 1) Rapid inversions of cPAH would likely impede their ability to form a stably bound complex, 2) Fluctuations of the dipole moment at flame temperatures could mean that the dipole moment decreases, thereby preventing the formation of a bound cPAH cluster. The small cPAH corannulene is well known to rapidly invert at room temperature with an experimental inversion barrier of 10.2 kcal/mol [373] and 11.5 kcal/mol [375]. This barrier is significantly lower than that anticipated from the strain energy in corannulene 24 kcal/mol [406], which was explained by the planar transition state that increases π-electron delocalisation, decreasing the energy by 11 kcal/mol [101]. Soon after corannulene was found to invert rapidly at room temperature it was found that by addition of a single extra pentagonal ring about the rim the inversion barrier was doubled and the inversion was halted at room temperature [1]. Calculations of larger cPAH have found a non-planar S-shaped transition state with a considerable increase in the inversion barrier. The one-pentagon,

10-ring species gave an inversion barrier of 56 kcal/mol while the two-pentagon, >14 ring species gave an inversion barrier of >100 kcal/mol [451].

Figure 6.8 shows the curved PAHs chosen for this study, including corannulene, the smallest aromatic curved by pentagon integration. Molecules of the size seen in early soot particles (0.9–1.2 nm) were chosen; a fifteen-ring structure with a single pentagonal ring and a five-member bay site **2** were then considered as the same single pentagon-containing structure with the closure of the bay site (**3**), a two-pentagon-containing 15-ring cPAH (**4**) suggested from HRTEM imaging of early soot nanoparticles [269] and a three-pentagon-containing cPAH is also provided (**5**). For each of the largest cPAH hydrogen was added to/removed from the site specified to consider the effect of having a π-radical on the barrier and rate of inversion.

1   **2**   **3** (R = H$_2$)
3'(R = H)

4 (R = H)   **5** (R = H)
4'(R = H$_2$)   **5'**(R = H$_2$)
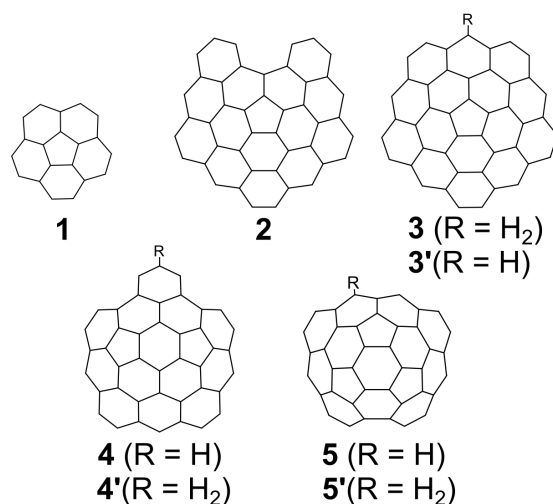
Figure 6.8 Curved PAH molecules chosen in this study with **3-5** chosen from a previous study [269].

The energies and frequencies of the minimum energy and transition state structures of the curved PAH were computed using the hybrid density functional theory B3LYP/6-311+G(d,p) level of theory. This has been found to correctly describe the equilibrium geometry of curved arenes compared with crystal structures and the inversion dynamics of these systems [451]. For all geometries located by DFT, the frequencies were checked to ensure the calculation had found the appropriate minima and transition states. To obtain a more accurate estimate of the energies of the minima and the transition state, single point energy calculations using the Minnesota hybrid density functional M06-2X/6-311g(d,p) were performed on the optimised geometries. This has been shown to give accurate energies for reactions involving PAH [188]. Energies are reported with the zero point energy correction included.

6.3.1 Inversion of curved PAH at flame temperatures/timescales

To introduce the inversion process the energies and geometries of the transition state for inversion of molecules are plotted **1**, **2** and **3** (Figure 6.9). For the smallest structure corannulene **1** the barrier is low, 11 kcal/mol, due to the planar transition state as discussed earlier. Enlarging the PAH so that it is similar in size to those found in soot (1 nm) increases the inversion barrier considerably, raising it to 59 kcal/mol. The transition state is still found to be planar for this geometry.
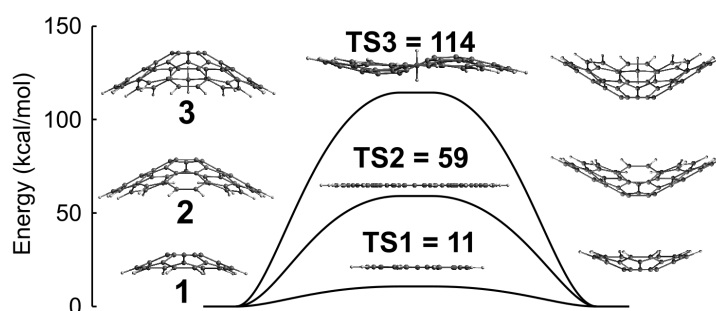
Figure 6.9 Energies and geometries of the inversion transition states.

Figure 6.10 shows the bond lengths of the equilibrium geometry and the transition state, which demonstrates the considerable strain in the system. The first thing noticed is the reduction in bond lengths at the pentagonal site which is due to the strain from the σ-bonding - skeleton strain. For the bay site, a considerable increase in the distance between the bay exterior carbons, 3.3 Å to 3.92 Å and a lengthening of the bonds around the bay site 1.5 Å to 1.58 Å was seen. This flattening expands the exterior rings and compresses the interior carbon network.

Closing the bay site of **2** to form species **3** gives rise to almost a doubling of the inversion barrier. Figure 6.9 shows the S-shaped transition state formed due to this bay closure. It is important to note that for the S-shaped transition state the inversion still involves all core carbon atoms flipping from one side to the other. Figure 6.11 shows the imaginary frequency associated with the planar transition state for **2** and the S-shaped transition state for **3**. The main difference in the transition state is the warped nature of **TS3**. This warping indicates the skeletal strain overcomes the π-bonding to produce the S-shape. This is similar to the interplay of curvature vs planarity with small pentagon-containing PAH found in Chapter 5.

Increasing the number of pentagons increases the barrier to inversion. Figure 6.12 shows the transition state energies and geometries for cPAH containing one (**3**), two (**4**) and three (**5**) pentagonal rings. A modest increase is seen between one and two pentagonal rings, 114
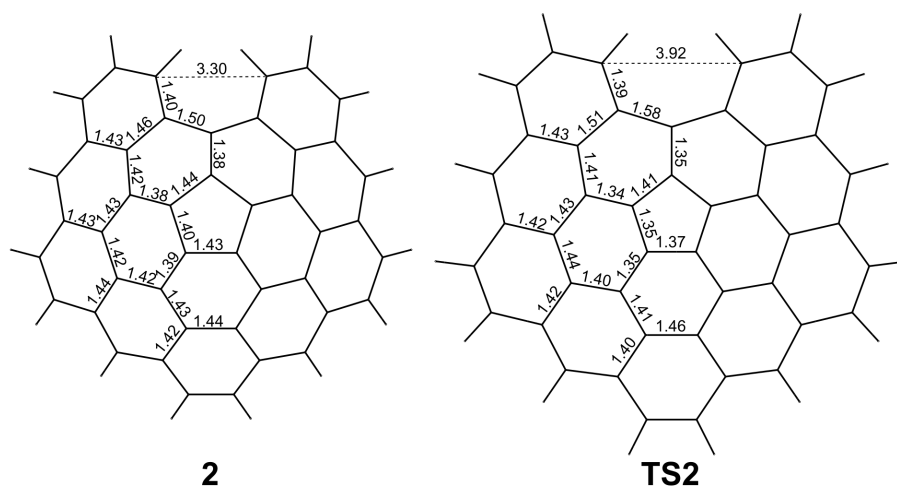
Figure 6.10 Geometries of molecule **2** at equilibrium and at the transition state **TS2**.
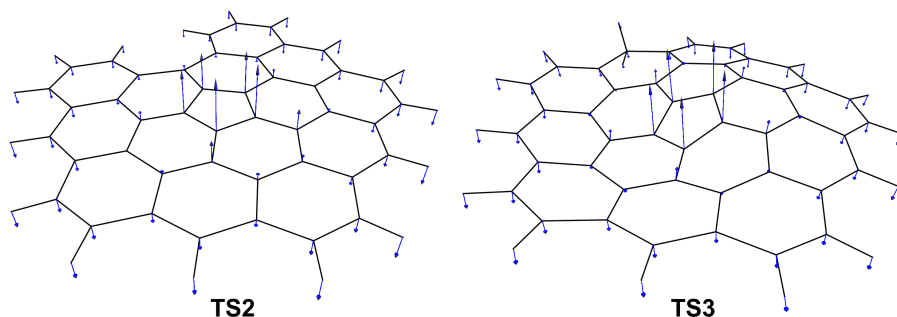
Figure 6.11 Molecular geometries with blue arrows indicating the relative amplitude and direction of the imaginary vibrations associated with the transition states of molecules **2** and **3**.

to 138 kcal/mol, respectively. Integration of three pentagonal rings significantly increases the inversion barrier with molecule **5** rising to 360 kcal/mol. The transition state geometries are heavily pyramidalised and warped with no internal carbon atoms being completely planar, thus significantly disrupting the π-bonding.

Minimal change in the inversion barrier is seen for the π-radicals compared with the closed shell species. In the case of **TS3'** an increase in the barrier to inversion was seen. This is thought to be due to the loss of hydrogen leading to an increased aromaticity and therefore stability of the transition state. This suggests that the aromaticity is less important than the skeletal σ strained carbon network at these transition states, with the π-radical not reducing the barrier for inversion. Little change is seen for the two-pentagon-containing molecule transition state **TS4/TS4'**. The most strained structure **5** has the most significant effect with the radical decreasing the barrier for inversion by 26 kcal/mol.
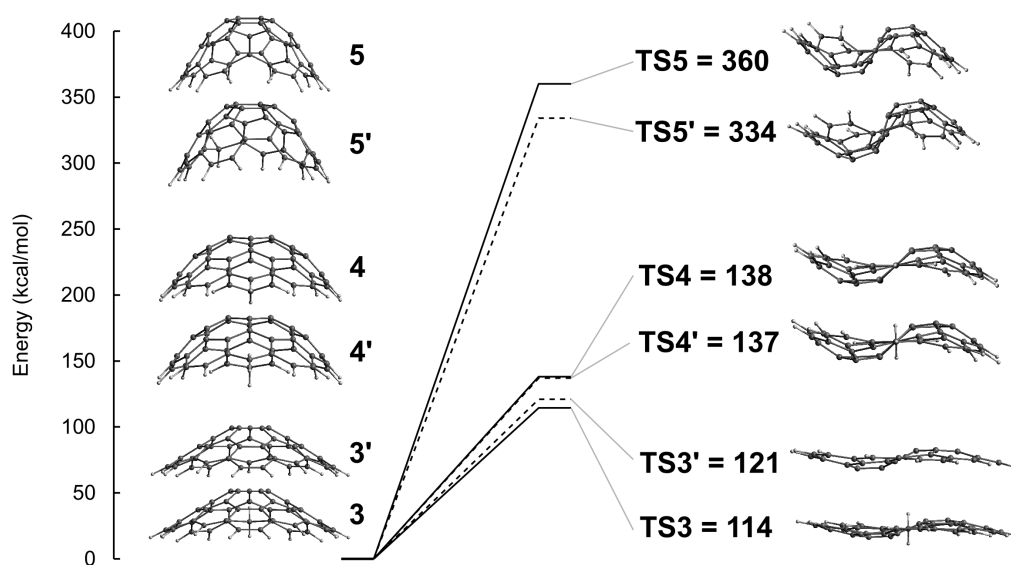
Figure 6.12 Inversion barriers and molecular geometries for molecules **3**, **4** and **5** as well as their π-radicals **3'**, **4'** and **5'** dashed line.

Colleagues Angiras Menon and Chung Lao then made use of these transition state geometries and frequencies to compute an inversion rate for the species in Figure 6.8. More details can be found in Martin et al. [273]. The reciprocal of the inversion rate constant is used, $1/k = \tau$, which can be thought of as a characteristic time for inversion. The characteristic time can be compared to the time scale of soot formation, which in a flame is from micro to millisecond [129]. Any characteristic time below a millisecond will then be important for soot formation and above this value minimal inversion can occur on the time scale of soot formation. Another distinction can be made considering the temperatures in the flame where soot forms, which are near 1500 K [438].

In order to extend the analysis to consider the onset of rigidity in smaller curved PAH the size dependency of the inversion was considered. This was achieved by using the exponential relationship between the characteristic time and the barrier for inversion calculated for the species in Figure 6.8. A barrier of 66.3 kcal/mol was found to provide a characteristic time of 1 millisecond at 1500 K. This allowed consideration of the inversion barriers previously calculated by others at similar levels of theory [34, 64] to provide a clear picture for when inversion will be halted at flame temperatures/timescales of interest. Figure 6.13 shows the inversion barrier for different species as a function of the total number of hexagonal and pentagonal rings. (From previous study of the integration of curvature in Chapter 5, internal pentagons were defined as being surrounded by 5 hexagonal rings and exterior pentagons as having >3 neighbouring hexagonal rings that are adjacent to each other.)
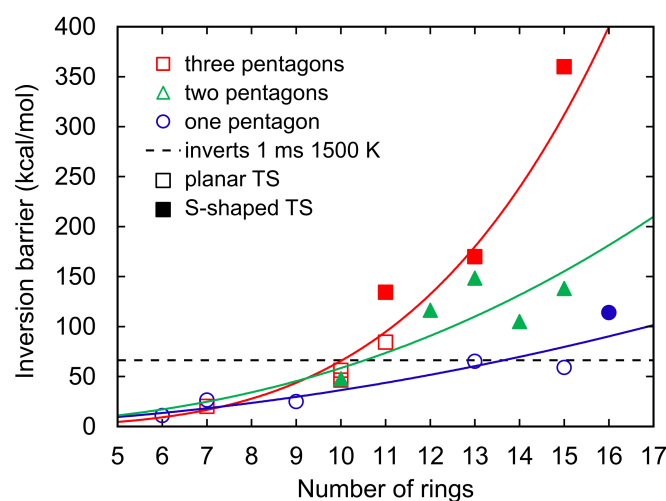
Figure 6.13 Inversion barrier as a function of the number of rings for structures in this work and from previously studied cPAH [34, 64]. The dashed line highlights the inversion barrier 66.3 kcal/mol which provides a characteristic time of 1 ms at 1500 K.

Three different size ranges were found for the inversion behaviour of pericondensed cPAH. For $6 \leq N_{rings} < 11$ inversion occurs rapidly at flame temperature. For $11 \leq N_{rings} \leq 15$ inversion does not occur during soot formation for species with ≥ 2 pentagonal rings but is possible for species containing a single pentagonal ring. For $15 < N_{rings}$ structures are stably curved during the entirety of soot formation.

A few conclusions may be drawn when considering the impact of inversion on soot formation. For small curved PAH the inversion is expected to be an important consideration with corannulene inverting rapidly, which will average out the flexoelectric dipolar effects. This is somewhat seen in the similar vapour pressure of perylene and corannulene [65]. Addition of rings increases the inversion barrier so that for the size of PAH seen in early soot particles the inversion is not rapid enough to be important at flame temperatures and timescales. The π-radical nature does not significantly lower the barrier for inversion, indicating the skeletal strain dictates the inversion dynamics.

Further work is needed to understand the rate of inversion of cPAH within clusters as barriers for inversion of cPAH have been found to decrease in the presence of a planar PAH [211, 94] or in different molecular environments [208]. These effects only operate for cPAH with planar transition states. It appears that the transition from planar to S-shaped transition states determines when the cPAH becomes rigid at flame temperatures. This can be seen in Figure 6.13 where the larger barriers for inversion are predominantly for those species with S-shaped transition states.

As it seems unlikely that inversion will occur for cPAH found in early soot particles, the suggestion of an interaction with a chemi-ion needs to be considered to see if it can catalyse an inversion. This will be considered for molecule **4** in the presence of $C_3H_3^+$. Figure 6.14 shows the barrier for inversion, which is lowest when going from the convex arrangement to the transition state **4+(**. The transition state energy barrier is similar, 140 kcal/mol, compared to without an ion, 138 kcal/mol, indicating the presence of the ion has a minimal effect on the inversion barrier and therefore the dynamics of the bowl.
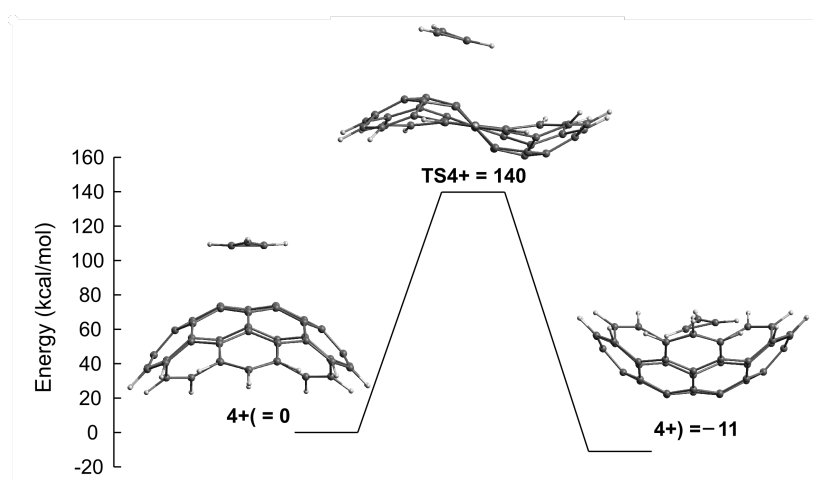
Figure 6.14 Barrier for inversion for molecule **4** in the presence of an ion.

In summary, cPAH of the size seen to cluster during soot formation are unable to invert at flame temperatures. Considering the previously mentioned molecular dynamics simulations, rigid corannulene clustering with ions is not well described as corannulene would be likely to invert rapidly. However, these results are considered to be representative for non-inverting larger cPAH.

6.3.2 Fluctuations of the dipole moment

In order to consider the fluctuations of the dipole moment of a cPAH at temperatures in the flame where soot inception occurs, AIMD simulations were performed. Due to the expense of the calculations a chemi-ion was included. This allows for insight into the impact of the cPAH flexoelectric dipole at high temperatures and as the inversion dynamics are minimally impacted by the chemi-ion the cPAH fluctuations can be considered independent. The chemi-ion was placed on the top surface of the bowl as this is the expected binding site for an ion approaching from a large distance with the flexoelectric dipole aligning to interact with the positive charge. The simulation was run for half a picosecond in order for

the thermal energy to equilibrate and stabilise after which the dynamics of the molecule in Figure 6.14 with the chemi-ion $C_3H_3^+$, **4+(**, were followed over 2 ps.

For the AIMD simulation a more economical level of theory was used, B97D/6-31G(d). The hybrid density functional theory with dispersion correction B97D [155] has performed well compared with benchmark coupled cluster calculations for cation-benzene clusters and dimers of corannulene (error <1 kcal/mol B97D/cc-pVTZ) [201, 297, 270]. For the molecular system **4** a dipole moment of 5.00 D was calculated, which is slightly under (<4%) the value calculated at a higher level of theory, 5.32 D. A binding energy of 40.9 kcal/mol was calculated, which is larger than that calculated at a higher level of theory (B97D/cc-pVTZ = 38.1 kcal/mol) but should provide preliminary insight into the dynamics of the system. In simulating the $C_3H_3^+$ -**4** system little impact of the fictitious mass on the energetics was found, as noted by others [366] and therefore the default mass of 100 amu was used. A timestep of 0.1 fs was used to ensure energy conservation during the simulation. No angular momentum was added to the system to provide a better understanding of the vibrational degrees of freedom. Gaussian 16 was used for the AIMD calculations performed [135].

Figure 6.15a shows the trajectory of the atomic positions over the first picosecond. When looking at the cPAH fluctuations, it is clear that the carbon atoms near the middle of the aromatic plane have a reduced range of motion compared to the atoms around the rim of the cPAH.

The main low frequency vibrations observed were bending mode vibrations where the edge warps. This bending mode occurred with a frequency of 250–350 fs. The local flexoelectric dipole moment changed with this vibration. Instead of calculating the dipole moment at every time step, which would have been prohibitively slow, geometries were chosen over one of these bending modes and single point energy calculations performed of the cPAH only (Figure 6.15b). The dipole moment at this level of theory is 5.00 D and therefore was found to fluctuate by ± 0.5–1.0 D, ± 10–20%. This analysis shows that at temperatures in the flame where soot forms, large cPAH have a persistent polarity that does not decrease substantially during thermal excitation.

The movement of the chemi-ion was then considered in the presence of the cPAH. While the ground state equilibrium geometry shows a binding site above the pyramidalised carbon atoms the chemi-ion was found to move freely across the surface from the middle/hub to the edge of the bowl. Figure 6.15a shows the chemi-ion trapped at the rim of the cPAH for the first picosecond. From the electrostatics, the edge binding can be explained by the charge concentration at the edge of the PAH due to the induced dipole on the rim carbon atom caused by the C–H bond. The binding at the pyramidalised atoms is due to the flexoelectric dipole moment [267]. The binding of the chemi-ion does not appear to be influenced strongly
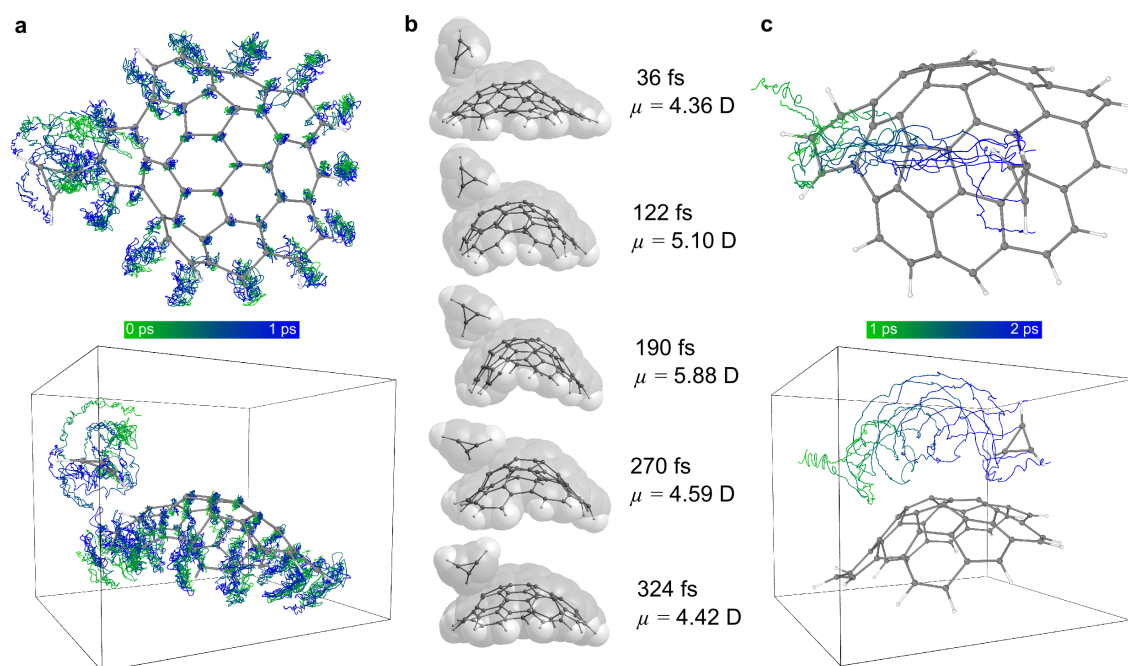
Figure 6.15 Dynamics of molecule **4+(**. a) Dynamics of the complex over the first picosecond shown with a line at each atom with the geometry at 1 ps shown with a ball and stick model. b) Fluctuation of the bowl during a low frequency bending mode vibration. The dipole moment is also calculated for the bowl fragment. c) Dynamics of the complex over the second picosecond with the geometry shown with the ball and stick model for the final structure at 2 ps.

by the bending mode of the cPAH as seen in Figure 6.15b. Figure 6.15c shows the movement of the chemi-ion across the top surface of the cPAH, where the flexoelectric effect is greatest.

Further work is required on the dynamics of cPAH ion systems. Only one cPAH chemi-ion pair is considered, however there are innumerable other combinations, some of which are worth considering in detail, such as the CHO^+ cPAH combination and other, smaller cPAH. The main conclusions about dipole fluctuations found for molecule **4** hold for all cPAH with a large inversion barrier (>66 kcal/mol). For another ionic interaction CHO^+ has the potential to interact more strongly than $C_3H_3^+$ [62]. This study of chemi-ion-cPAH interactions does not capture long term dynamics for accurate statistics of the chemi-ion-cPAH system and less costly descriptions to study this clustering behaviour are being developed. The impact of rotational degrees of freedom in order for the cPAH fluctuations to be more clearly observed were not considered, but this is expected to improve the binding tendencies as studies have previously found for planar PAH homodimers [369, 449]. The movement of the chemi-ion across the surface of the bowl and rim provides an opportunity for reactions with the rim carbon atoms [62]. These reactions would provide positively charged PAH which have been

observed previously using mass spectrometry [186]. The clustering behaviour of cPAH$^+$ with other cPAH is also worth considering in future work.

In summary, it has been demonstrated that cPAH of the size found in early soot particles (1 nm in diameter with ≥ 2 pentagonal rings) are unable to invert and are persistently polar at flame temperatures. The transition from easily inverted to being rigid at 1500 K for cPAH was found to be between 11 and 15 rings and often corresponded to a S-shaped transition state that is not stabilised by an increased aromaticity as with the planar transition state. π-radicals and chemi-ions were not found to influence the inversion barrier substantially with the number of pentagonal rings and total rings being of primary importance. *Ab initio* MD was used to study the fluctuation of the dipole moment for molecule **4** at flame temperatures. The dipole moment was found to fluctuate on the timescale of the bending mode of the bowl, ≈ 300 fs, by ± 10-20%. Some brief dynamics of the chemi-ion cPAH system were considered with the chemi-ion found to interact with the pentagonal atoms with a flexoelectric effect as well as the rim due to charge concentration around the rim.

6.4 Role of cPAH in physical mechanisms for soot formation

The role of cPAH and chemi-ions in physical nucleation will be discussed given the results in this chapter. The similar intermolecular interactions between flat and curved PAH of the size found to cluster in flames (≈ 500 Da) means they will be unable to form a supersaturated vapour at flame temperatures. Classical nucleation theory with ions, as discussed in Chapter 2.1.2, suggests a small ionic cluster, n_{min} (see Figure 2.5), can exist even below the supersaturation point of the vapour given sufficiently strong interactions. Interpreting the experimental results for the positive ion mass spectrometry particle mode at 3×10^3 Da [24] suggests ion-induced nuclei are present. The mass suggests four to six cPAH molecules (depending on a mass of 700 or 500 Da, respectively) would be required to form this mode. This size is approximately what one would expect to be the limit for ion-dipole interactions being able to overcome the thermal energy at flame temperatures. This could explain why experimentally this mode does not appear to grow past 10^4 Da, however, more work is required to confirm such a hypothesis. The lack of this mode in benzene flames is also puzzling. This could be due to a more efficient chemical mechanism that results in insufficient concentration of free cPAH in the gas phase to form ionic clusters. This fact and the ability of soot to be formed in pyrolysis reactors without chemi-ions present suggests that physical and electrical interactions are insufficient by themselves to explain the formation of soot. However, the

molecular dynamics simulations demonstrated an increased collision efficiency which could aid in species being close enough to form chemical crosslinks.

In conclusion, the binding energy between homodimers was used to compare the homogeneous nucleation of cPAH to fPAH. Similar interaction energies were found between cPAH with one to two embedded pentagonal rings and fPAH. For three or more pentagonal rings, significant steric effects reduce the dispersion interaction to be less than that of a similar sized fPAH. These results suggest homogeneous nucleation of curved PAH found in the flame of mass $\sim$500 Da is not possible. Heterogeneous nucleation of cPAH on ions was then considered. A new forcefield, curPAHIP, was developed to describe the electrostatics of corannulene and molecular dynamics simulations were undertaken. A significant effect was found for corannulene clustering in the presence of ions with a doubling of the collision efficiency compared with coronene. For larger cPAH present in flames electronic structure calculations were undertaken between a representative curved PAH and the flame ion $C_3H_3^+$. Binding energies suggest that strong interactions are possible for small clusters that could be stable at flame temperatures. The persistence of polarity at flame temperatures was then explored with the barrier for inversion and some AIMD simulations. Inversion energies suggested species found to cluster in the flame, $\approx$500 Da, are unable to invert during the soot formation process. In quantum molecular dynamics simulations the dipole moment was found to change on the timescale of the bending mode of the bowl, $\approx$300 fs, by $\pm$10-20%. Some brief dynamics of the chemi-ion cPAH system were considered with the chemi-ion found to interact with the pentagonal atoms (due to the flexoelectric effect), as well as the rim (due to charge concentration around the rim). When it comes to electrical nucleation, it is suggested that ions are able to stabilise clusters of $<$10 cPAH in number due to the short range of the ion-dipole interactions but cannot explain, generally, the formation of soot.

Chapter 7

Reactivity of cPAH and aromatic radicals
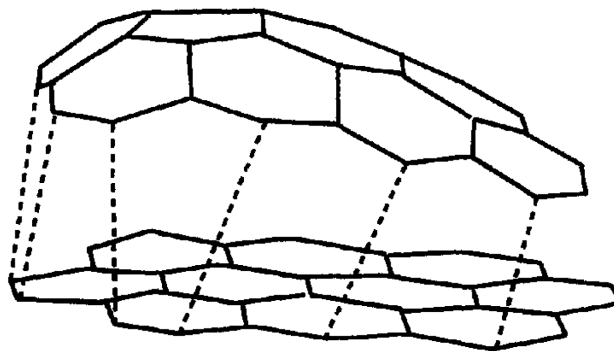
Fig. 13. Model of the formation of five- and six-membered rings through the connection of two PAHs by the zipper mechanism.

Fullerenes and their ions in hydrocarbon flames [5] (1994) - Credit: Elsevier © (used with permission)

> *"Once coagulated they will quickly become chemically knit together since a significant fraction of the aromatic species are radicals."*
>   – Stephen Harris and Anita Weiner, A picture of soot particle inception (1989), Symposium (International) on Combustion 22, 333-342

> The work in this section was published as a paper in *The Journal of Physical Chemistry C* in collaboration with a group at the University of Cambridge and Tsinghua University. Contributions from the team include benchmarked calculations for H-abstraction from Ms Hou; Mr Menon helped to perform the M06-2X-D3 calculations for the bond dissociation energies and the other authors edited the manuscript. The calculations of the reactivity, interpretation, analysis and writing were performed by the author.

In this chapter, the reactivity of curved and planar aromatics is investigated to explore chemical mechanisms for soot formation. The reactivity of various aromatic soot precursors is quantified and compared using electronic structure calculations. Reactive sites are then bonded systematically to explore the strength of bonds between various crosslinked reactive sites. A combination of covalent and physical interactions are then explored for localised π-radicals showing a new type of rim-bonding. Finally, the role of these reactive sites is discussed in the context of chemical mechanisms for soot formation.

Reactive aromatic species have long been thought to contribute to soot inception [353, 170]. These species can be grouped into either open shell radical species or closed shell aromatic species. The former are significantly more reactive but present in lower concentrations, and the latter less reactive and present in higher concentrations. Therefore, reactions between radical species and closed shell species are often the focus of soot mechanisms. Beginning with the radicals, the most reactive species is generated by hydrogen being abstracted from the rim of aromatics by collision with gas phase radicals, forming highly reactive aromatic carbon σ-radicals [188]. This provides the reactive site for acetylene addition and extension of the aromatic network through the well known hydrogen abstraction acetylene addition (HACA) growth mechanism [132, 129]. Radicals can also arise in the π-bonding network if there is an odd number of π-electrons. These π-radicals can be stabilised due to delocalisation, providing long-lived resonantly stabilised radicals (RSR), although these have reduced reactivity. They are critical for the formation of the first aromatic ring [164] and have long been suggested to be present in aromatic species, indicated by the odd-numbered carbon species measured using flame mass spectrometry [213]. High-resolution atomic force microscopy (HR-AFM) and photoionisation mass spectrometry (PIMS) have also recently confirmed the presence of RSR [371, 204]. It was suggested that these react with carbon aryl-type σ-radicals leading to a chemical polymerisation that did not require subsequent hydrogen abstraction [204]. However, Keller et al. [213] found that for PAH with molecular mass greater than 400 Da odd-numbered carbon fragments in mass spectrometry were of similar concentration to closed shell, even-numbered carbon fragments, suggesting that the

larger RSR lose their reactivity. Evidence has also been found for a π-radical that arises from a partially protonated rim-based pentagonal ring, which has unknown reactivity [371].

The aromatic σ- and π-radicals have also been suggested to react with closed shell species that possess significantly electrophilic sites such as double or triple bonds. This is well illustrated by the reaction between the aromatic σ-radical with the acetylene triple bond, which is critical for the HACA mechanism, but is not rapid enough alone to explain soot formation [129]. Benzene and high symmetry aromatic species are strongly aromatically stabilised leading to aromatic bonds with low reactivity compared with double bonded carbon. However, in many low symmetry polycyclic aromatic hydrocarbons, some rings possess a reduced aromaticity. Well known examples are the 9,10-free edge of phenanthrene and pyrene, which is more vulnerable to electrophilic or free radical attack [72]. Rim-based pentagonal rings have also been observed and shown to be thermally stable [398, 189]. 5-membered rings are not aromatically stabilised and thus provide a free edge with double-bond character and significant reactivity. These low aromaticity free edges have been suggested to react with carbon σ-radicals, forming nanoparticles in the flame through the aromatic aliphatically linked hydrocarbon (AALH) mechanism [85, 430]. Evidence for this growth mode has been shown by mass spectrometry of benzene-oxygen flames where high radical concentrations allow for significant carbon σ-radical concentrations [430]. Partial integration of the pentagonal ring within the hexagonal network has been directly imaged [78] and provides edges with greater reactivity, with HACA growth on the 5-membered bay site found to proceed rapidly [336]. Fully integrated pentagonal rings curve the aromatic network and have been experimentally observed [239, 268]. This curvature leads to a reduced aromaticity [101] due to reduced π-overlap on pyramidalised carbon atoms. This has been shown to increase the edge oxidation reactivity [402, 338] and speed up HACA growth on an armchair edge of hexagonal rings [336], as has been discussed. The presence of these reactive aromatics leads to a number of questions: how does the reactivity of different sites compare? How thermally stable are the crosslinks formed between these sites?

The proposed chemical inception mechanisms involving reactive aromatics proposed to date are not fast enough to explain the experimental observations [438]. Physical condensation, however, is rapid enough to explain soot formation, but lacks strong enough intermolecular interactions [129]. Direct evidence for physical dimerisation has been found using photoionisation mass spectrometry of species sampled from the flame, revealing a series of peaked distributions separated by approximately 500 Da (without any change in the C/H ratio, which would imply a chemical reaction) [165, 57]. Laser induced fluorescence (LIF) experiments have provided evidence for π-stacked aromatics that are able to form an excited excimer state [288]. Time resolved LIF has shown this signal to be long-lived,

providing further evidence for the stacked excimer hypothesis [391, 282]. However, van der Waals or physical dispersion interactions are not sufficient to allow the 500 Da aromatic species (as commonly found in flames) to cluster at temperatures in the flame where soot forms, 1500–2000 K [419]. Previous authors have suggested a combination of covalent bonding and physical interactions to explain the rapid condensation [170, 287, 219]. A recent electron spin resonance study found a significant change in the radical character when soot growth begins [433]. The authors suggested a combination of physical stacking interactions and covalent bonding between π-radicals such as pancake bonds (multicentre π-bonds) [215] to explain this experimental feature. This poses a further question: can a combination of physical interaction and covalent bonding explain the rapid growth of soot?

In this chapter, the location of reactive sites are determined and compared using the average local ionisation potential. The energies of the bonds formed between the different site types is then systematically calculated revealing possible covalent bonding options. Finally, physically and covalently bonded structures are computed revealing the possibility of π-radical pancake and rim-based complexes.

7.1 Locating and quantifying reactivity

As mentioned reactive aromatics have been recently imaged and a wide variety of new edges found [371, 78]. In this section electronic structure calculations will allow for a coherent quantification and comparison between these molecules. For the aromatic complexes, as mentioned, the dispersion corrected B97 hybrid density functional theory performs well for geometries and electrostatics describing the dipole moment of curved arenes [154, 266]. A variety of geometry optimisations were performed for each edge couple to determine the lowest energy isomer. The B97D/cc-pVTZ level of theory was used in order to ensure minimal basis set superposition errors ($<$2 kcal/mol) as the bonded and stacked geometries were unable to be counterpoise corrected.

The average local ionisation potential is used to locate reactive sites and compare their propensity to electrophilic attack by, for example, carbon radicals [393] and is computed as,

$$\bar{I}(\mathbf{r}) = \sum_i^{N_{occ}} \frac{\rho_i(\mathbf{r})|\varepsilon_i|}{\rho_{tot}(\mathbf{r})}, \tag{7.1}$$

where ρ_i is the electron density of the i-th molecular orbital at the point $\mathbf{r}$, ε_i is the orbital energy and $\rho_{tot}(\mathbf{r})$ is the total electron density at the point $\mathbf{r}$ where the sum is over the N_{occ} occupied molecule orbitals. $\bar{I}(\mathbf{r})$ is then a local measure of the energy required to ionise an electron from a certain point in space and therefore a lower value indicates a

higher reactivity to electrophiles such as radicals. The Fukui function $f^-(\mathbf{r})$ has also been used to compute the reactivity of sites towards radicals in the context of soot [461]. $f^-(\mathbf{r})$ requires that the electron density of the ionised molecule be computed and the difference taken with the molecule in its standard state. This is often approximated with the highest occupied molecular orbital (HOMO) but for larger aromatics with many low lying occupied molecular orbitals that could also contribute, i.e. HOMO-1, HOMO-2 etc. this is not possible. Therefore, two calculations would be required to compute $f^-(\mathbf{r})$. The average local ionisation potential and the Fukui functions are formally related in the local density approximation as $\bar{I}(\mathbf{r}) = \sum_i |\varepsilon_i| f_i(\mathbf{r})$, where the index is over the i-th occupied molecular orbitals, indicating they will both provide the most electrophilic site [414]. The advantage of using $\bar{I}(\mathbf{r})$ is that only a single electronic structure is required as it considers ionisation from all of the occupied MO while also providing a convenient comparison across our molecular series due to the the multiplication with the orbital energies. Multiwfn 3.3.9 was used to compute the average local ionisation potential on the isosurface 0.002 atomic units (a.u.) of the electron density (near the van der Waals surface) computed from the electronic structure calculations [258]. Spin population isosurfaces for the resonantly stabilised radicals were also prepared using the same software. In the context of aromatic species, $\bar{I}(\mathbf{r})$ has been found to accurately predict the sites most reactive to electrophilic attack of hydrogen radicals [49]. We can then suggest that $\min_r[\bar{I}(\mathbf{r})]$ is appropriate for comparison between the different radical and closed shell species' reactivity. For ease of reading, the minimum in the average local ionisation of the site $\min_r[\bar{I}(\mathbf{r})]$ this will be simply referred to it as $\bar{I}_S$.

Figure 7.1 shows the average local ionisation potential calculated on the molecular surface for aromatic species ordered by their $\bar{I}_S$. This serves two main purposes: classification and ordering of the different radicals and closed shell species, as well as an understanding of the location of the potential reactive sites that are capable of crosslinking reactions, which will be explored in the next section.

For the closed shell species the ordering can also be discussed according to the $\bar{I}_S$. Partially embedded cyclopentaphenathrene type pentagonal rings **D)** possess the lowest $\bar{I}_S$ site with values $\bar{I}_S = 7.28 - 7.41$ eV. The lowest $\bar{I}_S$ are concentrated on the aromatic face on the pentagonal's edge, with the pentagonal ring being partially embedded with three bond-sharing hexagonal rings. This non-aromatic site has been observed in HR-AFM and is an intermediate towards completely curved species [371]. Other partially embedded pentagonal rings were explored such as fluoranthene or benzo[ghi]pyrene type but these were found to have $\bar{I}_S$ matching that of low-aromaticity free edges shown in the scheme below.
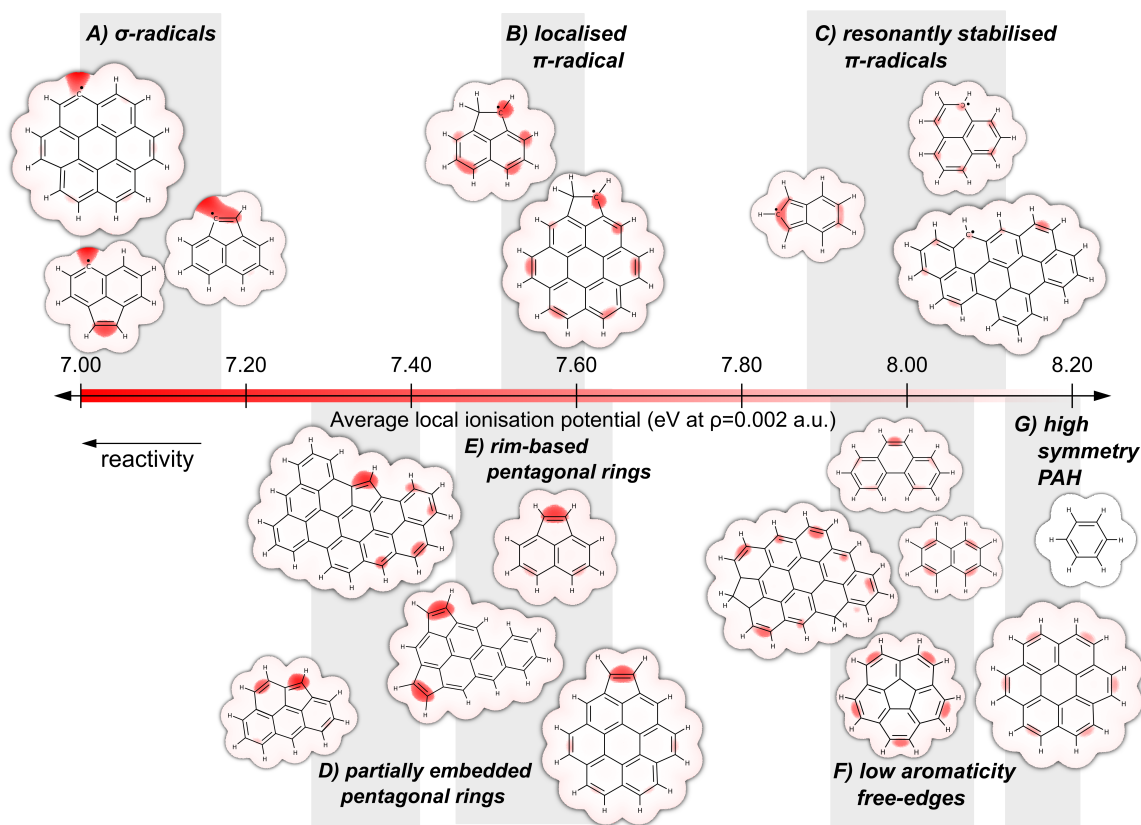
Figure 7.1 The average localised ionisation potential is plotted on the molecular surface produced from the electron density at the isovalue $\rho = 0.002$ a.u. (B97D/6-311G(d,p)) for a variety of aromatic species. Inset shows one of the possible Kekulé structures.
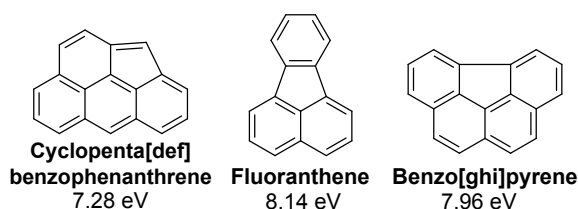
This indicates that aromaticity is lowest for the cyclopentaphenathrene type edges. This could explain why this site type is most often seen to be methylated like fluorene, having two hydrogens bonded to this edge carbon [78].

Rim-based pentagonal rings **E)** possess values of $\bar{I}_S = 7.45 - 7.64$ eV. The minima is concentrated on the edge carbon atoms of the pentagonal ring. In this case only two neighbouring bonds are shared with the hexagonal aromatic rings and due to the antiaromatic pentagonal ring the $\bar{I}$ indicates a free edge with a double-bond character. There is little effect due to system size and many of these sites can be present on a single aromatic. Experimentally this was found to be one of the most common edge types [78].

Low aromaticity free edges **F)** possess values of $\bar{I}_S = 7.91 - 8.08$ eV. These arise in hexagonal aromatic networks due to the topology of the network. Clar provided a framework for describing these low-aromaticity edges [72, 19]. The maximum number of sextets are placed within the network with double bonds placed elsewhere. The symmetrically equivalent arrangements of sextets (denoted by a circle within the ring) and double bonds are then considered to be in resonance. The edge sites where double bonds are prevalent in the resonance structures are found to be reactive. This is shown in the scheme below.

Naphthalene   Phenanthrene   Corannulene
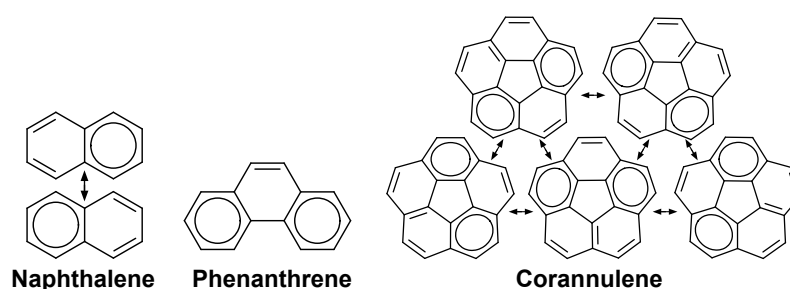
Naphthalene contains a single sextet that is in resonance (otherwise known as a travelling sextet). This allows for the free edges to possess a double-bond character with an increased reactivity. Phenanthrene is an example of a molecule with a single Clar structure with two sextets leaving the 9,10-free edge with a significant double bond character and higher reactivity than the rings with the sextets [72]. Corannulene can have two sextets and five resonance structures [19]. This provides low-aromaticity free edges with double-bond character. These Clar descriptions match with the sites with low $\bar{I}_S$ and with the reactivity trends for these species [72]. Corannulene has an added reduction in aromaticity due to the pyramidalisation of the carbon network as others have shown [101]. This might explain the lower $\bar{I}_S$ compared with phenanthrene or naphthalene found for corannulene. Another cause of low aromaticity edges was methylation of hexagonal aromatic edge sites. In the Clar framework this is due to the reduction in the number of sextets that can be placed. Finally, high symmetry PAH **G)** such as benzene or coronene are found to possess the highest $\bar{I}_S$ value of all of the closed shell edges with values $\bar{I}_S = 8.12 - 8.21$ eV. The symmetry of these species being close to circular in extent provide highly pericondensed networks with high aromaticity and no low aromaticity free edges.

Turning now to the radicals, the site of lowest $\bar{I}_S$ was found to be the σ-radical **A)** with minimum values from 7.00–7.17 eV. The reactive site minima lies on the edge of the aromatic, parallel to the carbon–hydrogen bonds. Little difference was found from the rim-based pentagon σ-radical compared with the hexagonal ring based one. This reactive site is known to react with acetylene readily and drives the growth of the aromatic network.

The next lowest $\bar{I}_S$ is the localised π-radical **B)** with minimum values from 7.51–7.61 eV. The minima in both cases lies on the rim-based pentagonal carbon atom with a single hydrogen attached. Unlike the σ-radical the $\bar{I}_S$ is on the face of the aromatic plane. There are also regions of low $\bar{I}$ around the rim, which have similar values to the low aromaticity free edges (and will be discussed later), indicating this site can modify the other edge sites on the same molecule.

In order to determine the localisation of this radical two partially saturated pentagonal rings were added to a 7-ring aromatic coronene (Figure 7.2a). The triplet with two free electrons (a diradical) was found to be significantly more stable (-24.3 kcal/mol) compared to the singlet. If the radical was able to delocalise, the diradical would provide a stable singlet spin configuration across the aromatic network. However, as the triplet dominates it can be confirmed that thbe radical is indeed localised to the pentagonal ring and that multiple localised π-radicals could be formed on a single aromatic with the low $\bar{I}_S = 7.54$ eV preserved as shown in Figure 7.2a.
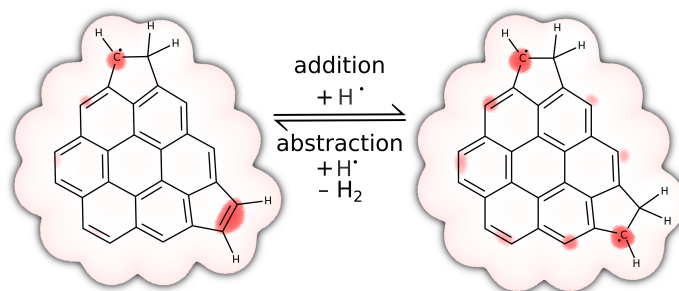
(a) Mechanism for forming two **B)** edge types showing the two independent localised π-radicals.
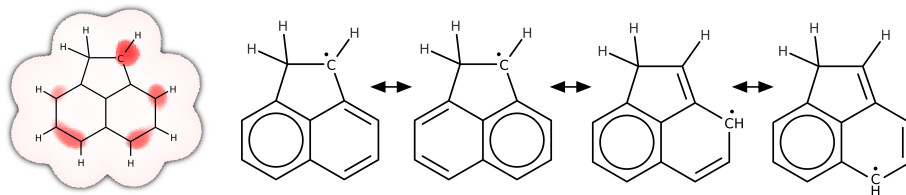
(b) Clar analysis.

Figure 7.2 $\bar{I}(\mathbf{r})$ surface plotted as in Figure 7.1 for the partially hydrogenated edges of type **B)**.

To understand why the radical is localised a Clar analysis is insightful (Figure 7.2b). Considering the average local ionisation potential three major and one minor Clar structures can be drawn. The first two resonance structures have a sextet on the hexagonal rings with the radical localised to the pentagonal ring. The third resonance structure has the radical on the aromatic ring, i.e. the β-position from the pentagonal site. The fourth minor resonance structure has the radical on the left-hand aromatic ring but does not appear to contribute

significantly to the $\bar{I}(\mathbf{r})$. Similar patterns in the $\bar{I}(\mathbf{r})$ are also found for the larger species in Figure 7.2a where the radical site only appears to be delocalised to the β-position relative the pentagonal site. It can therefore be suggested that the radical is localised in order to keep the high aromaticity of the 6-membered ring network.

The radical with the highest $\bar{I}_S$ was found to be the resonantly stabilised π-radical RSR C) with $\bar{I}_S = 7.88 - 8.12$ eV. These arise from an odd number of π-electrons in an aromatic network providing a radical stabilised by delocalisation. The smallest species indenyl was found to have the lowest $\bar{I}_S$ value (7.88 eV) concentrated on the surface of the pentagonal ring while for increasing size the value drops to 8.12 eV and is concentrated on the face of the aromatic on the zig zag edge sites. This reduction will be explored later as it will impact the reactivity of the RSR as they enlarge and the radical becomes more resonantly stabilised.

The reactive edges have been described and grouped. Importantly, the location of reactive sites has been found allowing for potential crosslinks between these reactive sites to be explored on a smaller subset of edges in the following section.

7.2   Crosslinking reactions between reactive aromatics

In order to compare the reactivity of a variety of edge types only the first bond formed between a series of small species was computed for a number of reasons. Firstly, the formation of the first bond will provide insight into the edge site reactivity and provide further evidence for the reactivity ordering predicted from $\bar{I}_S$. Secondly, the first bond is important for the crosslinking reaction as the reaction is not entropically favoured, due to the reduction in number of species, and therefore the energy of the first bond directly corresponds to the likelihood for the reaction to proceed. Thirdly, molecular beam mass spectrometry shows that the clustering process, in low pressure flames, does not involve crosslinking reactions with dehydrogenation but a constant C/H ratio [165, 57]. Finally, any aliphatic bridges with methyl or longer aliphatics that have recently been observed in specific inverse diffusion flames were not included [2]. These would modify the C/H ratio and therefore would represent a different growth mode than what is being focused on in this chapter. Furthermore, in premixed flames these aliphatic bridges would be prone to radical-induced fragmentation, just as the fuel is. Therefore, our search was restricted to crosslinks that do not modify the C/H ratio and have been seen in aromatics directly imaged using HR-AFM [78].

The bond dissociation energies were calculated from a homolytic bond cleavage using single point energies calculated using the dispersion corrected hybrid density functional M06-2X-D3/cc-pVTZ, which uses the same dispersion correction that was added to the B97D functional but provides significantly better bond energies, as will be detailed in the

next section. The van der Waals complexes were compared with reference SAPT(DFT) calculations [419] and found the DFT calculations to overestimate the binding energy by -6 ± 1 kcal/mol.

Figure 7.3 shows the matrix of bond energies between the species containing different edge types ordered by their bond energy with the σ-radical. A general trend was found where edge sites with low $\bar{I}_S$ produced more stable bonds compared with high $\bar{I}_S$ (as seen in the inset graph). However, steric effects also contribute to these bond energies leading to slightly different orderings compared with $\bar{I}_S$ values. The site with the lowest $\bar{I}_S$ or its neighbour was always found to be the most reactive. Bond energies can be compared to the bond enthalpy benchmark values (NIST thermodynamic database) as the thermal correction is minimal <1 kcal/mol. The biphenyl C–C bond has a benchmark value of -117.6 kcal/mol [421], using our methodology provided a value of -119.4 kcal/mol, showing a slight overestimation of the bond energy (+1.5%). Therefore, these values should be viewed within this error providing a comparative look at the reactivity of the different edge sites. To consider the flame stability of bonded species a comparison with other species is helpful. The thermal energy necessary for homolytic bond cleavage can be approximated as $6RT$ ($3/2RT$ for the translational and $3/2RT$ for rotational degrees of freedom for each species), which is 17 kcal/mol at 1500 K and 24 kcal/mol at 2000 K. However, to be persistently stable at flame temperatures larger bond energies have been found to be needed. The primary fragmentation pathway for fuels is radical induced fragmentation, such as β-scission, where the β site can have bond energies of -30 to -40 kcal/mol that readily break at flame temperatures [339]. For the physical dimerisation of flat PAH, a full statistical approach revealed a binding energy of < -40 kcal/mol was required for clustering above 1500 K [438]. Single bonds C–H and C–C in benzene and aliphatics have bond dissociation energies of -113 and -90 kcal/mol, respectively, and require high temperatures for unimolecular decomposition (>2000 K). Anything below -40 kcal/mol was considered to be of interest for soot formation and any above -10 kcal/mol not considered of interest for forming any thermally stable bond.

The most significant bond energies are formed with σ-radicals **A)**, as shown by the first and second row of the grid in Figure 7.1. The bond energies follow the ordering suggested from $\bar{I}(\mathbf{r})$ for the radicals. The strongest bonds are formed with other sigma radicals with < -120 kcal/mol these bond energies are lower than single bond energies (-90 kcal/mol) indicating that these species are significantly conjugated and stabilised by delocalisation. In another publication we have demonstrated that crosslinking between two aromatics leads to a drop in the band gap [281]. The bond energy between two pentagonal ring σ-radicals **Ai)** is particularly interesting as the minimum energy isomer is planar, providing the greatest amount of delocalisation and the highest bond energy. Being planar, this crosslink would
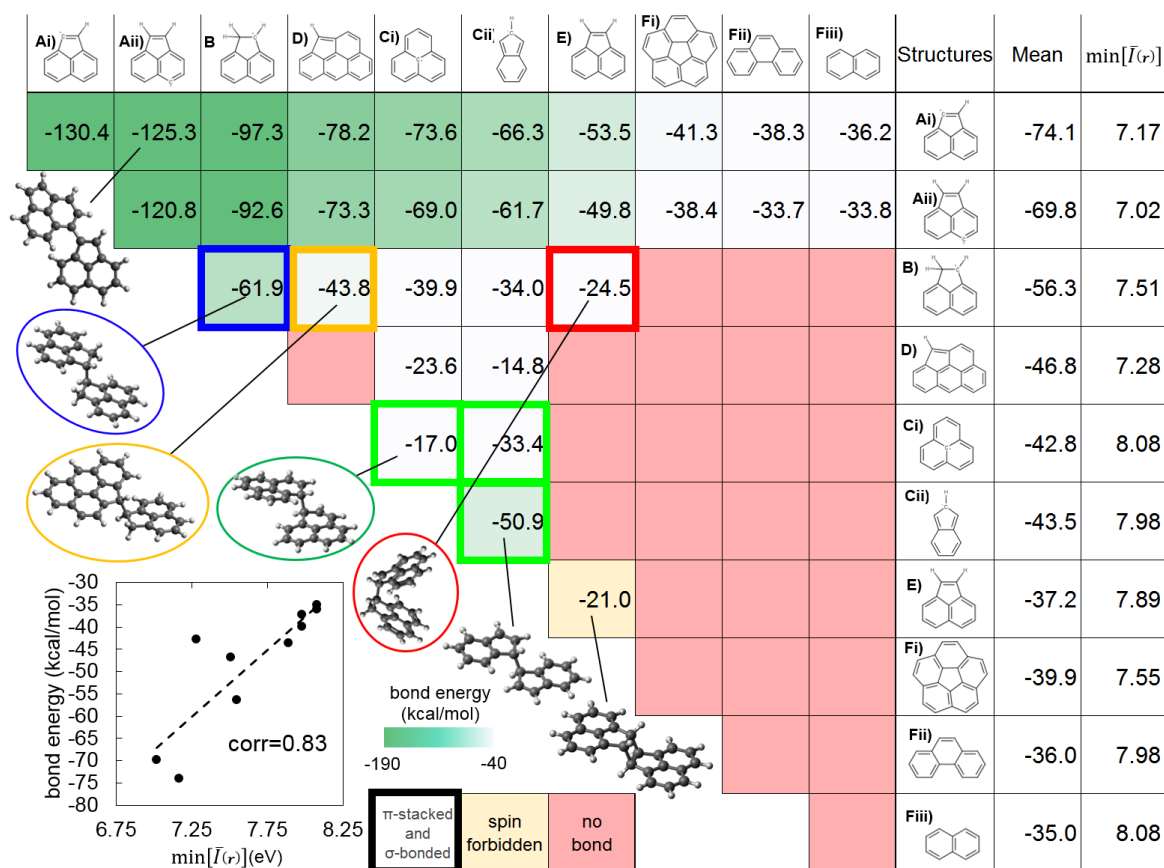
Figure 7.3 The bond energies (kcal/mol) between different species representing edge types shown in Figure 7.1. Inset graph shows the correlation between the bond energies and the $\bar{I}_S$ and a selection of geometries.

also allow for more effective van der Waals clustering. These σ-radical σ-radical crosslinks would be long-lived in the flame based on these calculated bond energies. However, the low concentration of radicals makes this mechanism possible only in systems with many aromatic radicals such as the pyrolysis of PAHs [293]. The next strongest crosslinks with **A)** are localised π-radicals **B)** with bond energies indicating single C–C bond formation between these edge types. Subsequent hydrogen abstraction could provide an **Ai) + Ai)** bond type which, as mentioned, is favourable for clustering. The partially embedded pentagonal ring **D)** also reacts readily with this site forming bonds of strong energy (< -73 kcal/mol). The concentration of this site in flame aromatics is unknown and will likely be considerable given its possible equilibrium with hydrogen radicals and the methylated version as shown in Figure 7.2a. Resonantly stabilised radicals follow with bond energies of < -61 kcal/mol. One question surrounding this crosslink is how the bond energy varies with the size of the RSR as mentioned by Homann [213]. Computing the bond energies of site **Aii)** with the

small RSR indenyl **Cii)** through to a 10-ring RSR species (shown in Figure 7.5). The bond energy had a mean value of -65.9 ± 2.8 kcal/mol with no significant decrease with system size. This indicates that while the bond energies with RSR are lower than a single bond, they do not vary greatly and that upon reaction with a σ-radical the π-radical is localised to form a bond. Calculations have shown that hydrogen can be easily lost from the RSR, reforming the radical and leading to potential chain reactions [204]. However, the concentration of RSR in the flame needs to be determined to see how common these reactions could be. The presence of odd-numbered carbon species is not sufficient to establish an RSR due to the hydrogenation of the edge as has been demonstrated in HR-AFM recently, i.e. species with an odd number of carbon atoms that are protonated can become closed shell species [78].

The reaction between a rim-based pentagonal ring **E)** and **A)** is the first step detailed in the AALH mechanism [85, 430] and provides bond energies < -50 kcal/mol. For the curved aromatics with low aromaticity free edges **Fi)**, bonds formed with **A)** species were found to be at the threshold of what is stable at flame temperature while crosslinks with phenanthrene **Fii)** and naphthalene **Fiii)** did not provide stable bonds at flame temperatures. The mechanisms including σ-radicals often require crosslinking followed by a hydrogen abstraction or loss to transform a weakened bonded structure into an **A) + A)** type crosslink. These mechanisms require a large number of σ-radicals and hydrogen radicals to allow for chemical polymerisations. However, in most atmospheric flames clustering occurs with a constant C/H ratio indicating chemical polymerisation is not occurring. While this is the case, crosslinking of σ-radicals providing strong bonds with energies < -40 kcal/mol is found to be possible with edge types **Fi)**, **E)**, **C)**, **D)** and **B)**.

After the σ-radicals, the π-radicals are found to also form strong bonds with themselves and some high reactivity closed shell species edges. Localised π-radicals on rim-based pentagons **B)**, row three of the table in Figure 7.3, show high reactivity, forming bonds with themselves of energy -62 kcal/mol. Bonds with **D)** type edges are found to provide bonds below -40 kcal/mol while bonds with **C)** and **E)** type edges are above this threshold. Of particular interest are the bonds formed with the rim-based pentagonal rings **E)** as these closed shell species are prevalent in the flame. The RSR radicals are found to form weak bonds with themselves and with the partially embedded pentagonal rings and no stable bonds with the rim-based pentagonal rings **E)** were found to be possible. The exception is the small indenyl species, which forms a strong bond with itself **Cii) + Cii)** showing that reactivity between RSR decreases with the size of the species as indicated from the $\bar{I}_S$.

Finally, rim-based pentagonal rings **E)** were found to form a weak bond with themselves, which is unlikely to be of interest. This [2+2] pericyclic reaction is not thermally allowed and requires optical excitation to form due to symmetry restrictions [361]. The band gap for

these species was found to be between 3.6–3.7 eV ($\approx$350 nm deep UV) [281]. These high energy photons are not prevalent in flames indicating this bond is unlikely to form in the flame. The bond energy is also very low suggesting rapid fragmentation. Santos et al. have previously experimentally and computationally shown that the energetics of acenaphthylene dimerisation is not possible above 550 K [361], further supporting the weak nature of these bonds.

In summary, from this systematic study, only σ-radicals **A)** and localised π-radicals **B)** were found to be capable of forming strong enough bonds to be long-lived in the flame. However, the π-radicals being able to bond on the aromatic face hold the possibility of combined physically held and covalently bound configurations.

7.3 Combining stacking and covalent bonding

As mentioned, physical dispersion forces are insufficient to stably bind clusters of small aromatic species at flame temperatures [438, 419] and so covalently stabilised π-stacked structures are sought. The σ-radicals are unable to accomplish this feat as the reactive radical site points outwards from the aromatic ring, making bonding only achievable parallel to the aromatic planes, which will not allow for π-stacking. The thick bordered entries in the matrix of Figure 7.3 show the reactive edges were able to covalently bond as well as π-stack. These binding energies will be compared with van der Waals interactions and the unstrained covalent bonds i.e. the energies of the covalent bond when there is no stacking from Figure 7.3.

Figure 7.4 shows the binding energy and molecular geometries of the reactive dimerisations for their average monomer mass. For comparison, physical dimerisation due to dispersion or van der Waals interactions have also been computed (black dashed lines). The benchmark SAPT(DFT) calculations are also shown from previous works, which have been found to accurately predict the virial coefficient of benzene and the exfoliation energy of graphite (solid black lines) [418]. From this an overbinding of nonbonded planar aromatics by the hybrid density functional method M06-2X-D3 was seen, which has previously been seen for these empirically corrected DFT methods. Given that this overbinding is linear in molecular mass, this allows for the enhancement $\Delta E = E_{VdW} - E_{C+VdW}$ due to any covalent interactions, E_{C+VdW}, to be determined compared to the van der Waals dimers E_{VdW} calculated with the dispersion corrected DFT for an equivalent mass monomer (blue and green arrows in Figure 7.4).

Figure 7.4a insets show the single bonds formed between the species and demonstrate, in the case of the localised π-bonds (**B**), how rotation about the single bond does not impact the
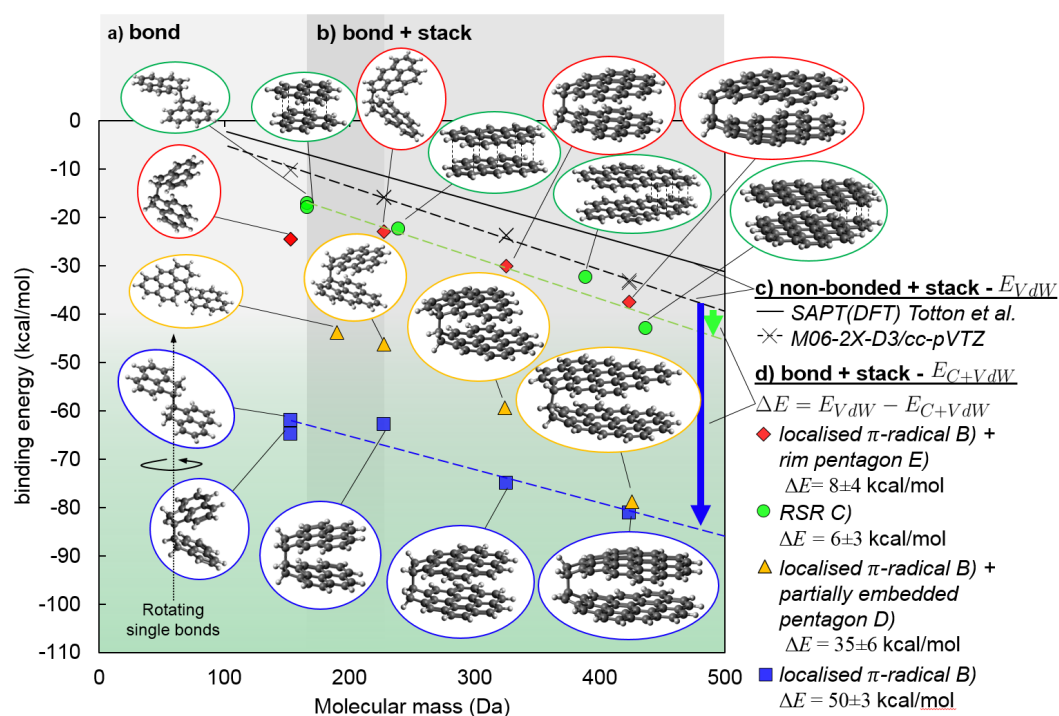
Figure 7.4 a) Binding energy (kcal/mol) as a function of molecular mass of the monomers (Da) is shown for different covalently bonded structures from Figure 7.3. b) Bonded and stacked geometries are found for enlarged monomers. c) Binding energy solely from van der Waals interactions E_{VdW} is also shown for comparison with the method chosen compared with our reference calculations from Totton et al. [419]. d) The bonding enhancement compared with the non-bonded case ΔE is also shown.

binding energy of these species. Figure 7.4b shows how as the molecular mass increases this binding is enhanced by van der Waals interactions either by maintaining a rim-based bond across the fragments, in the case of **B)** type edges, or through multicentre π-bonds, in the case of RSR **C)**.

The localised π-radicals **B)** are found to most strongly bind with themselves, having an enhancement of some $\Delta E = 50 \pm 4$ kcal/mol. This is allowed for by the minimal strain in going from the tetrahedrally oriented species to the π-stacked configuration due to the ability of the saturated pentagonal ring hydrogens to be placed far from each other. These edges also form strong bonds with partially embedded pentagonal rings **D)** with an enhancement of $\Delta E = 35 \pm 6$ kcal/mol. The reaction of **B)** with the rim-based pentagonal ring **E)** provided a minor enhancement of $\Delta E = 8 \pm 4$ kcal/mol. This might be explained by the low initial bond energy in the unstacked configuration. When stacked the added strain provides reduced bond energies.

Resonantly stabilised π-radicals are able to form multicentre π-bonds – a so-called "pancake bond" – and have been suggested to stabilise clustering aromatics [433]. Enhancements of $\Delta E = 6 \pm 3$ kcal/mol were found compared with non-bonded configurations indicating a minor increase in binding energy. This is comparable to binding energies previously computed [215]. It was found that for the most stable isomers the multicentre bond was not
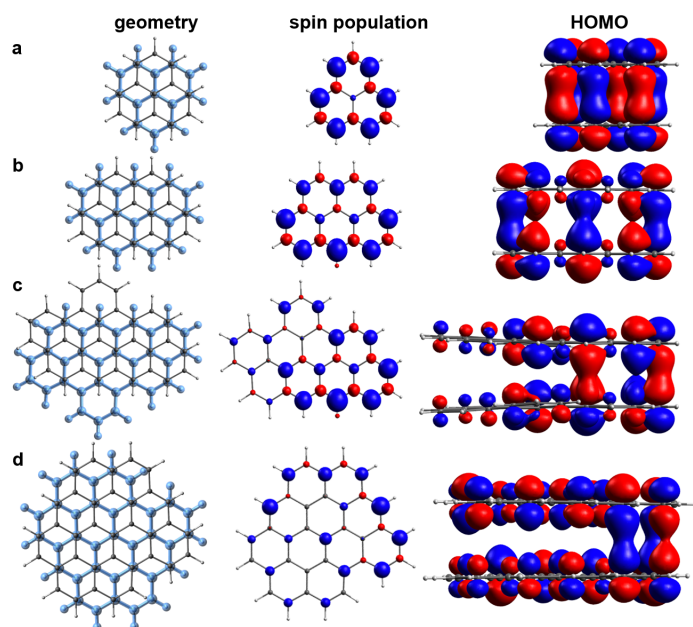
Figure 7.5 a-d) Dimer geometries, spin population at $iso = 0.003$ a.u. and HOMO at $iso = 0.025$ a.u. for a selection of RSRs showing the localisation of the radical on the most triangulene-like edge.

formed across the entire molecule but was partially localised to the most triangulene-like part of the fragment. This is illustrated in Figure 7.5 where its orientation, spin population and HOMO are plotted for four of the RSR molecules. From the pancake bonding molecular orbital it can be seen that the multicentre bond is concentrated on one end of the dimer. This can be geometrically measured in the optimised structures where the region of bonding possesses a lower interlayer distance of 3.38 Å compared with the opposing edge of 3.7 Å. This can be understood from examining the spin population indicating that the π-radical is concentrated on the most triangulene-like region of the molecule from where it forms the multicentre bond.

In summary, π-radicals can allow for rim-bonding and multicentre pancake bonds with the former providing sufficiently strong bonds to be of importance at flame temperatures.

7.4   Role of curved and reactive PAH in chemical mechanisms for soot formation

The role of reactive PAH in chemical inception will be discussed given the results from this chapter. Firstly, σ-radicals present crosslinks with the most significant bond energies. These cover mechanisms that have previously been proposed, for example Howard in 1991, described that as the PAH grow many aryl σ-radicals are formed on each, which then react into **A)**–**A)** structures [189]. Rim-based pentagonal rings **E)** crosslinking with σ-radicals **A)** followed by hydrogen abstraction to form **A)**–**A)** structures is called the aromatic aliphatically-linked hydrocarbons (AALH) mechanism. Another mechanism suggested has been σ-radicals crosslinked with RSR (delocalised π-radicals) **C)** formed via the radical-chain reactions (CHRCR) mechanism [204]. However, new possible crosslinks were found such as those with cPAH **Fi)** or localised π-radicals **B)**. Therefore, a more coherent naming strategy can be suggested based on the different crosslinks that are possible, see Figure 7.6.

Mechanistically, however, these aryl-linked pathways have been questioned as to whether the crosslinks can form fast enough even with a significant concentration of aryl radicals. Reactive molecular dynamics showed an order of magnitude lower collision efficiency than what is required to form nanoparticles at the rate required for soot nucleation [263]. There is also the possibility of radical-induced fragmentation leading to crosslinked species becoming hydrogenated and breaking down. Given kinetic Monte Carlo schemes and more complete understandings of PAH growth mechanisms the feasibility of the σ-radical reactions will be able to be deduced and the comparative impact of cPAH reacting with these radicals understood.

Figure 7.6 Proposed naming strategy for reactive crosslinking reactions in chemical mechanisms for soot formation. Based on Figure 7.3.

Pathways involving π-radicals are of considerable interest because they can involve physical condensation and then chemical crosslinking. This covalently stabilised soot nucleation mechanism (sticking coefficients of unity) has been found to be computationally useful for modelling soot nucleation [170, 287, 219]. In particular, the ability of multiple localised π-radicals to be formed on a single aromatic suggests that the rim-based pentagonal ring, in partial equilibrium with hydrogen radicals in the flame (as shown in Figure 7.2a), could provide a constant supply of reactive sites to polymerise into soot. Another interesting question is how stable the crosslinks will be, given radical-induced fragmentation. Physical interactions could aid in keeping the molecule bound after radical production from collision with gas-phase radicals, which would provide greater stability than aryl-type crosslinks. Curved PAH with these reactive sites will be attracted to chemi-ions in the flame and could also electrostatically aid in the seeding of soot particles that then grow through a chemical reaction. The ionic physical interactions would therefore be dependent on chemical growth mechanisms as has been experimentally found [121]. This will require a more detailed mechanism than can be generated from electronic structure calculations alone as physical condensation and chemical bond formation must be considered concurrently – reactive molecular dynamics may be a possible solution.

These covalently bound complexes could also allow for the fluorescence signal to be explained. Recent calculations by Krueger and Blanquart of stacked aromatics sp^3 bonded through aliphatics showed that these long-lived excimer states can indeed exist in stacked and bonded complexes [235]. Therefore, it is anticipated that the localised π-radical **B)** bonded

complexes will possess a fluorescence signal. For the pancake bonded complexes, however, it is unclear whether an excimer state would be bound given that the $\pi \to \pi^*$ transition would be expected to lead to a breaking of the pancake bond. Pancake bonds are also highly phase dependent, breaking if they are rotated by $30°$ [79], further casting doubt on whether they could be stable at flame temperatures.

In conclusion, the average local ionisation potential was used to explore the reactivity of a variety of edge types that have been recently directly imaged in aromatic soot precursors. The radical sites and closed shell edge types were characterised with seven reactive edge types, which were detailed and compared. The location of reactive sites also allowed for a systematic study of the bond energies between different covalently crosslinked reactive edge types. σ-radicals were found to form strong bonds with curved PAH low aromaticity free edges **Fi)**, rim-based pentagonal ring free edges **E)**, resonantly stabilised radicals **C)**, partially embedded pentagonal ring edges **D)** and localised π-radicals on partially saturated rim-based pentagonal rings **B)**, indicating the importance of such crosslinks in certain flame types. π-radicals possess lower covalent bond energies, however, they were found to allow for stacked and bonded configurations, significantly enhancing the interaction energy as the monomers' mass increased. Localised π-radicals **B)** are suggested to be important due to their significant binding energy and the potential to rapidly generate them via protonation of abundant rim-based pentagonal rings. More work is required to determine the thermal stability of these covalently stabilised stacked complexes and to establish the concentration of each edge type within sooting flames. However, it was demonstrated that covalent bonds and stacked configurations are not necessarily mutually exclusive and that strongly bound complexes of interest to soot formation can be formed.

Chapter 8

Curvature in thermally annealed soot

Rosalind Franklin (1950) - Credit: National Portrait Gallery, London ©

"It remains to consider by what mechanism the crystallites continue to grow,
both in breadth and height, once the non-organized carbon has been consumed."
    – Rosalind Franklin, Crystallite growth in graphitizing and non-graphitizing carbons
(1951), Proceedings of the Royal Society of London A

The work in this section was published as a paper in the journal *Physical Review Letters* in collaboration with a group at the University of Cambridge and Curtin University. Contributions from the team included nanostructures provided by Dr Marks, Dr Suarez-Martinez and Dr de Tomas from previous publications with the other author editing the manuscript. Dr Wells, Hughes Hall, Cambridge also contributed to helpful discussions on differential topology. The calculations of the angular defect, the rendering of the structures, observation of defects, analysis and writing were performed by the author.

In this chapter, the nanostructure of thermally annealed soot and other non-graphitising materials is explored. Curved ribbons are found to develop during carbonisation and graphitisation inhibiting alignment of aromatic planes required for complete conversion to graphite. A new mesh-based approach was developed to analyse a set of nanocarbon models that reproduce the experimental textures. The overall Gauss curvature was found to be negative for these networks and layered ribbon regions arise due to screw dislocations. Finally, implications for such a nanostructure in relation to preparing carbon materials and soot oxidation are briefly discussed.

In Section 2.2.2 the non-graphitising class of carbon materials was described. The various textures that have been observed were also detailed. Despite the evidence for all of these nanostructural textures, it is not clear how to combine the various structural elements into a coherent 3D model. In this chapter, this problem is approached by making use of a suite of recently constructed 3D graphene networks that provide an excellent representation of nanoporous and glassy carbons. Using a surface mesh approach, the geometry of the networks was analysed and the global Gaussian curvature extracted, a quantity which has not previously been considered for carbon networks. This analysis allows for two key questions to be addressed: to what degree does each texture contribute to the curvature of these networks, and how do these textures coexist?

The 3D graphene networks had been previously reported by the Carbon Group at Curtin University and were generated via self-assembly of carbon atoms using an annealed molecular dynamics methodology [91]. The models span a density range from 0.5 to 1.5 g/cc. Containing around 32,000 atoms, the structures were large enough to contain all of the textures of non-graphitising carbons, including ribbons, micropores, fullerene-like curvature and schwarzite-like curvature. Extensive characterisation agreed well with experimental data, such as HRTEM, X-ray and neutron diffraction scattering, electron energy loss spectroscopy, pore-size distributions, mechanical properties and thermal conductivity [403, 89–91].
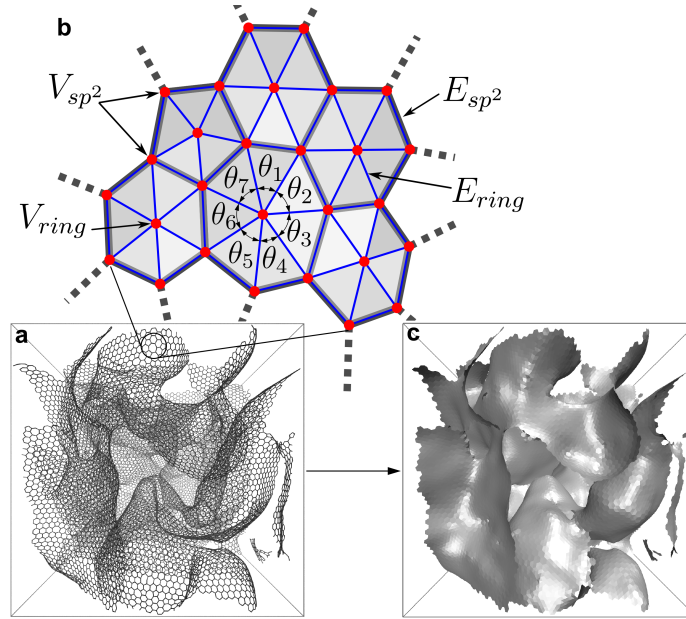
Figure 8.1 a) Periodic disordered carbon network. b) Enlarged region of the network showing the construction of the triangular mesh: vertices (red dots) are placed on sp^2 atomic sites (V_{sp^2}) and at the centre of each polyaromatic ring (V_{rings}); vertices are connected via edges (blue lines) overlapping atomic bonds (E_{sp^2}) and linking the centre of each ring to its vertices (E_{ring}). The angles around one vertex are shown for the computation of the angular defect. c) Surface mesh resulting from the procedure.

8.1 Angular defect for measuring local curvature

The standard approach to probe the topology of disordered graphene networks used ring statistics [412, 95, 91]. An excess of pentagons over heptagons gives a net positive curvature, as in fullerenes, and an excess of heptagons and octagons over pentagons gives negative curvature, as in schwarzites. As mentioned rings are related to connectivity according to the well-known Euler-Poincaré polyhedral equation 2.58. However, Eq. 2.58 does not hold for disordered carbon structures as the networks are not purely sp^2-bonded.

An approach was developed that allowed the curvature to be determined within a disordered carbon network. The first step involves the construction of a triangular mesh from the ring network. In Figure 8.1a one of the graphene networks is shown (0.5 g/cc), with an enlarged region in Figure 8.1b illustrating the mesh construction. The Franzblau algorithm [127] was used to locate rings up to octagons, as larger rings are found to be associated with non-sp^2 vacancies. A vertex is placed at the geometric centre of each ring, V_{ring} and at each atomic site in the rings, V_{sp^2}. These vertices are then joined by edges to the adjacent carbon atoms, E_{sp^2} and to the ring vertices, E_{ring}. This mesh provides a unique surface

or graph, $G = \left\{ V_{sp^2}, V_{ring}, E_{sp^2}, E_{ring} \right\}$, as shown in Figure 8.1c. The angular defect, δ, is defined as the difference between the sum of m angles, θ_i, around each vertex, as shown in Figure 8.1b,

$$\delta = 2\pi - \sum_{i=1}^{m} \theta_i. \tag{8.1}$$

This means that a vertex on a plane has an angular sum of 2π giving $\delta = 0$, while a vertex at a bowl-shaped region has an angular sum less than 2π giving $\delta > 0$ and for saddle-shaped vertices $\delta < 0$. Thus δ gives the sign of the Gaussian curvature for these triangular meshes [40]. The angular defect is not computed at vertices at the perimeter/edge (sp-bonded carbons) or tetrahedral carbon atoms (sp^3-bonded carbons), providing insight into the local curvature of the sp^2 surfaces.

8.2   Curvature in disordered 3D graphenes

Figure 8.2 shows a subset of the analysed networks. At the lowest densities, significant porosity and no stacking of layers is observed, while above 0.9 g/cc stacks of at least three graphene layers appear. Figure 8.2a-d shows non-hexagonal rings coloured by cycle number n: blue pentagons, red heptagons and yellow octagons. These rings form chains known as line dislocations or grain boundaries of alternating pentagons and heptagons, which have been imaged in 2D polycrystalline graphenes [458] and 3D porous carbons [159]. When these dislocations arrange into closed loops with equal numbers of 5- and 7-membered rings they cancel any net global curvature and allow for 2D connectivity. Both closed and open loops have been identified in these networks, as observed in the Figure 8.2a, with a predominance of open loops and isolated non-hexagonal rings. While the closed loops gives rise to planar regions, open loops and isolated non-hexagonal rings are identified in regions of local positive and negative Gaussian curvature. However as mentioned, non-hexagonal rings counting will not suffice for determining the global curvature in these disordered 3D networks.

Computing the angular defects on each network surface, as shown in Figure 8.2e-h, reveals regions of both saddle-shaped topology in red and bowl-shaped topology in blue. Visual examination of the structures confirms that the angular defect accurately captures the regions of positive and negative Gaussian curvature. Plotting the histograms of the angular defects, in Figure 8.2i-l, shows a distribution closely centred around $\delta = 0$, which means $K = 0$. However, a clear asymmetry was found in all distributions towards negative curvature, as shown by the average angular defect $\bar{\delta} < 0$.
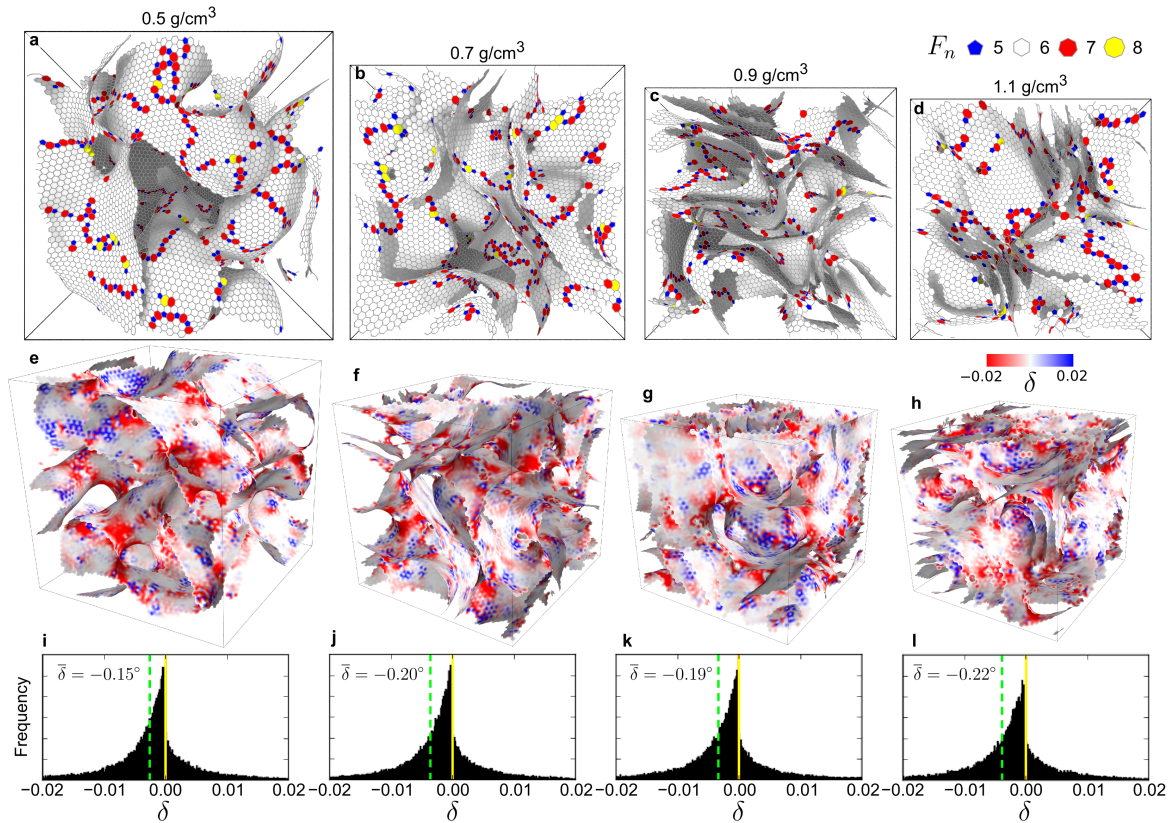
Figure 8.2 a-d) Annealed molecular dynamics geometries at densities 0.5, 0.7, 0.9 and 1.1 g/cc with pentagonal, heptagonal and octagonal rings being coloured blue, red and yellow respectively. e-h) Angular defect plotted on the mesh. i-l) Histogram of the angular defect with the zero defect (yellow line) and average angular defect $\bar{\delta}$ value in degrees (dashed green line).

To estimate the sensitivity of the average angular defect and microstructure to the initial configuration, a series of replicate simulations were analysed from previous work from my collaborators at Curtin University [91]. Smaller systems were chosen with 8770 carbon atoms and two sets of five replicas were generated using annealed molecular dynamics. Each set of five replicas was generated at two different densities, 0.5 g/cc and 1.1 g/cc. Figure 8.3 shows a slice of the full structure and the plots of the angular defect distributions. Tables 8.1 and 8.2 detail the variability in the coordination fraction, ring statistics and average angular defect $\bar{\delta}$. The mean angular defect for the 0.5 g/cc and 1.1 g/cc of the smaller system are higher compared with the larger systems ($-0.39°$ and $-0.40°$ compared with the larger systems $-0.15°$ and $-0.22°$). This increase in curvature for the smaller system is anticipated as the smaller extent of the periodic cell will require greater curvature to connect the network periodically. The percentage error for these duplicates can be estimated using a 90% confidence interval as given by Student's t-distribution providing percentage errors

of 8% and 4% for the 0.5 and 1.1 g/cc respectively. As shown in our previous work, the microstructure is consistent with the coordination fractions and rings per carbon atoms found to vary minimally. The same non-sp^2 defects were present in all of the structures consistent with the larger structures analysed in Table I in the main text.
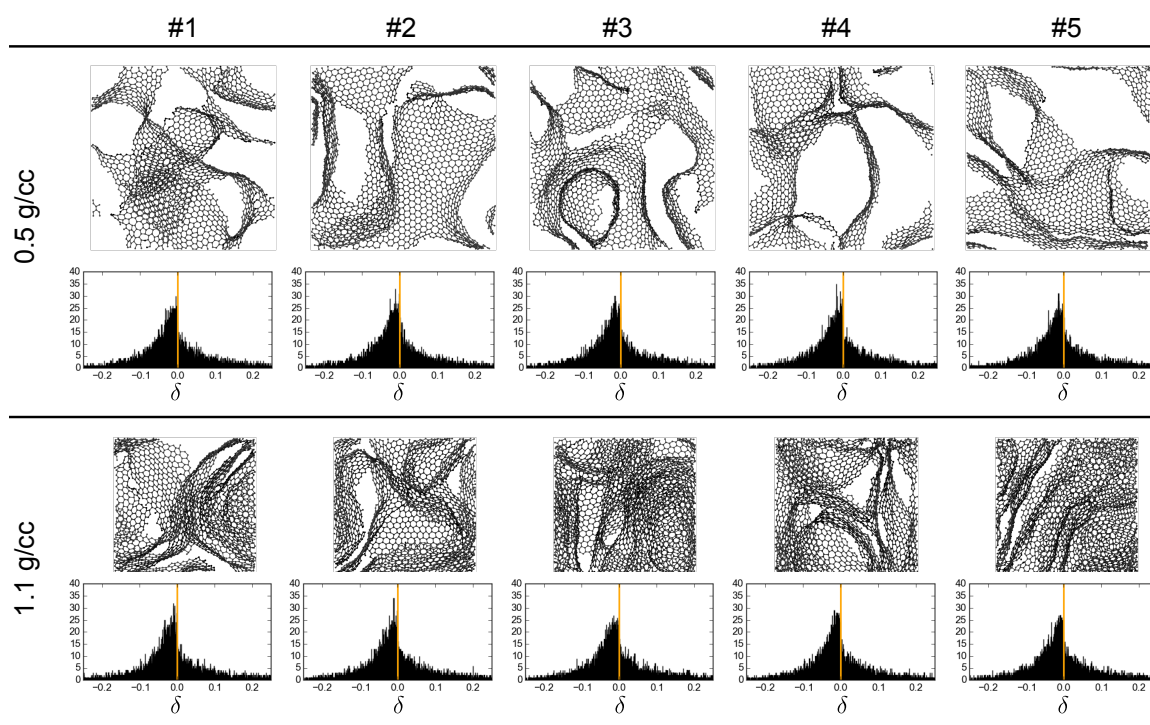
Figure 8.3 Sensitivity analysis showing a 2 nm cross section of the geometry and the distributions of angular defects at 0.5 g/cc and 1.1 g/cc. An orange line is shown to denote the zero angular defect value in the plots of the angular defect.

The significance of this net-negative curvature for 3D disordered graphene networks can be further understood in terms of idealised sp^2 nanoforms. For schwarzites the excess negative curvature allows for openings in the networks while continuously connecting in 3D, as given by Eq. 1. In contrast, fullerenes having an excess positive curvature are periodically closed. Ideal graphite, having average curvature of zero, can only possess connectivity in two dimensions. As our networks are predominantly sp^2 (95–97%), therefore approximating ideal carbon nanoforms, the connectivity could be expected to arise from a similar topological argument that net-negative curvature is a requirement for continuous 3D connectivity.

Considering the naming of these networks it would be inappropriate to describe them as purely schwarzite-like due to the presence of positively curved, fullerene-like regions. Recently Schwerdtfeger [372] proposed the name G_n-*fulleroid* to define a high genus net negatively curved closed carbon network containing both 5-membered and $\geq$ 7-membered

Table 8.1 Statistical variability analysis at density of 0.5 g/cc. Coordination fractions sp^n, rings per carbon atom[a] N_n from [91] and average angular defects $\bar{\delta}$ are listed for the five small structures. The mean, standard deviation (SD) and standard-error-in-the-mean (SEM) are also computed.

Structure	sp (%)	sp^2 (%)	sp^3 (%)	N_5	N_6	N_7	N_8	$\bar{\delta}$ (deg)
#1	2.01	96.83	0.48	0.026	0.429	0.030	0.001	−0.44
#2	2.29	96.32	0.47	0.023	0.436	0.025	0.001	−0.34
#3	2.57	96.03	0.44	0.030	0.419	0.031	0.002	−0.38
#4	2.09	96.68	0.41	0.027	0.431	0.027	0.003	−0.41
#5	1.79	96.50	0.32	0.026	0.430	0.029	0.001	−0.37
Mean	2.15	96.47	0.42	0.026	0.429	0.028	0.002	−0.39
SD	0.26	0.28	0.06	0.002	0.005	0.002	0.001	0.03
SEM	0.13	0.14	0.03	0.001	0.003	0.001	0.000	0.02

Table 8.2 Statistical variability analysis at density of 1.1 g/cc. Coordination fractions sp^n, rings per carbon atom N_n and average angular defects $\bar{\delta}$ are listed for the five small structures. The mean, standard deviation (SD) and standard-error-in-the-mean (SEM) are also computed.

Structure	sp (%)	sp^2 (%)	sp^3 (%)	N_5	N_6	N_7	N_8	$\bar{\delta}$ (deg)
#1	1.98	97.21	0.59	0.024	0.435	0.023	0.002	−0.41
#2	1.79	97.41	0.44	0.026	0.434	0.024	0.002	−0.36
#3	1.93	97.29	0.55	0.025	0.435	0.024	0.002	−0.39
#4	2.21	97.09	0.60	0.025	0.431	0.026	0.001	−0.42
#5	2.08	97.27	0.47	0.028	0.424	0.029	0.002	−0.40
Mean	2.00	97.25	0.53	0.026	0.432	0.025	0.002	−0.40
SD	0.14	0.10	0.06	0.001	0.004	0.002	0.000	0.02
SEM	0.07	0.05	0.03	0.001	0.002	0.001	0.000	0.01

rings, i.e. regions of both positive and negative Gauss curvature (as opposed to a fullerene which contains only 5- and 6-membered rings). As it is inappropriate to ascribe a genus related to the topology due to the presence of edge defects, we suggest these disordered graphene networks have *net negative fulleroid-like* topology.

8.3   Combining curved and stacked structures

While the global curvature of these networks are all similar, the microstructure is very different depending on the density of the network. At low densities, the network consists of

single-layer graphene enclosing connected pores, while at high densities randomly oriented stacks of graphitic ribbons develop reducing the porosity of the network to a few isolated voids [91]. Figure 8.4 shows the computed XRD spectra with the region corresponding to the 002 X-ray reflection highlighted, characteristic of layered graphene [126]. For the highest density network prepared at 1.5 g/cc this 002 peak is clearly observed [89]. For the porous carbon series the peak starts to develop from 0.9 g/cc, as a low scattering angle shoulder appears corresponding to the visual inspection of two or three stacked ribbons.
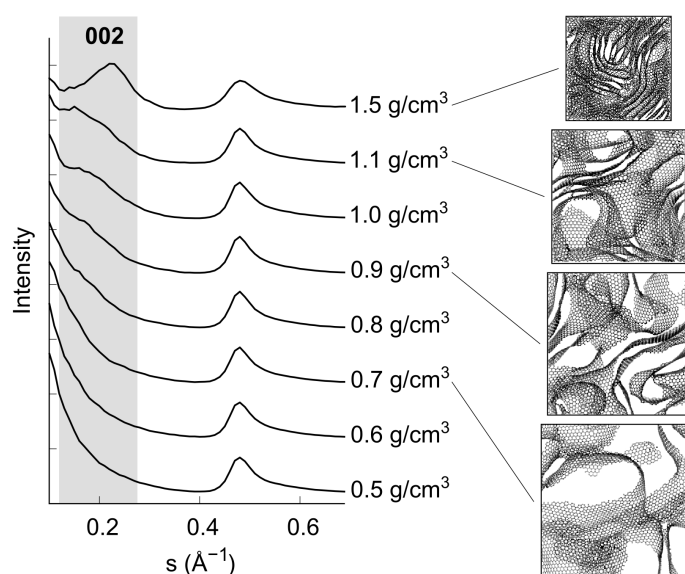
Figure 8.4 Computed X-ray diffraction pattern for simulated glassy carbon (top) [89] and porous carbon networks [90, 91]. The 002 peak associated with layering is highlighted. The snapshots show a 10 Å slab of the full structures.

Further detailed visualisation of the bonding networks allows identification of non-sp^2-bonded atom defects as the key to the coexistence of curved ribbons and stacked layers (see Figure 8.5a-d). Table 8.3 shows the number of defects as a function of density. Y/T-shaped junctions involve a line of sp^3 defects terminating a graphene sheet perpendicularly to another (see Figure 8.5a). These dominate at intermediate densities. Free edges involve sp-bonded atoms terminating a graphene sheet (see Figure 8.5b)i). These defects are found at all densities and vary in length; in the case of the 0.9 g/cc structure the free edges are extensive (>10 rings). Interlayer bonding occurs when two regions of positive Gaussian curvature are bonded via an sp^3 atom (see Figure 8.5b)ii). While these defects are rare, they contribute to the 3D connectivity by linking two regions of positive curvature.

In Figure 8.5c,d a screw dislocation defect is highlighted from two different angles. As density increases and layering occurs, these defects become more common. Screw dislocations are free edges wound into a spiral (resembling a $\log(z)$ Riemann surface), well-

known in graphite [176, 404], anthracite [453] and found in computationally generated 2D pyrocarbon models [248]. These screw dislocations allow the stacked layers to continuously connect and inhibit ideal ABAB (Bernal) stacking. At the highest densities a small number of buckled edges are observed, which form lines of sp-bonded atoms (see Figure 8.5e). These resemble closed edges seen in HRTEM of bilayer graphene [256].
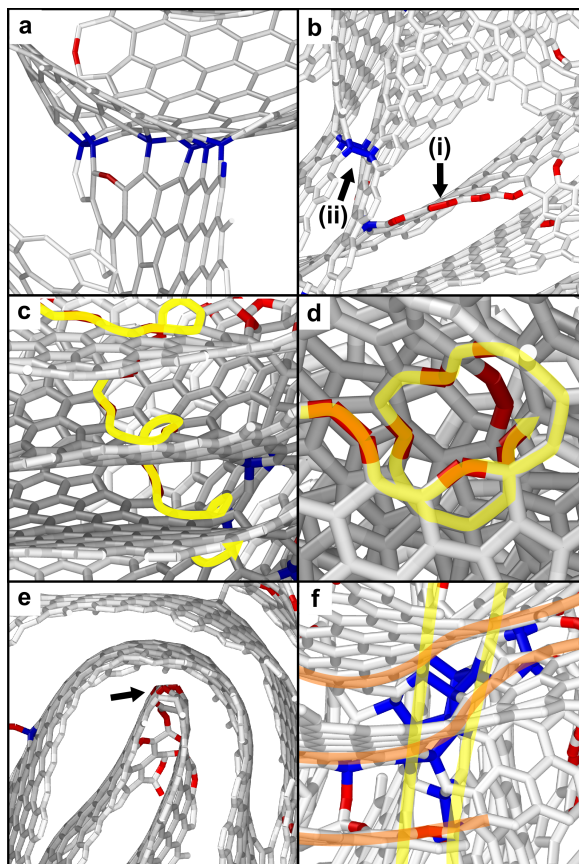
Figure 8.5 Slices of the bonding network with sp atoms coloured red and sp^3 atoms coloured blue. a) Y/T junction, b) free edges (i) and interlayer bonding (ii), c) and d) a screw dislocation from two different angles, e) buckled edges and f) crosshatched ribbons. Yellow and orange highlighting are provided to guide the eye.

Crosshatching occurs when two ribbons, parallel to each other in one of their axes but perpendicular in the other, form a region of sp^3-bonding, as shown in Figure 8.5f. This common feature in HRTEM imaging of glassy carbon has been proposed theoretically by Balaban [18] but has not been previously achieved in atomistic simulations. The presence of sp^3 bonding in the crosshatching is significant, as traditionally glassy carbon has been used as the purely sp^2-bonded standard calibration material in electron energy loss spectroscopy (EELS) [382]. Recently, using magic angle corrections in EELS measurements, evidence was found for a small fraction of non-sp^2-bonded atoms in glassy carbon [382], matching the 5%

Table 8.3 Number of non-sp^2 defects as a function of density for the defects shown in Figure 8.5.

Density (g/cc)	Y/T-junction	Free edge	Interlayer	Screw	Buckled	Crosshatch
0.5	4	11	0	0	0	0
0.7	10	16	2	2	0	0
0.9	10	4	0	2	0	1
1.1	6	7	0	6	1	2
1.5	3	6	3	8	2	8

predicted from the self-assembled carbon model (corresponding to the 1.5 g/cc network) [89]. These non-sp^2 defects are critical to resolving the topological complexities arising from layering. In particular, the screw dislocations enable the development of layers in these continuously curved disordered graphene networks by avoiding the requirement of high symmetry in layered schwarzite nanoforms. Based on the carbon science nomenclature [405], we propose that high-density isotropic carbons have a *screwed, stacked, net negative fulleroid-like* nanostructure (see Figure 8.6).
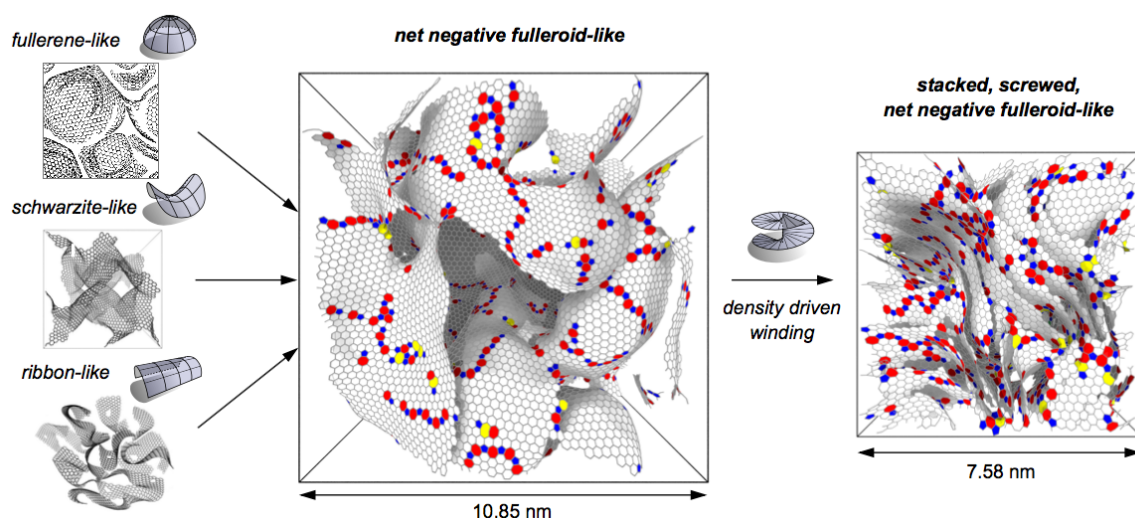
Figure 8.6 Schematic of the disordered 3D graphene's nanostructure.

These results provide insights into the synthesis of porous 3D graphenes. Since layering is linked to density, densities below ≈0.9 g/cc should be sought to synthesise nanoporous carbons. These low density, negatively curved, foam-like networks are suitable for adsorption applications as the topological features hold pores open and inhibit layering. The regions of positive Gauss curvature are of particular interest as they give rise to reactivity for catalytic applications [266] and a strong flexoelectric charge polarisation, which is anticipated to

significantly affect the adsorption of chemical species such as H_2, CO_2 and CH_4 [267]. To synthesise a 3D graphene that maintains the unique electronic properties of planar graphene, such as the Dirac fermion electron dynamics, the number of non-sp^2 defects must also be reduced. This requires that orientable networks be constructed to allow for the graphene to continuously connect in 3D preventing free edges and Y/T junctions. Such networks can be achieved via templating strategies, as demonstrated by growing graphene on porous sintered metal supports [198, 300] and as suggested computationally via zeolite templating [48].

This analysis also contributes to the ongoing debates on graphitisation. In particular, it is suggested that the 3D connectivity of these *net negative fulleroid-like* networks is the origin of their non-graphitisability. Despite containing stacked ribbons, the whole network would not convert to graphite, since significant bond breaking would be required to reduce the connectivity from three to the two dimensions found in a graphitic network. Such a change in the dimensionality of glassy carbon was recently observed. Compressing glassy carbon to >35 GPa in a diamond anvil cell at room temperature, the significant amount of bond breaking necessary to orient the ribbons in 2D and partially graphitise the glassy carbon network was achieved [382].

Finally, destruction of soot will be influenced by thermal annealing. Firstly, soot emitted from an engine, for example, is partially carbonised and possesses a hard shell that is often more crosslinked than the core [218, 416]. Oxidation of such a nanostructure is still not fully understood. Secondly, after-treatment systems in engines can provide longer thermal annealing of soot to transform it into ribbon-like, non-graphitising carbons. Oxidation will then proceed most rapidly at the edges with oxidation dynamics of screw defects being of particular interest. Apart from edges, regions of positive Gaussian curvature will present reactive sites for oxidation, which will need to be further explored. Thirdly, concurrent annealing and oxidation have been found to reduce the density of the soot particles and restructure them into porous disordered 3D graphenes [416]. Evidence was shown in Chapter 1 for this restructuring of soot during *in situ* HRTEM with mild oxidation at temperatures >900 °C (see Figure 1.4b). This porous carbon will have unique oxidation dynamics and will also provide insights into the oxidation resistance of activated carbon materials.

In conclusion, the analysis of experimentally verified self-assembled nanocarbon models, using a discrete surface mesh approach, allows for the curvature of the networks to be revealed. These models capture, for the first time, all the experimentally observed features in disordered graphene materials from nanoporous through to glassy carbons. All structures therefore possess a *net negative fulleroid-like* topology independent of the microstructural textures present. Densification of the networks is found to give rise to layered ribbons.

Coexistence of stacks of ribbons within a curved graphene network is made topologically possible by a small fraction of non-sp^2-bonded defects such as screw dislocations. These results have interesting implications for forming defect-free 3D graphenes, for producing synthetic graphite and for soot oxidation and will be discussed in the concluding comments.

Chapter 9

Conclusions

"You never change things by fighting the existing reality. To change something, build a new model that makes the existing model obsolete."

– Buckminster Fuller, *As quoted in Beyond Civilization: Humanity's Next Great Adventure (1999), by Daniel Quinn, p. 137*

9.1   Summary

This dissertation is concluded by summarising the main contributions of the work presented.

- A review of soot nanoparticle formation was provided. The mechanisms were categorised into chemical, physical and chemical + physical allowing for critical comparison and an initial mapping from the experimental results to possible models.

- The flexoelectric effect was computed for a wide range of cPAH. A significant polarity was found and the inability of current forcefields to capture this charge polarisation was shown.

- Curvature of aromatic molecules was quantified using electron microscopy and image simulation, showing that the majority of aromatic molecules in early soot particles are curved through pentagon incorporation. The earliest curvature that can be integrated into growing aromatics was then computationally explored, with six rings being the minimum size required. A cyclic fuel with 5-membered rings was then shown to provide an increase in soot formation while also integrating significant curvature compared with a 6-membered ring fuel.

- The intermolecular forces between cPAH and chemi-ions were determined by electronic structure calculations. Homodimer energies for cPAH with one to two pentagons integrated were found to be comparable to fPAH, indicating that cPAH are unable to achieve a supersaturation and condense at flame temperatures. Binding energies between cPAH and chemi-ions were found to be significant and a new forcefield was developed with off-site charges to capture the flexoelectric effect. Corannulene was found to cluster more efficiently than coronene in the presence of charged species. The impact of cPAH's thermal fluctuation showed that larger cPAH found in early soot nanoparticles are unable to invert rapidly at flame temperatures. Quantum molecular dynamics simulations showed that cPAH's polarity was persistent at flame temperatures. Ion-induced nuclei were then suggested to explain the 3×10^3 Da positive particle mode but would be unable to stabilise more than a few cPAH due to the short range of the ion-dipole interaction at such high temperatures.

- Chemical crosslinks between reactive aromatics were systematically compared using electronic structure calculations. The average local ionisation potential was used to locate and compare aromatic radicals and closed shell species. Curved PAH were found to form strong crosslinks with aryl-type σ-radicals, as were a variety of other reactive edges. A new reactive site was found on a partially saturated rim-based pentagonal

ring, forming a localised π-radical. The π-radicals were found to form crosslinked and stacked geometries and were suggested to cluster rapidly during soot formation.

- Finally, the nanostructure of non-graphitising or disordered carbons was studied. A new mesh-based approach was developed that allowed for the global curvature to be determined as net-negative. This curvature was suggested to be the cause for the reluctance of disordered carbon materials to graphitise. Non-sp^2 carbon atoms were then found to allow for the layered regions to become dominant in high density models. The screw defect is of particular importance in allowing for densification of the carbon networks.

9.2   Suggestions for further work

Many important and open questions still remain. Four main directions are proposed for further work – two based on reducing soot emissions and two based on understanding and developing new carbon materials.

9.2.1   Electrical control of soot formation

In this thesis significant interactions were demonstrated between cPAH and ionic species in the flame. However, the link between these observations and the exact soot formation mechanism can only be uncovered by careful experimentation matched to detailed mechanistic understandings. The positive particle mode at 3×10^3 Da needs to be further understood as either contributing to or being separated from other mechanisms. Experiments to modify the flame with electric fields or charge injection with particle mass spectrometers could provide this much-needed insight. Recently, injections of ionised air (that also contained ozone) were shown to reduce soot formation considerably [207]. This was initially considered to be due to the ozone allowing for cool combustion processes. Similar strategies have been detailed by a large number of patents published recently on the injection of charge into engines. One patent from 2001 (EP 1 146 220 A1) claims a reduction of up to 80% of soot for diesel engines running under high load and a 21% reduction at idling. It is unclear whether it is the injection of the *charged species* or the *ozone* that contributes most significantly to the reductions in soot emissions from these experiments.

9.2.2   Chemical pathways for soot compared

The motivation of Chapter 7 was to compare the reactivity of aromatic soot precursors. We found that cPAH have edges of low aromaticity that provide strong bonds with aryl-type σ-radicals. This systematic study also revealed new pentagon localised π-radicals with interesting reactivity. More work is required to determine the concentration of these reactive soot species and to develop detailed kinetic mechanisms. Description of the fragmentation pathways will be necessary to model both the forward and reverse reactions. Colleagues have already begun integrating new pathways into our custom software using electronic structure calculations and transition state theory. Once the various mechanisms can be shown to operate under different conditions, new fuel mixtures or additives could be devised to avoid soot generation under each of these conditions.

9.2.3   Flexoelectricity and a new anisotropic forcefield for cPAH

As well as soot, many of the contributions of this dissertation also provide insight into other carbon materials. The charge polarisation found in sp^2 carbon curved from pentagon integration has significant implications. Therefore, a combination of the insights from Chapter 4 on flexoelectricity and Chapter 8 on the nanostructure of disordered carbons could be fruitful. Some examples include:

- hard electrodes for sodium ion batteries could be influenced by the flexoelectric effect.

- electrodes for supercapacitors will interact strongly with the electrolyte in the vicinity of flexoelectric regions.

- polar gas adsorbents (H_2O, pollutants, ions) will be strongly bound to flexoelectric regions.

- non-polar adsorbents (H_2, CO_2 etc.) will also interact at low temperatures through induced-dipole dipole interactions.

To explore these effects a new forcefield must be implemented to describe the charge polarisation of these solid carbon materials. This will allow these effects to be quantified and potentially tuned through synthesis of new carbon materials.

9.2.4   Pathways to graphite or defect-free 3D graphene

A possible solution to the question of non-graphitisability of carbonaceous materials is their net-negative Gaussian curvature (as suggested in Chapter 8). However, this needs to

be tested. Firstly, there is preliminary evidence that higher annealing temperatures in the reactive molecular dynamics simulations provide a pathway to 2D graphite and prevent the formation of the disordered net-negative fulleroid-like nanostructure. By applying the topological metrics developed in Chapter 8 to the transformation of amorphous carbon into 3D disordered carbons or 2D graphite, the mechanism for graphitisation can be fully understood. This has important implications for strategies to form 2D graphite from naturally occurring materials, such as biomass, which could replace graphite mining. Secondly, the removal of defects in low density structures could allow for the formation of an ordered defect-free 3D graphene. This has been suggested to be the next allotrope of carbon, with previous nanocarbons following a trajectory of increasing dimensionality (0D fullerenes, 1D nanotubes, 2D graphite etc.) [465]. Defect-free 3D graphenes could be used in electronic applications as they have been predicted to have similar rapid Dirac fermion electron transport as 2D graphenes.

   In conclusion, evidence has been provided for the thesis that curvature within aromatic molecules significantly impacts soot formation and thermal transformations of carbon materials. New possible directions have been outlined but we cannot yet, as stated by Palmer and Cullis;

> "...account for the entire course of nucleation and growth of carbon on the basis
> of a fundamental knowledge of reaction rates and mechanisms."

This will be the next focus, with the aim of using this knowledge to improve our health and that of the planet.

Bibliography

[1] A. H. Abdourazak, A. Sygula, and P. W. Rabideau. "Locking" the bowl-shaped geometry of corannulene: cyclopentacorannulene. *Journal of the American Chemical Society*, 115(7):3010–3011, 1993. URL https://doi.org/10.1021/ja00060a073.

[2] B. D. Adamson, S. A. Skeen, M. Ahmed, and N. Hansen. Detection of aliphatically bridged multi-core polycyclic aromatic hydrocarbons in sooting flames with atmospheric-sampling high-resolution tandem mass spectrometry. *The Journal of Physical Chemistry A*, 122(48):9338–9349, 2018. URL https://doi.org/10.1021/acs.jpca.8b08947.

[3] S. Ahmad. Information-theoretic model of self-organizing fullerenes and the emergence of C_{60}. *Chemical Physics Letters*, 713:52–57, 2018. URL https://doi.org/10.1016/J.CPLETT.2018.10.024.

[4] F. Ahmadpoor and P. Sharma. Flexoelectricity in two-dimensional crystalline and biological membranes. *Nanoscale*, 7(40):16555–16570, 2015. URL https://doi.org/10.1039/C5NR04722F.

[5] J. Ahrens, M. Bachmann, T. Baum, J. Griesheimer, R. Kovacs, P. Weilmünster, and K.-H. Homann. Fullerenes and their ions in hydrocarbon flames. *International Journal of Mass Spectrometry and Ion Processes*, 138:133 – 148, 1994. URL https://doi.org/10.1016/0168-1176(94)04036-2.

[6] P. M. Ajayan, T. W. Ebbesen, T. Ichihashi, S. Iijima, K. Tanigaki, and H. Hiura. Opening carbon nanotubes with oxygen and implications for filling. *Nature*, 362 (6420):522–525, 1993. URL https://doi.org/10.1038/362522a0.

[7] A. B. Alquaity, J. Han, M. Chahine, H. Selim, M. Belhi, S. M. Sarathy, F. Bisetti, and A. Farooq. Measurements of positively charged ions in premixed methane-oxygen atmospheric flames. *Combustion Science and Technology*, 189(4):575–594, 2017. URL https://doi.org/10.1080/00102202.2016.1226821.

[8] H. M. Amin, A. Bennett, and W. L. Roberts. Determining fractal properties of soot aggregates and primary particle size distribution in counterflow flames up to 10atm. *Proceedings of the Combustion Institute*, 37(1):1161 – 1168, 2019. URL https://doi.org/10.1016/j.proci.2018.07.057.

[9] K. Y. Amsharov, K. Simeonov, and M. Jansen. Formation of fullerenes by pyrolysis of 1, 2'-binaphthyl and 1, 3-oligonaphthylene. *Carbon*, 45(2):337–343, 2007. URL https://doi.org/10.1016/j.carbon.2006.09.013.

[10] B. An, S. Fukuyama, K. Yokogawa, M. Yoshimura, M. Egashira, Y. Korai, and I. Mochida. Single pentagon in a hexagonal carbon lattice revealed by scanning tunneling microscopy. *Applied Physics Letters*, 78(23):3696–3698, 2001. URL https://doi.org/10.1063/1.1377859.

[11] B. Apicella, M. Millan, A. Herod, A. Carpentieri, P. Pucci, and A. Ciajolo. Separation and measurement of flame-formed high molecular weight polycyclic aromatic hydrocarbons by size-exclusion chromatography and laser desorption/ionization time-of-flight mass spectrometry. *Rapid Communications in Mass Spectrometry*, 20(7): 1104–1108, 2006. URL https://doi.org/10.1002/rcm.2419.

[12] B. Apicella, A. Ciajolo, A. Tregrossi, J. Abrahamson, R. L. Vander Wal, and C. Russo. HRTEM and EELS investigations of flame-formed soot nanostructure. *Fuel*, 225: 218–224, 2018. URL https://doi.org/10.1016/j.fuel.2018.03.091.

[13] A. Ashton and A. Hayhurst. Kinetics of collisional ionization of alkali metal atoms and recombination of electrons with alkali metal ions in flames. *Combustion and Flame*, 21(1):69–75, 1973. URL https://doi.org/10.1016/0010-2180(73)90008-4.

[14] M. Bachmann, W. Wiese, and K.-H. Homann. PAH and aromers: Precursors of fullerenes and soot. *Symposium (International) on Combustion*, 26(2):2259 – 2267, 1996. URL https://doi.org/10.1016/S0082-0784(96)80053-1.

[15] H. Badenhorst. Microstructure of natural graphite flakes revealed by oxidation: Limitations of XRD and Raman techniques for crystallinity estimates. *Carbon*, 66: 674–690, 2014. URL https://doi.org/10.1016/j.carbon.2013.09.065.

[16] R. F. Bader. *Atoms in Molecules*. Clarendon Press, 1994.

[17] W. M. Baird, L. A. Hooven, and B. Mahadevan. Carcinogenic polycyclic aromatic hydrocarbon-dna adducts and mechanism of action. *Environmental and Molecular Mutagenesis*, 45(2-3):106–114, 2005. URL https://doi.org/10.1002/em.20095.

[18] A. Balaban, D. Klein, and C. Folden. Diamond-graphite hybrids. *Chemical Physics Letters*, 217(3):266–270, 1994. URL https://doi.org/10.1016/0009-2614(93)E1379-U.

[19] A. T. Balaban and D. J. Klein. Claromatic carbon nanostructures. *The Journal of Physical Chemistry C*, 113(44):19123–19133, 2009. URL https://doi.org/10.1021/jp9082618.

[20] N. L. Balàzs. Formation of Stable Molecules within the Statistical Theory of Atoms. *Physical Review*, 156(1):42–47, 1967. URL https://doi.org/10.1103/PhysRev.156.42.

[21] L. L. Ban. Direct study of structural imperfections by high-resolution electron microscopy. In M. W. Roberts and J. M. Thomas, editors, *Surface and Defect Properties of Solids: Volume 1*, volume 1, pages 54–94. The Royal Society of Chemistry, 1972. URL https://doi.org/10.1039/9781847556943-00054.

[22] T. G. Baquet, H.-H. Grotheer, and M. Aigner. Simultaneous detection of two types of soot precursor particles using photoionization mass spectrometry. *Rapid Communications in Mass Spectrometry*, 21(24):4060–4064, 2007. URL https://doi.org/10.1002/rcm.3297.

[23] T. Bauert, L. Zoppi, G. Koller, A. Garcia, K. K. Baldridge, and K. H. Ernst. Large induced interface dipole moments without charge transfer: Buckybowls on metal surfaces. *Journal of Physical Chemistry Letters*, 2(21):2805–2809, 2011. URL https://doi.org/10.1021/jz2012484.

[24] T. Baum, S. Löffler, P. Löffler, P. Weilmünster, and K.-H. Homann. Fullerene ions and their relation to PAH and soot in low-pressure hydrocarbon flames. *Berichte der Bunsengesellschaft für physikalische Chemie*, 96(7):841–857, 1992. URL https://doi.org/10.1002/bbpc.19920960702.

[25] A. D. Becke. Density-functional exchange-energy approximation with correct asymptotic behavior. *Physical Review A*, 38(6):3098, 1988. URL https://doi.org/10.1103/PhysRevA.38.3098.

[26] A. D. Becke. Density-functional thermochemistry. III. The role of exact exchange. *The Journal of Chemical Physics*, 98(7):5648, 1993. URL https://doi.org/10.1063/1.464913.

[27] A. D. Becke and K. E. Edgecombe. A simple measure of electron localization in atomic and molecular systems. *The Journal of Chemical Physics*, 92(9):5397–5403, 1990. URL https://doi.org/10.1063/1.458517.

[28] H. Behrens. Flame instabilities and combustion mechanism. *Symposium (International) on Combustion*, 4(1):538–545, 1953. URL https://doi.org/10.1016/S0082-0784(53)80075-5.

[29] M. Bendikov, H. M. Duong, K. Starkey, K. Houk, E. A. Carter, and F. Wudl. Oligoacenes: theoretical prediction of open-shell singlet diradical ground states. *Journal of the American Chemical Society*, 126(24):7416–7417, 2004. URL https://doi.org/10.1021/ja048919w.

[30] J. D. Bernal and R. H. Fowler. A theory of water and ionic solution, with particular reference to hydrogen and hydroxyl ions. *The Journal of Chemical Physics*, 1(8):515–548, 1933. URL https://doi.org/10.1063/1.1749327.

[31] C. Betrancourt, F. Liu, P. Desgroux, X. Mercier, A. Faccinetto, M. Salamanca, L. Ruwe, K. Kohse-Höinghaus, D. Emmrich, A. Beyer, A. Gölzhäuser, and T. Tritscher. Investigation of the size of the incandescent incipient soot particles in premixed sooting and nucleation flames of n-butane using LII, HIM, and 1 nm-SMPS. *Aerosol Science and Technology*, 51(8):916–935, 2017. URL https://doi.org/10.1080/02786826.2017.1325440.

[32] H. Bhowmick and S. K. Biswas. Relationship between physical structure and tribology of single soot particles generated by burning ethylene. *Tribology Letters*, 44(2):139–149, 2011. URL https://doi.org/10.1007/s11249-011-9831-5.

[33] H. Bhowmick, S. K. Majumdar, and S. K. Biswas. Dry tribology and nanomechanics of gaseous flame soot in comparison with carbon black and diesel soot. *Proceedings of the Institution of Mechanical Engineers, Part C: Journal of Mechanical Engineering Science*, 226(2):394–402, 2011. URL https://doi.org/10.1177/0954406211429410.

[34] P. U. Biedermann, S. Pogodin, and I. Agranat. Inversion barrier of corannulene. a benchmark for bowl-to-bowl inversions in fullerene fragments. *The Journal of Organic Chemistry*, 64(10):3655–3662, 1999. URL https://doi.org/10.1021/jo9900174.

[35] J. Birks, D. Dyson, and I. Munro. 'excimer' fluorescence II. lifetime studies of pyrene solutions. *Proceedings of the Royal Society of London. Series A. Mathematical and Physical Sciences*, 275(1363):575–588, 1963. URL https://doi.org/10.1098/rspa.1963.0187.

[36] H. Bockhorn. *Soot Formation in Combustion: Mechanisms and Models*. Springer Science & Business Media, 1994.

[37] H. Bockhorn, A. D'Anna, A. Sarofim, and H. Wang, editors. *Combustion Generated Fine Carbonaceous Particles*. KIT Scientific Publishing, 2009.

[38] P. Bonczyk. Effects of metal additives on soot precursors and particulates in a $C_2H_4/O_2/N_2/Ar$ premixed flame. *Fuel*, 70(12):1403–1411, 1991. URL https://doi.org/10.1016/0016-2361(91)90006-V.

[39] T. C. Bond, S. J. Doherty, D. W. Fahey, P. M. Forster, T. Berntsen, B. J. Deangelo, M. G. Flanner, S. Ghan, B. Kärcher, D. Koch, S. Kinne, Y. Kondo, P. K. Quinn, M. C. Sarofim, M. G. Schultz, M. Schulz, C. Venkataraman, H. Zhang, S. Zhang, N. Bellouin, S. K. Guttikunda, P. K. Hopke, M. Z. Jacobson, J. W. Kaiser, Z. Klimont, U. Lohmann, J. P. Schwarz, D. Shindell, T. Storelvmo, S. G. Warren, and C. S. Zender. Bounding the role of black carbon in the climate system: A scientific assessment. *Journal of Geophysical Research Atmospheres*, 118(11):5380–5552, 2013. URL https://doi.org/10.1002/jgrd.50171.

[40] V. Borrelli, F. Cazals, and J.-M. Morvan. On the angular defect of triangulations and the pointwise approximation of curvatures. *Computer Aided Geometry D.*, 20(6):319 – 341, 2003. URL https://doi.org/10.1016/S0167-8396(03)00077-3.

[41] M. L. Botero, E. M. Adkins, S. González-Calera, H. Miller, and M. Kraft. PAH structure analysis of soot in a non-premixed flame using high-resolution transmission electron microscopy and optical band gap analysis. *Combustion and Flame*, 164:250–258, 2016. URL https://doi.org/10.1016/j.combustflame.2015.11.022.

[42] M. L. Botero, E. M. Adkins, S. González-Calera, H. Miller, and M. Kraft. PAH structure analysis of soot in a non-premixed flame using high-resolution transmission electron microscopy and optical band gap analysis. *Combustion and Flame*, 164:250–258, 2016. URL https://doi.org/10.1016/j.combustflame.2015.11.022.

[43] M. L. Botero, Y. Sheng, J. Akroyd, J. Martin, J. A. Dreyer, W. Yang, and M. Kraft. Internal structure of soot particles in a diffusion flame. *Carbon*, 141:635–642, 2018. URL https://doi.org/10.1016/j.carbon.2018.09.063.

[44] M. L. Botero, N. Eaves, J. A. Dreyer, Y. Sheng, J. Akroyd, W. Yang, and M. Kraft. Experimental and numerical study of the evolution of soot primary particles in a diffusion flame. *Proceedings of the Combustion Institute*, 37(2):2047–2055, 2019. URL https://doi.org/10.1016/j.proci.2018.06.185.

[45] H. Bové, E. Bongaerts, E. Slenders, E. M. Bijnens, N. D. Saenen, W. Gyselaers, P. Van Eyken, M. Plusquin, M. B. Roeffaers, M. Ameloot, et al. Ambient black carbon particles reach the fetal side of human placenta. *Nature Communications*, 10(1):1–7, 2019. URL https://doi.org/10.1038/s41467-019-11654-3.

[46] K. Bowal, J. W. Martin, A. J. Misquitta, and M. Kraft. Ion-induced soot nucleation using a new potential for curved aromatics. *Combustion Science and Technology*, 191 (5):1–19, 2019. URL https://doi.org/10.1080/00102202.2019.1565496.

[47] W. T. Brande. XXII. On some new electro-chemical phenomena. *The Philosophical Magazine*, 44(196):124–130, 1814. URL https://doi.org/10.1080/14786441408637425.

[48] E. Braun, Y. Lee, S. M. Moosavi, S. Barthel, R. Mercado, I. A. Baburin, D. M. Proserpio, and B. Smit. Generating carbon schwarzites via zeolite-templating. *Proceedings of the National Academy of Sciences of the United States of America*, 115 (35):8116–8124, 2018. URL https://doi.org/10.1073/pnas.1805062115.

[49] F. A. Bulat, J. S. Burgess, B. R. Matis, J. W. Baldwin, L. Macaveiu, J. S. Murray, and P. Politzer. Hydrogenation and fluorination of graphene models: Analysis via the average local ionization energy. *The Journal of Physical Chemistry A*, 116(33): 8644–8652, 2012. URL https://doi.org/10.1021/jp3053604.

[50] F. Bundy, W. Bassett, M. Weathers, R. Hemley, H. Mao, and A. Goncharov. The pressure-temperature phase and transformation diagram for carbon; updated through 1994. *Carbon*, 34(2):141–153, 1996. URL https://doi.org/10.1016/0008-6223(96)00170-4.

[51] L. A. Burns, Á. V. Mayagoitia, B. G. Sumpter, and C. D. Sherrill. Density-functional approaches to noncovalent interactions: A comparison of dispersion corrections (DFT-D), exchange-hole dipole moment (XDM) theory, and specialized functionals. *The Journal of Chemical Physics*, 134(8):084107, 2011. URL https://doi.org/10.1063/1.3545971.

[52] E. M. Cabaleiro-Lago, B. Fernandez, and J. Rodríguez-Otero. Dissecting the concave–convex π-π interaction in corannulene and sumanene dimers: SAPT (DFT) analysis and performance of DFT dispersion-corrected methods. *Journal of Computational Chemistry*, 39(2):93–104, 2018. URL https://doi.org/10.1002/jcc.25084.

[53] J. Cain, A. Laskin, R. Kholghy, and J. Thomson. Molecular characterization of organic content of soot along the centerline of a coflow diffusion flame. *Physical Chemistry Chemical Physics*, 16:25862–25875, 2014. URL https://doi.org/10.1039/C4CP03330B.

[54] H. F. Calcote. Electrical properties of flames: Burner flames in transverse electric fields. *Symposium on Combustion and Flame, and Explosion Phenomena*, 3(1):245 – 253, 1948. URL https://doi.org/10.1016/S1062-2896(49)80033-X. Third Symposium on Combustion and Flame and Explosion Phenomena.

[55] H. F. Calcote. Mechanisms of soot nucleation in flames-A critical review. *Combustion and Flame*, 42(C):215–242, 1981. URL https://doi.org/10.1016/0010-2180(81)90159-0.

[56] H. F. Calcote, D. B. Olson, and D. G. Keil. Are ions important in soot formation? *Energy & Fuels*, 2(4):494–504, 1988. URL https://doi.org/10.1021/ef00010a016.

[57] F. Carbone, M. R. Canagaratna, A. T. Lambe, J. T. Jayne, D. R. Worsnop, and A. Gomez. Exploratory analysis of a sooting premixed flame via on-line high resolution (APi-TOF) mass spectrometry. *Proceedings of the Combustion Institute*, 37:1–8, 2018. URL https://doi.org/10.1016/j.proci.2018.08.020.

[58] F. Carbone, M. R. Canagaratna, A. T. Lambe, J. T. Jayne, D. R. Worsnop, and A. Gomez. Exploratory analysis of a sooting premixed flame via on-line high resolution (APi-TOF) mass spectrometry. *Proceedings of the Combustion Institute*, 37:919–926, 2019. URL https://doi.org/10.1016/j.proci.2018.08.020.

[59] D. Carroll, P. Redlich, P. Ajayan, J. Charlier, X. Blase, A. De Vita, and R. Car. Electronic Structure and Localized States at Carbon Nanotube Tips. *Physical Review Letters*, 78(14):2811–2814, 1997. URL https://doi.org/10.1103/PhysRevLett.78.2811.

[60] C. Casiraghi, F. Piazza, A. Ferrari, D. Grambole, and J. Robertson. Bonding in hydrogenated diamond-like carbon by raman spectroscopy. *Diamond and Related Materials*, 14(3-7):1098–1102, 2005. URL https://doi.org/10.1016/j.diamond.2004.10.030.

[61] D. M. Ceperley and B. J. Alder. Ground State of the Electron Gas by a Stochastic Method. *Physical Review Letters*, 45(7):566–569, 1980. URL https://doi.org/10.1103/PhysRevLett.45.566.

[62] D. Chen and H. Wang. Cation-π Interactions between Flame Chemi-ions and Aromatic Compounds. *Energy & Fuels*, 31(3):2345–2352, 2017. URL https://doi.org/10.1021/acs.energyfuels.6b02354.

[63] D. Chen, T. S. Totton, J. W. J. Akroyd, S. Mosbach, and M. Kraft. Size-dependent melting of polycyclic aromatic hydrocarbon nano-clusters: A molecular dynamics study. *Carbon*, 67:79–91, 2014. URL https://doi.org/10.1016/j.carbon.2013.09.058.

[64] M.-K. Chen, H.-J. Hsin, T.-C. Wu, B.-Y. Kang, Y.-W. Lee, M.-Y. Kuo, and Y.-T. Wu. Highly Curved Bowl-Shaped Fragments of Fullerenes: Synthesis, Structural Analysis, and Physical Properties. *Chemistry - A European Journal*, 20(2):598–608, 2014. URL https://doi.org/10.1002/chem.201303357.

[65] J. S. Chickos, P. Webb, G. Nichols, T. Kiyobayashi, P.-C. Cheng, and L. Scott. The enthalpy of vaporization and sublimation of corannulene, coronene, and perylene at T= 298.15 K. *The Journal of Chemical Thermodynamics*, 34(8):1195–1206, 2002. URL https://doi.org/10.1006/jcht.2002.0977.

[66] D. Childress. *Johannes Gutenberg and the printing press*. Twenty-First Century Books, 2007.

[67] T. Christiansen, M. Cotte, R. Loredo-Portales, P. E. Lindelof, K. Mortensen, K. Ryholt, and S. Larsen. The nature of ancient egyptian copper-containing carbon inks is revealed by synchrotron radiation based X-ray microscopy. *Scientific Reports*, 7(1):15346, 2017. URL https://doi.org/10.1038/s41598-017-15652-7.

[68] S.-H. Chung and A. Violi. Peri-condensed aromatics with aliphatic chains as key intermediates for the nucleation of aromatic hydrocarbons. *Proceedings of the Combustion Institute*, 33(1):693–700, 2011. URL https://doi.org/10.1016/j.proci.2010.06.038.

[69] S. L. Chung and N. L. Lai. Suppression of soot by metal additives during the combustion of polystyrene. *Journal of the Air and Waste Management Association*, 42(8):1082–1088, 1992. URL https://doi.org/10.1080/10473289.1992.10467056.

[70] A. Chuvilin, U. Kaiser, E. Bichoutskaia, N. a. Besley, and A. N. Khlobystov. Direct transformation of graphene to fullerene. *Nature Chemistry*, 2(6):450–453, 2010. URL https://doi.org/10.1038/nchem.644.

[71] A. Chuvilin, E. Bichoutskaia, M. Gimenez-Lopez, T. Chamberlain, G. Rance, N. Kuganathan, J. Biskupek, U. Kaiser, and A. Khlobystov. Self-assembly of a sulphur-terminated graphene nanoribbon within a single-walled carbon nanotube. *Nature Materials*, 10(9):687, 2011. URL https://doi.org/10.1038/nmat3082.

[72] E. Clar, B. McAndrew, and M. Zander. The establishment of double bond character in methyl derivatives of phenanthrene, pyrene, chrysene and coronene by NMR. *Tetrahedron*, 23(2):985–993, 1967. URL https://doi.org/10.1016/0040-4020(67)85046-4.

[73] A. Comandini and K. Brezinsky. Theoretical study of the formation of naphthalene from the radical/π-bond addition between single-ring aromatic hydrocarbons. *The Journal of Physical Chemistry A*, 115(22):5547–5559, 2011. URL https://doi.org/10.1021/jp200201c.

[74] A. Comandini, T. Malewicki, and K. Brezinsky. Chemistry of polycyclic aromatic hydrocarbons formation from phenyl radical pyrolysis and reaction of phenyl and acetylene. *The Journal of Physical Chemistry A*, 116(10):2409–2434, 2012. URL https://doi.org/10.1021/jp207461a.

[75] A. Comandini, S. Abid, and N. Chaumeix. Polycyclic aromatic hydrocarbon growth by diradical cycloaddition/fragmentation. *The Journal of Physical Chemistry A*, 121 (31):5921–5931, 2017. URL https://doi.org/10.1021/acs.jpca.7b05562.

[76] M. Commodo, L. A. Sgro, P. Minutolo, and A. D'Anna. Characterization of combustion-generated carbonaceous nanoparticles by size-dependent ultraviolet laser photoionization. *Journal of Physical Chemistry A*, 117(19):3980–3989, 2013. URL https://doi.org/10.1021/jp401061d.

[77] M. Commodo, A. D'Anna, G. De Falco, R. Larciprete, and P. Minutolo. Illuminating the earliest stages of the soot formation by photoemission and Raman spectroscopy. *Combustion and Flame*, 181:1339–1351, 2017. URL https://doi.org/10.1016/j.combustflame.2017.03.020.

[78] M. Commodo, K. Kaiser, G. De Falco, P. Minutolo, F. Schulz, A. D'Anna, and L. Gross. On the early stages of soot formation: Molecular structure elucidation by high-resolution atomic force microscopy. *Combustion and Flame*, 205:154–164, 2019. URL https://doi.org/10.1016/j.combustflame.2019.03.042.

[79] Z.-H. Cui, H. Lischka, H. Z. Beneberu, and M. Kertesz. Rotational barrier in phenalenyl neutral radical dimer: Separating pancake and van der Waals interactions. *Journal of the American Chemical Society*, 136(15):5539–5542, 2014. URL https://doi.org/10.1021/ja412862n.

[80] R. F. Curl, M. K. Lee, and G. E. Scuseria. C_{60} Buckminsterfullerene High Yields Unraveled. *The Journal of Physical Chemistry A*, 112(46):11951–11955, 2008. URL https://doi.org/10.1021/jp806951v.

[81] G. Curtis. *The cave painters: Probing the mysteries of the world's first artists*. Anchor, 2007.

[82] E. Dames, B. Sirjean, and H. Wang. Weakly bound carbon- carbon bonds in acenaphthene derivatives and hexaphenylethane. *The Journal of Physical Chemistry A*, 114(2):1161–1168, 2009. URL https://doi.org/10.1021/jp909662m.

[83] A. D'Anna. Combustion–formed nanoparticles. *Proceedings of the Combustion Institute*, 32:593–613, 2009. URL https://doi.org/10.1016/j.proci.2008.09.005.

[84] A. D'Anna, A. D'Alessio, and P. Minutolo. Spectroscopic and chemical characterization of soot inception processes in premixed laminar flames at atmospheric pressure. In *Soot Formation in Combustion*, pages 83–103. Springer, 1994.

[85] A. D'Anna, A. Violi, A. D'Alessio, and A. F. Sarofim. A reaction pathway for nanoparticle formation in rich premixed flames. *Combustion and Flame*, 127(1):1995–2003, 2001. URL https://doi.org/10.1016/S0010-2180(01)00303-0.

[86] A. Das, K. Mahato, and T. Chakraborty. Excimer formation in the mixed dimers of naphthalene and 1-methoxynaphthalene in a supersonic jet. *Physical Chemistry Chemical Physics*, 3(10):1813–1818, 2001. URL https://doi.org/10.1039/B010098F.

[87] R. Das and P. K. Chattaraj. Gas storage potential of ExBox4+and its Li-decorated derivative. *Physical Chemistry Chemical Physics*, 16(40):21964–21979, 2014. URL https://doi.org/10.1039/c4cp02199a.

[88] G. De Falco, F. Picca, M. Commodo, and P. Minutolo. Probing soot structure and electronic properties by optical spectroscopy. *Fuel*, 259:116244, 2020.

[89] C. de Tomas, I. Suarez-Martinez, and N. A. Marks. Graphitization of amorphous carbons: A comparative study of interatomic potentials. *Carbon*, 109:681–693, 2016. URL https://doi.org/10.1016/j.carbon.2016.08.024.

[90] C. de Tomas, I. Suarez-Martinez, F. Vallejos-Burgos, M. J. López, K. Kaneko, and N. A. Marks. Structural prediction of graphitization and porosity in carbide-derived carbons. *Carbon*, 119:1–9, 2017. URL https://doi.org/10.1016/j.carbon.2017.04.004.

[91] C. de Tomas, I. Suarez-Martinez, and N. A. Marks. Carbide-derived carbons for dense and tunable 3D graphene networks. *Applied Physics Letters*, 112(25):251907, 2018. URL https://doi.org/10.1063/1.5030136.

[92] P. Degryse, J. Henderson, and G. Hodgins. *Isotopes in vitreous materials*, volume 1. Leuven University Press, 2009.

[93] S. Denifl, S. Ptasińska, B. Sonnweber, P. Scheier, D. Liu, F. Hagelberg, J. Mack, L. T. Scott, and T. D. Märk. Free-electron attachment to coronene and corannulene in the gas phase. *The Journal of Chemical Physics*, 123(10):104308, 2005. URL https://doi.org/10.1063/1.2008947.

[94] P. A. Denis. Pristine graphene-based catalysis: Significant reduction of the inversion barriers of adsorbed and confined corannulene, sumanene, and dibenzo[a, g]corannulene. *Journal of Physical Chemistry A*, 119(22):5770–5777, 2015. URL https://doi.org/10.1021/acs.jpca.5b02181.

[95] V. L. Deringer, C. Merlet, Y. Hu, T. H. Lee, J. A. Kattirtzi, O. Pecher, G. Csányi, S. R. Elliott, and C. P. Grey. Towards an atomistic understanding of disordered carbon electrode materials. *Chemical Communications*, 54:5988–5991, 2018. URL https://doi.org/10.1039/C8CC01388H.

[96] P. Desgroux, X. Mercier, and K. A. Thomson. Study of the formation of soot and its precursors in flames using optical diagnostics. *Proceedings of the Combustion Institute*, 34(1):1713–1738, 2013. URL https://doi.org/10.1016/j.proci.2012.09.004.

[97] P. Desgroux, A. Faccinetto, X. Mercier, T. Mouton, D. Aubagnac Karkar, and A. El Bakali. Comparative study of the soot formation process in a "nucleation" and a "sooting" low pressure premixed methane flame. *Combustion and Flame*, 184:153–166, 2017. URL https://doi.org/10.1016/j.combustflame.2017.05.034.

[98] S. Di Stasio, J. L. Legarrec, and J. B. Mitchell. Synchrotron radiation studies of additives in combustion, II: Soot agglomerate microstructure change by alkali and alkaline-earth metal addition to a partially premixed flame. *Energy and Fuels*, 25(3): 916–925, 2011. URL https://doi.org/10.1021/ef1012209.

[99] J. R. Dias. Resonance Topology of Fluoranthenoid/Fluorenoid Hydrocarbons and Related Systems. *Polycyclic Aromatic Compounds*, 31(1):48–60, 2011. URL https://doi.org/10.1080/10406638.2011.545732.

[100] F. Ding and B. I. Yakobson. Energy-Driven Kinetic Monte Carlo Method and Its Application in Fullerene Coalescence. *The Journal of Physical Chemistry Letters*, 5 (17):2922–2926, 2014. URL https://doi.org/10.1021/jz501324y.

[101] M. a. Dobrowolski, A. Ciesielski, and M. K. Cyrański. On the aromatic stabilization of corannulene and coronene. *Physical Chemistry Chemical Physics*, 13(46):20557, 2011. URL https://doi.org/10.1039/c1cp21994d.

[102] J.-B. Donnet. *Carbon black: science and technology*. CRC Press, 1993.

[103] L. Dontot, F. Spiegelman, and M. Rapacioli. Structures and energetics of neutral and cationic pyrene clusters. *The Journal of Physical Chemistry A*, 123(44):9531–9543, 2019. URL https://doi.org/10.1021/acs.jpca.9b07007.

[104] M. S. Dresselhaus, G. Dresselhaus, and P. C. Eklund. *Science of fullerenes and carbon nanotubes: their properties and applications*. Elsevier, 1996.

[105] J. A. Dreyer, M. Poli, N. A. Eaves, M. L. Botero, J. Akroyd, S. Mosbach, and M. Kraft. Evolution of the soot particle size distribution along the centreline of an n-heptane/toluene co-flow diffusion flame. *Combustion and Flame*, 209:256–266, 2019. URL https://doi.org/10.1016/j.combustflame.2019.08.002.

[106] J. A. Dreyer, R. I. Slavchov, E. J. Rees, J. Akroyd, M. Salamanca, S. Mosbach, and M. Kraft. Improved methodology for performing the inverse abel transform of flame images for color ratio pyrometry. *Applied Optics*, 58(10):2662–2670, 2019. URL https://doi.org/10.1364/AO.58.002662.

[107] T. Dumitrică, C. M. Landis, and B. I. Yakobson. Curvature-induced polarization in carbon nanoshells. *Chemical Physics Letters*, 360(1-2):182–188, 2002. URL https://doi.org/10.1016/S0009-2614(02)00820-5.

[108] R. C. Dunbar. Binding of transition-metal ions to curved π surfaces: corannulene and coronene. *The Journal of Physical Chemistry A*, 106(42):9809–9819, 2002. URL https://doi.org/10.1021/jp020313b.

[109] P. W. Dunk, N. K. Kaiser, C. L. Hendrickson, J. P. Quinn, C. P. Ewels, Y. Nakanishi, Y. Sasaki, H. Shinohara, A. G. Marshall, and H. W. Kroto. Closed network growth of fullerenes. *Nature Communications*, 3(May):855–859, 2012. URL https://doi.org/10.1038/ncomms1853.

[110] N. A. Eaves, S. B. Dworkin, and M. J. Thomson. Assessing relative contributions of PAHs to soot mass by reversible heterogeneous nucleation and condensation. *Proceedings of the Combustion Institute*, 36(1):935–945, 2017. URL https://doi.org/10.1016/j.proci.2016.06.051.

[111] P. Ehrenfreund and B. H. Foing. Fullerenes and Cosmic Carbon. *Science*, 329(5996):1159–1160, 2010. URL https://doi.org/10.1126/science.1194855.

[112] P. Elvati and A. Violi. Thermodynamics of poly-aromatic hydrocarbon clustering and the effects of substituted aliphatic chains. *Proceedings of the Combustion Institute*, 34(1):1837 – 1843, 2013. URL https://doi.org/10.1016/j.proci.2012.07.030.

[113] P. Elvati, V. Dillstrom, and A. Violi. Oxygen driven soot formation. *Proceedings of the Combustion Institute*, 36(1):825–832, 2017. URL https://doi.org/10.1016/j.proci.2016.09.019.

[114] P. Elvati, K. Turrentine, and A. Violi. The role of molecular properties on the dimerization of aromatic compounds. *Proceedings of the Combustion Institute*, 37(1):1099–1105, 2019. URL https://doi.org/10.1016/j.proci.2018.05.065.

[115] A. Faccinetto, P. Desgroux, M. Ziskind, E. Therssen, and C. Focsa. High-sensitivity detection of polycyclic aromatic hydrocarbons adsorbed onto soot particles using laser desorption/laser ionization/time-of-flight mass spectrometry: An approach to studying the soot inception process in low-pressure flames. *Combustion and Flame*, 158(2):227–239, 2011. URL https://doi.org/10.1016/j.combustflame.2010.08.012.

[116] A. Fahr, W. G. Mallard, and S. E. Stein. Reactions of phenyl radicals with ethene, ethyne, and benzene. *Symposium (International) on Combustion*, 21(1):825–831, 1988. URL https://doi.org/10.1016/S0082-0784(88)80314-X.

[117] M. Faraday. XX. On new compounds of carbon and hydrogen, and on certain other products obtained during the decomposition of oil by heat. *Philosophical Transactions of the Royal Society of London*, 115:440–466, 1825. URL https://doi.org/10.1098/rstl.1825.0022.

[118] M. Faraday. *A course of six lectures on the chemical history of a candle: to which is added a lecture on platinum*. Harper & Brothers, 1861.

[119] G. Ferenczy, C. Reynolds, P. Winn, and A. Stone. MULFIT: a program for calculating electrostatic potential-fitted charges, 1998. *May be obtained by contacting AJ Stone, email address: ajs1@ cam. ac. uk*.

[120] A. C. Ferrari and J. Robertson. Interpretation of raman spectra of disordered and amorphous carbon. *Physical Review B*, 61(20):14095, 2000. URL https://doi.org/10.1103/PhysRevB.61.14095.

[121] A. Fialkov. Investigations on ions in flames. *Progress in Energy and Combustion Science*, 23:399–528, 1997. URL https://doi.org/10.1016/S0360-1285(97)00016-6.

[122] A. S. Filatov, L. T. Scott, and M. A. Petrukhina. π-π Interactions and Solid State Packing Trends of Polycyclic Aromatic Bowls in the Indenocorannulene Family: Predicting Potentially Useful Bulk Properties. *Crystal Growth & Design*, 10(10): 4607–4621, 2010. URL https://doi.org/10.1021/cg100898g.

[123] A. M. Fiore, V. Naik, and E. M. Leibensperger. Air quality and climate connections. *Journal of the Air & Waste Management Association*, 65(6):645–685, 2015. URL https://doi.org/10.1080/10962247.2015.1040526.

[124] E. Frankland. On the influence of atmospheric pressure upon some of the phenomena of combustion. *Journal of the Chemical Society*, 15(1861):168–196, 1862. URL https://doi.org/10.1039/JS8621500168.

[125] E. Frankland. On the source of light in luminous flames. *Journal of the Franklin Institute*, 87(5):330 – 335, 1869. URL https://doi.org/10.1016/0016-0032(69)90579-1.

[126] R. E. Franklin. Crystallite Growth in Graphitizing and Non-Graphitizing Carbons. *Proceedings of the Royal Society of London A: Mathematical, Physical and Engineering Sciences*, 209(1097):196–218, 1951. URL https://doi.org/10.1098/rspa.1951.0197.

[127] D. S. Franzblau. Computation of ring statistics for network models of solids. *Physical Review B*, 44(10):4925–4930, 1991. URL https://doi.org/10.1103/PhysRevB.44.4925.

[128] M. Frenklach. On surface growth mechanism of soot particles. *Symposium (International) on Combustion*, 26(2):2285–2293, 1996. URL https://doi.org/10.1016/S0082-0784(96)80056-7.

[129] M. Frenklach. Reaction mechanism of soot formation in flames. *Physical Chemistry Chemical Physics*, 4(11):2028–2037, 2002. URL https://doi.org/10.1039/b110045a.

[130] M. Frenklach and L. B. Ebert. Comment on the proposed role of spheroidal carbon clusters in soot formation. *The Journal of Physical Chemistry*, 92(2):561–563, 1988. URL https://doi.org/10.1021/j100313a061.

[131] M. Frenklach and H. Wang. Detailed modeling of soot particle nucleation and growth. *Symposium (International) on Combustion*, 23(1):1559–1566, 1991. URL https://doi.org/10.1016/S0082-0784(06)80426-1.

[132] M. Frenklach, D. W. Clary, W. C. Gardiner Jr, and S. E. Stein. Detained kinetic modeling of soot formation in shock-tube pyrolysis of acetylene. *Symposium (International) on Combustion*, 20(1):887–901, 1985. URL https://doi.org/10.1016/S0082-0784(85)80578-6.

[133] M. Frenklach, C. A. Schuetz, and J. Ping. Migration mechanism of aromatic-edge growth. *Proceedings of the Combustion Institute*, 30(1):1389–1396, 2005. URL https://doi.org/10.1016/j.proci.2004.07.048.

[134] M. J. Frisch, G. W. Trucks, H. B. Schlegel, G. E. Scuseria, M. A. Robb, J. R. Cheeseman, G. Scalmani, V. Barone, G. A. Petersson, H. Nakatsuji, X. Li, M. Caricato, A. Marenich, J. Bloino, B. G. Janesko, R. Gomperts, B. Mennucci, H. P. Hratchian, J. V. Ortiz, A. F. Izmaylov, J. L. Sonnenberg, D. Williams-Young, F. Ding, F. Lipparini, F. Egidi, J. Goings, B. Peng, A. Petrone, T. Henderson, D. Ranasinghe, V. G. Zakrzewski, J. Gao, N. Rega, G. Zheng, W. Liang, M. Hada, M. Ehara, K. Toyota, R. Fukuda, J. Hasegawa, M. Ishida, T. Nakajima, Y. Honda, O. Kitao, H. Nakai, T. Vreven, K. Throssell, J. A. Montgomery, J. E. Peralta, F. Ogliaro, M. Bearpark, J. J. Heyd, E. Brothers, K. N. Kudin, V. N. Staroverov, T. Keith, R. Kobayashi, J. Normand, K. Raghavachari, A. Rendell, J. C. Burant, S. S. Iyengar, J. Tomasi, M. Cossi, J. M. Millam, M. Klene, C. Adamo, R. Cammi, J. W. Ochterski, R. L. Martin, K. Morokuma, O. Farkas, J. B. Foresman, and D. J. Fox. Gaussian 09, Revision A 02, 2009.

[135] M. J. Frisch, G. W. Trucks, H. B. Schlegel, G. E. Scuseria, M. A. Robb, J. R. Cheeseman, G. Scalmani, V. Barone, G. A. Petersson, H. Nakatsuji, X. Li, M. Caricato, A. V. Marenich, J. Bloino, B. G. Janesko, R. Gomperts, B. Mennucci, H. P. Hratchian, J. V. Ortiz, A. F. Izmaylov, J. L. Sonnenberg, D. Williams-Young, F. Ding, F. Lipparini, F. Egidi, J. Goings, B. Peng, A. Petrone, T. Henderson, D. Ranasinghe, V. G. Zakrzewski, J. Gao, N. Rega, G. Zheng, W. Liang, M. Hada, M. Ehara, K. Toyota, R. Fukuda, J. Hasegawa, M. Ishida, T. Nakajima, Y. Honda, O. Kitao, H. Nakai, T. Vreven, K. Throssell, J. A. Montgomery, Jr., J. E. Peralta, F. Ogliaro, M. J. Bearpark, J. J. Heyd, E. N. Brothers, K. N. Kudin, V. N. Staroverov, T. A. Keith, R. Kobayashi, J. Normand, K. Raghavachari, A. P. Rendell, J. C. Burant, S. S. Iyengar, J. Tomasi, M. Cossi, J. M. Millam, M. Klene, C. Adamo, R. Cammi, J. W. Ochterski, R. L. Martin, K. Morokuma, O. Farkas, J. B. Foresman, and D. J. Fox. Gaussian~16 Revision B.01, 2016. Gaussian Inc. Wallingford CT.

[136] W. C. Gardiner. The chemistry of flames. *Scientific American*, 246(2):110–125, 1982.

[137] A. Gaydon and A. Fairbairn. Carbon formation from C_2H_2 and CO in discharge tubes. *Symposium (International) on Combustion*, 5(1):324 – 328, 1955. URL https://doi.org/10.1016/S0082-0784(55)80043-4.

[138] A. G. Gaydon. *Spectroscopy and Combustion Theory Lond*. S, 1948.

[139] M. Ge and K. Sattler. Observation of fullerene cones. *Chemical Physics Letters*, 220 (3-5):192–196, 1994. URL https://doi.org/10.1016/0009-2614(94)00167-7.

[140] R. Gerald, C. Johnson, J. Rathke, R. Klingler, G. Sandí, and L. Scanlon. ^{7}Li NMR study of intercalated lithium in curved carbon lattices. *Journal of Power Sources*, 89 (2):237–243, 2000. URL https://doi.org/10.1016/S0378-7753(00)00435-3.

[141] P. Gerhardt and K. Homann. Ions and charged soot particles in hydrocarbon flames. 2. positive aliphatic and aromatic ions in ethyne/oxygen flames. *Journal of Physical Chemistry*, 94(13):5381–5391, 1990. URL https://doi.org/10.1021/j100376a039.

[142] P. Gerhardt, S. Löffler, and K. Homann. Polyhedral carbon ions in hydrocarbon flames. *Chemical Physics Letters*, 137(4):306 – 310, 1987. URL https://doi.org/10.1016/0009-2614(87)80889-8.

[143] H. Ghiassi, P. Toth, I. C. Jaramillo, and J. A. S. Lighty. Soot oxidation-induced fragmentation: Part 1: The relationship between soot nanostructure and oxidation-induced fragmentation. *Combustion and Flame*, 163:179–187, 2016. URL https://doi.org/10.1016/j.combustflame.2015.09.023.

[144] A. Giordana, A. Maranzana, and G. Tonachini. Carbonaceous nanoparticle molecular inception from radical addition and van der waals coagulation of polycyclic aromatic hydrocarbon-based systems. a theoretical study. *The Journal of Physical Chemistry C*, 115(35):17237–17251, 2011. URL https://doi.org/10.1021/jp2010698.

[145] V. V. Gobre and A. Tkatchenko. Scaling laws for van der waals interactions in nanostructured materials. *Nature communications*, 4:2341, 2013. URL https://doi.org/10.1038/ncomms3341.

[146] G. Godard, M. L. Frezzotti, R. Palmeri, and D. C. Smith. 5 - origin of high-pressure disordered metastable phases (lonsdaleite and incipiently amorphized quartz) in metamorphic rocks: Geodynamic shock or crystal-scale overpressure? In L. F. Dobrzhinetskaya, S. W. Faryad, S. Wallis, and S. Cuthbert, editors, *Ultrahigh-Pressure Metamorphism*, pages 125 – 148. Elsevier, London, 2011. URL https://doi.org/10.1016/B978-0-12-385144-4.00004-7.

[147] A. Goel, P. Hebgen, J. B. Vander Sande, and J. B. Howard. Combustion synthesis of fullerenes and fullerenic nanostructures. *Carbon*, 40(2):177–182, 2002. URL https://doi.org/10.1016/S0008-6223(01)00170-1.

[148] L. Goerigk and S. Grimme. A thorough benchmark of density functional methods for general main group thermochemistry, kinetics, and noncovalent interactions. *Physical Chemistry Chemical Physics*, 13:6670–6688, 2011. URL https://doi.org/10.1039/C0CP02984J.

[149] M. D. Gottsegen. *The painter's handbook: a complete reference*. Watson-Guptill, 2006.

[150] S. Grabowsky, M. Weber, Y. S. Chen, D. Lentz, B. M. Schmidt, M. Hesse, and P. Luger. Electron density of corannulene from synchrotron data at 12 K, comparison with fullerenes. *Zeitschrift fur Naturforschung - Section B Journal of Chemical Sciences*, 65(4):452–460, 2010. URL https://doi.org/10.1515/znb-2010-0403.

[151] S. M. Graham and J. M. Goodings. Metallic ions in hydrocarbon flames. ii. mechanism for the reduction of c3h3+ by metals in relation to soot suppression. *International journal of mass spectrometry and ion processes*, 56(2):205–222, 1984. URL https://doi.org/10.1016/0168-1176(84)85044-2.

[152] F. Granger. *Vitruvius. On Architecture, Volume II: Books 6-10.*, volume 2. Harvard University Press, 1934.

[153] W. J. Grieco, J. B. Howard, L. C. Rainey, and J. B. V. Sande. Fullerenic carbon in combustion-generated soot. *Carbon*, 38(4):597 – 614, 2000. URL https://doi.org/10.1016/S0008-6223(99)00149-9.

[154] S. Grimme. Semiempirical GGA-type density functional constructed with a long-range dispersion correction. *Journal of Computational Chemistry*, 27(15):1787–1799, 2006. URL https://doi.org/10.1002/jcc.20495.

[155] S. Grimme. Semiempirical GGA-type density functional constructed with a long-range dispersion correction. *Journal of Computational Chemistry*, 27(15):1787–1799, 2006. URL https://doi.org/10.1002/jcc.20495.

[156] S. Grimme, J. Antony, T. Schwabe, and C. Mück-Lichtenfeld. Density functional theory with dispersion corrections for supramolecular structures, aggregates, and complexes of (bio)organic molecules. *Organic & Biomolecular Chemistry*, 5(5): 741–758, 2007. URL https://doi.org/10.1039/b615319b.

[157] H.-H. Grotheer, K. Wolf, and K. Hoffmann. Photoionization mass spectrometry for the investigation of combustion generated nascent nanoparticles and their relation to laser induced incandescence. *Applied Physics B*, 104(2):367–383, 2011. URL https://doi.org/10.1007/s00340-011-4403-9.

[158] J. Guan, Z. Jin, Z. Zhu, C. Chuang, B. Y. Jin, and D. Tománek. Local curvature and stability of two-dimensional systems. *Physical Review B - Condensed Matter and Materials Physics*, 90(24):1–6, 2014. URL https://doi.org/10.1103/PhysRevB.90.245403.

[159] J. Guo, J. R. Morris, Y. Ihm, C. I. Contescu, N. C. Gallego, G. Duscher, S. J. Pennycook, and M. F. Chisholm. Topological Defects: Origin of Nanopores and Enhanced Adsorption Performance in Nanoporous Carbon. *Small*, 8(21):3283–3288, 2012. URL https://doi.org/10.1002/smll.201200894.

[160] S. Gupta and A. Saxena. A topological twist on materials science. *MRS Bulletin*, 39 (3):265–279, 2014. URL https://doi.org/10.1557/mrs.2014.28.

[161] R. C. Haddon. Hybridization and the orientation and alignment of π-orbitals in nonplanar conjugated organic molecules: π-orbital axis vector analysis (POAV2). *Journal of the American Chemical Society*, 108(11):2837–2842, 1986. URL https://doi.org/10.1021/ja00271a009.

[162] R. B. Hamanaka and G. M. Mutlu. Particulate matter air pollution: Effects on the cardiovascular system. *Frontiers in Endocrinology*, 9:680, 2018. URL https://doi.org/10.3389/fendo.2018.00680.

[163] S. Han, X. Li, F. Nie, M. Zheng, X. Liu, and L. Guo. Revealing the Initial Chemistry of Soot Nanoparticle Formation by ReaxFF Molecular Dynamics Simulations. *Energy & Fuels*, 31(8):8434–8444, 2017. URL https://doi.org/10.1021/acs.energyfuels.7b01194.

[164] N. Hansen, T. A. Cool, P. R. Westmoreland, and K. Kohse-Höinghaus. Recent contributions of flame-sampling molecular-beam mass spectrometry to a fundamental understanding of combustion chemistry. *Progress in Energy and Combustion Science*, 35(2):168–191, 2009. URL https://doi.org/10.1016/j.pecs.2008.10.001.

[165] J. Happold, H.-H. Grotheer, and M. Aigner. Soot precursors consisting of stacked pericondensed PAHs. In H. Bockhorn, A. D'Anna, A. Sarofim, and H. Wang, editors, *Combustion Generated Fine Carbonaceous Particles*, chapter 18, pages 277 – 288. KIT Scientific Publishing, Karlsruhe, Germany, 2009.

[166] P. J. F. Harris. Structure of non-graphitising carbons. *International Materials Reviews*, 42(5):206–218, 1997. URL https://doi.org/10.1179/095066097790093172.

[167] P. J. F. Harris. Fullerene-related structure of commercial glassy carbons. *Philosophical Magazine*, 84(29):3159–3167, 2004. URL https://doi.org/10.1080/14786430410001720363.

[168] P. J. F. Harris. Fullerene-like models for microporous carbon. *Journal of Materials Science*, 48(2):565–577, 2013. URL https://doi.org/10.1007/s10853-012-6788-1.

[169] P. J. F. Harris, Z. Liu, and K. Suenaga. Imaging the atomic structure of activated carbon. *Journal of Physics: Condensed Matter*, 20(36):362201, 2008. URL https://doi.org/10.1088/0953-8984/20/36/362201.

[170] S. J. Harris and A. M. Weiner. A picture of soot particle inception. *Symposium (International) on Combustion*, 22(1):333 – 342, 1989. URL https://doi.org/10.1016/S0082-0784(89)80039-6.

[171] A. N. Hayhurst and H. R. N. Jones. Ions and soot in flames. *Journal of the Chemical Society, Faraday Transactions 2*, 83(1):1, 1987. URL https://doi.org/10.1039/f29878300001.

[172] B. Haynes, H. Jander, and H. Wagner. The effect of metal additives on the formation of soot in premixed flames. *Symposium (International) on Combustion*, 17(1):1365–1374, 1979. URL https://doi.org/10.1016/S0082-0784(79)80128-9.

[173] B. S. Haynes and H. G. Wagner. Soot Formation. *Progress in Energy and Combustion Science*, 7(4):229–273, 1981. URL https://doi.org/10.1016/0360-1285(81)90001-0.

[174] R. D. Heidenreich, W. M. Hess, and L. L. Ban. A test object and criteria for high resolution electron microscopy. *Journal of Applied Crystallography*, 1(1):1–19, 1968. URL https://doi.org/10.1107/S0021889868004930.

[175] T. Helgaker, J. Gauss, P. Jörgensen, and J. Olsen. The prediction of molecular equilibrium structures by the standard electronic wave functions. *The Journal of Chemical Physics*, 106(15):6430–6440, 1997. URL https://doi.org/10.1063/1.473634.

[176] G. R. Hennig. Screw dislocations in graphite. *Science*, 147(3659):733–734, 1965. URL https://doi.org/10.1126/science.147.3659.733.

[177] D. Heymann, L. P. Chibante, R. R. Brooks, W. S. Wolbach, and R. E. Smalley. Fullerenes in the Cretaceous-Tertiary boundary layer. *Science*, 265(5172):645–647, 1994. URL https://doi.org/10.1126/science.265.5172.645.

[178] A. L. Hickey and C. N. Rowley. Benchmarking quantum chemical methods for the calculation of molecular dipole moments and polarizabilities. *The Journal of Physical Chemistry A*, 118(20):3678–3687, 2014. URL https://doi.org/10.1021/jp502475e.

[179] F. Hirsch, P. Constantinidis, I. Fischer, S. Bakels, and A. M. Rijs. Dimerization of the benzyl radical in a high-temperature pyrolysis reactor investigated by IR/UV ion dip spectroscopy. *Chemistry–A European Journal*, 24(30):7647–7652, 2018. URL https://doi.org/10.1002/chem.201800852.

[180] F. Hirsch, E. Reusch, P. Constantinidis, I. Fischer, S. Bakels, A. M. Rijs, and P. Hemberger. Self-reaction of ortho-benzyne at high temperatures investigated by infrared and photoelectron spectroscopy. *The Journal of Physical Chemistry A*, 122(49): 9563–9571, 2018. URL https://doi.org/10.1021/acs.jpca.8b09640.

[181] M. M. Hirschler. Soot from fires: II. mechanisms of soot formation. *Journal of fire sciences*, 3(6):380–414, 1985. URL https://doi.org/10.1177/073490418500300602.

[182] J. Hoche, H.-C. Schmitt, A. Humeniuk, I. Fischer, R. Mitrić, and M. I. Röhr. The mechanism of excimer formation: an experimental and theoretical study on the pyrene dimer. *Physical Chemistry Chemical Physics*, 19(36):25002–25015, 2017. URL https://doi.org/10.1039/C7CP03990E.

[183] B. Hoffmann, S. Moebus, S. Möhlenkamp, A. Stang, N. Lehmann, N. Dragano, A. Schmermund, M. Memmesheimer, K. Mann, R. Erbel, and K.-H. Jöckel. Residential exposure to traffic is associated with coronary atherosclerosis. *Circulation*, 116 (5):489–496, 2007. URL https://doi.org/10.1161/CIRCULATIONAHA.107.693622.

[184] P. Hohenberg and W. Kohn. Inhomogeneous Electron Gas. *Physical Review*, 136(3B): B864–B871, 1964. URL https://doi.org/10.1103/PhysRev.136.B864.

[185] K. Homann and H. Wagner. Some new aspects of the mechanism of carbon formation in premixed flames. *Symposium (International) on Combustion*, 11(1):371–379, 1967. URL https://doi.org/10.1016/S0082-0784(67)80161-9.

[186] K. H. Homann. Fullerenes and soot formation - New pathways to large particles in flames. *Angewandte Chemie, International Edition in English*, 37(18):2435–2451, 1998. URL https://doi.org/10.1002/(SICI)1521-3773(19981002)37:18%3C2434:: AID-ANIE2434%3E3.0.CO;2-L.

[187] K.-H. Homann and H. G. Wagner. *Some aspects of soot formation*. Carbon and Breach Publishers, 1996.

[188] D. Hou and X. You. Reaction kinetics of hydrogen abstraction from polycyclic aromatic hydrocarbons by H atoms. *Physical Chemistry Chemical Physics*, 19(45): 30772–30780, 2017. URL https://doi.org/10.1039/c7cp04964a.

[189] J. B. Howard. Carbon addition and oxidation reactions in heterogeneous combustion and soot formation. 23(1):1107–1127, 1991. URL https://doi.org/10.1016/S0082-0784(06)80371-1.

[190] J. B. Howard and W. J. Kausch. Soot control by fuel additives. *Progress in Energy and Combustion Science*, 6(3):263–276, 1980. URL https://doi.org/10.1016/0360-1285(80)90018-0.

[191] C.-H. Huang and R. L. Vander Wal. Partial premixing effects upon soot nanostructure. *Combustion and Flame*, 168:403–408, 2016. URL https://doi.org/10.1016/j.combustflame.2016.01.006.

[192] J. Y. Huang, F. Ding, K. Jiao, and B. I. Yakobson. Real Time Microscopy, Kinetics, and Mechanism of Giant Fullerene Evaporation. *Physical Review Letters*, 99(17):175503, 2007. URL https://doi.org/10.1103/PhysRevLett.99.175503.

[193] S. Iavarone, L. Pascazio, M. Sirignano, A. De Candia, A. Fierro, L. De Arcangelis, and A. D'Anna. Molecular dynamics simulations of incipient carbonaceous nanoparticle formation at flame conditions. *Combustion Theory and Modelling*, 21(1):49–61, 2017. URL https://doi.org/10.1080/13647830.2016.1242156.

[194] S. Iijima. Direct observation of the tetrahedral bonding in graphitized carbon black by high resolution electron microscopy. *Journal of Crystal Growth*, 50(3):675–683, 1980. URL https://doi.org/10.1016/0022-0248(80)90013-5.

[195] Industry Experts. Carbon Black – A Global Market Overview. Technical report, Industry experts, 2012. URL http://industry-experts.com/verticals/chemicals-and-materials/carbon-black-a-global-market-overview.

[196] C. Irimiea, A. Faccinetto, X. Mercier, I.-K. Ortega, N. Nuns, E. Therssen, P. Desgroux, and C. Focsa. Unveiling trends in soot nucleation and growth: When secondary ion mass spectrometry meets statistical analysis. *Carbon*, 144:815 – 830, 2019. URL https://doi.org/10.1016/j.carbon.2018.12.015.

[197] S. Irle, G. Zheng, Z. Wang, and K. Morokuma. The C_{60} formation puzzle "solved": QM/MD simulations reveal the shrinking hot giant road of the dynamic fullerene self-assembly mechanism. *Journal of Physical Chemistry B*, 110:14531–14545, 2006. URL https://doi.org/10.1021/jp061173z.

[198] Y. Ito, Y. Tanabe, K. Sugawara, M. Koshino, T. Takahashi, K. Tanigaki, H. Aoki, and M. Chen. Three-dimensional porous graphene networks expand graphene-based electronic device applications. *Phys. Chem. Chem. Phys.*, 20(9):6024–6033, 2018. URL https://doi.org/10.1039/C7CP07667C.

[199] S. S. Iyengar, H. B. Schlegel, J. M. Millam, G. A. Voth, G. E. Scuseria, and M. J. Frisch. Ab initio molecular dynamics: Propagating the density matrix with Gaussian orbitals. II. Generalizations based on mass-weighting, idempotency, energy conservation and choice of initial conditions. *Journal of Chemical Physics*, 115(22):10291–10302, 2001. URL https://doi.org/10.1063/1.1416876.

[200] T. Janowski and P. Pulay. A benchmark comparison of σ/σ and π/π dispersion: The dimers of naphthalene and decalin, and coronene and perhydrocoronene. *Journal of the American Chemical Society*, 134(42):17520–17525, 2012. URL https://doi.org/10.1021/ja303676q.

[201] T. Janowski, P. Pulay, A. A. Sasith Karunarathna, A. Sygula, and S. Saebø. Convex-concave stacking of curved conjugated networks: Benchmark calculations on the corannulene dimer. *Chemical Physics Letters*, 512(4-6):155–160, 2011. URL https://doi.org/10.1016/j.cplett.2011.07.030.

[202] G. M. Jenkins and K. Kawamura. Structure of glassy carbon. *Nature*, 231:175–176, 1971. URL https://doi.org/10.1038/231175a0.

[203] G. R. Jenness and K. D. Jordan. DF-DFT-SAPT Investigation of the Interaction of a Water Molecule to Coronene and Dodecabenzocoronene: Implications for the Water - Graphite Interaction. *The Journal of Physical Chemistry C*, 113(23):10242–10248, 2009. URL https://doi.org/10.1021/jp9015307.

[204] K. Johansson, M. Head-Gordon, P. Schrader, K. Wilson, and H. Michelsen. Resonance-stabilized hydrocarbon-radical chain reactions may explain soot inception and growth. *Science*, 361(6406):997–1000, 2018. URL https://doi.org/10.1126/science.aat3417.

[205] K. O. Johansson, T. Dillstrom, M. Monti, F. El Gabaly, M. F. Campbell, P. E. Schrader, D. M. Popolan-Vaida, N. K. Richards-Henderson, K. R. Wilson, A. Violi, et al. Formation and emission of large furans and oxygenated hydrocarbons from flames. *Proceedings of the National Academy of Sciences*, 113(30):8374–8379, 2016. URL https://doi.org/10.1073/pnas.1604772113.

[206] W. L. Jorgensen, J. Chandrasekhar, J. D. Madura, R. W. Impey, and M. L. Klein. Comparison of simple potential functions for simulating liquid water. *The Journal of Chemical Physics*, 79(2):926–935, 1983. URL https://doi.org/10.1063/1.445869.

[207] Y. Ju, J. K. Lefkowitz, C. B. Reuter, S. H. Won, X. Yang, S. Yang, W. Sun, Z. Jiang, and Q. Chen. Plasma assisted low temperature combustion. *Plasma Chemistry and Plasma Processing*, 36(1):85–105, 2016. URL https://doi.org/10.1007/s11090-015-9657-2.

[208] M. Juríček, N. L. Strutt, J. C. Barnes, A. M. Butterfield, E. J. Dale, K. K. Baldridge, J. F. Stoddart, and J. S. Siegel. Induced-fit catalysis of corannulene bowl-to-bowl inversion. *Nature Chemistry*, 6(3):222–228, 2014. URL https://doi.org/10.1038/nchem.1842.

[209] S. V. Kalinin and V. Meunier. Electronic flexoelectricity in low-dimensional systems. *Physical Review B*, 77(3):1–4, 2008. URL https://doi.org/10.1103/PhysRevB.77.033403.

[210] G. A. Kaminski, R. A. Friesner, J. Tirado-Rives, and W. L. Jorgensen. Evaluation and reparametrization of the OPLS-AA force field for proteins via comparison with accurate quantum chemical calculations on peptides. *The Journal of Physical Chemistry B*, 105(28):6474–6487, 2001. URL https://doi.org/10.1021/jp003919d.

[211] A. Karton. Inversion and rotation processes involving non-planar aromatic compounds catalyzed by extended polycyclic aromatic hydrocarbons. *Chemical Physics Letters*, 614:156–161, 2014. URL https://doi.org/10.1016/j.cplett.2014.09.032.

[212] D. Kashchiev. *Nucleation*. Butterworth-Heinemann, 2000.

[213] A. Keller, R. Kovacs, and K.-H. Homann. Large molecules, ions, radicals and small soot particles in fuel-rich hydrocarbon flames. part iv. large polycyclic aromatic hydrocarbons and their radicals in a fuel-rich benzene–oxygen flame. *Physical Chemistry Chemical Physics*, 2(8):1667–1675, 2000. URL https://doi.org/10.1039/A908190I.

[214] M. Keller, T. de Bruin, M. Matrat, e. Nicolle, Andr and L. Catoire. A theoretical multiscale approach to study the initial steps involved in the chemical reactivity of soot precursors. *Energy & Fuels*, 33(10):10255–10266, 2019. URL https://doi.org/10.1021/acs.energyfuels.9b02284.

[215] M. Kertesz. Pancake bonding: An unusual pi-stacking interaction. *Chemistry–A European Journal*, 25(2):400–416, 2019. URL https://doi.org/10.1002/chem.201802385.

[216] J. Kewley and J. S. Jackson. The burning of mineral oils in wick-fed lamps. *Journal of the Institute of Petroleum*, 13:364–394, 1927.

[217] M. Kholghy, M. Saffaripour, C. Yip, and M. J. Thomson. The evolution of soot morphology in a laminar coflow diffusion flame of a surrogate for Jet A-1. *Combustion and Flame*, 160(10):2119–2130, 2013. URL https://doi.org/10.1016/j.combustflame.2013.04.008.

[218] M. R. Kholghy, A. Veshkini, and M. J. Thomson. The core-shell internal nanostructure of soot - A criterion to model soot maturity. *Carbon*, 100(January):508–536, 2016. URL https://doi.org/10.1016/j.carbon.2016.01.022.

[219] M. R. Kholghy, G. A. Kelesidis, and S. E. Pratsinis. Reactive polycyclic aromatic hydrocarbon dimerization drives soot nucleation. *Physical Chemistry Chemical Physics*, 20:10926–10938, 2018. URL https://doi.org/10.1039/C7CP07803J.

[220] D. Klein. Graphitic polymer strips with edge states. *Chemical Physics Letters*, 217(3): 261–265, 1994. URL https://doi.org/10.1016/0009-2614(93)E1378-T.

[221] M. Kleman, O. D. Lavrentovich, and Y. A. Nastishin. Chapter 66 - dislocations and disclinations in mesomorphic phases. In F. Nabarro and J. Hirth, editors, *Dislocations in Solids*, volume 12 of *Dislocations in Solids*, pages 147 – 271. Elsevier, 2004. URL https://doi.org/10.1016/S1572-4859(05)80005-1.

[222] M. Knaapila, O. T. Rømoen, E. Svåsand, J. P. Pinheiro, Ø. G. Martinsen, M. Buchanan, A. T. Skjeltorp, and G. Helgesen. Conductivity Enhancement in Carbon Nanocone Adhesive by Electric Field Induced Formation of Aligned Assemblies. *ACS Applied Materials & Interfaces*, 3(2):378–384, 2011. URL https://doi.org/10.1021/am100990c.

[223] K. Kobayashi. Electronic structure of a stepped graphite surface. *Physical Review B*, 48(3):1757, 1993. URL https://doi.org/10.1103/PhysRevB.48.1757.

[224] Y. Kobayashi, T. Furuhata, K. Amagai, and M. Arai. Soot precursor measurements in benzene and hexane diffusion flames. *Combustion and Flame*, 154(3):346–355, 2008. URL https://doi.org/10.1016/j.combustflame.2008.03.022.

[225] W. Kohn and L. J. Sham. Self-consistent equations including exchange and correlation effects. *Physical Review*, 140(4A), 1965. URL https://doi.org/10.1103/PhysRev.140.A1133.

[226] S. Kolakkandy, S. Pratihar, A. J. A. Aquino, H. Wang, and W. L. Hase. Properties of Complexes Formed by Na^+, Mg^{2+}, and Fe^{2+} Binding with Benzene Molecules. *The Journal of Physical Chemistry A*, 118(40):9500–9511, 2014. URL https://doi.org/10.1021/jp5029257.

[227] D. Koley, E. Arunan, and S. Ramakrishnan. Computational investigations on covalent dimerization/oligomerization of polyacenes: Is it relevant to soot formation? *Journal of Computational Chemistry*, 33(21):1762–1772, 2012. URL https://doi.org/10.1002/jcc.23014.

[228] M. Kono, K. Iinuma, and S. Kumagai. The effect of DC to 10 mhz electric field on flame luminosity and carbon formation. *Symposium (International) on Combustion*, 18(1):1167–1174, 1981. URL https://doi.org/10.1016/S0082-0784(81)80121-X.

[229] C. Kramer, P. Gedeck, and M. Meuwly. Atomic multipoles: Electrostatic potential fit, local reference axis systems, and conformational dependence. *Journal of Computational Chemistry*, 33(20):1673–1688, 2012. URL https://doi.org/10.1002/jcc.22996.

[230] W. Krätschmer, L. D. Lamb, K. Fostiropoulos, and D. R. Huffman. Solid $C_6$0: a new form of carbon. *Nature*, 347(6291):354, 1990. URL https://doi.org/10.1038/347354a0.

[231] A. Krestinin. Polyyne model of soot formation process. *Symposium (International) on Combustion*, 27(1):1557–1563, 1998. URL https://doi.org/10.1016/S0082-0784(98)80564-X.

[232] A. Krishnan, E. Dujardin, M. M. J. Treacy, J. Hugdahl, S. Lynum, and T. W. Ebbesen. Graphitic cones and the nucleation of curved carbon surfaces. *Nature*, 388(6641):451–454, 1997. URL https://doi.org/10.1038/41284.

[233] H. W. Kroto and K. McKay. The formation of quasi-icosahedral spiral shell carbon particles. *Nature*, 331(6154):328–331, 1988. URL https://doi.org/10.1038/331328a0.

[234] H. W. Kroto, J. R. Heath, S. C. O'Brien, R. F. Curl, and R. E. Smalley. C60: Buckminsterfullerene. *Nature*, 318(6042):162–163, 1985. URL https://doi.org/10.1038/318162a0.

[235] R. A. Krueger and G. Blanquart. Predicting aromatic exciplex fluorescence emission energies. *Phys. Chem. Chem. Phys.*, 21(20):10325–10335, 2019. URL https://doi.org/10.1039/C9CP02027F.

[236] S. I. Kundalwal, S. A. Meguid, and G. J. Weng. Strain gradient induced polarization in graphene. *Carbon*, 1(416):1–35, 2017. URL https://doi.org/10.1016/j.carbon.2017.03.013.

[237] A. G. Kvashnin, P. B. Sorokin, and B. I. Yakobson. Flexoelectricity in Carbon Nanostructures: Nanotubes, Fullerenes, and Nanocones. *The Journal of Physical Chemistry Letters*, 6(14):2740–2744, 2015. URL https://doi.org/10.1021/acs.jpclett.5b01041.

[238] A. L. Lafleur, J. B. Howard, J. A. Marr, and T. Yadav. Proposed fullerene precursor corannulene identified in flames both in the presence and absence of fullerene production. *The Journal of Physical Chemistry*, 97(51):13539–13543, 1993. URL https://doi.org/10.1021/j100153a020.

[239] A. L. Lafleur, J. B. Howard, K. Taghizadeh, E. F. Plummer, L. T. Scott, A. Necula, and K. C. Swallow. Identification of $C_{20}H_{10}$ Dicyclopentapyrenes in Flames: Correlation with Corannulene and Fullerene Formation. *The Journal of Physical Chemistry*, 100 (43):17421–17428, 1996. URL https://doi.org/10.1021/jp9605313.

[240] J. Lahaye and G. Prado. Formation of carbon particles from a gas phase: Nucleation phenomenon. *Water, Air, and Soil Pollution*, 3(4):473–481, 1974. URL https://doi.org/10.1007/BF00341000.

[241] P. J. Landrigan, R. Fuller, N. J. R. Acosta, O. Adeyi, R. Arnold, N. N. Basu, A. B. Baldé, R. Bertollini, S. Bose-O'Reilly, J. I. Boufford, P. N. Breysse, T. Chiles, C. Mahidol, A. M. Coll-Seck, M. L. Cropper, J. Fobil, V. Fuster, M. Greenstone, A. Haines, D. Hanrahan, D. Hunter, M. Khare, A. Krupnick, B. Lanphear, B. Lohani, K. Martin, K. V. Mathiasen, M. A. McTeer, C. J. L. Murray, J. D. Ndahimananjara, F. Perera, J. Potočnik, A. S. Preker, J. Ramesh, J. Rockström, C. Salinas, L. D. Samson, K. Sandilya, P. D. Sly, K. R. Smith, A. Steiner, R. B. Stewart, W. A. Suk, O. C. P. van Schayck, G. N. Yadama, K. Yumkella, and M. Zhong. The Lancet Commission on pollution and health. *The Lancet*, 2017. URL https://doi.org/10.1016/S0140-6736(17)32345-0.

[242] J. Lawton and F. Weinberg. *Electrical aspects of combustion.* Clarendon P., 1969.

[243] R. G. Lawton and W. E. Barth. Synthesis of corannulene. *Journal of the American Chemical Society*, 93(7):1730–1745, 1971. URL https://doi.org/10.1021/ja00736a028.

[244] K. C. Le, C. Lefumeux, P.-E. Bengtsson, and T. Pino. Direct observation of aliphatic structures in soot particles produced in low-pressure premixed ethylene flames via online raman spectroscopy. *Proceedings of the Combustion Institute*, 37(1):869–876, 2019. URL https://doi.org/10.1016/j.proci.2018.08.003.

[245] A. R. Leach and A. R. Leach. *Molecular modelling: principles and applications.* Pearson education, 2001.

[246] C. Lee, W. Yang, and R. G. Parr. Development of the Colle-Salvetti correlation-energy formula into a functional of the electron density. *Physical Review B*, 37(2):785–789, 1988. URL https://doi.org/10.1103/PhysRevB.37.785.

[247] V. B. Lewes. XXV.–the luminosity of coal-gas flames. *Journal of the Chemical Society, Transactions*, 61:322–339, 1892. URL https://doi.org/10.1039/CT8926100322.

[248] J.-M. Leyssale, J.-P. D. Costa, C. Germain, P. Weisbecker, and G. L. Vignoles. Structural features of pyrocarbon atomistic models constructed from transmission electron microscopy images. *Carbon*, 50(12):4388 – 4400, 2012. URL https://doi.org/10.1016/j.carbon.2012.05.015.

[249] W. Li, X. Zhou, W. Q. Tian, and X. Sun. A new scheme for significant enhancement of the second order nonlinear optical response from molecules to ordered aggregates. *Physical Chemistry Chemical Physics*, 15(6):1810, 2013. URL https://doi.org/10.1039/c2cp43536e.

[250] X. Li, D. T. Moore, and S. S. Iyengar. Insights from first principles molecular dynamics studies toward infrared multiple-photon and single-photon action spectroscopy: Case study of the proton-bound dimethyl ether dimer. *The Journal of Chemical Physics*, 128(18):184308, 2008. URL https://doi.org/10.1063/1.2903446.

[251] J. Lighty, V. Romano, and A. Sarofim. Soot precursors consisting of stacked peri-condensed PAHs. In H. Bockhorn, A. D'Anna, A. Sarofim, and H. Wang, editors, *Combustion Generated Fine Carbonaceous Particles*, pages 487–500. KIT Scientific Publishing, Karlsruhe, Germany, 2009.

[252] H. Liu, T. Ye, and C. Mao. Fluorescent carbon nanoparticles derived from candle soot. *Angewandte Chemie - International Edition*, 46(34):6473–6475, 2007. URL https://doi.org/10.1002/anie.200701271.

[253] J. Liu, H. Ke, K. Zhong, X. He, X. Xue, L. Wang, and C. Zhang. Higher activity leading to higher disorder: A case of four light hydrocarbons to variable morphological carbonaceous materials by pyrolysis. *The Journal of Physical Chemistry C*, 122(51): 29516–29525, 2018. URL https://doi.org/10.1021/acs.jpcc.8b07762.

[254] M. Liu, V. I. Artyukhov, H. Lee, F. Xu, and B. I. Yakobson. Carbyne from first principles: chain of C atoms, a nanorod or a nanorope. *ACS nano*, 7(11):10075–10082, 2013. URL https://doi.org/10.1021/nn404177r.

[255] S. Liu, M. F. Jarrold, and M. T. Bowers. Ion-molecule clustering in simple systems. a study of the temperature dependence of the dimerization reactions of $CH_2CF_2^+$, $C_6H_6^+$ (benzene), and $C_6D_6^+$ (benzene-d6) in their parent neutral gases: experiment and theory. *The Journal of Physical Chemistry*, 89(14):3127–3134, 1985. URL https://doi.org/10.1021/j100260a035.

[256] Z. Liu, K. Suenaga, P. J. Harris, and S. Iijima. Open and closed edges of graphene layers. *Physical Review Letters*, 102(1):015501, 2009.

[257] F. J. Lovas, R. J. McMahon, J. U. Grabow, M. Schnell, J. Mack, L. T. Scott, and R. L. Kuczkowski. Interstellar chemistry: A strategy for detecting polycyclic aromatic hydrocarbons in space. *Journal of the American Chemical Society*, 127(12):4345–4349, 2005. URL https://doi.org/10.1021/ja0426239.

[258] T. Lu and F. Chen. Multiwfn: a multifunctional wavefunction analyzer. *Journal of Computational Chemistry*, 33(5):580–592, 2012. URL https://doi.org/10.1002/jcc.22885.

[259] A. Mackay and H. Terrones. Diamond from graphite. *Nature*, 352(6338):762, 1991. URL https://doi.org/10.1038/352762a0.

[260] L. Madden, L. Moskaleva, S. Kristyan, and M. Lin. Ab initio MO study of the unimolecular decomposition of the phenyl radical. *The Journal of Physical Chemistry A*, 101(36):6790–6797, 1997. URL https://doi.org/10.1021/jp970723d.

[261] E. R. Magaril and R. Z. Magaril. *Engine fuels*. KDU, Moscow, 2008.

[262] Q. Mao, A. C. T. van Duin, and K. H. Luo. Formation of incipient soot particles from polycyclic aromatic hydrocarbons: A ReaxFF molecular dynamics study. *Carbon*, 121:380–388, 2017. URL https://doi.org/10.1016/j.carbon.2017.06.009.

[263] Q. Mao, D. Hou, K. H. Luo, and X. You. Dimerization of polycyclic aromatic hydrocarbon molecules and radicals under flame conditions. *The Journal of Physical Chemistry A*, 122(44):8701–8708, 2018. URL https://doi.org/10.1021/acs.jpca.8b07102.

[264] A. Maranzana and G. Tonachini. Antagonistic functionalized nucleation and oxidative degradation in combustive formation of pyrene-based clusters mediated by triplet O and O_2: Theoretical study. *ChemPhysChem*, 16(12):2615–2624, 2015. URL https://doi.org/10.1002/cphc.201500332.

[265] H. Marsh and F. R. Reinoso. *Activated carbon*. Elsevier, 2006.

[266] J. W. Martin, G. J. McIntosh, R. Arul, R. N. Oosterbeek, M. Kraft, and T. Söhnel. Giant fullerene formation through thermal treatment of fullerene soot. *Carbon*, 125: 132–138, 2017. URL https://doi.org/10.1016/j.carbon.2017.09.045.

[267] J. W. Martin, R. I. Slavchov, E. K. Yapp, J. Akroyd, S. Mosbach, and M. Kraft. The polarization of polycyclic aromatic hydrocarbons curved by pentagon incorporation: the role of the flexoelectric dipole. *The Journal of Physical Chemistry C*, 121(48): 27154–27163, 2017. URL https://doi.org/10.1021/acs.jpcc.7b09044.

[268] J. W. Martin, M. Botero, R. I. Slavchov, K. Bowal, J. Akroyd, S. Mosbach, and M. Kraft. Flexoelectricity and the formation of carbon nanoparticles in flames. *The Journal of Physical Chemistry C*, 122(38):22210–22215, 2018. URL https://doi.org/10.1021/acs.jpcc.8b08264.

[269] J. W. Martin, M. Botero, R. I. Slavchov, K. Bowal, J. Akroyd, S. Mosbach, and M. Kraft. Flexoelectricity and the Formation of Carbon Nanoparticles in Flames. *The Journal of Physical Chemistry C*, 122(38):22210–22215, 2018. URL https://doi.org/10.1021/acs.jpcc.8b08264.

[270] J. W. Martin, K. L. Bowal, A. Menon, R. I. Slavchov, J. Akroyd, S. Mosbach, and M. Kraft. Polar curved polycyclic aromatic hydrocarbons in soot formation. *Proceedings of the Combustion Institute*, 37(1):1117–1123, 2019. URL https://doi.org/10.1016/j.proci.2018.05.046.

[271] J. W. Martin, C. de Tomas, I. Suarez-Martinez, M. Kraft, and N. A. Marks. Topology of disordered 3D graphene networks. *Physical Review Letters*, 123(11):116105, 2019. URL https://doi.org/10.1103/PhysRevLett.123.116105.

[272] J. W. Martin, D. Hou, A. Menon, L. Pascazio, J. Akroyd, X. You, and M. Kraft. Reactivity of polycyclic aromatic hydrocarbon soot precursors: Implications of localized π-radicals on rim-based pentagonal rings. *The Journal of Physical Chemistry C*, 123 (43):26673–26682, 2019. URL https://doi.org/10.1021/acs.jpcc.9b07558.

[273] J. W. Martin, A. Menon, C. T. Lao, J. Akroyd, and M. Kraft. Dynamic polarity of curved aromatic soot precursors. *Combustion and Flame*, 206:150–157, 2019. URL https://doi.org/10.1016/j.combustflame.2019.04.046.

[274] D. Martin-Jimenez, S. Ahles, D. Mollenhauer, H. A. Wegner, A. Schirmeisen, and D. Ebeling. Bond-level imaging of the 3d conformation of adsorbed organic molecules using atomic force microscopy with simultaneous tunneling feedback. *Physical Review Letters*, 122:196101, 2019. URL https://doi.org/10.1103/PhysRevLett.122.196101.

[275] C. F. Matta and R. J. Boyd, editors. *The Quantum Theory of Atoms in Molecules*. Wiley-VCH Verlag GmbH & Co. KGaA, Weinheim, Germany, 2007. URL https://doi.org/10.1002/9783527610709.

[276] J. Maul, T. Berg, E. Marosits, G. Schönhense, and G. Huber. Statistical mechanics of fullerene coalescence growth. *Physical Review B*, 74(16):1–4, 2006. URL https://doi.org/10.1103/PhysRevB.74.161406.

[277] J. McArragher and K. Tan. Soot formation at high pressures: a literature review. *Combustion Science and Technology*, 5(1):257–261, 1972. URL https://doi.org/10.1080/00102207208952530.

[278] J. S. McDonald-Wharry, M. Manley-Harris, and K. L. Pickering. Reviewing, Combining, and Updating the Models for the Nanostructure of Non-Graphitizing Carbons Produced from Oxygen-Containing Precursors. *Energy and Fuels*, 30(10):7811–7826, 2016. URL https://doi.org/10.1021/acs.energyfuels.6b00917.

[279] J. T. McKinnon, E. Meyer, and J. B. Howard. Infrared analysis of flame-generated PAH samples. *Combustion and Flame*, 105(1-2):161–166, 1996. URL https://doi.org/10.1016/0010-2180(95)00185-9.

[280] S. Mebs, M. Weber, P. Luger, B. M. Schmidt, H. Sakurai, S. Higashibayashi, S. Onogi, and D. Lentz. Experimental electron density of sumanene, a bowl-shaped fullerene fragment; comparison with the related corannulene hydrocarbon. *Organic & Biomolecular Chemistry*, 10(11):2218, 2012. URL https://doi.org/10.1039/C2OB07040E.

[281] A. Menon, J. A. Dreyer, J. W. Martin, J. Akroyd, J. Robertson, and M. Kraft. Optical band gap of cross-linked, curved, and radical polyaromatic hydrocarbons. *Physical Chemistry Chemical Physics*, 21(29):16240–16251, 2019. URL https://doi.org/10.1039/C9CP02363A.

[282] X. Mercier, O. Carrivain, C. Irimiea, A. Faccinetto, and E. Therssen. Dimers of polycyclic aromatic hydrocarbons: the missing pieces in the soot formation process. *Physical Chemistry Chemical Physics*, 21(16):8282–8294, 2019. URL https://doi.org/10.1039/C9CP00394K.

[283] P. Michaud, J. Delfau, and A. Barassin. The positive ion chemistry in the post-combustion zone of sooting premixed acetylene low pressure flat flames. *Symposium (International) on Combustion*, 18(1):443 – 451, 1981. URL https://doi.org/10.1016/S0082-0784(81)80050-1.

[284] H. A. Michelsen. Probing soot formation, chemical and physical evolution, and oxidation: A review of in situ diagnostic techniques and needs. *Proceedings of the Combustion Institute*, 36(1):717–735, 2017. URL https://doi.org/10.1016/j.proci.2016.08.027.

[285] D. C. Miller, M. Terrones, and H. Terrones. Mechanical properties of hypothetical graphene foams: Giant Schwarzites. *Carbon*, 96:1191–1199, 2016. URL https://doi.org/10.1016/j.carbon.2015.10.040.

[286] J. A. Miller and S. J. Klippenstein. The recombination of propargyl radicals and other reactions on a C_6H_6 potential. *The Journal of Physical Chemistry A*, 107(39): 7783–7799, 2003. URL https://doi.org/10.1016/j.proci.2004.08.192.

[287] J. H. Miller. The kinetics of polynuclear aromatic hydrocarbon agglomeration in flames. *Symposium (International) on Combustion*, 23(1):91 – 98, 1991. URL https://doi.org/10.1016/S0082-0784(06)80246-8.

[288] J. H. Miller. Aromatic excimers: evidence for polynuclear aromatic hydrocarbon condensation in flames. *Proceedings of the Combustion Institute*, 30(1):1381–1388, 2005. URL https://doi.org/10.1016/j.proci.2004.08.192.

[289] J. H. Miller, W. G. Mallard, and K. C. Smyth. The observation of laser-induced visible fluorescence in sooting diffusion flames. *Combustion and Flame*, 47:205–214, 1982. URL https://doi.org/10.1016/0010-2180(82)90101-8.

[290] J. H. Miller, K. C. Smyth, and W. G. Mallard. Calculations of the dimerization of aromatic hydrocarbons: Implications for soot formation. *Symposium (International) on Combustion*, 20(1):1139–1147, 1985. URL https://doi.org/10.1016/S0082-0784(85)80604-4.

[291] C. Möller and M. S. Plesset. Note on an Approximation Treatment for Many-Electron Systems. *Physical Review*, 46(7):618–622, 1934. URL https://doi.org/10.1103/PhysRev.46.618.

[292] W. A. Morgan, E. D. Feigelson, H. Wang, and M. Frenklach. A new mechanism for the formation of meteoritic kerogen-like material. *Science*, 252(5002):109–112, 1991. URL https://doi.org/10.1126/science.252.5002.109.

[293] J. Mukherjee, A. F. Sarofim, and J. P. Longwell. Polycyclic aromatic hydrocarbons from the high-temperature pyrolysis of pyrene. *Combustion and Flame*, 96(3):191–200, 1994. URL https://doi.org/10.1016/0010-2180(94)90008-6.

[294] M. R. Mulay, A. Chauhan, S. Patel, V. Balakrishnan, A. Halder, and R. Vaish. Candle soot: Journey from a pollutant to a functional material. *Carbon*, 144:684–712, 2019. URL https://doi.org/10.1016/j.carbon.2018.12.083.

[295] B. Náfrádi, M. Choucair, K.-P. Dinse, and L. Forró. Room temperature manipulation of long lifetime spins in metallic-like carbon nanospheres. *Nature communications*, 7: 12232, 2016. URL https://doi.org/10.1038/ncomms12232.

[296] H. Nagai, M. Nakano, K. Yoneda, R. Kishi, H. Takahashi, A. Shimizu, T. Kubo, K. Kamada, K. Ohta, E. Botek, et al. Signature of multiradical character in second hyperpolarizabilities of rectangular graphene nanoflakes. *Chemical Physics Letters*, 489(4-6):212–218, 2010. URL https://doi.org/10.1016/j.cplett.2010.03.013.

[297] A. R. Neves, P. A. Fernandes, and M. J. Ramos. The accuracy of density functional theory in the description of cation-π and π-hydrogen bond interactions. *Journal of Chemical Theory and Computation*, 7(7):2059–2067, 2011. URL https://doi.org/10.1021/ct2001667.

[298] R. Niessner. The many faces of soot: Characterization of soot nanoparticles produced by engines. *Angewandte Chemie International Edition*, 53:12366–12379, 2014. URL https://doi.org/10.1002/anie.201402812.

[299] I. Nikiforov, E. Dontsova, R. D. James, and T. Dumitrică. Tight-binding theory of graphene bending. *Physical Review B*, 89(15):155437, 2014. URL https://doi.org/10.1103/PhysRevB.89.155437.

[300] H. Nishihara, T. Simura, S. Kobayashi, K. Nomura, R. Berenguer, M. Ito, M. Uchimura, H. Iden, K. Arihara, A. Ohma, et al. Oxidation-resistant and elastic mesoporous carbon with single-layer graphene walls. *Advanced Functional Materials*, 26(35):6418–6427, 2016. URL https://doi.org/10.1002/adfm.201602459.

[301] K. S. Novoselov, A. K. Geim, S. V. Morozov, D. Jiang, M. I. Katsnelson, I. V. Grigorieva, S. V. Dubonos, and A. A. Firsov. Two-dimensional gas of massless Dirac fermions in graphene. *Nature*, 438(7065):197–200, 2005. URL https://doi.org/10.1038/nature04233.

[302] A. Oberlin. Carbonization and graphitization. *Carbon*, 22(6):521 – 541, 1984. URL https://doi.org/10.1016/0008-6223(84)90086-1.

[303] L. Observatory, N. Bohrweg, and N.-C. A. Leiden. Formation of Covalently Bonded Polycyclic Aromatic Hydrocarbons in the Interstellar Medium. *The Astrophysical Journal*, 866(2):113, 2018. URL https://doi.org/10.3847/1538-4357/aae38f.

[304] V. Oja and E. M. Suuberg. Vapor pressures and enthalpies of sublimation of polycyclic aromatic hydrocarbons and their derivatives. *Journal of Chemical & Engineering Data*, 43(3):486–492, 1998.

[305] B. Öktem, M. P. Tolocka, B. Zhao, H. Wang, and M. V. Johnston. Chemical species associated with the early stage of soot growth in a laminar premixed ethylene–oxygen–argon flame. *Combustion and Flame*, 142(4):364–373, 2005. URL https://doi.org/10.1016/j.combustflame.2005.03.016.

[306] D. W. Olson, R. L. Virta, M. Mahdavi, E. S. Sangine, and S. M. Fortier. Natural graphite demand and supply—implications for electric vehicle battery requirements. *Geological Society of America Special Papers*, 520:67–77, 2016. URL https://doi.org/10.1130/2016.2520(08).

[307] K. Ono, Y. Matsukawa, K. Dewa, A. Watanabe, K. Takahashi, Y. Saito, Y. Matsushita, H. Aoki, K. Era, T. Aoki, et al. Formation mechanisms of soot from high-molecular-weight polycyclic aromatic hydrocarbons. *Combustion and Flame*, 162(6):2670–2678, 2015. URL https://doi.org/10.1016/j.combustflame.2015.03.022.

[308] M. Orchin and L. Reggel. Aromatic cyclodehydrogenation. v. a synthesis of fluoranthene1. *Journal of the American Chemical Society*, 69(3):505–509, 1947. URL https://doi.org/10.1021/ja01195a009.

[309] W. H. Organization. Burden of disease from household air pollution for 2012. Technical report, 2014.

[310] O. Orhan, E. Haffner-Staton, A. L. Rocca, and M. Fay. Characterisation of flame-generated soot and soot-in-oil using electron tomography volume reconstructions and comparison with traditional 2d-tem measurements. *Tribology International*, 104:272 – 284, 2016. URL https://doi.org/10.1016/j.triboint.2016.09.015.

[311] F. Ospitali, D. C. Smith, and M. Lorblanchet. Preliminary investigations by raman microscopy of prehistoric pigments in the wall-painted cave at roucadour, quercy, france. *Journal of Raman Spectroscopy*, 37(10):1063–1071, 2006. URL https://doi.org/10.1002/jrs.1611.

[312] M. Otani, S. Okada, and Y. Okamoto. Intrinsic dipole moment on the capped carbon nanotubes. *Physical Review B - Condensed Matter and Materials Physics*, 80(15):4–6, 2009. URL https://doi.org/10.1103/PhysRevB.80.153413.

[313] A. M. Oyarzún, C. D. Latham, L. R. Radovic, P. R. Briddon, and M. J. Rayson. Spin density distributions on graphene clusters and ribbons with carbene-like active sites. *Physical Chemistry Chemical Physics*, 20(42):26968–26978, 2018. URL https://doi.org/10.1039/C8CP03313G.

[314] M. Pabst, I. Letofsky-Papst, E. Bock, M. Moser, L. Dorfer, E. Egarter-Vigl, and F. Hofer. The tattoos of the tyrolean iceman: a light microscopical, ultrastructural and element analytical study. *Journal of Archaeological Science*, 36(10):2335 – 2341, 2009. URL https://doi.org/10.1016/j.jas.2009.06.016.

[315] H. B. Palmer and C. F. Cullis. The formation of carbon from gases. *Chemistry and Physics of Carbon*, 1:265–325, 1965.

[316] D. G. Park, B. C. Choi, M. S. Cha, and S. H. Chung. Soot Reduction Under DC Electric Fields in Counterflow Non-Premixed Laminar Ethylene Flames. *Combustion Science and Technology*, 186(4-5):644–656, 2014. URL https://doi.org/10.1080/00102202.2014.883794.

[317] J. Park, S. Burova, A. Rodgers, and M. Lin. Experimental and theoretical studies of the $C_6H_5^+$ C_6H_6 reaction. *The Journal of Physical Chemistry A*, 103(45):9036–9041, 1999. URL https://doi.org/10.1021/jp9920592.

[318] S. Park, D. Srivastava, and K. Cho. Generalized chemical reactivity of curved surfaces: Carbon nanotubes. *Nano Letters*, 3(9):1273–1277, 2003. URL https://doi.org/10.1021/nl0342747.

[319] W. Parker and H. Wolfhard. 418. Carbon formation in flames. *Journal of the Chemical Society (Resumed)*, pages 2038–2049, 1950. URL https://doi.org/10.1039/JR9500002038.

[320] L. Pascazio, M. Sirignano, and A. D. Anna. Simulating the morphology of clusters of polycyclic aromatic hydrocarbons : The influence of the intermolecular potential. *Combustion and Flame*, 185:53–62, 2017. URL https://doi.org/10.1016/j.combustflame.2017.07.003.

[321] L. Pascazio, J. Martin, A. Menon, D. You, J. Akroyd, and M. Kraft. Penta-linked planar aromatics in nascent soot formation. *In preparation*, 2020.

[322] J. R. Patterson, S. A. Catledge, Y. K. Vohra, J. Akella, and S. T. Weir. Electrical and mechanical properties of C_{70} fullerene and graphite under high pressures studied using designer diamond anvils. *Physical Review Letters*, 85(25):5364–5367, 2000. URL https://doi.org/10.1103/PhysRevLett.85.5364.

[323] C. Pérez, A. L. Steber, A. M. Rijs, B. Temelso, G. C. Shields, J. C. Lopez, Z. Kisiel, and M. Schnell. Corannulene and its complex with water: a tiny cup of water. *Physical Chemistry Chemical Physics*, 19(22):14214–14223, 2017. URL https://doi.org/10.1039/C7CP01506B.

[324] T. C. Petersen, I. K. Snook, I. Yarovsky, D. G. McCulloch, and B. O'Malley. Curved-Surface Atomic Modeling of Nanoporous Carbon. *The Journal of Physical Chemistry C*, 111(2):802–812, 2007. URL https://doi.org/10.1021/jp063973f.

[325] M. A. Petrukhina, K. W. Andreini, J. Mack, and L. T. Scott. X-ray quality geometries of geodesic polyarenes from theoretical calculations: What levels of theory are reliable? *Journal of Organic Chemistry*, 70(14):5713–5716, 2005. URL https://doi.org/10.1021/jo050233e.

[326] G. P. Pfeifer, M. F. Denissenko, M. Olivier, N. Tretyakova, S. S. Hecht, and P. Hainaut. Tobacco smoke carcinogens, DNA damage and p53 mutations in smoking-associated cancers. *Oncogene*, 21(48):7435, 2002. URL https://doi.org/10.1038/sj.onc.1205803.

[327] M. R. Philpott and Y. Kawazoe. Triplet states of zigzag edged hexagonal graphene molecules $c_{6m**2}h_{6m}$ (m= 1, 2, 3,. . . , 10) and carbon based magnetism. *The Journal of Chemical Physics*, 134(12):124706, 2011. URL https://doi.org/10.1063/1.3569135.

[328] E. R. Place and F. J. Weinberg. Electrical control of flame carbon. *Proceedings of the Royal Society A: Mathematical, Physical and Engineering Sciences*, 289(1417): 192–205, 1966. URL https://doi.org/10.1098/rspa.1966.0006.

[329] R. Podeszwa. Interactions of graphene sheets deduced from properties of polycyclic aromatic hydrocarbons. *The Journal of chemical physics*, 132(4):044704, 2010. URL https://doi.org/10.1063/1.3300064.

[330] C. Pope, J. Marr, and J. Howard. Chemistry of fullerenes C_{60} and C_{70} formation in flames. *The Journal of Physical Chemistry*, 97:11001–11013, 1993. URL https://doi.org/10.1021/j100144a018.

[331] G. Porter. Carbon formation in the combustion wave. *Symposium (International) on Combustion*, 4(1):248–252, 1953. URL https://doi.org/10.1016/S0082-0784(53)80031-7.

[332] P. Pott. Chirurgical observations relative to the cataract, the polypus of the nose, cancer of the scrotum, different types of the ruptures, and the modification of the toes and feet. *Chirurgical works of Percivall Pott, Bd*, 5:1–208, 1775.

[333] P. Pradhan, S. Tirumala, X. Liu, J. M. Sayer, D. M. Jerina, and H. J. C. Yeh. Solution structure of a trans-opened (10s)-da adduct of (+)-(7s,8r,9s,10r)-7,8-dihydroxy-9,10-epoxy-7,8,9,10-tetrahydrobenzo[a]pyrene in a fully complementary dna duplex: Evidence for a major syn conformation. *Biochemistry*, 40(20):5870–5881, 2001. URL https://doi.org/10.1021/bi002896q.

[334] H.-J. Qian, A. C. T. van Duin, K. Morokuma, and S. Irle. Reactive Molecular Dynamics Simulation of Fullerene Combustion Synthesis: ReaxFF vs DFTB Potentials. *Journal of Chemical Theory and Computation*, 7(7):2040–2048, 2011. URL https://doi.org/10.1021/ct200197v.

[335] P. W. Rabideau, A. H. Abdourazak, H. E. Folsom, Z. Marcinow, A. Sygula, and R. Sygula. Buckybowls: Synthesis and ab Initio Calculated Structure of the First Semibuckminsterfullerene. *Journal of the American Chemical Society*, 116(17):7891–7892, 1994. URL https://doi.org/10.1021/ja00096a054.

[336] A. Raj. Structural effects on the growth of large polycyclic aromatic hydrocarbons by C_2H_2. *Combustion and Flame*, 204:331 – 340, 2019. URL https://doi.org/10.1016/j.combustflame.2019.03.027.

[337] A. Raj, M. Celnik, R. Shirley, M. Sander, R. Patterson, R. West, and M. Kraft. A statistical approach to develop a detailed soot growth model using PAH characteristics. *Combustion and Flame*, 156(4):896–913, 2009. URL https://doi.org/10.1016/j.combustflame.2009.01.005.

[338] A. Raj, S. Y. Yang, D. Cha, R. Tayouo, and S. H. Chung. Structural effects on the oxidation of soot particles by O_2: Experimental and theoretical study. *Combustion and Flame*, 160(9):1812 – 1826, 2013. URL https://doi.org/10.1016/j.combustflame.2013.03.010.

[339] A. Ratkiewicz and T. N. Truong. Kinetics of the C–C bond beta scission reactions in alkyl radical reaction class. *The Journal of Physical Chemistry A*, 116(25):6643–6654, 2012. URL https://doi.org/10.1021/jp3018265.

[340] P. Reilly, R. Gieray, W. Whitten, and J. Ramsey. Direct observation of the evolution of the soot carbonization process in an acetylene diffusion flame via real-time aerosol mass spectrometry. *Combustion and Flame*, 122(1-2):90–104, 2000. URL https://doi.org/10.1016/S0010-2180(00)00105-X.

[341] A. Reis. Beiträge zur kenntnis der flammen. *Zeitschrift für Physikalische Chemie*, 88(1):513–568, 1914. URL https://doi.org/10.1515/zpch-1914-8836.

[342] Y. M. Rhee, T. J. Lee, M. S. Gudipati, L. J. Allamandola, and M. Head-Gordon. Charged polycyclic aromatic hydrocarbon clusters and the galactic extended red emission. *Proceedings of the National Academy of Sciences of the United States of America*, 104(13):5274–5278, 2007. URL https://doi.org/10.1073/pnas.0609396104.

[343] A. Richter, R. Riesa, R. Smith, M. Henkel, and B. Wolf. Nanoindentation of diamond, graphite and fullerene films. *Diamond and Related Materials*, 9:170–184, 2000. URL https://doi.org/10.1016/S0925-9635(00)00188-6.

[344] H. Richter and J. Howard. Formation of polycyclic aromatic hydrocarbons and their growth to soot: a review of chemical reaction pathways. *Progress in Energy and Combustion Science*, 26(4-6):565–608, 2000. URL https://doi.org/10.1016/S0360-1285(00)00009-5.

[345] H. Richter, A. J. Labrocca, W. J. Grieco, K. Taghizadeh, A. L. Lafleur, and J. B. Howard. Generation of Higher Fullerenes in Flames. *Journal of Physical Chemistry B*, 101(9):1556–1560, 1997. URL https://doi.org/10.1021/jp962928c.

[346] A. Rinkenburger, T. Toriyama, K. Yasuda, and R. Niessner. Catalytic Effect of Potassium Compounds in Soot Oxidation. *ChemCatChem*, 9(18):3513–3525, 2017. URL https://doi.org/10.1002/cctc.201700338.

[347] D. Robertson, D. Brenner, and C. White. On the way to fullerenes: molecular dynamics study of the curling and closure of graphitic ribbons. *The Journal of Physical Chemistry*, 96(15):6133–6135, 1992. URL https://doi.org/10.1021/j100194a011.

[348] J. Robertson. Diamond-like amorphous carbon. *Materials Science and Engineering: R: Reports*, 37(4-6):129–281, 2002. URL https://doi.org/10.1016/S0927-796X(02)00005-0.

[349] B. E. Rocher-Casterline, L. C. Ch'ng, A. K. Mollner, and H. Reisler. Communication: Determination of the bond dissociation energy (d0) of the water dimer, (h2o)2, by velocity map imaging. *The Journal of Chemical Physics*, 134(21):211101, 2011. URL https://doi.org/10.1063/1.3598339.

[350] A. Rodríguez-Fortea, S. Irle, and J. M. Poblet. Fullerenes: formation, stability, and reactivity. *Wiley Interdisciplinary Reviews: Computational Molecular Science*, 1(3): 350–367, 2011. URL https://doi.org/10.1002/wcms.21.

[351] K. Roth. Alle Jahre wieder: die Chemie der Weihnachtskerze. *Chemie in unserer Zeit*, 37(6):424–429, 2003. URL https://doi.org/10.1002/ciuz.200390086.

[352] G. Rouillé, C. Jäger, M. Steglich, F. Huisken, T. Henning, G. Theumer, I. Bauer, and H.-J. Knölker. IR, Raman, and UV/Vis spectra of corannulene for use in possible interstellar identification. *ChemPhysChem*, 9(14):2085–2091, 2008. URL https://doi.org/10.1002/cphc.200800387.

[353] K. Rummel and P.-O. Veh. Die Strahlung Leuchtender Flammen. Erster Teil: Schrifttumsgrundlagen, Arbeitshypothesen und Vorversuche (Translation: The radiance of glowing flames. Part 1: Foundations, working hypotheses and preliminary experiments). *Archiv für das Eisenhüttenwesen*, 14(10):489–499, 1941. URL https://doi.org/10.1002/srin.194101863.

[354] C. Russo, B. Apicella, J. Lighty, A. Ciajolo, and A. Tregrossi. Optical properties of organic carbon and soot produced in an inverse diffusion flame. *Carbon*, 124:372–379, 2017. URL https://doi.org/10.1016/j.carbon.2017.08.073.

[355] J. C. Ryan, A. Hubbard, M. Stibal, T. D. Irvine-Fynn, J. Cook, L. C. Smith, K. Cameron, and J. Box. Dark zone of the greenland ice sheet controlled by distributed biologically-active impurities. *Nature communications*, 9(1):1065, 2018. URL https://doi.org/10.1038/s41467-018-03353-2.

[356] H. Sabbah, L. Biennier, S. J. Klippenstein, I. R. Sims, and B. R. Rowe. Exploring the role of PAHs in the formation of soot: pyrene dimerization. *The Journal of Physical Chemistry Letters*, 1(19):2962–2967, 2010. URL https://doi.org/10.1021/jz101033t.

[357] B. Saha, S. Shindo, S. Irle, and K. Morokuma. Quantum chemical molecular dynamics simulations of dynamic fullerene self-assembly in benzene combustion. *ACS Nano*, 3 (8):2241–2257, 2009. URL https://doi.org/10.1021/nn900494s.

[358] B. Saha, S. Irle, and K. Morokuma. Hot giant fullerenes eject and capture C_2 molecules: QM/MD simulations with constant density. *Journal of Physical Chemistry C*, 115 (46):22707–22716, 2011. URL https://doi.org/10.1021/jp203614e.

[359] H. Sakurai. A Synthesis of Sumanene, a Fullerene Fragment. *Science*, 301(5641): 1878–1878, 2003. URL https://doi.org/10.1126/science.1088290.

[360] N. E. Sánchez, A. Callejas, A. Millera, R. Bilbao, and M. U. Alzueta. Polycyclic Aromatic Hydrocarbon (PAH) and Soot Formation in the Pyrolysis of Acetylene and Ethylene: Effect of the Reaction Temperature. *Energy & Fuels*, 26(8):4823–4829, 2012. URL https://doi.org/10.1021/ef300749q.

[361] R. C. Santos, C. E. Bernardes, H. P. Diogo, M. F. M. Piedade, J. N. Canongia Lopes, and M. E. Minas da Piedade. Energetics of the thermal dimerization of acenaphthylene to heptacyclene. *The Journal of Physical Chemistry A*, 110(6):2299–2307, 2006. URL https://doi.org/10.1021/jp056275o.

[362] A. F. Sarofim, J. P. Longwell, M. J. Wornat, and J. Mukherjee. The role of biaryl reactions in PAH and soot formation. In *Soot Formation in Combustion*, pages 485–499. Springer, 1994. URL https://doi.org/10.1007/978-3-642-85167-4_27.

[363] G. N. Sastry, E. D. Jemmis, G. Mehta, and S. R. Shah. Synthetic strategies towards C_{60}. Molecular mechanics and MNDO study on sumanene and related structures. *Journal of the Chemical Society, Perkin Transactions 2*, (10):1867, 1993. URL https://doi.org/10.1039/p29930001867.

[364] L. G. Scanlon, P. B. Balbuena, Y. Zhang, G. Sandi, C. K. Back, W. A. Feld, J. Mack, M. A. Rottmayer, and J. L. Riepenhoff. Investigation of corannulene for molecular hydrogen storage via computational chemistry and experimentation. *Journal of Physical Chemistry B*, 110(15):7688–7694, 2006. URL https://doi.org/10.1021/jp0574403.

[365] H. B. Schlegel, J. M. Millam, S. S. Iyengar, G. A. Voth, A. D. Daniels, G. E. Scuseria, and M. J. Frisch. Ab initio molecular dynamics: Propagating the density matrix with Gaussian orbitals. *The Journal of Chemical Physics*, 114(22):9758–9763, 2001. URL https://doi.org/10.1063/1.1372182.

[366] H. B. Schlegel, S. S. Iyengar, X. Li, J. M. Millam, G. A. Voth, G. E. Scuseria, and M. J. Frisch. Ab initio molecular dynamics: Propagating the density matrix with Gaussian orbitals. III. Comparison with Born–Oppenheimer dynamics. *The Journal of Chemical Physics*, 117(19):8694–8704, 2002. URL https://doi.org/10.1063/1.1514582.

[367] M. Schnaiter, C. Linke, O. Möhler, K.-H. Naumann, H. Saathoff, R. Wagner, U. Schurath, and B. Wehner. Absorption amplification of black carbon internally mixed with secondary organic aerosol. *Journal of Geophysical Research: Atmospheres*, 110(D19), 2005. URL https://doi.org/10.1029/2005JD006046.

[368] D. E. Schraufnagel, J. Balmes, C. T. Cowl, S. De Matteis, S.-H. Jung, K. Mortimer, R. Perez-Padilla, M. B. Rice, H. Riojas-Rodroguez, A. Sood, et al. Air pollution and non-communicable diseases: a review by the forum of international respiratory societies' environmental committee. part 2: air pollution and organ systems. *Chest*, 155(2):409–416, 2019. URL https://doi.org/10.1016/j.chest.2018.10.041.

[369] C. A. Schuetz and M. Frenklach. Nucleation of soot: Molecular dynamics simulations of pyrene dimerization. *Proceedings of the Combustion Institute*, 29(2):2307–2314, 2002. URL https://doi.org/10.1016/S1540-7489(02)80281-4.

[370] F. Schulz, M. Commodo, K. Kaiser, G. D. Falco, P. Minutolo, G. Meyer, A. D'Anna, and L. Gross. Insights into incipient soot formation by atomic force microscopy. *Proceedings of the Combustion Institute*, 37(1):885 – 892, 2019. URL https://doi.org/10.1016/j.proci.2018.06.100.

[371] F. Schulz, M. Commodo, K. Kaiser, G. D. Falco, P. Minutolo, G. Meyer, A. D'Anna, and L. Gross. Insights into incipient soot formation by atomic force microscopy. *Proceedings of the Combustion Institute*, 37(1):885 – 892, 2019. URL https://doi.org/10.1016/j.proci.2018.06.100.

[372] P. Schwerdtfeger, L. N. Wirz, and J. Avery. The topology of fullerenes. *Wiley Interdisciplinary Reviews: Computational Molecular Science*, 5(1):96–145, 2015. URL https://doi.org/10.1002/wcms.1207.

[373] L. T. Scott, M. M. Hashemi, and M. S. Bratcher. Corannulene bowl-to-bowl inversion is rapid at room temperature. *Journal of the American Chemical Society*, 114(5): 1920–1921, 1992. URL https://doi.org/10.1021/ja00031a079.

[374] L. T. Scott, M. S. Bratcher, and S. Hagen. Synthesis and Characterization of a $C_{36}H_{12}$ Fullerene Subunit. *Journal of the American Chemical Society*, 118(36):8743–8744, 1996. URL https://doi.org/10.1021/ja9621511.

[375] T. J. Seiders, K. K. Baldridge, G. H. Grube, and J. S. Siegel. Structure/energy correlation of bowl depth and inversion barrier in corannulene derivatives: Combined experimental and quantum mechanical analysis. *Journal of the American Chemical Society*, 123(4):517–525, 2001. URL https://doi.org/10.1021/ja0019981.

[376] K. Sendt and B. S. Haynes. Density functional study of the chemisorption of o_2 on the zig-zag surface of graphite. *Combustion and Flame*, 143(4):629–643, 2005. URL https://doi.org/10.1016/j.combustflame.2005.08.026.

[377] L. A. Sgro, A. D'Anna, and P. Minutolo. Charge distribution of incipient flame-generated particles. *Aerosol Science and Technology*, 44(8):651–662, 2010. URL https://doi.org/10.1080/02786826.2010.483701.

[378] S. Shabnam, Q. Mao, A. C. van Duin, and K. Luo. Evaluation of the effect of nickel clusters on the formation of incipient soot particles from polycyclic aromatic hydrocarbons via reaxff molecular dynamics simulations. *Physical Chemistry Chemical Physics*, 21(19):9865–9875, 2019. URL https://doi.org/10.1039/C9CP00354A.

[379] S. Shaik and P. C. Hiberty. Valence bond theory, its history, fundamentals, and applications: a primer. *Reviews in Computational Chemistry*, 20:1, 2004. URL https://doi.org/10.1002/0471678856.ch1.

[380] J. W. Sheldon. Use of the statistical field approximation in molecular physics. *Physical Review*, 99(4):1291–1301, 1955. URL https://doi.org/10.1103/PhysRev.99.1291.

[381] X. Shi and L. S. Bartell. Electron diffraction and monte carlo studies of liquids. 1. intermolecular interactions for benzene. *The Journal of Physical Chemistry*, 92(20): 5667–5673, 1988. URL https://doi.org/10.1021/j100331a024.

[382] T. B. Shiell, D. G. McCulloch, D. R. McKenzie, M. R. Field, B. Haberl, R. Boehler, B. A. Cook, C. de Tomas, I. Suarez-Martinez, N. A. Marks, and J. E. Bradby. Graphitization of glassy carbon after compression at room temperature. *Physical Review Letters*, 120:215701, 2018. URL https://doi.org/10.1103/PhysRevLett.120.215701.

[383] S. L. Shostak, W. L. Ebenstein, and J. S. Muenter. The dipole moment of water. I. Dipole moments and hyperfine properties of H_2O and HDO in the ground and excited vibrational states. *The Journal of Chemical Physics*, 94(9):5875, 1991. URL https://doi.org/10.1063/1.460471.

[384] B. Shukla and M. Koshi. A highly efficient growth mechanism of polycyclic aromatic hydrocarbons. *Physical Chemistry Chemical Physics*, 12(10):2427–2437, 2010. URL https://doi.org/10.1039/B919644G.

[385] B. Shukla, K. Tsuchiya, and M. Koshi. Novel products from $c_6h_5^+$ c_6h_6/c_6h_5 reactions. *The Journal of Physical Chemistry A*, 115(21):5284–5293, 2011. URL https://doi.org/10.1021/jp201817n.

[386] H. S. Silva, J. Cresson, A. Rivaton, D. Bégué, and R. C. Hiorns. Correlating geometry of multidimensional carbon allotropes molecules and stability. *Organic Electronics: physics, materials, applications*, 26:395–399, 2015. URL https://doi.org/10.1016/j.orgel.2015.08.004.

[387] J. Simonsson, N. E. Olofsson, H. Bladh, M. Sanati, and P. E. Bengtsson. Influence of potassium and iron chloride on the early stages of soot formation studied using imaging LII/ELS and TEM techniques. *Proceedings of the Combustion Institute*, 36 (1):853–860, 2017. URL https://doi.org/10.1016/j.proci.2016.07.003.

[388] R. Singh and M. Frenklach. A mechanistic study of the influence of graphene curvature on the rate of high-temperature oxidation by molecular oxygen. *Carbon*, 101:203–212, 2016. URL https://doi.org/10.1016/j.carbon.2016.01.090.

[389] S. Sinha and A. Raj. Polycyclic aromatic hydrocarbon (PAH) formation from benzyl radicals: a reaction kinetics study. *Physical Chemistry Chemical Physics*, 18(11): 8120–8131, 2016. URL https://doi.org/10.1039/C5CP06465A.

[390] S. Sinha, R. K. Rahman, and A. Raj. On the role of resonantly stabilized radicals in polycyclic aromatic hydrocarbon (PAH) formation: pyrene and fluoranthene formation from benzyl–indenyl addition. *Physical Chemistry Chemical Physics*, 19(29):19262–19278, 2017. URL https://doi.org/10.1039/C7CP02539D.

[391] M. Sirignano, A. Collina, M. Commodo, P. Minutolo, and A. D'Anna. Detection of aromatic hydrocarbons and incipient particles in an opposed-flow flame of ethylene by spectral and time-resolved laser induced emission spectroscopy. *Combustion and Flame*, 159(4):1663 – 1669, 2012. URL https://doi.org/10.1016/j.combustflame.2011.11.005.

[392] N. Sivin. *Science in ancient China: researches and reflections*, volume 506. Variorum, 1995.

[393] P. Sjoberg, J. S. Murray, T. Brinck, and P. Politzer. Average local ionization energies on the molecular surfaces of aromatic systems as guides to chemical reactivity. *Canadian Journal of Chemistry*, 68(8):1440–1443, 1990. URL https://doi.org/10.1139/v90-220.

[394] D. Small, S. V. Rosokha, J. K. Kochi, and M. Head-Gordon. Characterizing the dimerizations of phenalenyl radicals by ab initio calculations and spectroscopy: σ-bond formation versus resonance π-stabilization. *The Journal of Physical Chemistry A*, 109(49):11261–11267, 2005. URL https://doi.org/10.1021/jp054244n.

[395] E. C. W. Smith. The Emission Spectrum of Hydrocarbon Flames. *Proceedings of the Royal Society A: Mathematical, Physical and Engineering Sciences*, 174(956): 110–125, 1940. URL https://doi.org/10.1098/rspa.1940.0009.

[396] M. W. Smith, I. Dallmeyer, T. J. Johnson, C. S. Brauer, J.-S. McEwen, J. F. Espinal, and M. Garcia-Perez. Structural Analysis of Char by Raman Spectroscopy: Improving Band Assignments through First Principle Computational Calculations. *Carbon*, 100: 678–692, 2016. URL https://doi.org/10.1016/j.carbon.2016.01.031.

[397] I. Y. Stein, A. J. Constable, N. Morales-Medina, C. V. Sackier, M. E. Devoe, H. M. Vincent, and B. L. Wardle. Structure-mechanical property relations of non-graphitizing pyrolytic carbon synthesized at low temperatures. *Carbon*, 117:411–420, 2017. URL https://doi.org/10.1016/j.carbon.2017.03.001.

[398] S. E. Stein and A. Fahr. High-temperature stabilities of hydrocarbons. *The Journal of Physical Chemistry*, 89(17):3714–3725, 1985. URL https://doi.org/10.1021/j100263a027.

[399] B. D. Steinberg, E. A. Jackson, A. S. Filatov, A. Wakamiya, M. A. Petrukhina, and L. T. Scott. Aromatic π-Systems More Curved Than C_{60}. The Complete Family of All Indenocorannulenes Synthesized by Iterative Microwave-Assisted Intramolecular Arylations. *Journal of the American Chemical Society*, 131(30):10537–10545, 2009. URL https://doi.org/10.1021/ja9031852.

[400] P. J. Stephens, F. J. Devlin, C. F. Chabalowski, and M. J. Frisch. Ab Initio Calculation of Vibrational Absorption and Circular Dichroism Spectra Using Density Functional Force Fields. *The Journal of Physical Chemistry*, 98(45):11623–11627, 1994. URL https://doi.org/10.1021/j100096a001.

[401] A. Stone. *The Theory of Intermolecular Forces*. Oxford University Press, 2013. URL https://doi.org/10.1093/acprof:oso/9780199672394.001.0001.

[402] D. S. Su, R. E. Jentoft, J. O. Müller, D. Rothe, E. Jacob, C. D. Simpson, Ž. Tomović, K. Müllen, A. Messerer, U. Pöschl, R. Niessner, and R. Schlögl. Microstructure and oxidation behaviour of Euro IV diesel engine soot: a comparative study with synthetic model soot substances. *Catalysis Today*, 90(1-2):127–132, 2004. URL https://doi.org/10.1016/j.cattod.2004.04.017.

[403] I. Suarez-Martinez and N. Marks. Effect of microstructure on the thermal conductivity of disordered carbon. *Applied Physics Letters*, 99(3):033101, 2011. URL https://doi.org/10.1063/1.3607872.

[404] I. Suarez-Martinez, G. Savini, G. Haffenden, J. M. Campanera, and M. I. Heggie. Dislocations of Burgers vector c/2 in graphite. *Physica Status Solidi (C)*, 4(8):2958–2962, 2007. URL https://doi.org/10.1002/pssc.200675445.

[405] I. Suarez-Martinez, N. Grobert, and C. P. Ewels. Nomenclature of sp^2 carbon nanoforms. *Carbon*, 50(3):741–747, 2012. URL https://doi.org/10.1016/j.carbon.2011.11.002.

[406] C. H. Sun, G. Q. Lu, and H. M. Cheng. Nonplanar distortions and strain energies of polycyclic aromatic hydrocarbons. *Journal of Physical Chemistry B*, 110(10):4563–4568, 2006. URL https://doi.org/10.1021/jp054603e.

[407] Z. Sun and J. Wu. Open-shell polycyclic aromatic hydrocarbons. *Journal of Materials Chemistry*, 22(10):4151–4160, 2012. URL https://doi.org/10.1039/C1JM14786B.

[408] A. Szabo and N. S. Ostlund. *Modern quantum chemistry: introduction to advanced electronic structure theory*. Courier Corporation, 1989.

[409] T. Takatani and C. D. Sherrill. Performance of spin-component-scaled møller–plesset theory (scs-mp2) for potential energy curves of noncovalent interactions. *Physical Chemistry Chemical Physics*, 9(46):6106–6114, 2007. URL https://doi.org/10.1039/B709669K.

[410] E. Teller. On the stability of molecules in the Thomas-Fermi theory. *Reviews of Modern Physics*, 34(4):627–631, 1962. URL https://doi.org/10.1103/RevModPhys.34.627.

[411] A. Thomas. Carbon formation in flames. *Combustion and Flame*, 6:46 – 62, 1962. URL https://doi.org/10.1016/0010-2180(62)90066-4.

[412] M. Thompson, B. Dyatkin, H.-W. Wang, C. Turner, X. Sang, R. Unocic, C. Iacovella, Y. Gogotsi, A. van Duin, and P. Cummings. An Atomistic Carbide-Derived Carbon Model Generated Using ReaxFF-Based Quenched Molecular Dynamics. *C*, 3(4):32, 2017. URL https://doi.org/10.3390/c3040032.

[413] H.-R. Tian, M.-M. Chen, K. Wang, Z.-C. Chen, C.-Y. Fu, Q. Zhang, S.-H. Li, S.-L. Deng, Y.-R. Yao, S.-Y. Xie, R.-B. Huang, and L.-S. Zheng. An unconventional hydrofullerene c66h4 with symmetric heptagons retrieved in low-pressure combustion. *Journal of the American Chemical Society*, 141(16):6651–6657, 2019. URL https://doi.org/10.1021/jacs.9b01638.

[414] A. Toro-Labbé, P. Jaque, J. S. Murray, and P. Politzer. Connection between the average local ionization energy and the Fukui function. *Chemical Physics Letters*, 407(1):143 – 146, 2005. URL https://doi.org/10.1016/j.cplett.2005.03.041.

[415] P. Toth, A. B. Palotas, E. G. Eddings, R. T. Whitaker, and J. S. Lighty. A novel framework for the quantitative analysis of high resolution transmission electron micrographs of soot ii. robust multiscale nanostructure quantification. *Combustion and Flame*, 160 (5):920 – 932, 2013. URL https://doi.org/10.1016/j.combustflame.2013.01.003.

[416] P. Toth, D. Jacobsson, M. Ek, and H. Wiinikka. Real-time, in situ, atomic scale observation of soot oxidation. *Carbon*, 145:149–160, 2019. URL https://doi.org/10.1016/j.carbon.2019.01.007.

[417] T. S. Totton, A. J. Misquitta, and M. Kraft. A First Principles Development of a General Anisotropic Potential for Polycyclic Aromatic Hydrocarbons. *Journal of Chemical Theory and Computation*, 6(3):683–695, 2010. URL https://doi.org/10.1021/ct9004883.

[418] T. S. Totton, A. J. Misquitta, and M. Kraft. Assessing the Polycyclic Aromatic Hydrocarbon Anisotropic Potential with Application to the Exfoliation Energy of Graphite. *The Journal of Physical Chemistry A*, 115(46):13684–13693, 2011. URL https://doi.org/10.1021/jp208088s.

[419] T. S. Totton, A. J. Misquitta, and M. Kraft. A quantitative study of the clustering of polycyclic aromatic hydrocarbons at high temperatures. *Physical Chemistry Chemical Physics*, 14(12):4081–94, 2012. URL https://doi.org/10.1039/c2cp23008a.

[420] S. J. Townsend, T. J. Lenosky, D. A. Muller, C. S. Nichols, and V. Elser. Negatively curved graphitic sheet model of amorphous carbon. *Physical Review Letters*, 69(6): 921–924, 1992. URL https://doi.org/10.1103/PhysRevLett.69.921.

[421] R. S. Tranter, S. J. Klippenstein, L. B. Harding, B. R. Giri, X. Yang, and J. H. Kiefer. Experimental and theoretical investigation of the self-reaction of phenyl radicals. *The Journal of Physical Chemistry A*, 114(32):8240–8261, 2010. URL https://doi.org/10.1021/jp1031064.

[422] D. Ugarte. Curling and closure of graphitic networks under electron-beam irradiation. *Nature*, 359(6397):707–709, 1992. URL https://doi.org/10.1038/359707a0.

[423] D. Ugarte. Onion-like graphitic particles. *Carbon*, 33:989–993, 1995. URL https://doi.org/10.1016/0008-6223(95)00027-B.

[424] B. V. Unterreiner, M. Sierka, and R. Ahlrichs. Reaction pathways for growth of polycyclic aromatic hydrocarbons under combustion conditions, a DFT study. *Physical Chemistry Chemical Physics*, 6(18):4377, 2004. URL https://doi.org/10.1039/b407279k.

[425] A. Vasiliou, M. R. Nimlos, J. W. Daily, and G. B. Ellison. Thermal decomposition of furan generates propargyl radicals. *The Journal of Physical Chemistry A*, 113(30): 8540–8547, 2009. URL https://doi.org/10.1021/jp903401h.

[426] D. Vijay, H. Sakurai, V. Subramanian, and G. N. Sastry. Where to bind in buckybowls? The dilemma of a metal ion. *Physical Chemistry Chemical Physics*, 14(9):3057, 2012. URL https://doi.org/10.1039/c2cp22087c.

[427] A. Violi. Cyclodehydrogenation reactions to cyclopentafused polycyclic aromatic hydrocarbons. *Journal of Physical Chemistry A*, 109(34):7781–7787, 2005. URL https://doi.org/10.1021/jp052384r.

[428] A. Violi and A. Venkatnathan. Combustion-generated nanoparticles produced in a benzene flame: a multiscale approach. *The Journal of Chemical Physics*, 125(5): 054302, 2006. URL https://doi.org/10.1063/1.2234481.

[429] A. Violi, A. Sarofim, and T. Truong. Quantum mechanical study of molecular weight growth process by combination of aromatic molecules. *Combustion and Flame*, 126 (1-2):1506–1515, 2001. URL https://doi.org/10.1016/S0010-2180(01)00268-1.

[430] A. Violi, A. Kubota, T. Truong, W. Pitz, C. Westbrook, and A. Sarofim. A fully integrated kinetic monte carlo/molecular dynamics approach for the simulation of soot precursor growth. *Proceedings of the Combustion Institute*, 29(2):2343–2349, 2002. URL https://doi.org/10.1016/S1540-7489(02)80285-1.

[431] A. Violi, A. F. Sarofim, and G. A. Voth. Kinetic monte carlo-molecular dynamics approach to model soot inception. *Combustion Science and Technology*, 176(5-6): 991–1005, 2004. URL https://doi.org/10.1080/00102200490428594.

[432] A. D. Vita, J. Charlier, X. Blase, and R. Car. Electronic structure at carbon nanotube tips. *Applied Physics A*, 68(3):283–286, 1999. URL https://doi.org/10.1007/s003390050889.

[433] G. Vitiello, G. De Falco, F. Picca, M. Commodo, G. D'Errico, P. Minutolo, and A. D'Anna. Role of radicals in carbon clustering and soot inception: A combined EPR and raman spectroscopic study. *Combustion and Flame*, 205:286–294, 2019. URL https://doi.org/10.1016/j.combustflame.2019.04.028.

[434] D. J. Wales, M. A. Miller, and T. R. Walsh. Archetypal energy landscapes. *Nature*, 394(6695):758–760, 1998. URL https://doi.org/10.1038/29487.

[435] B. Wang, M. König, C. J. Bromley, B. Yoon, M.-J. Treanor, J. A. Garrido Torres, M. Caffio, F. Grillo, H. Früchtl, N. V. Richardson, F. Esch, U. Heiz, U. Landman, and R. Schaub. Ethene to graphene: Surface catalyzed chemical pathways, intermediates, and assembly. *The Journal of Physical Chemistry C*, 121(17):9413–9423, 2017. URL https://doi.org/10.1021/acs.jpcc.7b01999.

[436] B. T. Wang, M. A. Petrukhina, and E. R. Margine. Electronic transport properties of selected carbon π-bowls with different size, curvature and solid state packing. *Carbon*, 94:174–180, 2015. URL https://doi.org/10.1016/j.carbon.2015.06.041.

[437] C. Wang, T. Huddle, C. H. Huang, W. Zhu, R. L. Vander Wal, E. H. Lester, and J. P. Mathews. Improved quantification of curvature in high-resolution transmission electron microscopy lattice fringe micrographs of soots. *Carbon*, 117:174–181, 2017. URL https://doi.org/10.1016/j.carbon.2017.02.059.

[438] H. Wang. Formation of nascent soot and other condensed-phase materials in flames. *Proceedings of the Combustion Institute*, 33(1):41–67, 2011. doi: 10.1016/j.proci. 2010.09.009.

[439] H. Wang and M. Frenklach. A detailed kinetic modeling study of aromatics formation in laminar premixed acetylene and ethylene flames. *Combustion and Flame*, 110(1-2): 173–221, 1997. URL https://doi.org/10.1016/S0010-2180(97)00068-0.

[440] H. Wang, B. Weiner, and M. Frenklach. Theoretical Study of Reaction between Phenylvinyleum Ion and Acetylene. *Journal of Physical Chemistry*, 97(40):10364–10371, 1993. URL https://doi.org/10.1021/J100142a017.

[441] S. Wang, D. Wu, B. Yang, E. Ruckenstein, and H. Chen. Semimetallic carbon honeycombs: New three-dimensional graphene allotropes with Dirac cones. *Nanoscale*, 10 (6):2748–2754, 2018. URL https://doi.org/10.1039/c7nr07824b.

[442] W. Wang and Z. Li. Potential barrier of graphene edges. *Journal of Applied Physics*, 109(11):114308, 2011. URL https://doi.org/10.1063/1.3587186.

[443] Y. Wang and S. H. Chung. Soot formation in laminar counterflow flames. *Progress in Energy and Combustion Science*, 74:152–238, 2019. URL https://doi.org/10.1016/j. pecs.2019.05.003.

[444] P. Weilmünster, A. Keller, and K.-H. Homann. Large molecules, radicals, ions, and small soot particles in fuel-rich hydrocarbon flames: Part I: positive ions of polycyclic aromatic hydrocarbons (PAH) in low-pressure premixed flames of acetylene and oxygen. *Combustion and Flame*, 116(1-2):62–83, 1999. URL https://doi.org/10.1016/S0010-2180(01)00310-8.

[445] C. F. v. Weizsäcker. Zur Theorie der Kernmassen. *Zeitschrift für Physik*, 96(7-8): 431–458, 1935. URL https://doi.org/10.1007/BF01337700.

[446] R. Whitesides and M. Frenklach. Detailed kinetic Monte Carlo simulations of graphene-edge growth. *The Journal of Physical Chemistry A*, 114(2):689–703, 2010. URL https://doi.org/10.1021/jp906541a.

[447] R. Whitesides and M. Frenklach. Effect of reaction kinetics on graphene-edge morphology and composition. *Zeitschrift für Physikalische Chemie*, 229(4), 2015. URL https://doi.org/10.1515/zpch-2014-0633.

[448] R. Whitesides, D. Domin, R. Salomón-Ferrer, W. A. Lester, and M. Frenklach. Embedded-ring migration on graphene zigzag edge. *Proceedings of the Combustion Institute*, 32 I(1):577–583, 2009. URL https://doi.org/10.1016/j.proci.2008.06.096.

[449] D. Wong, R. Whitesides, C. Schuertz, and M. Frenklach. Molecular dynamics simulations of PAH dimerization. In H. Bockhorn, A. D'Anna, A. Sarofim, and H. Wang, editors, *Combustion Generated Fine Carbonaceous Particles*, pages 247–257. KIT Scientific Publishing Karlsruhe, 2009.

[450] T. C. Wu, H. J. Hsin, M. Y. Kuo, C. H. Li, and Y. T. Wu. Synthesis and Structural Analysis of a Highly Curved Buckybowl Containing Corannulene and Sumanene Fragments. *Journal of the American Chemical Society*, 133(41):16319–16321, 2011. URL https://doi.org/10.1021/ja2067725.

[451] T. C. Wu, M. K. Chen, Y. W. Lee, M. Y. Kuo, and Y. T. Wu. Bowl-shaped fragments of C_{70} or higher fullerenes: Synthesis, structural analysis, and inversion dynamics. *Angewandte Chemie - International Edition*, 52(4):1289–1293, 2013. URL https://doi.org/10.1002/anie.201208200.

[452] X. Z. Wu, Y. R. Yao, M. M. Chen, H. R. Tian, J. Xiao, Y. Y. Xu, M. S. Lin, L. Abella, C. B. Tian, C.-L. Gao, Q. Zhang, S. Y. Xie, R. B. Huang, and L. S. Zheng. Formation of Curvature Subunit of Carbon in Combustion. *Journal of the American Chemical Society*, 138(30):9629–9633, 2016. URL https://doi.org/10.1021/jacs.6b04898.

[453] F. Xu, H. Yu, A. Sadrzadeh, and B. I. Yakobson. Riemann surfaces of carbon as graphene nanosolenoids. *Nano Letters*, 16(1):34–39, 2016. URL https://doi.org/10.1021/acs.nanolett.5b02430.

[454] Z. Xu, Z. Liang, and F. Ding. Isomerization of sp^2-hybridized carbon nanomaterials: structural transformation and topological defects of fullerene, carbon nanotube, and graphene. *Wiley Interdisciplinary Reviews: Computational Molecular Science*, 7(2): e1283, 2017. URL https://doi.org/10.1002/wcms.1283.

[455] Y. Yamaguchi and S. Maruyama. A fullerene formation model proposed from molecular dynamics simulations. In *International Heat Transfer Conference Digital Library*. Begel House Inc., 1998.

[456] H. Yang, A. J. Mayne, M. Boucherit, G. Comtet, G. Dujardin, and Y. Kuk. Quantum interference channeling at graphene edges. *Nano Letters*, 10(3):943–947, 2010. URL https://doi.org/10.1021/nl9038778.

[457] E. K. Yapp, C. G. Wells, J. Akroyd, S. Mosbach, R. Xu, and M. Kraft. Modelling PAH curvature in laminar premixed flames using a detailed population balance model. *Combustion and Flame*, 176:172–180, 2017. URL https://doi.org/10.1016/j.combustflame.2016.10.004.

[458] O. V. Yazyev and Y. P. Chen. Polycrystalline graphene and other two-dimensional materials. *Nature Nanotechnology*, 9(10):755–767, 2014. URL https://doi.org/10.1038/nnano.2014.166.

[459] C. Yeretzian, K. Hansen, F. Diederichi, and R. L. Whetten. Coalescence reactions of fullerenes. *Nature*, 359(6390):44–47, 1992. URL https://doi.org/10.1038/359044a0.

[460] N. Yoshizawa, Y. Yamada, and M. Shiraishi. TEM lattice images and their evaluation by image analysis for activated carbons with disordered microtexture. *Journal of Materials Science*, 33(1):199–206, 1998. URL https://doi.org/10.1023/A:1004322402779.

[461] H. Yuan, W. Kong, F. Liu, and D. Chen. Study on soot nucleation and growth from PAHs and some reactive species at flame temperatures by reaxff molecular dynamics. *Chemical Engineering Science*, 195:748 – 757, 2019. URL https://doi.org/10.1016/j.ces.2018.10.020.

[462] A. V. Zabula, A. S. Filatov, S. N. Spisak, A. Y. Rogachev, and M. A. Petrukhina. A Main Group Metal Sandwich: Five Lithium Cations Jammed Between Two Corannulene Tetraanion Decks. *Science*, 333(6045):1008–1011, 2011. URL https://doi.org/10.1126/science.1208686.

[463] C. Zhang, C. Zhang, Y. Ma, and X. Xue. Imaging the C black formation by acetylene pyrolysis with molecular reactive force field simulations. *Physical Chemistry Chemical Physics*, 17(17):11469–11480, 2015. URL https://doi.org/10.1039/C5CP00926J.

[464] H. B. Zhang, X. You, H. Wang, and C. K. Law. Dimerization of polycyclic aromatic hydrocarbons in soot nucleation. *The Journal of Physical Chemistry A*, 118(8):1287–1292, 2014. URL https://doi.org/10.1021/jp411806q.

[465] J. Zhang, M. Terrones, C. R. Park, R. Mukherjee, M. Monthioux, N. Koratkar, Y. S. Kim, R. Hurt, E. Frackowiak, T. Enoki, et al. Carbon science in 2016: Status, challenges and perspectives. *Carbon*, 98(70):708–732, 2016. URL https://doi.org/10.1016/j.carbon.2015.11.060.

[466] L. Zhang, F. Zhang, X. Yang, G. Long, Y. Wu, T. Zhang, K. Leng, Y. Huang, Y. Ma, A. Yu, et al. Porous 3D graphene-based bulk materials with exceptional high surface area and excellent conductivity for supercapacitors. *Scientific reports*, 3:1408, 2013. URL https://doi.org/10.1038/srep01408.

[467] W. Zhang, C. Shao, and S. M. Sarathy. Analyzing the solid soot particulates formed in a fuel-rich flame by solvent-free MALDI FT ICR mass spectrometry. *Rapid Communications in Mass Spectrometry*, 2019. URL https://doi.org/10.1002/rcm.8596.

[468] G. A. Zickler, T. Schöberl, O. Paris, T. Schoberl, O. Paris, T. Schoeberl, O. Paris, T. Schöberl, T. Schoberl, and O. Paris. Mechanical properties of pyrolysed wood: a nanoindentation study. *Philosophical Magazine*, 86(10):1373–1386, 2006. URL https://doi.org/10.1080/14786430500431390.

[469] P. Zubko, G. Catalan, and A. K. Tagantsev. Flexoelectric Effect in Solids. *Annual Review of Materials Research*, 43(1):387–421, 2013. URL https://doi.org/10.1146/annurev-matsci-071312-121634.

Appendix A

Hartree-Fock calculation

```python
#! /usr/bin/python3
# Hartree Fock calculation of HeH+ based on the book by Szabo
    and Ostlund
# Jacob Martin

import numpy as np
import scipy.special as sp

def S_int(A,B,Rab2):
    """
    Calculates the overlap between two gaussian functions

    """
    return (np.pi/(A+B))**1.5*np.exp(-A*B*Rab2/(A+B))

def T_int(A,B,Rab2):
    """
    Calculates the kinetic energy integrals for un-normalised
        primitives

    """
    return A*B/(A+B)*(3.0-2.0*A*B*Rab2/(A+B))*(np.pi/(A+B))
        **1.5*np.exp(-A*B*Rab2/(A+B))

def V_int(A,B,Rab2,Rcp2,Zc):
    """
    Calculates the un-normalised nuclear attraction integrals
    """
    V = 2.0*np.pi/(A+B)*F0((A+B)*Rcp2)*np.exp(-A*B*Rab2/(A+B))
    return -V*Zc

# Mathematical functions
```

```python
30
31   def F0(t):
32       """
33       F function for 1s orbital
34       """
35       if (t<1e-6):
36           return 1.0-t/3.0
37       else:
38           return 0.5*(np.pi/t)**0.5*sp.erf(t**0.5)
39
40   def erf(t):
41       """
42       Approximation for the error function
43       """
44       P = 0.3275911
45       A = [0.254829592, -0.284496736, 1.421413741, -1.453152027,
           1.061405429]
46       T = 1.0/(1+P*t)
47       Tn=T
48       Poly = A[0]*Tn
49       for i in range(1,5):
50           Tn=Tn*T
51           Poly=Poly*A[i]*Tn
52       return 1.0-Poly*np.exp(-t*t)
53
54   def TwoE(A,B,C,D,Rab2,Rcd2,Rpq2):
55       """
56       Calculate two electron integrals
57       A,B,C,D are the exponents alpha, beta, etc.
58       Rab2 equals squared distance between centre A and centre B
59       """
60       return 2.0*(np.pi**2.5)/((A+B)*(C+D)*np.sqrt(A+B+C+D))*F0
           ((A+B)*(C+D)*Rpq2/(A+B+C+D))*np.exp(-A*B*Rab2/(A+B)-C*D
           *Rcd2/(C+D))
61
62   def Intgrl(N,R,Zeta1,Zeta2,Za,Zb):
63       """
64       Declares the variables and compiles the integrals.
65       """
66
67       global S12,T11,T12,T22,V11A,V12A,V22A,V11B,V12B,V22B,V1111
           ,V2111,V2121,V2211,V2221,V2222
68
69
70       S12 = 0.0
71       T11 = 0.0
```

```
72        T12 = 0.0
73        T22 = 0.0
74        V11A = 0.0
75        V12A = 0.0
76        V22A = 0.0
77        V11B = 0.0
78        V12B = 0.0
79        V22B = 0.0
80        V1111 = 0.0
81        V2111 = 0.0
82        V2121 = 0.0
83        V2211 = 0.0
84        V2221 = 0.0
85        V2222 = 0.0
86
87        R2 = R*R
88
89        # The coefficients for the contracted Gaussian functions
              are below
90        Coeff = np.array([[1.00000,0.0000000,0.000000],
91                          [0.678914,0.430129,0.000000],
92                          [0.444635,0.535328,0.154329]])
93
94        Expon = np.array([[0.270950,0.000000,0.000000],
95                          [0.151623,0.851819,0.000000],
96                          [0.109818,0.405771,2.227660]])
97        D1 = np.zeros([3])
98        A1 = np.zeros([3])
99        D2 = np.zeros([3])
100       A2 = np.zeros([3])
101
102       # This loop constructs the contracted Gaussian functions
103       for i in range(N):
104           A1[i] = Expon[N-1,i]*(Zeta1**2)
105           D1[i] = Coeff[N-1,i]*((2.0*A1[i]/np.pi)**0.75)
106           A2[i] = Expon[N-1,i]*(Zeta2**2)
107           D2[i] = Coeff[N-1,i]*((2.0*A2[i]/np.pi)**0.75)
108
109       # Calculate one electron integrals
110       # Centre A is first atom centre B is second atom
111       # Origin is on second atom
112       # V12A - off diagonal nuclear attraction to centre A etc.
113       for i in range(N):
114           for j in range(N):
115               # Rap2 - squared distance between centre A and
                      centre P
```

```
116            Rap = A2[j]*R/(A1[i]+A2[j])
117            Rap2 = Rap**2
118            Rbp2 = (R-Rap)**2
119            S12 = S12 + S_int(A1[i],A2[j],R2)*D1[i]*D2[j]
120            T11 = T11 + T_int(A1[i],A1[j],0.0)*D1[i]*D1[j]
121            T12 = T12 + T_int(A1[i],A2[j],R2)*D1[i]*D2[j]
122            T22 = T22 + T_int(A2[i],A2[j],0.0)*D2[i]*D2[j]
123            V11A = V11A + V_int(A1[i],A1[j],0.0,0.0,Za)*D1[i]*
                   D1[j]
124            V12A = V12A + V_int(A1[i],A2[j],R2,Rap2,Za)*D1[i]*
                   D2[j]
125            V22A = V22A + V_int(A2[i],A2[j],0.0,R2,Za)*D2[i]*
                   D2[j]
126            V11B = V11B + V_int(A1[i],A1[j],0.0,R2,Zb)*D1[i]*
                   D1[j]
127            V12B = V12B + V_int(A1[i],A2[j],R2,Rbp2,Zb)*D1[i]*
                   D2[j]
128            V22B = V22B + V_int(A2[i],A2[j],0.0,0.0,Zb)*D2[i]*
                   D2[j]
129
130    # Calculate two electron integrals
131
132    for i in range(N):
133        for j in range(N):
134            for k in range(N):
135                for l in range(N):
136                    Rap = A2[i]*R/(A2[i]+A1[j])
137                    Rbp = R - Rap
138                    Raq = A2[k]*R/(A2[k]+A1[l])
139                    Rbq = R - Raq
140                    Rpq = Rap - Raq
141                    Rap2 = Rap*Rap
142                    Rbp2 = Rbp*Rbp
143                    Raq2 = Raq*Raq
144                    Rbq2 = Rbq*Rbq
145                    Rpq2 = Rpq*Rpq
146                    V1111 = V1111 + TwoE(A1[i],A1[j],A1[k],A1[
                           l],0.0,0.0,0.0)*D1[i]*D1[j]*D1[k]*D1[l]
147                    V2111 = V2111 + TwoE(A2[i],A1[j],A1[k],A1[
                           l],R2,0.0,Rap2)*D2[i]*D1[j]*D1[k]*D1[l]
148                    V2121 = V2121 + TwoE(A2[i],A1[j],A2[k],A1[
                           l],R2,R2,Rpq2)*D2[i]*D1[j]*D2[k]*D1[l]
149                    V2211 = V2211 + TwoE(A2[i],A2[j],A1[k],A1[
                           l],0.0,0.0,R2)*D2[i]*D2[j]*D1[k]*D1[l]
150                    V2221 = V2221 + TwoE(A2[i],A2[j],A2[k],A1[
                           l],0.0,R2,Rbq2)*D2[i]*D2[j]*D2[k]*D1[l]
```

```python
                            V2222 = V2222 + TwoE(A2[i],A2[j],A2[k],A2[
                                l],0.0,0.0,0.0)*D2[i]*D2[j]*D2[k]*D2[l]
    return

def Colect(N,R,Zeta1,Zeta2,Za,Zb):
    """
    Takes the basic integrals and assembles the relevant
        matrices,
    that are S,H,X,XT and Two electron integrals
    """
    # Form core hamiltonian
    H[0,0] = T11+V11A+V11B
    H[0,1] = T12+V12A+V12B
    H[1,0] = H[0,1]
    H[1,1] = T22+V22A+V22B

    # Form overlap matrix
    S[0,0] = 1.0
    S[0,1] = S12
    S[1,0] = S12
    S[1,1] = 1.0

    # This is S^-1/2
    X[0,0] = 1.0/np.sqrt(2.0*(1.0+S12))
    X[1,0] = X[0,0]
    X[0,1] = 1.0/np.sqrt(2.0*(1.0-S12))
    X[1,1] = -X[0,1]

    # This is the coulomb and exchange term (aa|bb) and (ab|ba
        )
    TT[0,0,0,0] = V1111
    TT[1,0,0,0] = V2111
    TT[0,1,0,0] = V2111
    TT[0,0,1,0] = V2111
    TT[0,0,0,1] = V2111
    TT[1,0,1,0] = V2121
    TT[0,1,1,0] = V2121
    TT[1,0,0,1] = V2121
    TT[0,1,0,1] = V2121
    TT[1,1,0,0] = V2211
    TT[0,0,1,1] = V2211
    TT[1,1,1,0] = V2221
    TT[1,1,0,1] = V2221
    TT[1,0,1,1] = V2221
    TT[0,1,1,1] = V2221
    TT[1,1,1,1] = V2222
```

```
194
195  def SCF(N,R,Zeta1,Zeta2,Za,Zb,G):
196      """
197      Performs the SCF iterations
198      """
199      Crit = 1e-11 # Convergence critera
200      Maxit = 250 # Maximum number of iterations
201      Iter=0
202
203      ######## STEP 1. Guess an initial density matrix ########
204      # Use core hamiltonian for initial guess of F, I.E. (P=0)
205      P = np.zeros([2,2])
206
207      Energy = 0.0
208
209      while (Iter<Maxit):
210          Iter += 1
211          print(Iter)
212
213          ######## STEP 2. calculate the Fock matrix ########
214          # Form two electron part of Fock matrix from P
215          G = np.zeros([2,2]) # This is the two electron
                 contribution in the equations above
216          for i in range(2):
217              for j in range(2):
218                  for k in range(2):
219                      for l in range(2):
220                          G[i,j]=G[i,j]+P[k,l]*(TT[i,j,k,l]-0.5*
                              TT[i,j,k,l])
221
222          # Add core hamiltonian H^CORE to get fock matrix
223          F = H+G
224
225          # Calculate the electronic energy
226          Energy = np.sum(0.5*P*(H+F))
227
228          print('Electronic energy = ',Energy)
229
230          ######## STEP 3. Calculate F' (remember S^-1/2 is X
                 and S^1/2 is X.T) ########
231          G = np.matmul(F,X)
232          Fprime = np.matmul(X.T,G)
233
234          ######## STEP 4. Solve the eigenvalue problem ########
235          # Diagonalise transformed Fock matrix
236          Diag(Fprime,Cprime,E)
```

```python
237
238            ######## STEP 5. Calculate the molecular orbitals
                   coefficients ########
239            # Transform eigen vectors to get matrix C
240            C = np.matmul(X,Cprime)
241
242            ######## STEP 6. Calculate the new density matrix from
                   the old P ########
243            Oldp = np.array(P)
244            P= np.zeros([2,2])
245
246            # Form new density matrix
247            for i in range(2):
248                for j in range(2):
249                    #Save present density matrix before creating a
                           new one
250                    for k in range(1):
251                        P[i,j] += 2.0*C[i,k]*C[j,k]
252
253            ######## STEP 7. Check to see if the energy has
                   converged ########
254            Delta = 0.0
255            # Calculate delta the difference between the old
                   density matrix Old P and the new P
256            Delta = (P-Oldp)
257            Delta = np.sqrt(np.sum(Delta**2)/4.0)
258            print("Delta",Delta)
259
260            #Check for convergence
261            if (Delta<Crit):
262                # Add nuclear repulsion to get the total energy
263                Energytot = Energy+Za*Zb/R
264                print("Calculation converged with electronic
                       energy:",Energy)
265                print("Calculation converged with total energy:",
                       Energytot)
266                print("Density matrix", P)
267                print("Mulliken populations",np.matmul(P,S))
268                print("Coeffients",C)
269
270                break
271
272 def FormG():
273     """
274     Calculate the G matrix from the density matrix and two
           electron integals
```

```python
275          """
276          for i in range(2):
277              for j in range(2):
278                  G[i,j]=0.0
279                  for k in range(2):
280                      for l in range(2):
281                          G[i,j]=G[i,j]+P[k,l]*(TT[i,j,k,l]-0.5*TT[i
                                 ,j,k,l])

282
283      def Mult(A,B,C_,IM,M):
284          """
285          Multiples two square matrices A and B to get C
286          """
287          for i in range(M):
288              for j in range(M):
289                  for k in range(M):
290                      C_[i,j] = A[i,j]*B[i,j]

291
292      def Diag(Fprime,Cprime,E):
293          """
294          Diagonalises F to give eigenvectors in C and eigen values
                 in E, theta is the angle describing the solution
295          """
296          #
297          import math
298          # Angle for heteronuclear diatonic
299          Theta = 0.5*math.atan(2.0*Fprime[0,1]/(Fprime[0,0]-Fprime
                 [1,1]))
300          #print('Theta', Theta)

301
302          Cprime[0,0] = np.cos(Theta)
303          Cprime[1,0] = np.sin(Theta)
304          Cprime[0,1] = np.sin(Theta)
305          Cprime[1,1] = -np.cos(Theta)

306
307          E[0,0] = Fprime[0,0]*np.cos(Theta)**2+Fprime[1,1]*np.sin(
                 Theta)**2+Fprime[0,1]*np.sin(2.0*Theta)
308          E[1,1] = Fprime[1,1]*np.cos(Theta)**2+Fprime[0,0]*np.sin(
                 Theta)**2-Fprime[0,1]*np.sin(2.0*Theta)

309
310          if (E[1,1] <= E[0,0]):
311              Temp = E[1,1]
312              E[1,1] = E[0,0]
313              E[0,0] = Temp
314              Temp = Cprime[0,1]
315              Cprime[0,1] = Cprime[0,0]
```

```
316            Cprime [0 ,0] = Temp
317            Temp = Cprime [1 ,1]
318            Cprime [1 ,1]= Cprime [1 ,0]
319            Cprime [1 ,0]= Temp
320        return
321
322    def HFCALC (N ,R , Zeta1 , Zeta2 ,Za ,Zb ,G ):
323        """
324        Calculates the integrals constructs the matrices and then
                runs the SCF calculation
325        """
326        # Calculate one and two electron integrals
327        Intgrl (N ,R , Zeta1 , Zeta2 ,Za ,Zb )
328        # Put all integals into array
329        Colect (N ,R , Zeta1 , Zeta2 ,Za ,Zb )
330        # Perform the SCF calculation
331        SCF (N ,R , Zeta1 , Zeta2 ,Za ,Zb ,G )
332        return
333
334    """
335    Let 's set up the variables and perform the calculations
336    """
337    global H ,S ,X ,XT ,TT ,G ,C ,P , Oldp ,F , Fprime , Cprime ,E ,Zb
338
339    H = np . zeros ([2 ,2])
340    S = np . zeros ([2 ,2])
341    X = np . zeros ([2 ,2])
342    XT = np . zeros ([2 ,2])
343    TT = np . zeros ([2 ,2 ,2 ,2])
344    G = np . zeros ([2 ,2])
345    C = np . zeros ([2 ,2])
346
347    P = np . zeros ([2 ,2])
348    Oldp = np . zeros ([2 ,2])
349    F = np . zeros ([2 ,2])
350    Fprime = np . zeros ([2 ,2])
351    Cprime = np . zeros ([2 ,2])
352    E = np . zeros ([2 ,2])
353
354    Energy = 0.0
355    Delta = 0.0
356
357    N = 3
358    R = 1.4632
359    Zeta1 = 2.0925
360    Zeta2 = 1.24
```

```
361  Za = 2.0
362  Zb = 1.0
363  HFCALC(N,R,Zeta1,Zeta2,Za,Zb,G)
```